

*ÉCOLE DOCTORALE de Physique et Chimie Physique*  
UMR 7504

**THÈSE** présentée par :  
**Matteo BALESTRIERI**

soutenue le : **15 octobre 2014**

pour obtenir le grade de : **Docteur de l'université de Strasbourg**  
Discipline/ Spécialité : Sciences des Matériaux

**Oxydes transparents conducteurs et  
convertisseurs de photons pour des  
applications photovoltaïques :  
les cas de l'oxyde de zinc et de l'oxyde de  
cérium dopés aux terres rares**

**THÈSE dirigée par :**  
**M. COLIS Silviu**

Professeur associé, IPCMS – CNRS, université de Strasbourg

**RAPPORTEURS :**  
**M. PORTIER Xavier**  
**M. RINNERT Hervé**

Professeur, ENSICAEN, Caen  
Professeur, IJL – université de Lorraine, Nancy

**AUTRES MEMBRES DU JURY :**

**M. SLAOUI Abdelilah**  
**M. DINIA Aziz**  
**M. POORTMANS Jozef**

Docteur, ICube – CNRS, université de Strasbourg  
Professeur, IPCMS – CNRS, université de Strasbourg  
Professeur associé, Imec – KU Leuven, Belgium



English title

**Transparent conductive oxides with photon converting properties in view of photovoltaic applications: the cases of rare earth-doped zinc oxide and cerium oxide**



# TABLE OF CONTENTS

|  |           |
|--|-----------|
| <b>Introduction</b> .....                                    | <b>1</b>  |
| <b>1 Context</b> .....                                       | <b>3</b>  |
| 1.1 Photovoltaic market perspectives.....                    | 3         |
| 1.2 Loss processes in single-junction solar cells.....       | 4         |
| 1.3 Third generation PV technologies .....                   | 5         |
| 1.4 Photon management.....                                   | 7         |
| 1.4.1 Down shifting layers .....                             | 9         |
| 1.4.2 Luminescent solar concentrators (LSC).....             | 10        |
| 1.4.3 Down- and up-conversion layers.....                    | 10        |
| 1.4.4 Transfer mechanisms .....                              | 13        |
| 1.4.5 UC mechanisms .....                                    | 14        |
| 1.4.6 DC mechanisms .....                                    | 15        |
| 1.4.7 DC or UC?.....   | 16        |
| 1.4.8 Candidate materials for DC and DS .....                | 17        |
| 1.5 Rare earths .....  | 19        |
| 1.5.1 Photonic applications of rare earth materials.....     | 20        |
| 1.5.2 Spectroscopy of rare earth ions .....                  | 21        |
| 1.5.3 Energy level diagram of 4f states in lanthanides ..... | 24        |
| 1.5.4 Transitions between 4f states .....                    | 26        |
| 1.5.5 The crystal field .....                                | 28        |
| 1.5.6 The importance of the host matrix .....                | 29        |
| 1.6 ZnO .....  | 34        |
| 1.7 CeO <sub>2</sub> .....                                   | 37        |
| <b>2 Experimental techniques</b> .....                       | <b>43</b> |
| 2.1 Thin film deposition techniques.....                     | 43        |
| 2.1.1 Sputtering.....  | 43        |
| 2.1.2 Pulsed laser deposition (PLD).....                     | 44        |
| 2.2 Powder preparation and PLD target sintering .....        | 45        |
| 2.3 Annealing of ZnO thin films.....                         | 46        |
| 2.4 Thin film characterization techniques.....               | 46        |
| 2.4.1 Structural and morphological characterization.....     | 46        |

|  |    |
|--|----|
| X-ray diffraction (XRD).....   | 46 |
| Transmission electron microscopy (TEM) .....                         | 49 |
| Scanning electron microscopy (SEM) .....                             | 51 |
| Atomic force microscopy (AFM).....                                   | 51 |
| Rutherford backscattering spectroscopy (RBS).....                    | 52 |
| Near-edge X-ray absorption fine-structure spectroscopy (NEXAFS)..... | 53 |
| Atom-probe tomography .....  | 54 |
| 2.4.2 Optical characterization .....                                 | 54 |
| Spectrophotometry .....  | 54 |
| Photoluminescence spectroscopy.....                                  | 55 |
| Raman spectroscopy .....   | 57 |
| Ellipsometry.....  | 58 |
| Solar cell quantum efficiency .....                                  | 60 |
| 2.4.3 Electrical characterization .....                              | 61 |

## **Results and discussion - Overview.....63**

### **3 Results and discussion: Zinc Oxide .....65**

|   |     |
|---|-----|
| 3.1 Structural and morphological properties of sputtered ZnO..... | 65  |
| 3.1.1 XRD data and structural properties of the films.....        | 66  |
| 3.1.2 TEM observations .....                                      | 70  |
| 3.1.3 Morphology of the films.....                                | 72  |
| 3.1.4 Rare earth distribution in ZnO films .....                  | 74  |
| 3.1.5 NEXAFS data of ZnO(:RE) films .....                         | 76  |
| 3.1.6 Concluding remarks.....                                     | 80  |
| 3.2 Basic optical properties of ZnO(:RE) films .....              | 80  |
| 3.3 Electrical properties of ZnO:RE films .....                   | 84  |
| 3.4 Luminescence properties of ZnO(:RE) films .....               | 85  |
| 3.4.1 Introduction.....   | 85  |
| 3.4.2 Yb-doped ZnO.....   | 87  |
| 3.4.3 Pr-doped ZnO.....   | 95  |
| 3.4.4 Nd-doped ZnO .....  | 101 |
| 3.4.5 Concluding remarks.....                                     | 113 |

### **4 Results and discussion: Cerium Oxide .....115**

|   |     |
|---|-----|
| 4.1 RE-doped CeO <sub>2</sub> pellets.....                                      | 115 |
| 4.1.1 Structural and morphological properties of CeO <sub>2</sub> pellets ..... | 115 |

|          |   |            |
|----------|---|------------|
| 4.1.2    | Optical properties of CeO <sub>2</sub> pellets.....                         | 117        |
| 4.2      | RE-doped CeO <sub>2</sub> thin films .....                                  | 120        |
| 4.2.1    | Structural and morphological properties of CeO <sub>2</sub> thin films..... | 120        |
| 4.2.2    | Basic optical properties of CeO <sub>2</sub> (:RE) thin films .....         | 122        |
| 4.2.3    | Luminescence properties of RE-doped CeO <sub>2</sub> .....                  | 124        |
| <b>5</b> | <b>Converting layers tested on solar cells.....</b>                         | <b>127</b> |
| <b>6</b> | <b>Conclusions and perspectives.....</b>                                    | <b>129</b> |
|          | <b>APPENDIX A - Russell-Saunders term symbols.....</b>                      | <b>133</b> |
|          | <b>APPENDIX B - The 32 crystallographic point groups.....</b>               | <b>135</b> |
|          | <b>APPENDIX C – d-spacings and lattice constants .....</b>                  | <b>137</b> |
|          | <b>APPENDIX D – Optical absorption and band structure .....</b>             | <b>138</b> |
|          | <b>References .....</b>   | <b>143</b> |



## Introduction

Contrarily to the alternative solar cell technologies, the efficiency of solar cells based on crystalline silicon (representing 90% of the market) is close to the theoretical limit. Any technology that could increase this limit is likely to have a great impact not only on the future of these solar cells, but also of the whole photovoltaic (PV) market.

The technology described in this work is based on the simple, but audacious idea that the solar spectrum can be modified and adapted to the solar cell. The expression “photon management” describes pretty well the processes involved, where photons can be “split”, “added” or red-shifted. Rare earths count among the best candidates to do this job and this work will deal with rare earths embedded into a thin film (ZnO or CeO<sub>2</sub>), placed on top of the solar cell. The large predominance of silicon solar cells and the well-known properties of crystalline silicon induced us to choose a silicon wafer as a substrate. However, the results are potentially useful for all single junction solar cells and other emerging technologies like organic PV, but also for other optoelectronic devices.

This work is organized as follows. The first chapter will introduce the reader to the frame in which this work has been thought. The chapter starts with a brief overview over the current state and perspectives of the photovoltaic market (section 1.1). The leading position of silicon-based solar cells in the market explains why this work will be aimed (but not limited) to the improvement of silicon solar cells. The reasons why silicon solar cells need to be improved is the subject of section 1.2. Silicon single-junction solar cells are intrinsically limited to use only about 30% of the solar energy. This has encouraged the development of new technologies that can break this limit. Some of the new concepts are outlined in section 1.3. The potential of photon converting layers as well as the mechanisms that make it possible will be outlined in section 1.4. These processes might involve organic dyes, nanodots, nanoparticles or luminescent ions and in some cases even a combination of these. This work is focused on a particular type of luminescent ions, characterized by some of the most uncommon properties of all natural elements: the rare earths. The whole section 1.5 is dedicated to explaining why rare earths can be a key material for photovoltaics and other technologies. Since the most interesting properties of these elements come from their peculiar electronic structure, this section starts with a detailed description of the electronic properties. In the second part, the influence of the environment in which these elements are placed is taken into consideration and it will become clear that for photovoltaic applications the rare earths must be inserted into an appropriate host. This work will deal with two hosts: ZnO and CeO<sub>2</sub>. An overview of the principal characteristics of ZnO is given in sections 1.6, while CeO<sub>2</sub> is described in section 1.7. Both materials are good candidates as transparent windows on silicon devices (although only ZnO is widely used), but they provide two very different environments for rare earths. This difference is particularly useful to understand the real potential of this kind of photon conversion and motivate the choice of the two host materials.

The second chapter is dedicated to the experimental techniques used to produce and analyze the samples. The next two chapters are dedicated each to a single host material (Chapter 3 to ZnO and Chapter 4 to CeO<sub>2</sub>). There, the structural, electrical and optical properties of our films will be presented and thoroughly discussed, but without insisting on the effective photon-converting efficiency of the layers. This topic will be treated in Chapter 5, where the results obtained when the best films are integrated on silicon solar cells will be reported.

Finally, in Chapter 6 the results obtained with RE-doped ZnO and CeO<sub>2</sub> will be summarized and the perspectives of these systems in photovoltaics will be evaluated.



# 1 CONTEXT

## 1.1 Photovoltaic market perspectives

One of the greatest challenges in today world is to respond to the increasing energy demand related to human activities and demographic growth, in a context where fossil fuels become scarcer and nuclear power withstands a particularly negative public opinion due to security and environmental concerns. Nuclear fusion being still quite far from energy production, the only viable alternative is that of renewable energies. Thus, double-digit growth rates have been observed in the last decade for some renewable energy technologies [1].

In particular, solar energy has huge potential to fill a very large part of total energy needs economically in a secure and sustainable manner and it is no coincidence that solar energy has been the fastest-growing energy sector in the last few years [2].

The challenge for collecting renewable energy is to do so in a manner so efficient and cheap that its obvious advantages (it is inexhaustible, most often not import-dependent and does not pollute much) fully compensate for the initial disadvantage of lesser convenience due to the relatively low density of most renewable energy flows<sup>1</sup>. However, prospects for reaching competitive levels have improved dramatically in the last few years, and the highest energy density of all renewables by land surface area is offered by direct solar conversion into heat or electricity, and possibly fuels [2].

While solar energy is abundant, it represents a tiny fraction of the world's current energy mix (Figures 1 and 2).

Among solar energy technologies, photovoltaics (PV) is developing rapidly and its costs are falling just as fast. Like wind energy, solar energy is a variable renewable and its development strongly depends on the storage options available on the market. For this reason, its contribution to the energy mix of the future might be underestimated in some scenarios.

It is interesting to analyze in what proportion the PV market is shared by the different technologies. Still in 2011, the PV market was dominated by solar cells based on crystalline silicon (90%), the other 10% of the market being shared by thin-film-based modules (SERIS market research). Other technologies, such as organic and tandem solar cells, occupied only a negligible part of the module production.

This privileged position of silicon-based solar cells is due to the several advantages related to the use of silicon: relatively high module efficiency (14-20%), long-term module stability (> 20 yrs), raw material abundance and non-toxicity, easy scale up possibilities, and large number of manufacturers.

The initially high manufacturing cost of crystalline silicon, which had stimulated the development of alternative technologies in the past, has fallen below 0.5 \$/W<sub>p</sub><sup>2</sup> in 2012 and is expected to reach 0.36 \$/W<sub>p</sub> in 2017 [3]. Further reduction of the module price is one of the promises of the new "mono-like" fabrication method. Therefore, it is very probable that Si-based solar cells will dominate the market also for the next decades.

---

<sup>1</sup> One liter of gasoline can deliver 35 MJ of energy. This is the amount of energy one square meter of land receives from the sun in the best conditions in approximately ten hours.

<sup>2</sup> W<sub>p</sub> indicates a module with a nominal power of 1 W.

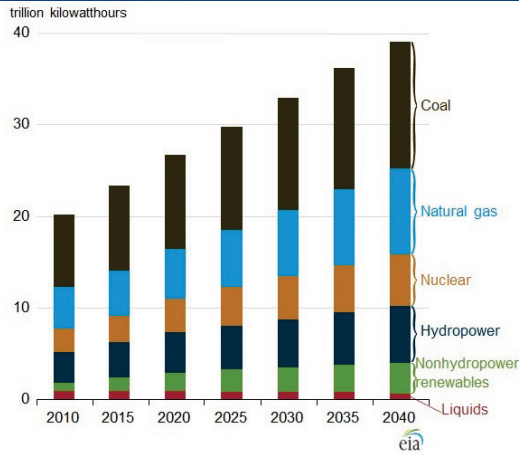


**Figure 1.1** - World net electricity generation by energy source, 2010-2040 (Source: *The International Energy Outlook 2013 (IEO2013)*)

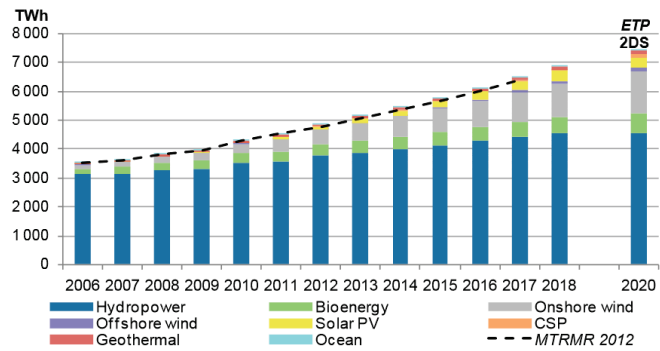


**Figure 1.2** - Global renewable electricity generation, the Medium-Term Renewable Market Report (MTRMR) 2013 projection versus the Energy Technology Perspectives 2012 (ETP2012) 2°C Scenario (2DS).

In order to understand the limits of today solar cells, an overview of the loss processes in single-junction silicon solar cells is presented in the following paragraph, which takes silicon as an example.

## 1.2 Loss processes in single-junction solar cells

The main problem characterizing single junction solar cells is that they use only a small part of the incoming solar energy. The band gap energy  $E_g$  of the semiconductor from which the PV device is fabricated establishes a fundamental upper limit for its conversion efficiency. If the cell reflectance is neglected, the two major loss mechanisms that need to be overcome to significantly enhance the device efficiencies are lattice thermalization and transparency to sub-band gap photons.

When a photon with high energy excites an electron across the band gap, the excess energy is lost as heat within the device (thermalization). This is illustrated by process 1 in Figure 1.3. The transparency of the semiconductor to sub-band gap photons is denoted as process 2.

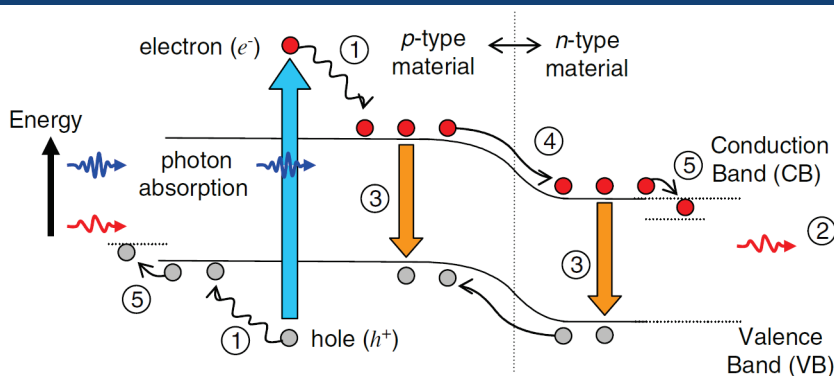


**Figure 1.3** - Loss processes in a single junction solar cell ① lattice thermalization, ② transparency, ③ recombination, ④ junction loss and ⑤ contact voltage loss [4].

A further loss mechanism is the recombination of photoexcited e-h pairs (process 3 in Figure 1.3), which can be minimized by maintaining high minority carrier lifetimes in the semiconducting material and does not contribute significantly to the theoretical efficiency limit. The voltage drops across the contacts and junction are denoted by processes 4 and 5 in Figure 1.3. Using the principle of detailed

balance between incident and escaping photons and extracted electrons, Shockley and Queisser demonstrated that the one-Sun efficiency limit for a single-junction cell, in which the absorbing material is characterized by a single band gap value, is around 31% with an optimal band gap of 1.3 eV [5]. With a slightly non-optimal band gap such as that of silicon ( $E_g = 1.12$  eV), the one-Sun efficiency limit is further reduced to 30%.

If the reflectance is taken into consideration, this value must be reduced by about ten percent points. In present-day silicon solar cells, the reflectance problem has been successfully handled thanks to texturing and anti-reflection coatings. The best lab-scale Si solar cells have a one-Sun efficiency of 25% (NREL)<sup>3</sup> and the missing 5% can be mainly ascribed to electrical losses, in particular to the recombination at contacts and interfaces. This means that silicon solar cells are very close to their theoretical limit and that if the efficiency has to be increased further, new concepts must be developed to bypass the intrinsic limits. These new concepts will put the bases for new solar cell technologies, some of which will be described in details in the following section.

### 1.3 Third generation PV technologies

Single junction solar cells based on crystalline silicon are the so-called “first generation” technology. Then, for a prolonged period starting from the early nineties, it seemed that the PV industry was on the verge to switch to a “second generation” solar cell technology based on thin films. This technology involves thin amorphous (a-Si) and microcrystalline ( $\mu\text{-Si}$ ) silicon absorber layers as well as new semiconductors such as CdTe and Cu(In,Ga)Se<sub>2</sub> (CIGS), but also organic polymers. Regardless of the semiconductor involved, this technology offered the perspective of large reduction in material costs and an increased size of the unit modules. The efficiency of these modules was expected to approach that of the first generation of modules. Today, these promises have been kept, but the strong reduction of the cost of silicon mentioned above, related to the introduction of new technologies in the manufacturing process, makes thin film solar cells less appealing. Even organic solar cells, whose production cost was expected to be very low, revealed that expensive processes are necessary in order to reach reasonable efficiencies and cell lifetimes.

In order to be competitive with other energy sources, it is crucial to use as much as possible of the low energy density of solar energy. Having theoretical efficiencies below 30%, none of the first two generations is a viable solution for the PV to be competitive in the future energy market. By comparing this value with the maximum photovoltaic conversion efficiency predicted by the Carnot limit (slightly more than 90% [6, 7]), it is clear that novel concepts have to be used in designing “third generation” PV cells. In particular, it is necessary to overcome the theoretical limits imposed by single junction solar cells, ultimately producing high-efficiency, low-cost modules.<sup>4</sup>

---

<sup>3</sup> More information about the path that led to this value can be found in M.A. Green, *The path to 25% silicon solar cell efficiency: history of silicon cell evolution*, Prog. Photovolt: Res. Appl. 2009; 17:183–189

<sup>4</sup> Recently, a new type of thin film solar cell has attracted the attention of the scientific community. Snaith’s group at the University of Oxford proved that a simple planar heterojunction solar cell incorporating vapour-deposited perovskite as the absorbing layer can have solar-to-electrical power conversion efficiencies of over 15 % (Liu, M., M.B. Johnston, and H.J. Snaith, Efficient planar heterojunction perovskite solar cells by vapour deposition. Nature, 2013. 501(7467): p. 395-398). The potential of this technology can be understood by considering that such high efficiencies have been reached with relatively small research effort and that the preparation of the absorber is almost as simple and cheap as spraying a surface. However, the perspectives of this technology are still uncertain and it will be not considered further in this work.

The easiest way to boost the efficiency limit is to address the two main loss processes described above, i.e. the lattice thermalization and the sub-band gap losses. The first idea has been to adapt the solar cell structure to the solar spectrum by juxtaposing two or more semiconductors with decreasing band gaps. This approach is that of “tandem” devices, whose working principle is represented in Figure 1.4. The cells can be operated separately, if the solar spectrum is split in its components (Figure 1.4a), or can be electrically connected, if the cells are stacked as in Figure 1.4b.

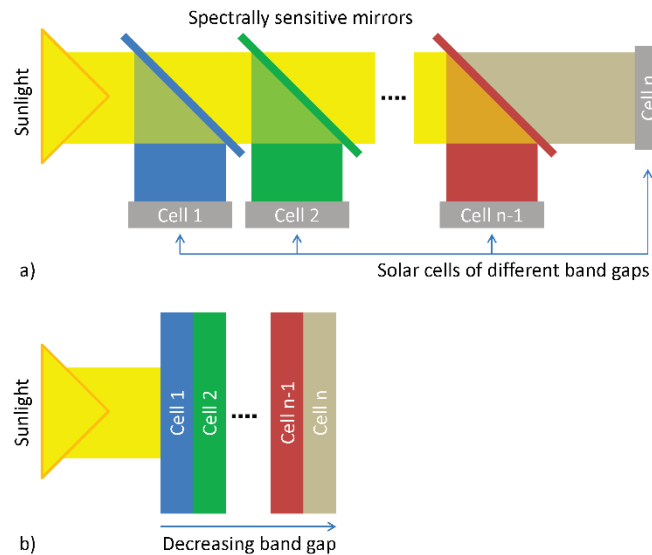


**Figure 1.4** - Tandem solar cell concepts: a) spectrum splitting and b) cell stacking.

The theoretical performance of such a device increases as the number of cells increases. Green has described the theoretical upper efficiency limits of tandem devices, being able to achieve efficiency limits ranging from 31% to 68.2% for one and an infinite number of band gaps, respectively, using unconcentrated sunlight. When operating under the maximum theoretical solar concentration of around 46,000 times, these values increase to 40.8% and 86.8%, respectively [8]. These values are calculated for an infinite stack of independently operated cells such as that of Figure 1.4a. Having to independently operate each cell is however complicated so that usually cells are designed with their current outputs matched so that they can be connected in series (Figure 1.4b) and form a “heterojunction”. A drawback of this approach is the non-trivial electrical matching of the cells and, more importantly, a design very sensitive to the spectral content of the sunlight, the total current being limited by the least efficient cell [9]. The tandem concept has been successfully applied to bulk semiconductors, but also to thin film and organic solar cells. The best results have been obtained using a stack of III-V semiconductors, but good electrical matching requires epitaxial growth of the multijunction onto expensive substrates (Ge, GaAs, InP)<sup>5</sup>. Hence, the use of solar concentrators is recommended with this type of devices not only to increase the efficiency, but also to reduce the fraction of the cell’s cost in the total system cost by substituting the area of expensive cells by less expensive collecting mirrors.

The second tandem configuration, which makes use of spectral splitters, requires less expensive solar cells that can be operated separately. However, the solar cell architecture can become quite complicated.

Apart from tandem cells, a number of better integrated “parallel” conversion approaches have been proposed, capable of similar efficiencies (hot carrier solar cells, multi electron generation ...) for a more

<sup>5</sup> The cost of a recent record efficiency (III-V) tandem solar cell (43.5%) exceeds 40,000 \$/m<sup>2</sup>.

reasonable price. An exhaustive overview of these processes is outside the purposes of this work and can be found in the work published by Green [9, 10] and Conibeer [11]. A brief overview of some of these processes will be given in the introduction of section 1.4.

Among these approaches, particularly promising is the use of photon conversion. This approach has a distinct advantage over tandem solar cells, which are characterized by a complex solar cell structure with several mismatch concerns. The idea is to adapt the solar spectrum to a particular semiconductor, and not vice versa. Unlike spectral splitters, these devices can modify the solar spectrum to adapt it to a single semiconductor. The application of this technology does not require modification of the existing single-junction solar cell as it is in principle passive and purely optical in operation.

Motivated by the predicted dominance of Si PV technologies for the next decades, the application of photon converting layers to single-junction silicon PV devices will be discussed in the following. However, the potential of this technology is even higher when applied on solar cells with a narrower and less intense spectral response.

## 1.4 Photon management

If silicon is used as semiconductor illuminated by AM1.5G<sup>6</sup> sunlight and step-like band gap absorption is assumed, the energy losses due to thermalization and sub-band gap transmittance (processes 1 and 2 in Figure 1.3) are about 32% and 19%, respectively. Figure 1.5 schematizes this picture: the gray area represents the AM1.5G solar spectrum and the green shaded area the fraction effectively used by silicon, if all other losses are neglected. This representation assumes that the energy loss due to thermalization is equivalent to a lower number of incoming photons with energy  $E_g$ . For a more detailed discussion about these losses, please refer to the work by Hirst *et al.* [12].

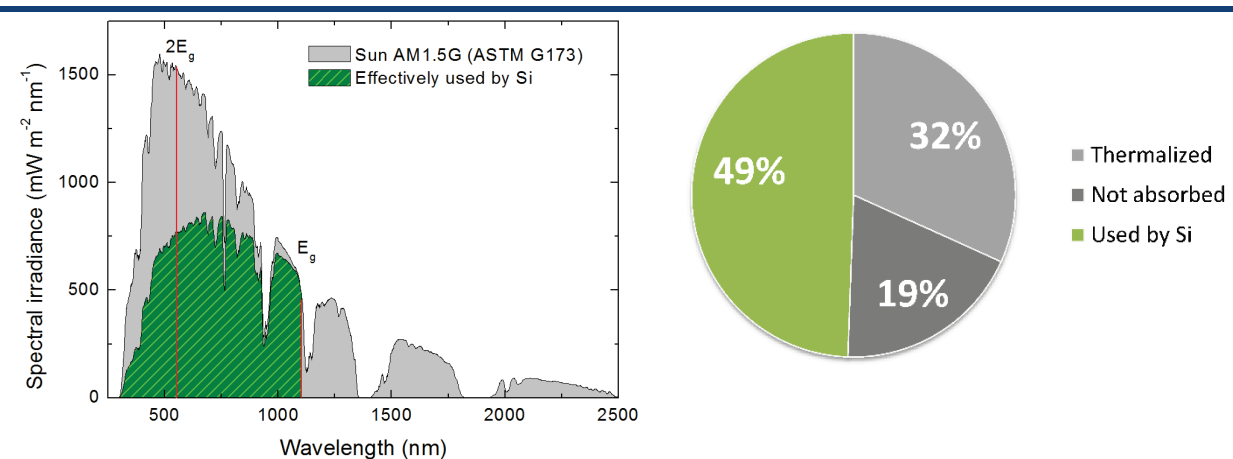


**Figure 1.5** – Fraction of the solar spectrum effectively available for current generation in a crystalline silicon absorber after the two main optical losses, namely thermalization and transmission.

Figure 1.5 also shows that part of the solar spectrum is composed of photons with an energy larger than twice the band gap of silicon. This means that the wasted energy would be enough to generate a

<sup>6</sup> The air mass (AM) coefficient defines the direct optical path length through the Earth's atmosphere, expressed as a ratio relative to the path length vertically upwards, i.e. at the zenith. As the nearly black body radiation of the sun travels through the atmosphere, chemicals interact with the sunlight and absorb certain wavelengths. Atmospheric scattering plays also a role, removing higher frequencies from sunlight. AM1.5 is almost universal when characterizing terrestrial power-generating panels because it represents quite well the overall yearly average for mid-latitudes (zenith angle 48°). The "global tilt" (G) spectrum includes direct (D) radiation from solar disk (nearly parallel radiation and surface-normal tracking pointing to the sun) plus sky diffuse and diffuse reflected from ground on south facing surface tilted 37° from horizontal.

second electron-hole pair in the semiconductor. Carrier multiplication (CM), either multiple exciton<sup>7</sup> generation (MEG) or impact ionization, has been amongst the most prominent “third generation” techniques considered for increasing the current efficiency limits for a single junction cell [7]. Although CM has been observed in a few material systems [13, 14], its plausibility for realistic efficiency increase is still uncertain. Competitive processes for the relaxation of the high energy photoexcited carriers are too efficient [10]. In practice, electron–phonon interaction must be excluded or at least largely suppressed in the solar cell material to achieve an efficiency improvement by impact ionization, an assumption which rules out all present solar cell materials [15].

In an analogous concept, an hypothetical material external to the cell can be imagined that splits all these high energy photons into two photons of energy  $E_g$ . When placed adjacent to the cell and if all photons are emitted towards the cell, a fraction of the lost energy could be effectively used to produce electricity. The splitting of one high-energy photon into two low-energy photons is known as quantum cutting (QC), quantum splitting (QS) or down-conversion (DC). The ideal quantum yield of this process, i.e. the number of outgoing photons per incoming photon, is 2.

The opposite process, i.e. the combination of two or more low energy photons into one single high-energy photon, is also possible. This process, known as up-conversion (UC) and whose maximum quantum yield is 0.5, is potentially useful to recover the transparency loss.

A third process consists in decreasing the photon energy (down-shifting, DS), while leaving the photon number unchanged. This process can be useful when the spectral response of the cell is low in the blue part of the spectrum. The three processes are schematized in Figure 1.6 and will be outlined with more details in the following paragraphs.

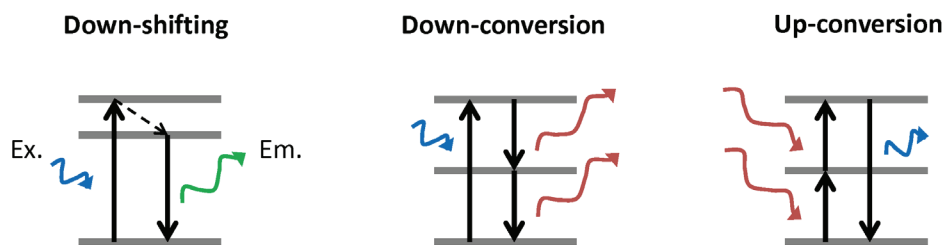


Figure 1.6 – Basic representation of the three available photon conversion mechanisms.

Assuming that all converted photons are absorbed by the semiconductor, the maximum energy fraction recovered by DC and UC processes is represented by the blue and red area in Figure 1.7.

Since photon-converting layers are not expected to be electrically connected to the solar cell, these layers can only increase the current and have no effect on the operating voltage. With optimistically assumed maximum yields for DC or UC, the theoretical photovoltaic conversion efficiency for a single-band gap (1.1 eV) solar cell reaches ~40% [16-19].

Of the three processes described above, the conceptually simplest process is downshifting. Examples of downshifting are very easily found. The thermalization losses in a direct band gap semiconductor are already an example of downshifting, where high energy photons are absorbed and re-emitted as band-to-band recombination at a red-shifted wavelength. In addition, almost all semiconductors have discrete levels in their band structure, due either to point defects or quantum confinement. In many cases, optical transitions between levels occur after part of the energy of the absorbed photon is lost as heat.

<sup>7</sup> Exciton: bound electron-hole pair that can move freely inside the semiconductor.

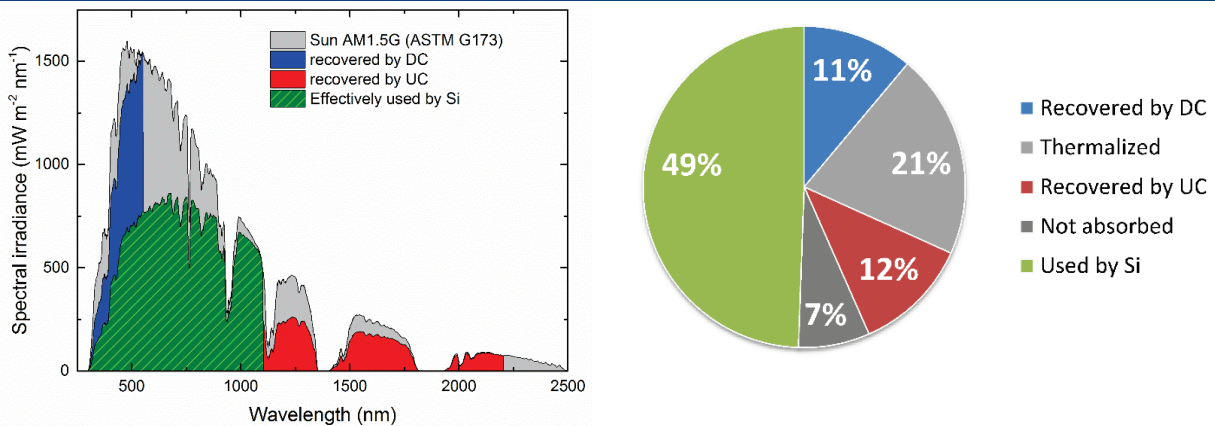


**Figure 1.7** – Fraction of the solar spectrum available in silicon and fraction of the lost energy potentially recovered by UC and DC processes. Use of incoming energy by ideal silicon single-junction solar cells and potential of DC and UC.

The next two sections will present the DS process showing how these layers can be implemented on solar cells, while DC and UC processes are left to section 1.4.3.

### 1.4.1 Down shifting layers

The large absorption coefficient of most semiconductors in the UV/blue spectral region causes the high-energy photons to be absorbed very close to the semiconductor surface. Electron-hole pairs created in this region are susceptible to be scattered towards the emitter, where carrier recombination is high. In the late 1970s, Hovel *et al.* [20] realized that wavelength shifting could be used to overcome the poor blue spectral response of solar cells. Luminescent centers embedded in a transparent medium could absorb the incident light and re-emit this at a red-shifted wavelength, where the spectral response of the solar cells is much higher.

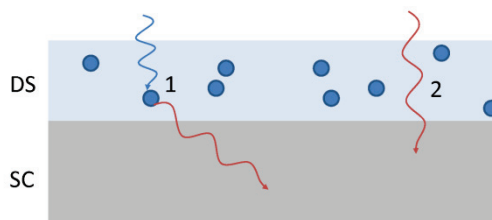


**Figure 1.8** - DS layer based on luminescent centers dispersed in a transparent medium. High-energy photons are absorbed by the layer and red shifted (1), while low energy photons can reach the solar cell (2).

Of course, improvement of front passivation may make down shifters obsolete, or at least less beneficial on Si-based solar cells, but the high technological cost for this improvement might still encourage the use of cheap DS layers.

Several second-generation solar cells would also benefit from such a layer. For example, thin film solar cells that rely on cadmium sulphide (CdS) window layers (e.g. CIGS and CdTe cells) actually exhibit a large amount of parasitic absorption at wavelengths shorter than 510 nm. Downshifting these photons to longer  $\lambda$  allowed substantial increase in power on CdTe-based solar cells [21, 22].

Parasitic absorption might also come from encapsulants and anti-reflection coatings. Huge efforts have been done in order to find more transparent materials, but most of the solutions present some drawback. For example, the very good transparency of indium-tin oxide is counterbalanced by its high cost. Other materials present poorer refractive index matching or low stability. Downshifting the

photons before or after the parasitic absorption can bypass the problem. DS can also prevent the UV irradiation damage of encapsulants and organic solar cells.

### 1.4.2 Luminescent solar concentrators (LSC)

By pushing the DS principle to the extremes, scientists came out with the idea of luminescent solar concentrators. Theoretically, the whole solar spectrum could be down-shifted and concentrated to a “single” wavelength just above the band gap. The reason for doing this is that single-junction solar cells optimally perform under this kind of monochromatic light and efficiencies over 80% are expected, slightly depending on band gap [23]. Unfortunately, it is very hard to create a complete spectral concentration and converting a small spectral region to monochromatic light is usually not enough to obtain high performances. Therefore, a brand new configuration for the cell has been conceived, where “geometrical” concentration adds to the spectral one. The simplest configuration is that reported in Figure 1.9, where large-area transparent DS sheets have small PV cells attached to the edges [4, 24, 25].

The upper limit on the concentration ratio is given by the geometric ratio of the sheet,  $G = A_{\text{front surface}}/A_{\text{perimeter}}$ , however, in practice the maximum concentration expected is up to 20 Suns [4, 26].

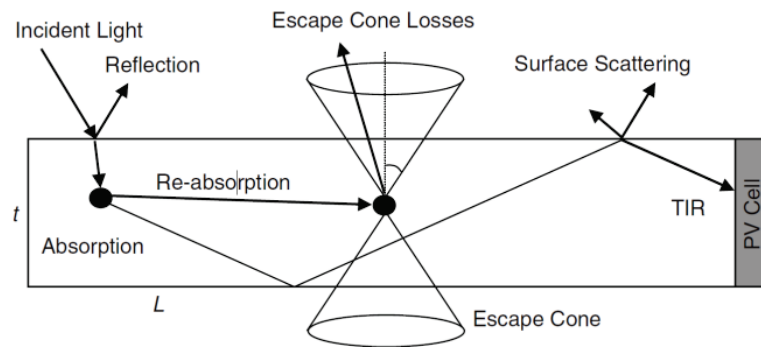


**Figure 1.9** - Cross-sectional diagram of a LSC with luminescence centers contained within thin, large-area transparent sheets with PV cells attached to the edge. Light is transported to the edge via total internal reflection (TIR), incurring some losses along the way, such as re-absorption, scattering and the escape of light emitted within the critical angle [4].

This approach is interesting because usually the cost of the DS material is much lower than that of the same area of solar cells. However, LSCs are not exempt from one of the most important drawbacks related to all kind of photon converters, i.e. concentration quenching.

### 1.4.3 Down- and up-conversion layers

Down-conversion was theoretically suggested first by Dexter in the 1950s [27, 28] and shown experimentally 20 years later using trivalent praseodymium ( $\text{Pr}^{3+}$ ) in an yttrium fluoride  $\text{YF}_3$  host [29, 30]. Up-conversion was also suggested in the same years by Bloembergen [31] and was initially related to the development of infrared detectors.

Before proceeding further, it is of basic importance to understand how the ideal converting layers should be built. Figure 1.10 depicts the ideal DC and UC converters in the simplest case of a two-step process.

An ideal DC converter absorbs all photons with energy higher than  $2E_g(\text{Si})$  and for each photon, two photons of energy  $E_g$  (or higher) are emitted. Such a broadband absorber could be a semiconductor or insulator with a direct band gap  $E_g \approx 2E_g(\text{Si})$ . Then, two radiative emissions might occur through an intermediate level at the midgap (see Figure 1.10a).

The ideal UC converter is also made of a broadband absorber with an intermediate level, but its gap equals that of the semiconductor (see Figure 1.10b). All photons with energy between  $E_g$  and  $E_g/2$  can be absorbed and converted into one photon of energy  $\geq E_g$ .

In practice, it is very hard to find a material with these characteristics and in particular it is hard to find an up-converter as that depicted in Figure 1.10b. Doping a semiconductor in order to create a level in the gap is not a viable solution. The momentum of the photon is not sufficient to allow transitions between electronic states that lay deep within the bands and the discrete level. The structure that most likely reproduces the ideal upconverter is a set of several three-level absorbers as that depicted in Figure 1.10c, at least if the cross sections of the levels are sufficiently large and the levels sufficiently close one to the other.

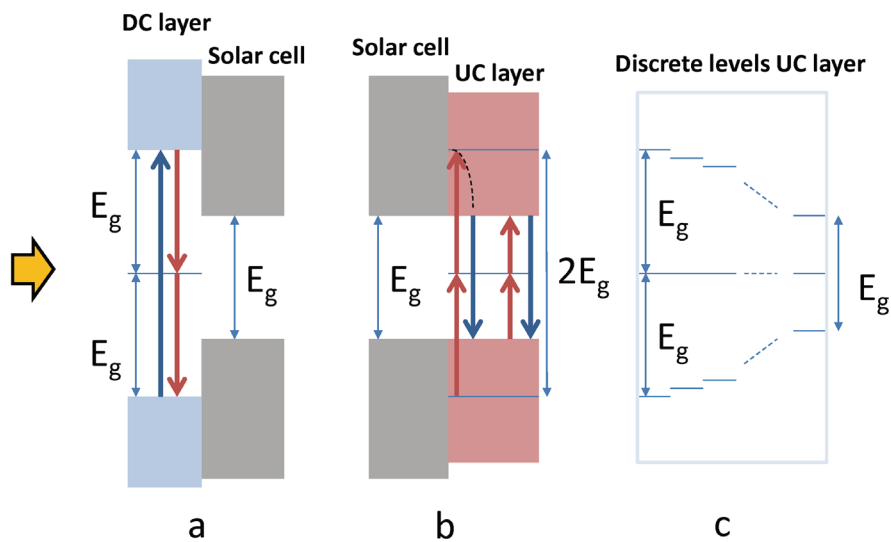


**Figure 1.10** – Electronic energy level structure of ideal two-step DC (a) and UC (b) layers. A more realistic UC material is depicted in (c).

There are both benefits and challenges in successfully applying UC and DC to PV technologies to solar cells devices. In principle, these layers are not electrically connected to the solar cell. However, the position in which the layers are placed with respect to the cell is very important. After the conversion process, the photons are re-emitted isotropically. As only the photons emitted in the direction of the solar cell contribute to the photocurrent, one might expect that half of the photons are lost if the layer is placed, for example, on the front of the solar cell.

A solution to this problem would be to put the layer at the back of the solar cell and to sandwich it with a reflector. This configuration allows increasing the theoretical photovoltaic conversion efficiency of about 10 percent points [16-18] for both DC and UC. However, if placing the layer on the back might be a viable solution for UC, which is based on low energy photons to which the solar cell is transparent, it might be a problem for DS and DC layers.

Trupke *et al.* [17] suggest that placing the layer on the back is possible, provided that the semiconductor bands are confined within  $2E_g$ . In this case, the solar cell would be transparent to photons with higher energy (see Figure 1.11). However, this approach requires non-trivial modification of the absorber in the cell and will not be considered here.

Fortunately, this loss can be partially recovered also when the layer is placed in front of the solar cell. This is possible by using materials with an appropriate refractive index. If the refractive index of the conversion layer is comprised between that of the incoming medium and that of the top part of the

solar cell (whether it is the semiconductor itself, an anti-reflection coating or an encapsulant), the total reflection at the layer’s surface reduces the loss to a narrow escape cone (see Figure 1.12a). The aperture of the cone decreases as the difference in refractive index between  $n_0$  and  $n_1$  increases. This limits the available materials, but with this precaution, the above-mentioned increase in efficiency of 10 percent points can be approached.

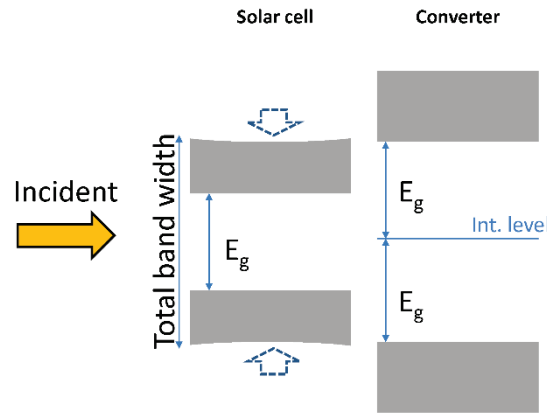


Figure 1.11 - Band configuration allowing the placement of a DC layer on the back of the cell.

In order to approach the escape cone described in Figure 1.12a, the surface roughness of the layer should be very low compared to the emission wavelength, so that surface scattering is reduced. However, qualitative observations during the photoluminescence measurements performed in this work indicate that the escape cone is quite larger than the ideal cone despite the relatively small surface roughness.

The typical configuration of solar cells with DC and UC layers is shown in Figure 1.12b.

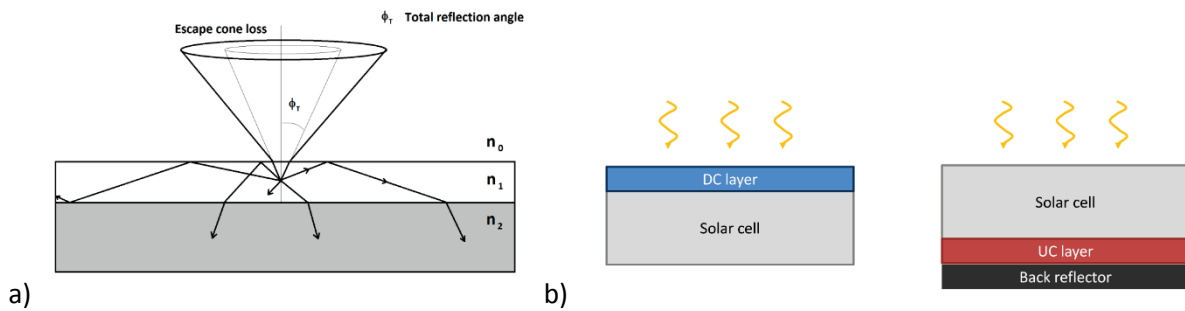


Figure 1.12 – a) Escape cone loss if  $n_0 < n_1 < n_2$  and b) typical configuration of DC and UC layers

The choice of a material with an appropriate refractive index is important for another reason. These layers should not absorb or reflect the part of the spectrum that is not used for photon conversion. If this happens, the consequent strong reduction of the cell efficiency could not be compensated by the benefits of photon conversion. To avoid this problem, many researchers are trying to functionalize with photon management properties existing parts of the solar cells, such as encapsulants and anti-reflection coatings.

We will see in the following that several other limiting factors might easily decrease the efficiency of these processes of several orders of magnitude.

### 1.4.4 Transfer mechanisms

As stated above, discrete levels in semiconductor materials can only be introduced by point defects or quantum confinement. In the first case, the defects can be either luminescent intrinsic defects or luminescent ions. If the absorption cross section of the emitting level is too small, a second ion with a larger cross section can be used as sensitizer. For this reason, the basic processes of energy transfer (ET) between two luminescent centers are presented in the following. From here on, the two luminescent centers are assumed to be rare earth ions.

Aside from ET involving the movement of charge, there remain four basic mechanisms involved in ET processes between ions [32-34]. A schematic diagram of the different ET processes between two ions is presented in Figure 1.13. Process (a) depicts the resonant radiative transfer through emission of sensitizer (S) and re-absorption by activator (A); process (b) the non-radiative transfer associated with resonance between absorber (sensitizer) and emitter (activator); process (c) multiphonon-assisted ET; and (d) cross-relaxation (CR) between two identical ions.

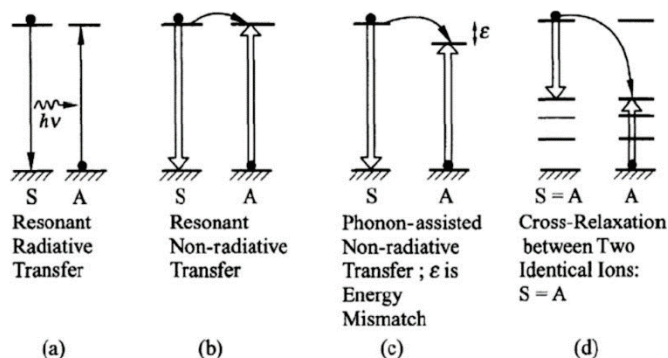


Figure 1.13 - Schematic diagram of the different ET processes between two ions [32].

The efficiency of radiative transfer depends on how efficiently the activator fluorescence is excited by the sensitizer emission. In particular, it requires a significant spectral overlap between the emission region of sensitizer and the absorption region of activator and an appreciable intensity of the absorption of activator. If the radiative ET takes place predominantly, then the decay time of sensitizer fluorescence does not vary with the activator concentration. However, the re-absorption probability of the first emitted photon does. Radiative transfer requires a considerable absorption capability of activator. For this reason, this transfer mechanism can usually be neglected compared to non-radiative ET in most inorganic systems. Phonon-assisted/non-resonant ET can also take place if the energy mismatch is not too large compared to the highest phonon energies. It is preferable to avoid cross-relaxation, because it leads to emission quenching.

Multipolar interactions between neighboring rare earth ions have been studied for some time. The first detailed treatment is that given by Förster [35] and Dexter [27]. A more detailed description of ion-ion interactions is given by the Inokuti-Hirayama theory [36], which explicitly deals with the dynamics of energy migration.

The ET rate between a donor and an acceptor derived by Dexter [27, 37] depends on the convolution of the normalized donor emission and acceptor absorption spectra, respectively. In addition, a matrix element is introduced that can be expressed as a function of the distance between donor and acceptor. The dependence with the distance varies with the interaction type. For exchange interaction it is exponential, while it is of the type  $R^{-n}$  for the multipolar interactions [27, 37].

In general, non-radiative energy transfer via dipole–dipole Förster–Dexter interaction is the dominant mechanism. As the sensitizer radiates, it generates an oscillating electric field  $E$  due to its oscillating dipole. This field falls off as  $1/r^3$  and, provided that its energy does not have the time to escape as a photon, it will directly stimulate a transition in the second ion. Since the energy density is proportional to  $E^2$ , the probability of the energy transfer depends on  $R^{-6}$ . Efficient energy transfer requires the ions to be in close proximity and thus depends on the RE concentration [38].

If both the sensitizer and the absorber are RE ions, the small absorption cross section can limit the transfer efficiency.

A possibility to increase the absorption cross section is to use the host (in which the luminescent centers are embedded) as sensitizer.

Perfect resonance between transitions is not always possible. If two ions present an energy mismatch between two transitions (even considering the phonon broadening), the probability for ET should drop to zero because of a lack of overlap of the wavefunctions. However, it has been found experimentally that ET can take place. Multiphonon-assisted phenomena have been considered by Miyakawa and Dexter [39, 40]. According to their theory, the probability of phonon-assisted transfer decreases exponentially with the energy gap.

$$W \propto e^{-\beta\Delta E}$$

where  $\beta$  is a parameter determined by the strength of electron-lattice coupling and by the nature of the phonon involved. The above equation has the same form as the energy gap dependence of the multiphonon relaxation (MPR) rate, which can be calculated using the modified energy gap law of van Dijk and Schuurmans [41, 42]:

$$W_{\text{NR}} = \beta_{\text{el}} \exp(-\alpha(\Delta E - 2\hbar\omega_{\text{max}}))$$

Where  $W_{\text{NR}}$  is the non-radiative transition rate, the  $\beta_{\text{el}}$  and  $\alpha$  are constants for a given host lattice,  $\Delta E$  is the energy difference between the energy levels considered, and  $\hbar\omega_{\text{max}}$  is the maximum phonon energy.

Note that the energy gap in the MPR rate is not the energy mismatch between two transitions, but the energy of the transition itself. In other words, it might represent the probability that the activator relaxes non-radiatively after the energy transfer. As a rule of thumb, many authors consider that MPR is a competitive process to radiative relaxation for  $\Delta E$  up to five times the phonon energy [43, 44]. The same rule is expected for phonon-assisted transfer.

In the next two sections, the UC and DC mechanisms based on one or two rare earth ions will be discussed. The transfer mechanisms between the RE ions and a sensitizing host will be treated in paragraph 1.5.6.

#### 1.4.5 UC mechanisms

Auzel [32] studied the different mechanisms related to UC based on discrete levels. The typical theoretical efficiencies<sup>8</sup> calculated using the Einstein coefficients are reported in Figure 1.14. The most efficient process involves the presence of a sensitizing ion, which means that energy transfer must occur between different ions. As stated above, several types of energy transfer mechanisms are possible, but non-radiative dipole–dipole energy transfer is usually the dominant mechanism. Non-resonant (Stokes) energy transfer requires the contribution of optical phonons from the host and the efficiency is therefore strongly host-dependent. The efficiency of this process is expected to be quite low due to its higher order.

---

<sup>8</sup> Since we are dealing with nonlinear processes, usual efficiency (as defined in percent) has no meaning because it depends linearly on excitation intensity.

The fact that the most efficient process requires two different ion types is no good news for the application on solar cells. By recalling the ideal UC made of several three-level absorbers as depicted in Figure 1.10c, we realize that it is not easy to find so many resonant ion couples. In addition, cooperative processes require that two sensitizer centers are situated close to the emitter. The requested high concentrations (20% is not uncommon) might also lead to luminescence quenching and solubility problems. The energy transfer rate is determined by the spectral overlap between the activator absorption and sensitizer emission, the lifetime of the sensitizer emission and the absorption strength of the activator ion [45]. In general, reasonable UC quantum yields reaching are obtained only by using very high irradiances, such as those reached in solar concentrators.

UC materials have greater potential if applied on semiconductors with a wider band gap.

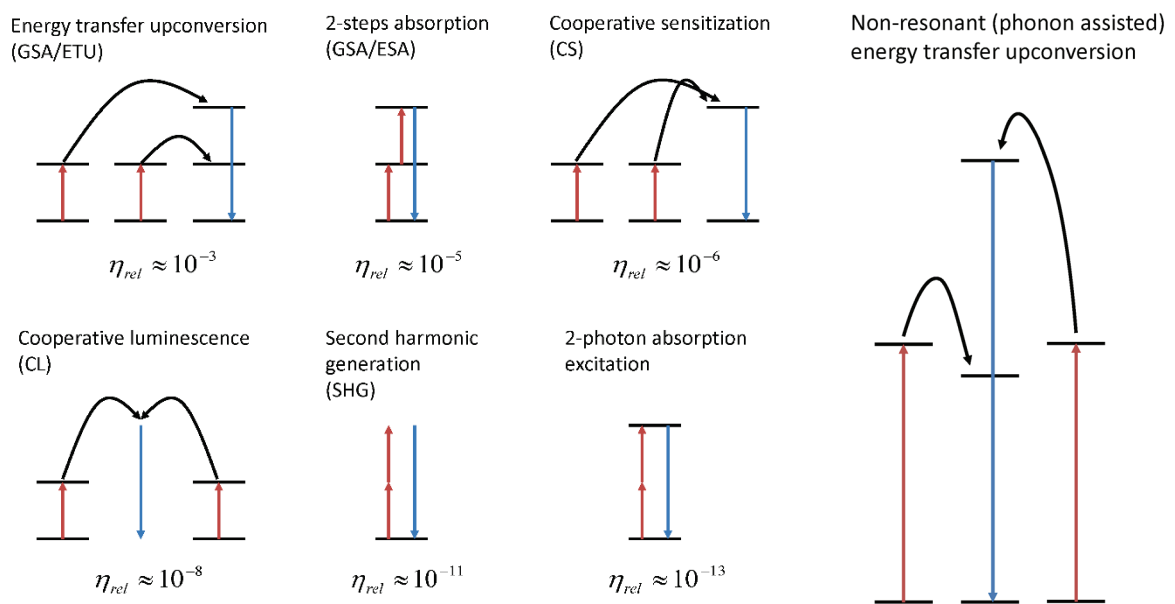


**Figure 1.14** - Overview over different resonant UC mechanisms and their relative efficiencies following Auzel [32]. An example of non-resonant cooperative UC is also illustrated. Vertical arrows describe radiative processes. The bent arrows describe non-radiative energy transfer processes.

#### 1.4.6 DC mechanisms

DC materials are much easier to conceive. Oxides, ceramic glasses, polymers and wide band gap semiconductors are often characterized by natural luminescent properties related to intrinsic defects. However, most of these transitions result in simple downshifting and it is also difficult to have a strong population of radiative defects while keeping the non-radiative defect population under control. Again, the most efficient method is to embed luminescent centers in the host. Transition metals and lanthanide ions are the most effective phosphors. The mechanisms involved in DC are the opposite of those involved in UC. The basic DC mechanisms are depicted in Figure 1.15.

DC via two-ion ET processes is generally more efficient than that based on a single ion, because the IR and UV-vis emission “losses” represented by the straight black arrows in mechanism A can be avoided.

Phonon-assisted DC is also possible, but strongly host-dependent. If the host has large phonon energy, larger energy mismatches can be encompassed. On the other hand, large phonon energy means higher

multi-phonon relaxation probability (the undulating arrow in mechanism A). Therefore, large phonon energy can be a double-edged sword.

A particular case is when the sensitizer has no intermediate level, as in the case of the Tb-Yb couple. Down conversion occurs through a virtual level, but the second order nature of this cooperative process strongly reduces its efficiency [46, 47].

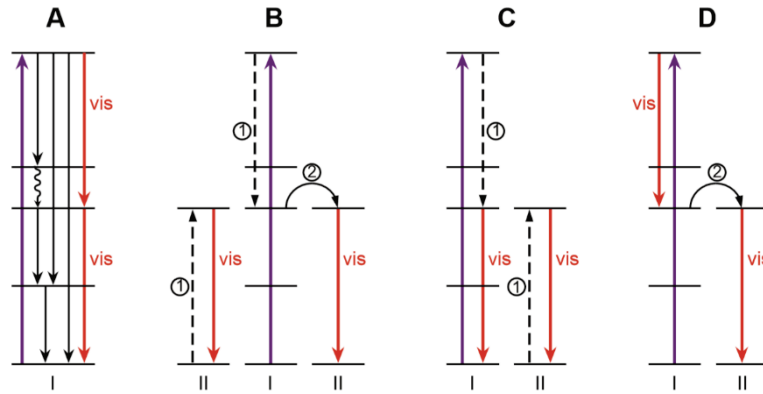


**Figure 1.15** - Hypothetical down-conversion mechanisms based on one or two lanthanide ions (denoted as I and II). (A) Quantum cutting on a single ion I by the sequential emission of two visible photons. The path leading to two equal photons is highlighted in red. (B) Quantum cutting by a two-step energy transfer (① indicates energy transfer by cross-relaxation, ② by other mechanisms). (C and D) Quantum cutting occurs via emission from both ions. [48]

#### 1.4.7 DC or UC?

The debate about which of the two processes (UC or DC) can achieve reasonable efficiencies has not finished stirring the scientific community. One of the objections made to UC is that, due to the non-linear nature of UC processes, high illumination power is required in order to reach exploitable conversion efficiencies for solar cell devices. On the other hand, DC layers need to be highly transparent to visible light and absorbent in the UV and blue regions of the spectrum, and to be characterized by an appropriate refractive index. In addition, DC layers usually operate in a region of the spectrum where the spectral response of the cell is not zero.

When it comes to PV modules, both DC and UC layers present one problem in common with tandem solar cells, i.e. that the solar spectrum changes throughout the day and with the geographic area. Figure 1.16 plots the spectral irradiance of the solar spectrum modeled by a 6000 K black body, the extraterrestrial solar spectrum of air-mass zero (AM0), and also the terrestrial solar spectrum for various positions of the sun throughout the day, reflected by the solar air-mass [49, 50]. While the power contained in the AM10G spectrum is only one-fifth of that in the AM1G spectrum, the most important difference is the reduced spectral irradiance at ultraviolet (UV) and visible wavelengths. Finally, a typical spectrum taken on a totally overcast day is plotted. This spectrum is blue-shifted due to the higher component of scattered light under cloudy skies.

Application of DC layers will therefore be more beneficial for regions with high diffuse irradiation fraction, such as Northwestern Europe, where the fraction can be 50% or higher. In contrast, solar cells with UC layers will be performing well in countries with high direct irradiation fractions or in early morning and evening due to the high air mass value. The variation of the conversion efficiency with the variations in the incident spectrum is also called “spectral robustness”.

This work is based on the assumption that DC and DS processes are more likely to reach efficiencies that are exploitable by low-power devices, such as standard silicon solar cells. For this reason, the rest of this work will be focused only on DC and DS layers. For more information about the up conversion processes, please refer to the exhaustive work done by Goldschmidt [24, 51].

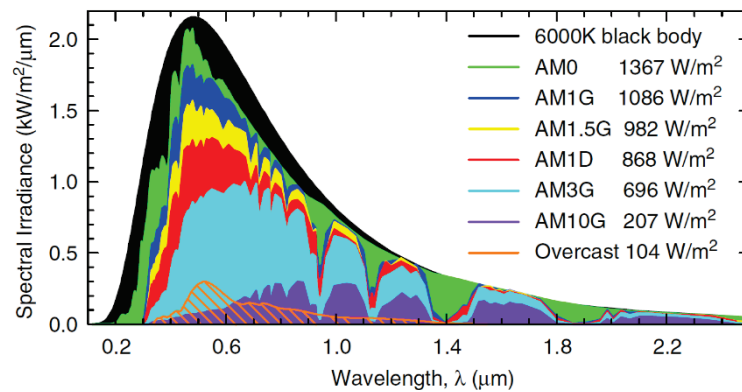


Figure 1.16 - Spectral irradiance and power contained within various solar spectra including global (G) and direct (D) [4].

#### 1.4.8 Candidate materials for DC and DS

From the previous paragraphs it can be concluded that the ideal material for DC is a material that absorbs all photons with energy higher than  $2E_g$  (2.25 eV in the case of Si) and have a single intermediate level, provided that the overall quantum efficiency is higher than 1 (these photons are normally absorbed by the semiconductor). On the other hand, an ideal material for DS is a material that absorbs only where the response of the cell is low or in a region where the parasitic absorption of a window layer limits the efficiency of the cell. DS can be performed either by converting the photons before the parasitic absorbing layer or by adding photon converting properties to the layer itself.

In paragraph 1.4.6 it was stated that wide band gap materials with intrinsic defects can act as DC or DS materials. However, high conversion efficiencies can be expected only if a very tight control over the defect population is ensured. In practice, it is hard to create a large number of radiative defects, while keeping the non-radiative defect population under control. Fortunately, it is possible to introduce discrete levels by embedding in the host a small amount of another element. Doping semiconductors with donor and acceptor impurities is a well established technique in order to control the electrical properties. In fact, when one or more levels have energy within the band gap of the host, they might exchange carriers with the conduction or valence bands. However, a number of impurities can be introduced in solids for their luminescence properties. This is the case when the charge transfer mentioned above results in radiative transitions. However, these transitions are strongly temperature- and host-dependent. A particularly interesting situation occurs when the dopant has some excited level that can be reached by optical frequencies. These levels can then be directly excited and their position with respect to the bands of the host is irrelevant. Luminescent centers with these characteristics are transition metals from the fourth period of the periodic table and rare earth ions. These impurities cannot be easily classified from the point of view of their electrical activity (e.g. when multiple levels are introduced in the gap), but have very interesting photon management properties.

Besides elemental impurities, larger and more complicated luminescent centers can be used, such as quantum dots and organic dyes. A brief description of these materials is given in the following paragraphs, while an entire section will be dedicated to rare earth ions.

The expected high efficiency of LSCs based on organic dyes [20, 52, 53] in practice was not reached as a result of not being able to meet the stringent requirements to the organic dye molecules, such as high quantum efficiency and stability, and the transparency of collector materials in which the dye molecules were dispersed. Nowadays, new organic dyes can have extremely high luminescence quantum efficiency (LQE) (near unity) and are available in a wide range of colors. However, the necessary UV stability has not been reached yet.

Quantum dots (QDs) are nanometer-sized semiconductor crystals, whose optical properties can be tuned by using quantum confinement [54]. The effects of quantum confinement on the band structure of a semiconductor are illustrated in Figure 1.17a.

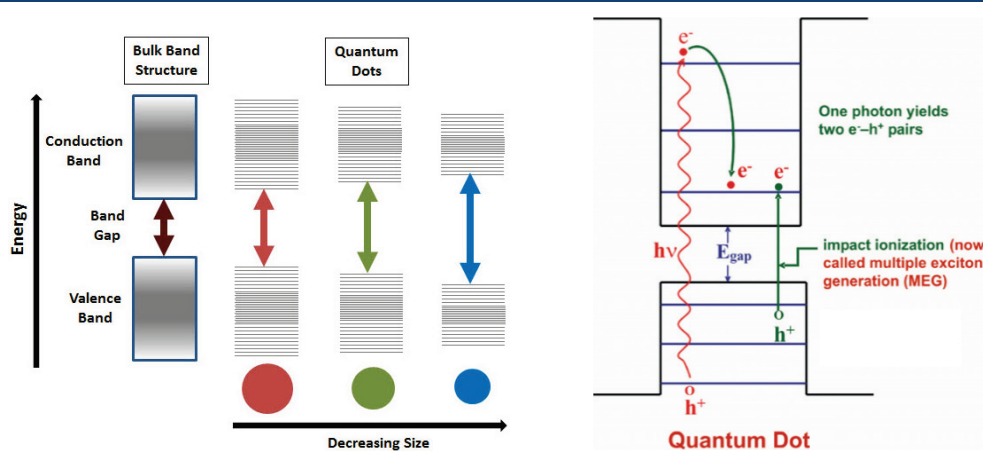


**Figure 1.17** – a) Effect of quantum confinement in quantum dots and b) multiple exciton generation process in a single quantum dot.

In bulk semiconductors, hot carriers are quickly cooled down and the extra energy is dispersed into heat. In a nanocrystal quantum dot, however, cooling is slowed down by size and structure effects (the bands split in discrete and well-spaced energy levels) and the process of MEG becomes competitive with respect to phonon emission [55, 56]. The extra energy of the electron is used to create a second exciton as shown in Figure 1.17b. The energy related to the cooling of the hole is lost as heat as in bulk semiconductors.

The advantages of QDs with respect to organic dye molecules are the high brightness, stability and quantum efficiency [57]. In addition, the absorption spectra are far broader, extending into the UV, and can be tuned simply by modulating the nanocrystal size.

Today, the best alternative to dye molecules and QDs are luminescent ions. Most industrial efficient luminescent materials rely on the luminescence of transition metal ions and lanthanide ions.

The most widely used transition metal ions exhibit luminescence resulting from electronic transitions between levels of the partially filled  $3d$  shell. These transitions are dipole-forbidden<sup>9</sup> ( $\Delta\ell = 0$ ), but become partially allowed thanks to the interaction with the electronic environment of the solid in which these ions are embedded.

The  $3d$  shell is an inner shell, but due to its relatively large radius, radiative transitions can be easily quenched by electron-phonon interactions. The luminescence of rare earth ions, instead, is based on

<sup>9</sup> Forbidden transitions are “forbidden” to first order, which means they may occur in practice, but with low probabilities.

transitions inside the partially filled  $4f$  shell. This shell has much smaller radius compared to the  $3d$ , which means that it is better shielded by the external  $5s$  and  $5p$  orbitals (See Figure 1.18). The influence of external fields is strong enough to partially alter the character of the transitions (making them partially allowed), but not enough to alter the atomic-like pattern of the emission spectrum.

However, having a shielded shell and an atomic-like spectrum also presents some disadvantages. In particular, the absorption cross section is small. As shown in paragraph 1.4.4, this problem can be solved by using a sensitizing ion, but then the conversion efficiency strongly depends on the transfer efficiency between the ions and on their concentration. An alternative is to use the host as sensitizer. In this case, the conversion efficiency does not depend on the concentration and is limited only by the transfer efficiency from the host. More information about the spectroscopy of the rare earth ions will be given in the following paragraphs.

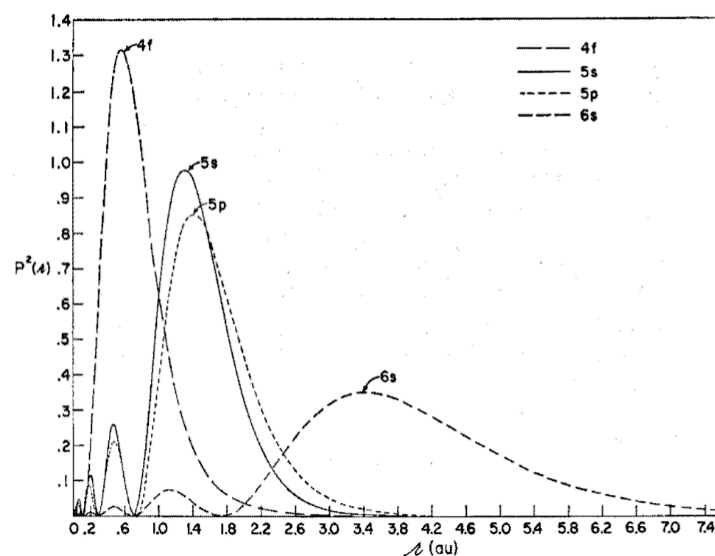


**Figure 1.18** - Square of the radial wavefunctions for the  $4f$ ,  $5s$ ,  $5p$ , and  $6s$  orbitals in  $Gd^+$  showing that the  $4f$  orbitals lie well inside the ion [58].

## 1.5 Rare earths

The lanthanides occupy a special place in the periodic table of elements. They are situated at the bottom of the periodic table, one row above the actinides. The word lanthanide has a Greek origin (“ $\lambda\alpha\nu\theta\alpha\nu\epsilon\iota\nu$ ”) which means “to lie hidden”. This may seem appropriate in view of the position of the lanthanides in the periodic table and the fact that it took more than a century to separate and discover all the lanthanides [46]. Silvery-white or gray in color, these metals have a high luster and tarnish readily when exposed to air.

Commercial applications of RE elements began after World War II, when their available quantity and purity were greatly enhanced by improved separation techniques developed as a part of the Manhattan Project. In the past sixty years, rare-earth-doped materials have encountered increasing success and have been intensively studied. The unique chemical, magnetic and optical properties of rare earths brought these materials to the top of almost all fields of technology. Many advances in data storage, optical communication, displays, light emitting devices and many other fields have been inextricably related to the development of rare-earth-doped materials.

When it comes to sustainable energy, rare earths are one of the key components in several devices, providing for instance high coercivity magnets [59] for windmills or electric bicycles, magnetocaloric refrigerators [60, 61], rechargeable lithium [62] or hydride [63] batteries and high efficiency lighting [64]. Today, they may also play a role in photovoltaics.

This section provides an overview over the potential and the limits of rare earths as photon managers, with particular focus on photovoltaics.

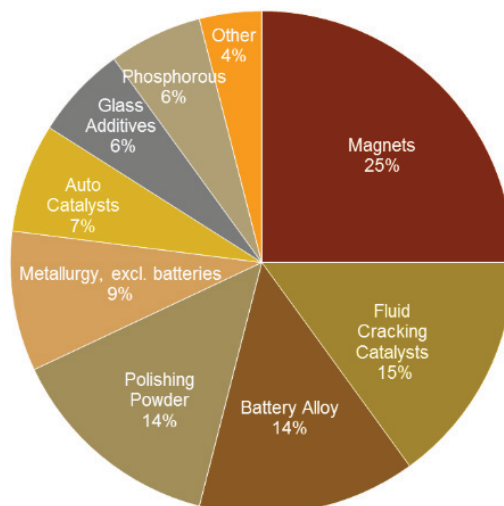


Figure 1.19 – RE oxide use by industry in 2010 (Source: CIBC World Markets)

### 1.5.1 Photonic applications of rare earth materials

For a long time, the main industrial application of RE elements has been related to permanent magnets. Indeed, the unpaired  $4f$  electrons result in some RE elements having the highest magnetic moments of any element and a large spin-orbit coupling, that leads to a large magnetic anisotropy. Although the optical properties of REs have been known for a long time, at least since the pioneering work of Dieke [65] and his collaborators, large industrial applications had to wait the development of optoelectronic devices. Just like for the magnetic properties, most of the unique optical properties of REs come from the partially filled  $4f$  subshell<sup>10</sup>. How these properties are related to the electronic configuration is the subject of the next sections.

The first commercial luminescent material based on lanthanide luminescence was  $\text{YVO}_4:\text{Eu}^{3+}$  [66]. This material was discovered in the early 1960s and found to efficiently convert the energy of high-energy electrons into visible (red) light, opening the way for color television. The high luminescence efficiency triggered the application of lanthanides in other areas, for example in luminescent materials for fluorescent tubes and X-ray imaging. Due to the mature status of the product, research on luminescent materials for mercury discharge fluorescent tubes, cathode ray tubes and X-ray imaging has strongly decreased in the past decades. On the other hand, new areas of research have emerged, such as solid state lasers, optical fibers, displays....

In the field of laser applications, significant successes have already been established with Nd as well as Er, Ho and Tm solid state lasers working in the near-IR region [67, 68]. Different approaches, such as up

<sup>10</sup> In general, the term “subshell” is replaced by the term “shell” for the sake of simplicity, when the use is unambiguous. In the following, this convention will be adopted.

conversion or frequency multiplication (doubling, tripling, etc.) phenomena, optical parametric oscillator tuning, or a combination of these mechanisms, led to UV and visible solid state lasers by using the same REs.

The first lanthanide-based optical-fibers were doped with Erbium [69], which provides optical gain in the 1530-1560 nm low-loss window of glass fibers. Other RE elements, such as  $\text{Pr}^{3+}$ ,  $\text{Nd}^{3+}$ , and  $\text{Dy}^{3+}$ , can also be used with the same purpose, while  $\text{Yb}^{3+}$ ,  $\text{Nd}^{3+}$  or co-doping with  $\text{Yb}^{3+}$ - $\text{Er}^{3+}$  may be used for fiber lasers.

The unusual optical properties of RE elements have also been explored for optical data storage. Significant increases in storage density can be achieved when multiple data bits are stored at the same location but multiplexed spectrally [70].

Visible and infrared (IR) light-emission can be obtained when RE ions are embedded in wide band gap semiconductors like GaN. Red (Pr, Eu), green (Er), and blue (Tm) emissions can be obtained, which means that simultaneous co-doping with two RE species can produce mixed hues between the primary colors and white light GaN diodes [71, 72].

The incorporation of RE elements into a variety of host materials has been investigated for achieving color displays. Visible emission can be obtained in primary colors: red ( $\text{Pr}^{3+}$  and  $\text{Eu}^{3+}$ ), green ( $\text{Tb}^{3+}$  and  $\text{Er}^{3+}$ ), and blue ( $\text{Ce}^{3+}$  and  $\text{Tm}^{3+}$ ). The most typical display devices based on RE elements are plasma displays, thin-film electroluminescent displays, field emission displays, and volumetric (3D) displays.

REs also provided more efficient and stable luminescent materials for the conversion of high-energy UV (vacuum ultraviolet, VUV) radiation into visible light for xenon-based fluorescent tubes and plasma display panels. This kind of research introduced a new objective for lanthanide-doped materials: finding ways for the generation of two visible photons for a single UV photon. Efficient quantum cutting by cooperative energy transfer is demonstrated for the Tb–Yb couple converting one visible photon into two infrared photons [46].

In 1979, Dexter [73] proposed to add an organic dye to solar cells which would harvest UV light, transfer the absorbed energy, and therefore improve the efficiency of the device. The use of rare earths in photovoltaics was pioneered by Munz and Bucher [74] and by Reisfeld [75, 76] shortly after this idea was formulated. As stated in the previous sections, UV-visible to infrared down-conversion as well as up-conversion may be used to increase the efficiency of solar cells. However, two issues remain to be solved before RE-based photon converters can be successfully applied in solar cells: the absorption strength needs to be increased, as the transitions involved for the trivalent lanthanides are sharp and weak (parity forbidden), and concentration quenching has to be handled properly.

### 1.5.2 Spectroscopy of rare earth ions

In order to determine the atomic structure of rare earths, the Schrödinger equation of a multi-electron atom must be solved. This is non-trivial matter, as even for two-electron atoms solving the equation requires some approximations. The first approximation that needs to be done is the so-called “central field approximation”, which assumes that every electron moves in an average central potential that takes into account the attraction of the nucleus and the average effect of the repulsive interactions due to the other electrons. This potential can be determined by the relativistic Hartree-Fock (HF) self-consistent field approach [77].

For an atom with only one electron outside a close shell, the Hartree potential is spherically symmetric. This is the case of hydrogenic atoms, i.e. with only one unpaired electron moving in the central potential of the nucleus and of the inner electronic shells. Since the potential is spherically symmetric, the single-particle wavefunctions may be written as the product of a radial function, a spherical harmonic and a spin function. For atoms having incomplete (sub)shells, the Hartree-Fock potential is no longer

spherically symmetric, but the deviation from spherical symmetry is often small due to the fact that in many cases (and in particular for the ground state) it arises from only one incomplete shell. If this is the case, the atom can be described by adding two main corrections to the central field approximation that can be treated as perturbations. These corrections must take into account the actual interaction with the other electrons (H1) and the spin-orbit coupling (H2). The case for which both perturbations H1 and H2 are of the same order of magnitude is difficult to handle. This situation is known as intermediate coupling. The two extreme situations are those for which  $H1 \gg H2$  and  $H1 \ll H2$ . The first one is the most frequently encountered. It occurs for atoms (ions) with small and intermediate values of  $Z$  and is called the L-S (or Russell-Saunders) coupling case. The second situation, which arises for atoms (ions) with large  $Z$ , is known as the  $j$ - $j$  coupling case.

The Hartree calculations, which yield the energetic ordering of the outer filled shells, predict that all REs have a ground state of the form  $[\text{Xe}]-4f^n 6s^2$ . However, in some of the rare earths (La, Ce, Gd, Lu) there is a  $5d$  electron in their ground state, leading to a configuration  $[\text{Xe}]-4f^{n-1} 5d^1 6s^2$ . This reveals that the electron configurations of atoms with large values of  $Z$  are clearly difficult to explain on the basis of simple qualitative arguments. One reason is that various levels are very close in energy. Also, for large  $Z$ , relativistic shifting of the energies of the electron energy levels accentuates the spin-orbit coupling effect and prevents the simple decoupling of the space and spin parts of the wave functions.

The  $4f$  and  $5d$  shells being so close in energy, it is relatively easy to excite  $4f$  electrons to the  $5d$  shell.

Having potentially two partially filled shells at their disposal, the electrons of rare earth ions can create a large number of different configurations. If the only acting forces were central, these levels would be highly degenerate. The existence of non-central forces such as the Coulomb interactions with the other electrons and the spin-orbit interaction spans the degenerated levels over a wide energy range ( $\sim 10$  eV) and thus creates the complex energy level diagram of rare earths.

Figure 1.20 illustrates, with an example, how the energy levels split under the different effects. With only the influence from the central potential of the nucleus and the inner electrons, it is sufficient to identify the state with the principal quantum number of the shell (4 in this case), the individual angular momentum ( $f$  in this case) and the number of electrons  $n$  that are in this state. Because of the Coulomb interaction between the outer electrons, the total orbital angular momentum of all outer electrons  $L$  and their total spin  $S$  become relevant. Because of the spin-orbit coupling also the total angular momentum  $J=L+S$  is important. Each level splits into several components with  $J$  values comprised between  $|L-S|$  and  $|L+S|$ . For lanthanides, the spin-orbit interaction is approximately as large as the Coulomb interaction between the outer electrons. In consequence, neither the Russell-Saunders nor the  $j$ - $j$  coupling are good approximations. Nevertheless, the Russell-Saunders notation is generally used by the scientific community to identify the different energy levels (See [Appendix A](#) for more details). The corresponding energy level is labeled  $^{2S+1}L_J$  and its degeneracy is  $2J+1$ . The degeneracy of these Russell-Saunders LSJ manifolds can be partially lifted if the rare-earth ion experiences an electric field, such as that exerted by a crystalline environment. The number of components depends on the symmetry of the applied electric field. Depending on the  $J$  value, a magnetic field might be necessary to completely remove the degeneracy.

It must be said that the electron configuration is, in reality, not composed of pure  $^{2S+1}L_J$  states that could be derived from the Russell-Saunders approximation, but rather of a superposition of different states that have the same total angular momentum  $J$ . Only the ground states are almost pure  $^{2S+1}L_J$  states [78]. This has deep consequences when it comes to photon absorption and emission as it will be explained in paragraph 1.5.4.

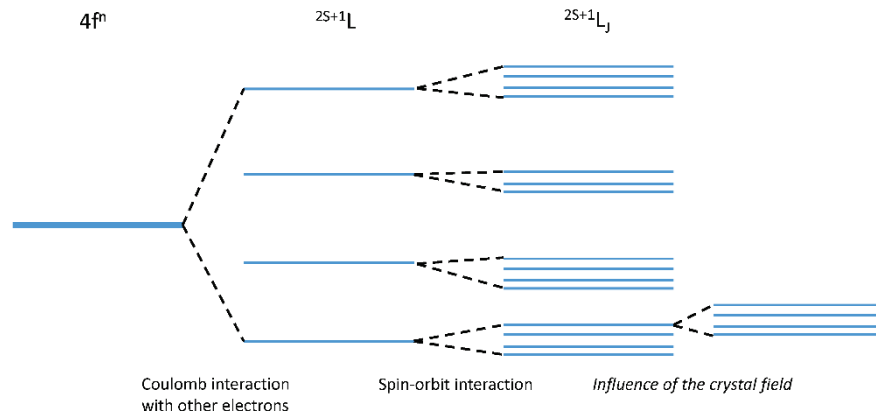


**Figure 1.20** - Illustration of how the energy levels split under the influence of the different effects. At the top, the quantum numbers that describe the energy states are given.

It is clear from Figure 1.20 that, if non-central forces are neglected, the atom presents single, highly degenerate levels. The degree of degeneracy will determine the complexity of the energy level diagram after the degeneracy lift and its value depends on the number of electrons in the partially filled shells. For example, the 4f shell has 14 electron states. The configuration of  $n$  external electrons in the 4f shell is noted as  $4f^n$ . The total degeneracy of the  $4f^n$  configuration corresponds to the different combinations (without repetitions) of  $n$  electrons in the 14 states of the f shell:

$$C_{14}^n = \frac{14!}{n!(14-n)!}$$

Because of the electrostatic and spin-orbit interactions, the degeneracy is partially lifted and the single level splits into many levels (327 in the case of the  $4f^7$  configuration). If electric or magnetic fields are applied, the degeneracy can be totally lifted.

Other low configurations for three electrons are  $4f^{n-1}5d$ ,  $4f^{n-1}6s$  and  $4f^{n-1}6p$ . Of these three mixed configurations, only the first sometimes lies in the near UV region of the spectrum ( $Ce^{3+}$ ,  $Eu^{2+}$ ) and is interesting for solar cell applications. The maximum degeneracy of the  $4f^{n-1}5d$  configuration is ten times (only one electron in the 5d shell with 10 different states) that of  $4f^{n-1}$ . More information about the  $4f^{n-1}6s$  can be found in the work by Saxena *et al.* [79].

Table 1.1 reports the number of non-degenerate levels induced by the different perturbations to the spherical symmetry for the  $4f^n$  configuration corresponding to different oxidation states (the  $4f^n$  configuration for the 2+ state being equivalent to that of the neutral atom). The number of non-degenerate levels under the effect of the interaction with the outer electrons is reported also for the  $4f^{n-1}5d$  configuration [65]. Since the combination of all perturbations leads to a full degeneracy lift, the last two columns of Table 1.1 also indicate the total degeneracy  $C_{14}^n$  and  $10 \cdot C_{14}^n$  of the  $4f^n$  and  $4f^{n-1}5d$  configurations, respectively.

Table 1.1 shows that a certain configuration is not proper of a particular rare earth. Instead, neighboring RE ions can have the same configuration in different oxidation states. A closer look to the number of levels in the different configurations reveals another symmetry. From a statistical point of view, the  $4f^n$  and  $4f^{14-n}$  configurations are equivalent. In other words, the configuration of  $n$  electrons in the band is equivalent to that in which there are  $n$  empty spaces. Despite these configurational symmetries, the energy of these levels is not the same, due the different nuclear charge and the larger number of electrons in the shells. This creates a similar pattern under the effect of an external field, but spanned over a different energy range.

The higher degeneracy of the mixed 4f-5d configuration, combined with the larger radius of the 5d orbital, leads to the creation of wide bands when these levels are split by an external field. In addition,

4f-5d transitions are parity-allowed. This creates a large and strong absorption band in the UV region of the spectrum. For some rare earth ions this band falls within the range of the solar spectrum, which makes them very promising sensitizing ions for photon converting applications. On the other hand, a large orbital radius means that the associated levels have stronger dependence on the external field and are more subject to quenching effects.

**Table 1.1** - Number of non-degenerated levels induced by the Coulomb (C) and spin-orbit (SO) interaction, an external electric field (Stark) and electric + magnetic fields (Zeeman) of the rare earth ions in the lowest configurations. The total number of electrons  $n$  in the incomplete shells and the ground-state Russell-Saunders multiplet are indicated.

| n  | RE <sup>2+</sup> | RE <sup>3+</sup> | RE <sup>4+</sup> | Gr. st.                        | Number of levels |       |        |                 |                      |
|----|------------------|------------------|------------------|--------------------------------|------------------|-------|--------|-----------------|----------------------|
|    |                  |                  |                  |                                | C+SO             | Stark | Zeeman | 4f <sup>n</sup> | 4f <sup>n-1</sup> 5d |
| 0  |                  | La               | Ce               | <sup>1</sup> S <sub>0</sub>    | 1                | -     | 1      | 1               | -                    |
| 1  | La               | Ce               | Pr               | <sup>2</sup> F <sub>5/2</sub>  | 2                | 2     | 7      | 14              | 10                   |
| 2  | Ce               | Pr               | Nd               | <sup>3</sup> H <sub>4</sub>    | 13               | 20    | 91     | 91              | 140                  |
| 3  | Pr               | Nd               | Pm               | <sup>4</sup> I <sub>9/2</sub>  | 41               | 107   | 182    | 364             | 910                  |
| 4  | Nd               | Pm               | Sm               | <sup>5</sup> I <sub>4</sub>    | 107              | 386   | 1001   | 1001            | 6340                 |
| 5  | Pm               | Sm               | Eu               | <sup>6</sup> H <sub>5/2</sub>  | 198              | 977   | 1001   | 2002            | 10010                |
| 6  | Sm               | Eu               | Gd               | <sup>7</sup> F <sub>0</sub>    | 295              | 1878  | 3003   | 3003            | 20020                |
| 7  | Eu               | Gd               | Tb               | <sup>6</sup> S <sub>7/2</sub>  | 327              | 2725  | 1716   | 3432            | 30030                |
| 8  | Gd               | Tb               | Dy               | <sup>7</sup> F <sub>8</sub>    | 295              | 3006  | 3003   | 3003            | 34320                |
| 9  | Tb               | Dy               | Ho               | <sup>6</sup> H <sub>15/2</sub> | 198              | 2725  | 1001   | 2002            | 30030                |
| 10 | Dy               | Ho               | Er               | <sup>5</sup> I <sub>6</sub>    | 107              | 1878  | 1001   | 1001            | 20020                |
| 11 | Ho               | Er               | Tm               | <sup>4</sup> I <sub>15/2</sub> | 41               | 977   | 182    | 364             | 10010                |
| 12 | Er               | Tm               | Yb               | <sup>3</sup> H <sub>6</sub>    | 13               | 386   | 91     | 91              | 3640                 |
| 13 | Tm               | Yb               | Lu               | <sup>2</sup> F <sub>7/2</sub>  | 2                | 107   | 7      | 14              | 910                  |
| 14 | Yb               | Lu               |                  | <sup>1</sup> S <sub>0</sub>    | 1                | 20    | 1      | 1               | 140                  |

In the next sections, more information will be given on the rich 4f energy level diagrams (Section 1.5.3) and how the partially-allowed 4f transitions can be treated theoretically (Section 1.5.4). Additional information on the energy of the 4f<sup>n-1</sup>5d states and on the importance of 4f ↔ 5d transitions will be treated in Section 1.5.6 and 1.7, where the importance of the host in which the rare earths are embedded is also considered.

### 1.5.3 Energy level diagram of 4f states in lanthanides

Due to the limited interaction of the 4f electrons with the environment, the position of the energy levels is only weakly affected by the nature of the host material, with variations typically of the order of 1000 cm<sup>-1</sup> (~0.1 eV). This allows a “universal map” of the energy level structure to be constructed, such as the classic diagram reported by Dieke [65] for trivalent lanthanides and shown in Figure 1.21b.

The fact that all lanthanides generally prefer the trivalent form when embedded in compounds led to the association of a particular energy level diagram to the respective trivalent rare earth instead of the respective 4f<sup>n</sup> configuration. However, Table 1.1 shows that the same configuration can be attributed to at least three rare earths in different oxidation states. The energy level diagram corresponding to the first excited levels of the 4f<sup>n</sup> configuration in free divalent lanthanides is reported in Figure 1.21a. By comparing Figure 1.21a and b, it can be seen that the energy level configuration of trivalent lanthanides is the same as that of divalent lanthanides, but shifted of one position to the right. Thus, for example, the configuration of La<sup>2+</sup> “equals” that of Ce<sup>3+</sup>, that of Sm<sup>2+</sup> “equals” that of Eu<sup>3+</sup> and so on until Tm<sup>2+</sup> and Yb<sup>3+</sup>. Of course, the higher atomic number of the 3+ ion slightly increases the level spacing, indicating



highly-delocalized nature of the  $5d6s^2$  valence electrons allows high coordination values (up to 12) for the RE ions. In practice, it was found that the 4f orbitals of the lighter lanthanide elements contribute to chemical bonding through orbital hybridization, or mixing. Thus, although electrons in the f orbitals are not strongly concerned with the formation of compounds, they definitely have a second-order effect on the chemical properties [81].

In the next paragraph, some theoretical considerations about the transition probability between 4f states will be presented. Inter-configurational 4f-5d transitions will not be considered with the same detail because for most ions, the 4f5d states are situated in the far UV. Only for  $Ce^{3+}$ , these levels are situated at optical frequencies (blue) above the ground state, causing the strong blue luminescence of  $Ce^{3+}$ -doped phosphors [82]. However, it will be shown that 4f5d states play an important role in the 4f-4f transition probability.

#### 1.5.4 Transitions between 4f states

For one-electron atoms in vacuum, radiative transitions between different 4f states are parity forbidden. In fact, the photon carrying odd parity<sup>11</sup>, Laporte's rule predicts vanishing electric dipole<sup>12</sup> matrix element if the initial and final states have the same parity (both odd in the case of f states).

Even for multi-electron atoms, the most usual case is that in which the orbital of only one electron in the atom changes in the transition. If the orbital concerned has an angular momentum quantum number  $l_j$ , then  $\Delta l_j = \pm 1$  in accordance with Laporte's rule. In general, though, the selection rules should deal with the quantum numbers of a multi-electron system.

The selection rules for electric dipole transitions in multi-electron atoms are [77]:

$$\Delta J = 0, \pm 1 \quad (J = 0 \rightarrow J' = 0)$$

$$\Delta M = 0, \pm 1$$

When the spin-orbit interaction is weak, then the Russell-Saunders approximation is accurate and two additional selection rules hold in addition to those previously mentioned:

$$\Delta L = 0, \pm 1 \quad (L = 0 \rightarrow L' = 0)$$

$$\Delta S = 0$$

The rule concerning the total angular momentum  $L$  seems to contradict Laporte's rule requiring a parity change. However, this rule was established for one-electron atoms. In multi-electron atoms, two or more configurations can be strongly mixed in a particular state, so that more than one electron can make a transition simultaneously even though only one photon is emitted or absorbed.

For rare earths, the spin orbit interaction is particularly strong and the superposition of  $^{2S+1}L_J$  states mentioned above partially relaxes the selection rules for dipole transitions. This introduces a small transition probability resulting in narrow absorption/emission lines. Typical oscillator strengths<sup>13</sup> are of around  $10^{-6}$ , much lower than the typical values observed for the 4f-5d allowed transitions ( $10^{-2}$ ) [83].

When these ions are embedded into a crystal, the transition probability increases due to admixture of opposite parity states by odd-parity crystal field components or vibrations. The spectral lines remain sharp because the coupling with vibrations is generally weak. In other words, the probability of Stokes' shifts for the optical transitions is low, resulting in strongly reduced vibrational energy losses [45].

<sup>11</sup> By convention, the parity of a photon is given by the radiation field involved: electric (-1), magnetic (+1).

<sup>12</sup> When the electric dipole matrix elements vanish, the transition may still occur through higher order terms, but observed spectra of rare-earth ions in crystalline fields consists mainly of electric-dipole transitions.

<sup>13</sup> In spectroscopy, "oscillator strength" is a dimensionless quantity that expresses the probability of absorption or emission of electromagnetic radiation in transitions between energy levels of an atom or molecule. Oscillator strengths may be defined by comparing the emission rate or absorption rate of the atom with the emission or absorption rate of a classical, single-electron oscillator. The maximum value is 1.

When considering RE-doped materials for applications, it is important to know the transition probabilities, or oscillator strengths, for the various transitions between energy levels in rare-earth ions when these are embedded in crystals. Unfortunately, these are extremely difficult to measure. Theoretical calculations are practically a necessity for guiding the interpretation of the empirical results.

The methods of calculating the transition probabilities were developed first by Slater in 1929 [84]. Then, in 1937, Van Vleck [85] suggested that the crystal field mixes states of different parity, which makes electric dipole transitions possible. In 1945, Broer [86] considered the different transition mechanisms (electric and magnetic dipole, quadrupole, ...) and confirmed that electric dipole transitions dominate. Few years later, Racah [87] applied group theory and created the tools required to make detailed spectroscopic calculations involving states of the 4f shell. By 1962, the stage was set for the next major development. Based on static, free-ion and single configuration approximations, the theory developed by Judd and Ofelt [36, 88, 89] explains the intensities of the forbidden 4f-4f transitions by taking into account the admixture of configurations of opposite parity 4f<sup>n-1</sup>5d configurations into the 4f configuration. In other words, the rare earth ion is affected by the surrounding host ions via a 'static' electric field, in which the host environment is treated as a perturbation to the free ion Hamiltonian. Interaction of electrons between configurations are neglected, except for the interaction with 4f<sup>n-1</sup>5d states.

Two more assumptions have to be made in order to make the many fold sum of perturbation expansions suitable for numerical applications. First, the 4f<sup>n-1</sup>5d states must be degenerate in  $J$  (i.e. an average energy for the configuration is considered). Second, the difference of average energies of the f and d shells,  $\Delta E(4f-5d)$ , is assumed to equal the difference between the average energy of the 4f<sup>n-1</sup>5d and the energy of the initial and final states of the 4f<sup>n</sup>. These assumptions are only moderately met, but offer a great simplification.

The "full solution" of the Judd-Ofelt theory can be used to find electric dipole matrix elements between mixed parity states for individual Stark level to Stark level transitions [90]. An "approximate solution" of the Judd-Ofelt theory can be used to find electric dipole matrix elements between mixed parity states for manifold to manifold transitions.

The application of the theory requires the computation of three parameters  $\Omega_2$ ,  $\Omega_4$ , and  $\Omega_6$  by a fit to a number of experimental data usually obtained by ground state absorption. These three parameters are then used to calculate the electric dipole oscillator strength between any states [91]. In principle, the Judd-Ofelt parameters can be calculated "ab-initio" if the crystal structure is known, but radial integrals between configurations and crystal field components are difficult to calculate. Thus, Judd-Ofelt parameters are usually treated as phenomenological parameters, determined by fitting experimental line strength data. A first drawback of this method is that it often requires non-trivial deconvolution of the several components. In addition, the calculation does not take phonon-related line broadening into account. Finally, the existence of multiple lattice sites for the ions is not considered. Despite all that, the Judd-Ofelt theory has successfully explained the transition intensities of 4f transitions in various hosts [92]. In particular, the measurement of the line strength of few transitions is sufficient to calculate the parameters and the line strength of the other transitions can be estimated.

In the same years, additional theoretical work has been done by Wybourne [93-95]. Then, in 1967, an extensive work on the optical properties of all rare earths in different crystals has been carried out by Dieke [65] and compared with the theoretical results.

It is outside the scope of this work to perform a comparison between the experimental results and the theory. The experimental intensity of the absorption and emission lines is used to have an idea of their relative oscillator strengths and if the RE-host system used can be beneficial for solar cell applications.

### 1.5.5 The crystal field

A free-ion level with total angular momentum  $J$  is  $(2J+1)$ -fold degenerate. Part or all of this spatial degeneracy is removed if the ion is surrounded by other atoms, because such an environment has always less than spherical symmetry. The number of components depends on the symmetry of the electric field created by the other atoms. In an amorphous host, this symmetry cannot be foreseen and many possible configurations exist. In a crystal, however, a small number of possible configurations exist and their symmetry is known. The relation between crystal symmetry and level structure was first established by Bethe in 1929 [96].

Of the 32 crystallographic point groups, the most important groups for crystal field symmetry are related to the cyclic groups  $C_g$  (see [Appendix B](#) for more details).

It must be emphasized that what is of interest here is the symmetry of the electric field at the position of the rare earth ion. This may or may not have the same symmetry as the macroscopic structure of the crystal.

Besides pure rare earth compounds (like chlorides, fluorides and oxides), in which the rare earth site does not undergo particular stress besides that induced by the crystal field symmetry, a second category of compounds includes all materials in which the RE ion substitutes another element in a certain number of sites of the lattice. If the rare earth has the same valence as the substituted ion, the same lattice structure and approximately the same radius, there is little modification with respect to pure rare earth compounds. However, this is rarely the case.

When the ion radii are very different, substitution of a particular ion by a rare earth cannot be made without serious distortions of the crystal lattice. In some cases, the substitution cannot be made at all. A particular symmetry will have much stronger influence on the 4f levels if the crystal field is strong. The compressive stress induced by the insertion of a large RE ion in a small lattice site might increase the wavefunction overlap between the RE and its nearest neighbors, thus increasing the term mixing and the transition rates. As a counterpart, when the radius mismatch is large, the insertion is more difficult and the impurities can form precipitates.

If the valence is different, the mere substitution would result in an extra charge at the ion site, which must be compensated for. This charge compensation might not be identical at all substitution sites, which means that the compensating ion does not take up exactly the same position with respect to the axes of the local field. This results in broadened lines and often the appearance of many additional lines.

The last case is that of a different symmetry at the lattice site. For example, trivalent RE ions usually have octahedral configuration. Thus, unless they substitute another ion with the same symmetry, some distortion will occur. To minimize the energy, the local environment of the RE ion is usually modified to approach the octahedral configuration.

In addition, the optically active site might not be a substitutional site. RE-O clusters might be dispersed in the lattice, while keeping a strong interaction with the crystal (partial distortion, interaction with phonon, energy transfer). For example, much work has been focused in the past on the nature and symmetry of the erbium center responsible for 1.5  $\mu\text{m}$  emission in silicon, with sometimes-contradictory results. Theoretical studies have concluded from energetic considerations that the isolated tetrahedral interstitial erbium site is favored [97, 98]. However, the emitting species in oxygen-doped Er:c-Si has been shown from EXAFS studies to be an Er-O cluster with a six-fold coordination between the central erbium ion and surrounding oxygen ions [99]. The simplest six-fold configuration is an octahedron formed with an erbium atom at the center and six equally spaced oxygen atoms at the vertices (symmetry  $O_h$ ). However, the crystal field from this arrangement will not provide the required modification of the  $\text{Er}^{3+}$  local environment to make the intra-4f transitions allowed. The active species must therefore be a distorted octahedron. A quite recent theoretical work by Ishii and Komukai [100]

has investigated different possible configurations of sixfold coordinated by Er–O clusters. Using molecular orbital calculations, the effect of distorting the “ErO<sub>6</sub>” octahedron by selectively shortening one, two, or three Er–O bonds to produce species with symmetries of C<sub>4v</sub>, C<sub>2v</sub> and C<sub>3v</sub> respectively, have been investigated. It was found that the preferred site has C<sub>4v</sub> symmetry, corresponding to an octahedron in which one Er–O bond has been reduced in length by around 0.1 Å [38].

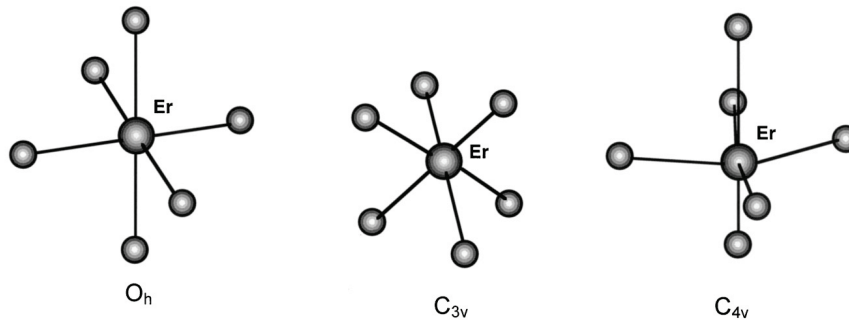


Figure 1.22 – Three different point symmetries of six-fold coordinated Er<sup>3+</sup> ions [38].

The coordination may also depend on the preparation method, in particular on the oxygen doping concentration. Extended X-ray-absorption fine structure (EXAFS) analyses have shown that Er in Czochralski (Cz) Si (which contains  $\sim 10^{18}$  O/cm<sup>3</sup>) is coordinated with 6 oxygen (and not Si) atoms, while in float-zone (FZ) Si (containing  $\sim 10^{16}$  O/cm<sup>3</sup>) its coordination is with 12 Si atoms [99].

### 1.5.6 The importance of the host matrix

Rare earth ions can be incorporated into a countless number of compounds with different crystal fields. Changes of few tenths of an eV in the location of the lanthanide states with respect to each other can have dramatic consequences on the transition rates. The performance of a specific RE-host system is largely determined by the electronic structure.

If both absorption and emission rely on RE ions (eventually using a sensitizing ion), the “only” requests on the host are that it must have a crystal field ensuring high radiative transition rates and high transparency to optical and/or NIR frequencies.

In some cases, the host can be used as sensitizer (see Figure 1.23). In particular, when the rare earths are embedded in TCOs, the small thickness of the film and the usually small RE concentration prevent strong direct absorption from the RE ions. In this case, the use of the TCO as sensitizer is strongly recommended. However, the requirement to have a good refractive index matching complicates the choice of the host. Usually, materials with small band gaps have high refractive index values. For example, materials with the optimal refractive index on silicon usually have band gap values above 3 eV. This limits the light available for DC, but keeps the reflection losses at a reasonable level.

Following the excitation of the host, RE 4f electrons can be excited following two different energy transfer mechanisms. The first is when an exciton recombines across the band gap or through some defect state and (radiatively or not) transfers part of its energy to the 4f electron. The second is when an electron is trapped by the RE and falls into the 4f shell. This second mechanism implies a valence change and the configuration of the RE is temporarily modified to 4f<sup>n+1</sup>.

When charge transfer occurs, the energy location of the lanthanide excited states with respect to the band states of the host becomes important. The presence or absence of emission, thermal quenching of emission [101], charge carrier trapping by lanthanides [102], and the preferred valence of the lanthanides [103] are all controlled by the level location relative to the band states.

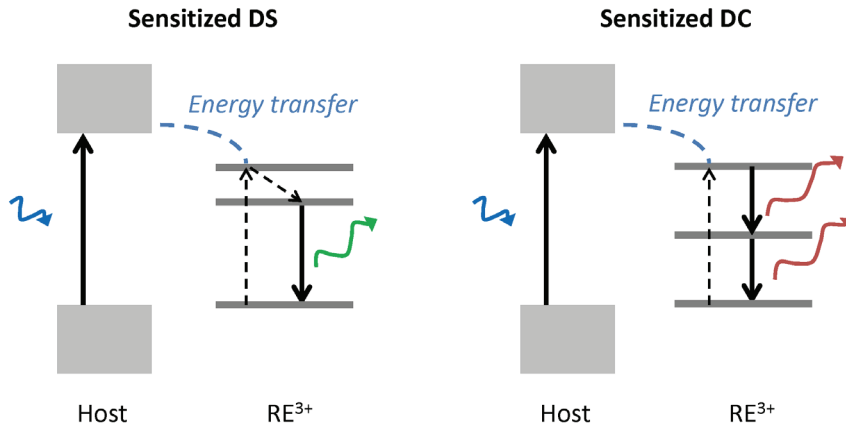


Figure 1.23 – Sensitized DS and DC with energy transfer from the host.

In addition, the energy of the  $4f^n$  state relative to the valence band determines the stability of the ionized state. While any ion valence may be produced with sufficient excitation of the system, some of these states will rapidly relax to their normal valence whereas others may persist indefinitely. In fact, the energies of the rare-earth states relative to both the valence and conduction band determine the stabilities of all possible valence states in each material, as summarized in Table 1.2, and can even cause particular structures to be chemically unstable. To understand this, first consider how the  $4f^n$  binding energies of the trivalent ions influence the valence stability. If the  $4f^n$  binding energy is greater than the valence band maximum (i.e. the ground state lies within or below the valence band), the tetravalent state is unstable since it is energetically favorable for a valence band electron to fill the “hole” on the tetravalent rare-earth ion, returning the ion to the trivalent state. If the  $4f^n$  energy is in the band gap, there are no bonding electrons with sufficient energy to fill the hole on a tetravalent rare-earth ion; hence, the tetravalent state is metastable since it cannot return to a trivalent state unless additional electrons are introduced into the conduction band. If the  $4f^n$  binding energy is small enough that it overlaps the conduction band, the system may reduce the total energy by transferring a  $4f$  electron to the lower energy conduction band states. As a result, the trivalent state would be unstable so that the normal ion valence in the material would be tetravalent. Furthermore, since the different valence would be inconsistent with the trivalent chemical bonding, either the entire crystal structure would be unstable or charge-compensating defects would form in the lattice. For the  $4f^{n+1}$  binding energy, similar relationships exist that predict the stability of the divalent state [78].

Table 1.2 – Relationship between the stability of different rare earth valence states and the relative energies of the  $4f^n$ ,  $4f^{n+1}$  and host band states [78].

|                                   | $4f^n$  | $4f^{n+1}$                                    |
|-----------------------------------|---|---|
| Above the conduction band minimum | $4f^n$ is unstable<br>$4f^{n-1}$ is stable    | $4f^n$ is stable<br>$4f^{n+1}$ is unstable    |
| Within the band gap               | $4f^n$ is stable<br>$4f^{n-1}$ is meta-stable | $4f^n$ is stable<br>$4f^{n+1}$ is meta-stable |
| Below the valence band maximum    | $4f^n$ is stable<br>$4f^{n-1}$ is unstable    | $4f^n$ is unstable<br>$4f^{n+1}$ is stable    |

When a RE ion is embedded into a host, it has to enter a crystal with a specific structure. If the lattice site involves divalent bonding (like in ZnO) and if the trivalent state is the RE stable state, the crystal

structure is locally unstable. For this reason, the formation of charge-compensating defects such as interstitial oxygen is often required in order to have trivalent ions. It will be shown in this work that adding more oxygen and using high deposition temperatures during thin film growth allow better atomic organization (alternatively, a partial reorganization can be obtained by post-deposition annealing), which is beneficial for trivalent ion formation in ZnO. In addition, rare earth ions can also be active outside the lattice sites, provided that a convenient crystal field is formed. In this case, the stability rules discussed above are not completely valid.

Theoretical calculations of the level location of trivalent and divalent lanthanides in substitutional position with respect to the bands of several hosts have been performed by Dorenbos *et al.* [104]. Figure 1.24a reports the complete scheme in a large band gap material ( $\text{Y}_3\text{Al}_5\text{O}_{12}$ ) and Figure 1.24b a possible location for the 4f states in ZnO. The ground state 4f-electron binding energies follow a characteristic double zigzag curves when increasing of the number  $n$  of electrons in the 4f-shell. The curves connecting the open circles show that the 5d-electron (ground state) binding energy does not change much with the type of lanthanide.

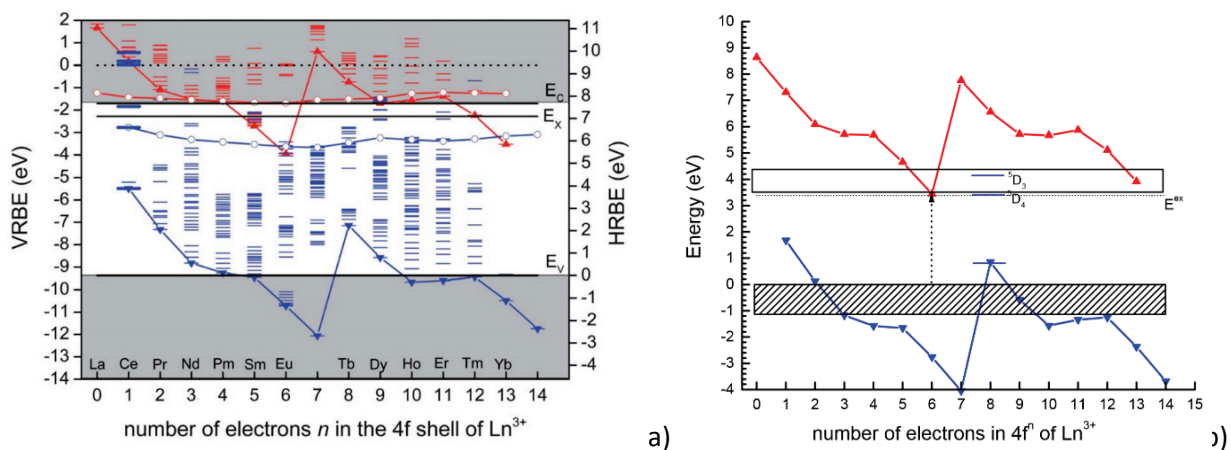


**Figure 1.24** – a) Scheme with the location of divalent (red) and trivalent (blue) lanthanide 4f and 5d levels in  $\text{Y}_3\text{Al}_5\text{O}_{12}$ . Left hand scale shows the vacuum referred and right hand scale the host referred binding energies. For  $\text{Ce}^{3+}$  all five 5d-levels are shown [104]. b) The proposed location of the lowest 4f states of divalent and trivalent lanthanides in ZnO. The top of the valence band is at zero energy. The ZnO exciton state is at 3.38 eV [105].

The principal electronic transitions that can be observed in lanthanide-activated compounds are represented in Figure 1.25. From the left, the first electronic transition is an inter-band transition in the host compound and the second involves the creation of an exciton. These transitions provide information on the fundamental absorption threshold and the location of the mobility edge or conduction band bottom. Then, one may distinguish two types of intra-lanthanide electronic transitions: the intra-configurational  $4f^n-4f^n$  and the inter-configurational  $4f^n-f^{n-1}5d$  transitions. The next process represented is the electron transfer from a lanthanide to a host band or vice versa, which causes a valence change of the lanthanide. If before the transfer the lanthanide ground state is in the forbidden gap, that lanthanide may act as an electron donor to the conduction band or as a hole acceptor from the valence band. Similarly, if after the transfer the ground state is within the gap, the lanthanide may act as an electron acceptor or as a hole donor. Excitation of the lanthanide can occur also by energy transfer from the host. In this case, the valence of the lanthanide is unchanged.

The last electronic transition mechanisms can occur when two lanthanides are simultaneously present in the host. In one case, one lanthanide acts as a donor and the other as an acceptor, and both lanthanides change valence during the transition. For example, efficient down-conversion using Tb-Yb

ions can be obtained with this process [47]. In the second case, no charge transfer occurs and energy transfer takes place if resonance between two transitions is met.

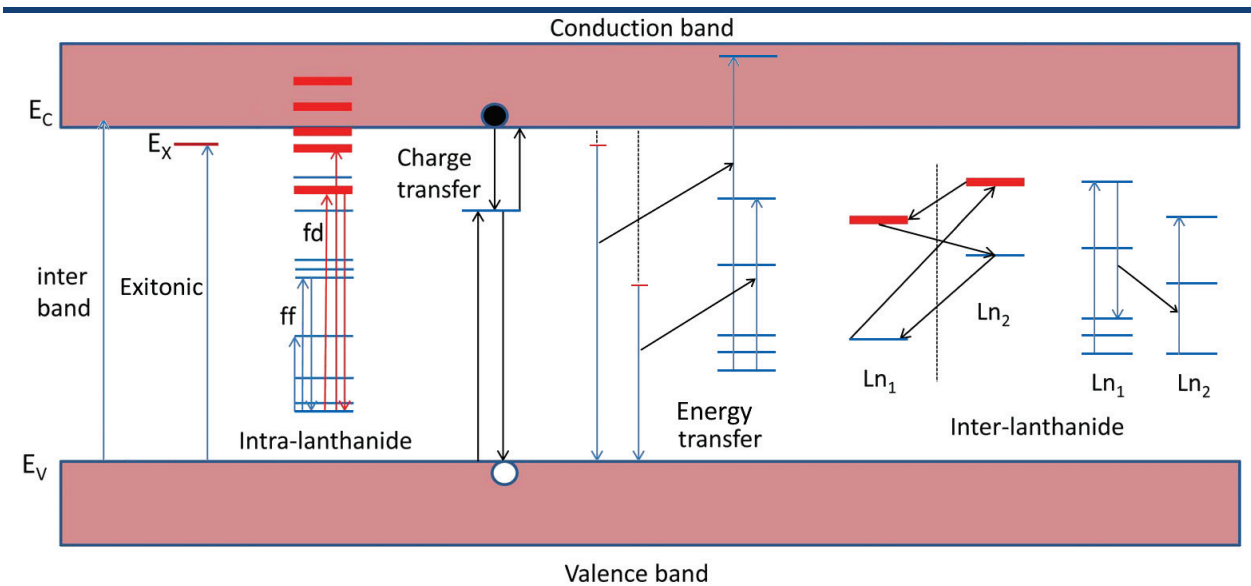


**Figure 1.25** - Principal electronic transitions that can be observed in lanthanide-activated compounds.

Figure 1.25 depicts the electronic transitions of rare earths in a static lattice. In general, the shielding of the 4f electrons strongly reduces the dynamic interactions with the vibrational modes of the host lattice. As a result, most of the 4f-4f transition intensity is concentrated in sharp zero-phonon lines with very little intensity in the phonon sidebands. The weak electron-phonon coupling also slows down non-radiative relaxation processes. In some cases, the excited states lifetime can reach the microsecond range for near-infrared emitters and the millisecond range for visible-emitting ions such as Eu or Tb [106], so that the efficiency of radiative emission can approach the fundamental limit with very little energy wasted by phonon emission.

It would be wrong, however, to completely neglect phonon-assisted transitions. In particular, the competitiveness of these processes depends on the value of the maximum phonon energy of the host with respect to the gap between the excited level of interest and the first lower lying levels. In addition, the interaction with phonons can make some resonant condition less stringent.

The choice of an appropriate host from the point of view of the phonon energy depends on the energy level structure of the RE and the photon conversion process that is involved. For example, if only one rare earth is used, there might be no resonance condition to fulfill. In this case, a host with a low phonon energy is more appropriate. On the other hand, if a cooperative process should occur and the rare earth levels are well spaced, it might be more interesting to have a host with a high phonon energy.

The rate of multi-phonon relaxation (MPR) decreases exponentially with the number of phonons necessary to cover the spacing [107]. As a rule of thumb, it holds that when energy levels are separated by less than 5 times the maximum phonon energy of the host, non-radiative MPR will be dominant, while for energy differences of more than 5 times, radiative decay will dominate [43].

Low phonon hosts are e.g. fluorides, chlorides, iodides, bromides and higher phonon energy hosts are usually oxides, such as silicates, borates or phosphates [45]. For example, an  $\text{YCl}_3$  crystal has maximum phonon energy of 32 meV [108] and  $\text{KPB}_2\text{Br}_5$  of only 17 meV [109]. Unfortunately, most low-phonon hosts are not suited for thin layers in front of solar cells. For this application, oxides are the best candidates.

Also, when the excitation occurs through a sensitizing host the transfer efficiency might depend on the ionization energy of excitons. Materials with large exciton binding energy are expected to be more efficient hosts for rare-earth emission. In fact, when the exciton binding energy is higher than the thermal energy (25 meV at room temperature), most carriers move in the semiconductor as excitons and only few are dissociated by thermal energy. The advantage for optical applications is that excitonic recombination occurs with a narrow spectrum, while free carrier recombination occurs on a wide range of energies above  $E_g$ . This narrow, intense emission can be more efficiently optically coupled with other transitions.

Table 1.3 reports the maximum phonon energy, the optical band gap and the exciton binding energy of several materials that are potential candidates for TCOs and anti-reflection coatings and that can be doped with rare earths.

**Table 1.3** - Maximum optical phonon energy with relative mode, band gap and exciton binding energy of some potential thin film hosts for rare earths.

| Oxide                      | Phonon energy (meV)                                | Mode                 | Band gap (eV)  | Exciton binding energy (meV) |
|----------------------------|--|----------------------|--|------------------------------|
| ZnO                        | 72 <sup>[110]</sup>                                | $E^1$ LO             | 3.37 <sup>b [110]</sup>  | ~60 <sup>[111]</sup>         |
| GaN                        | ~90 <sup>[112, 113]</sup>                          | $A_1$ LO             | 3.4 <sup>[114]</sup>   | ~25 <sup>[115]</sup>         |
| SnO <sub>2</sub> (rutile)  | ~80 <sup>[116]</sup><br>~100 <sup>[116]</sup>      | $A_{1g}$<br>$B_{2g}$ | ~3.6* <sup>[116]</sup>   | ~130 <sup>[117]</sup>        |
| TiO <sub>2</sub> (rutile)  | ~100 <sup>[118, 119]</sup>                         | $E^3_u$ LO           | 3 ÷ 4* <sup>[120]</sup>  |                              |
| SrTiO <sub>3</sub> (cubic) | ~50 <sup>[121]</sup><br>~100 <sup>[122, 123]</sup> | $t_{1u}$ LO3         | 3.2 (indirect) <sup>[124]</sup>                                |                              |
| CeO <sub>2</sub>           | 58 <sup>[125, 126]</sup>                           |                      | 3.6 <sup>[127]</sup>   |                              |
| SiO <sub>2</sub> (amorph.) | ~130-150 <sup>[128]</sup>                          |                      | ~9 (indirect) <sup>[129]</sup><br>11 (direct) <sup>[129]</sup> |                              |
| CdS                        |  |                      | ~2.4 <sup>[130]</sup>  | 28 <sup>b [131]</sup>        |

\* These materials do not have simple direct gaps. More information can be found in the respective references.

<sup>b</sup> Measured on bulk material.

Among the most promising host materials, zinc oxide (ZnO) and cerium oxide (CeO<sub>2</sub>) will be studied in this work. Both materials have potential applications as transparent conductive oxides because of the similar band gap value and refractive index. While ZnO is a low cost material widely used in optoelectronic devices, CeO<sub>2</sub> is much more expensive. Nevertheless, the large ionic radius of Ce makes it a potential better host for rare earth ions. In this work, differences and similarities between these two materials doped with various rare earths will be presented and discussed.

In addition, several rare earth oxide powders have been produced by thermal decomposition of salts. The main reason for this is to have a reference in case the luminescence observed from the films came from oxide particles, instead of substitutional ions, but it could also help understanding the PL mechanisms.

The observed absorption and emission spectra of RE oxides are complicated by the fact that the unit cell often contains several nonequivalent ions. For this reason, and because it would be outside the scope of this work, no detailed analysis of these spectra will be done in this work.

## 1.6 ZnO

---

ZnO is an intrinsic n-type wide band gap ( $\sim 3.3$  eV) semiconductor with a direct band gap that generates a steep absorption edge and high transparency to visible light. Up to  $\sim 10^{21}$  cm $^{-3}$  charge carriers can be introduced by heavy substitutional Al doping leading to resistivities  $< 10^{-3}$   $\Omega$  cm [132, 133]. By controlling the doping level, electrical properties can be changed from insulator through n-type semiconductor to metal while maintaining optical transparency. This explains why in recent years ZnO has been investigated as a low-cost replacement of GaN in optoelectronic devices and ITO in transparent electronic devices such as solar cells and LCD screens.

In spite of many decades of investigations, even some of the basic intrinsic properties of ZnO still remain unclear. For example, n-type conduction of oxide semiconductors is usually based on oxygen vacancies. The nature of the residual n-type conductivity in undoped ZnO films, whether being due to impurities or some native defects, is still under some degree of debate. This is particularly true in ZnO films grown by chemical deposition techniques, where the conductivity might be either due to the large amount of intrinsic defects (oxygen vacancies  $V_O$  and interstitial zinc atoms  $Zn_i$ ) or to non-controllable hydrogen impurities introduced during growth [134].

A similar controversy affects the origin of the ZnO luminescence. ZnO films are well known to exhibit an intense UV and visible broadband luminescence [135-142]. The UV band is usually referred to as the excitonic band, as it is related to exciton recombination across the band gap. The wide visible band is due to defect states in the band gap [135-139, 143-149] and its shape and position depend on the defect state populations. A green emission band is commonly associated with oxygen deficiency [150] and in particular with the presence of ionized oxygen vacancies [140, 151-154]. However, other authors attribute its origin to zinc interstitials in the ZnO matrix [155] or antisite  $O_{Zn}$  defects [135]. Yellow and orange-red luminescence is usually detected for ZnO samples with an excess of oxygen [140, 150, 156] and associated to interstitial oxygen atoms [155, 157-159] or zinc vacancies [140]. Orange-red emission (centered around 640-680 nm) has been less commonly observed than green and yellow emissions [138]. These different understandings of the nature behind the visible luminescent phenomenon in ZnO possibly result from different treatment conditions, Zn precursors and preparation methods, as well as from different theoretical models of the distribution of defects in the gap. Overall, most authors agree to associate green emission to oxygen deficiency and orange-red emission to oxygen excess. Chen *et al.* also show that upon annealing treatment in  $O_2$  atmosphere, the green band is changed into the yellow band and the yellow band is changed into the orange-red band [151]. This could explain why strong green and orange-red bands are never observed simultaneously [150, 160].

It is interesting to point out that, as observed by Studenikin *et al.* [150], the best green luminescent films usually exhibit large porosity. As for the orange luminescence, it is yielded by structures composed of close-packed grains.

Even the band structure of ZnO has been object of some debate in the past. Some discrepancies between the experimental results and *ab initio* calculations have struggled scientists for a long time [134].

Behind the difficulties in theoretical approaches was the partial covalent nature of the bonding and the interplay between four different orbitals. The development of more powerful computers allowed more precise calculations and the result is the following: the lowest conduction band is mainly formed of the partially filled 4s orbital of  $Zn^{2+}$  and the valence band is mainly formed by O 2p states, with an admixture of Zn 3d. From X-ray photoelectron spectra, the admixture of Zn 3d states in the O 2p band has been determined to be about 9% indicating a small covalent contribution to bonding [161].

The band structure of the semiconductor determines the electrical and optical properties of the material and its full understanding is of basic importance. For example, the band gap can be tuned via divalent substitution on the cation site using transition metals, whose d shell can mix with the Zn 4s band and change the position of the bottom of the conduction band. Cd substitution leads to a smaller band gap around 3 eV [162] and Mg substitution to a larger band gap around 4 eV [163].

Like most of the group-II-VI binary compound semiconductors, ZnO crystallizes in either cubic zincblende or hexagonal wurtzite structure, where each anion is surrounded by four cations at the corners of a tetrahedron, and vice versa. At ambient conditions, the thermodynamically stable phase is wurtzite [134]. The zinc-blende ZnO structure can be stabilized only by growth on cubic substrates, and a rocksalt NaCl-type structure may be obtained at relatively high pressures.

Several decades of intense research proved that ZnO can be grown with good hexagonal wurtzite structure with both chemical and physical approaches, on almost any substrate and at all temperatures. The simple crystal-growth technology results in a potentially low cost for ZnO-based devices.

The wurtzite structure belongs to the space group  $P6_3mc$ , corresponding to the point group  $C_{6v}^4$ . A schematic representation of the wurtzite ZnO structure is shown in Figure 1.26. The Zn atoms are tetrahedrally coordinated to four O atoms. In the lattice, layers occupied by Zn atoms alternate with layers occupied by O atoms, creating two interpenetrating hexagonal-close-packed (hcp) sublattices, each of which consists of one type of atom displaced with respect to each other along the threefold  $c$ -axis by the amount of  $u$ . The lattice parameters for ZnO are  $a = 3.25 \text{ \AA}$  and  $c = 5.12 \text{ \AA}$ . The  $u$  parameter is defined as the length of the bond parallel to the  $c$  axis, in units of  $c$ .

In a real ZnO crystal, the wurtzite structure deviates from the ideal arrangement, by changing the  $c/a$  ratio or the  $u$  value.

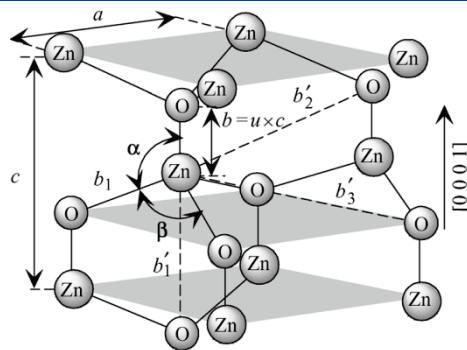


**Figure 1.26** - Schematic representation of a wurtzite ZnO structure with lattice constants  $a$  and  $c$ ,  $u$  parameter, which is expressed as the bond length or the nearest-neighbor distance  $b$  divided by  $c$  (0.375 in ideal crystal),  $\alpha$  and  $\beta$  ( $109.47^\circ$  in ideal crystal) bond angles, and three types of second-nearest-neighbor distances  $b'_1$ ,  $b'_2$ , and  $b'_3$  [134].

When ZnO is used as transparent conductive oxide (TCO) for solar cell applications, the addition of luminescent rare earth (RE) ions can further functionalize the film and photon-management properties can be obtained. By adapting the incident solar spectrum to a specific single junction solar cell, the photovoltaic conversion efficiency can be enhanced. However, due to the small absorption cross section of RE ions, energy transfer from the absorbing host might be the only way to obtain a reasonable quantum yields. Wide band gap semiconductors like ZnO can provide the necessary absorption in the UV region and have been therefore considered as host materials.

One might argue that doping a low-cost host with expensive rare earths is non-sense for the PV market. However, the additional cost per square meter of solar cell can be easily calculated and it turns

out that despite the high cost of rare earth oxides ( $\geq 100$  \$/Kg), the small amount used for doping the TCO maintains the price lower than 0.01 \$/m<sup>2</sup> of solar cell<sup>14</sup>.

Compared to other TCOs, ZnO combines several advantages when considered as a host for rare earth ions. First, it has a strong absorption cross section between 300 and 400 nm, so that it is potentially a good sensitizer for DS and DC. Second, it has a good exciton-binding energy of 60 meV. This value is larger than the thermal energy ( $k_B T = 25$  meV), so that excitons can travel longer distances in the semiconductor and reach radiative (and non-radiative) defects. Thus, ZnO potentially possesses the second essential property for a sensitizer: excited carrier relaxation can occur in the neighborhood of the RE ion. From this point of view, ZnO compares favorably to semiconductors with a small exciton binding energy like GaN, but not to others like SnO<sub>2</sub> (130 meV).

Another advantage of ZnO is related to dipole-allowed direct transitions across the gap. Although many oxide semiconductors possess wide band gaps in the ultraviolet (UV) regime, currently the majority of them cannot efficiently emit UV light because the band-edge optical transition is forbidden in a perfect lattice as a result of the symmetry of the band-edge states. This quantum mechanical rule severely constrains the optical applications of wide-band gap oxides, which is also the reason why so few oxides enjoy the success of ZnO [116]. When it comes to energy transfer to rare earth ions, the dipole-forbidden nature of the gap can prevent dipole-dipole energy transfer.

Finally, the phonon energy also compares favorably to other materials like GaN, SnO<sub>2</sub> and TiO<sub>2</sub> (see Table 1.3) for the simple reason that smaller phonon energy implies lower rate of non-radiative relaxation between 4f levels (see paragraph 1.4.4).

For all these reasons, strong research work has been done on RE doping of ZnO powders, nanostructures and nanocrystals [164-176]. Compared to the years of research on ZnO, this is quite a recent topic. Except for the work of Bachir *et al.* [176], all other works have less than ten years.

Recently, efficient doping of ZnO thin films with several REs has been achieved by means of physical<sup>15</sup> deposition techniques [177-179]. Chemical approaches like spray, sol-gel and spin coating usually lead to poor optical activation, probably due to the poor crystalline quality and the related high amount of non-radiative defects [143, 180].

An in-depth discussion of the mechanical, chemical, electrical, and optical properties of ZnO in addition to the technological issues such as growth, defects, p-type doping, band-gap engineering, devices, and nanostructures can be found in the literature [110, 134, 147, 181-183] and is outside the scope of this work.

More important here is to understand how RE ions enter the wurtzite ZnO crystal. REs in their 3+ form are ideally surrounded by six oxygen atoms forming a pseudo-octahedron structure with a  $C_{4v}$  symmetry. In the bulk wurtzite structure, the site symmetry of any atom of the lattice is  $C_{3v}$  and the coordination is only tetrahedral. This means that a RE ion replacing Zn in the ZnO lattice does not normally act as an optically active center (there is not enough oxygen to create the 3+ state), unless the local structure is changed e.g. by interstitial oxygen or zinc vacancies. Non-stoichiometric growth, high deposition temperatures or annealing treatments are often needed in order to activate the rare earth ion. We will see that in real RE oxides the  $C_{4v}$  symmetry is not always respected and that charge compensating defects also alter the  $C_{3v}$  symmetry of Zn sites.

---

<sup>14</sup> A cost of about 0.001 \$/m<sup>2</sup> has been calculated using the average price of a 99% pure rare earth oxide of about 100 \$/Kg (Frontier Rare Earths, 2014), a ZnO thickness of 100 nm and a doping level of 1%. Material losses related to the growth technique have been ignored.

<sup>15</sup> Physical deposition techniques start from solid precursors, while chemical techniques start from gases or solutions.

In addition, the ionic radius of Zn<sup>2+</sup> in the tetrahedral coordination of ZnO is small compared to the radius of REs. The effect of the symmetry breaking is therefore stronger and a large Stark splitting of the electronic levels is expected.

Paragraph 1.5.6 indicated that the band structure is also important when considering the energy transfer, if this occurs via charge transfer to the RE. The position of the f and d energy levels with respect to the ZnO bands has to be considered case by case, depending on the RE.

In conclusion, there are both potential advantages and disadvantages in using ZnO as host for RE insertion. However, theoretical considerations and conjectures based on ideal crystals can hardly replace experimental tests. The success of a certain RE-host couple can be strongly dependent on the presence (or absence) of certain defects in the lattice, whose population is characteristic of the preparation method (and procedure).

This work will investigate Yb-, Pr- and Nd-doped ZnO films deposited by the sputtering technique. All these rare earths potentially present efficient NIR emission just above the band gap of silicon. If Yb can only lead to downshifting due to its single excited level, Pr and Nd could also lead to down-conversion. The combination of Pr and Yb is also particularly promising for cooperative down-conversion [184]. Several works have shown that appreciable down-conversion efficiencies can be reached [185-187] by using the appropriate host. Therefore, the down converting properties of Pr-Yb co-doped ZnO will be also tested.

## 1.7 CeO<sub>2</sub>

Unlike ZnO, CeO<sub>2</sub> is a material that is completely unknown in photovoltaics. Some of the most interesting applications depend directly on properties induced by non-stoichiometry and the presence of the related point defects. For example, the applications in catalysis [188-190] and the potential applications in spintronics as CeO<sub>2</sub> nanostructures exhibit room temperature ferromagnetism [191, 192]. For this reason, considerable attention has been devoted to the investigation of the electronic properties of nanocrystalline non-stoichiometric CeO<sub>2</sub> due to the changes of electronic structure induced by the presence of oxygen vacancies and the reduction of Ce<sup>4+</sup> ions to Ce<sup>3+</sup> ions. This ability to release oxygen is intimately connected to the facility with which the Ce sites can be converted reversibly between the +4 and the +3 oxidation states.

Defect-related electronic states present in the band gap of non-stoichiometric CeO<sub>2</sub> play vital role in these applications. Other practical uses of ceria are in polishing [193], automobile exhaust catalysts [194] and solid electrolytes in solid oxide fuel cells [195, 196].

Cerium dioxide (CeO<sub>2</sub>) has a cubic fluorite-type structure with a lattice constant  $a$  of 5.411 Å. The fluorite crystal belongs to the space group  $Fm\bar{3}m$  [197], which corresponds to the point group  $O_h^5$  [198]. Ce<sup>4+</sup> ions are coordinated to 8 oxygen atoms in a cubic O<sub>h</sub> symmetry.

Figure 1.27 illustrates the crystal structure of CeO<sub>2</sub> and the coordination of Ce<sup>4+</sup> lattice sites. The CeO<sub>2</sub> lattice is formed by two interpenetrating lattices: a face-centered cubic sublattice formed by the Ce ions and a simple cubic sublattice formed by the oxygen ions.

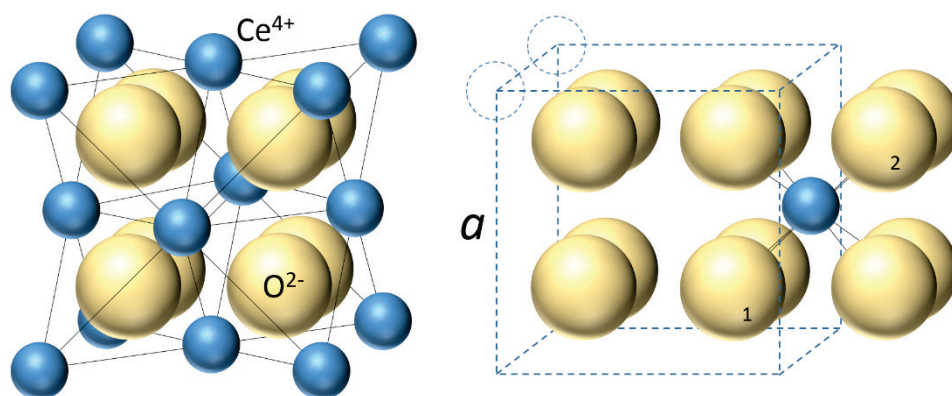


Figure 1.27 – CeO<sub>2</sub> fluorite-type crystal structure and Ce<sup>4+</sup> coordination.

Most of the interesting properties of CeO<sub>2</sub> come from its band structure. In the following, the band structure of rare earth oxides will be explained in order to understand why CeO<sub>2</sub> is the only oxide that can be used in solar cell applications. The band gaps of rare earth oxides are reported in Table 1.4.

In RE oxides, the conduction band is usually formed of RE 5d(6s) states and the valence band of O 2p states. The position in the electron spectrum of the f band remains questionable. Using qualitative considerations based on the atomic theory, that 4f levels are expected to lie within the valence band. However, calculations compared with the results of XPS studies [104, 199, 200] have shown that the binding energy of 4f-orbitals varies across the series with a characteristic double zigzag curve (see Figure 1.24). The position of the f states with respect to the O 2p band can explain why the band gap values of sesquioxides are so different, despite the almost constant energy of 5d states.

Table 1.4 - Band gaps of rare earth oxides [201].

| Sesquioxides                                | E <sub>g</sub> (eV) | Dioxides                        | E <sub>g</sub> (eV) |
|---|---------------------|---------------------------------|---------------------|
| La <sub>2</sub> O <sub>3</sub>              | 5.5                 |                                 |                     |
| Ce <sub>2</sub> O <sub>3</sub> <sup>*</sup> | 2.4                 | CeO <sub>2-x</sub>              | 3.6                 |
| Pr <sub>2</sub> O <sub>3</sub> <sup>*</sup> | 3.9                 | PrO <sub>2-x</sub> <sup>a</sup> | <1 <sup>b</sup>     |
| Nd <sub>2</sub> O <sub>3</sub>              | 4.7                 |                                 |                     |
| Gd <sub>2</sub> O <sub>3</sub>              | 5.4                 |                                 |                     |
| Tb <sub>2</sub> O <sub>3</sub> <sup>*</sup> | 3.8                 |                                 |                     |
| Dy <sub>2</sub> O <sub>3</sub>              | 4.9                 |                                 |                     |
| Ho <sub>2</sub> O <sub>3</sub>              | 5.3                 |                                 |                     |
| Er <sub>2</sub> O <sub>3</sub>              | 5.3                 |                                 |                     |
| Tm <sub>2</sub> O <sub>3</sub>              | 5.4                 |                                 |                     |
| Yb <sub>2</sub> O <sub>3</sub>              | 4.9                 |                                 |                     |
| Lu <sub>2</sub> O <sub>3</sub>              | 5.5                 |                                 |                     |

<sup>a</sup> usually Pr<sub>6</sub>O<sub>11</sub>

<sup>b</sup> estimated from diffuse reflectance

The empty 4f-levels in La<sup>3+</sup> lie much higher than the bottom of the 5d-band. Beginning from Ce<sup>3+</sup>, the energy of the f-shell becomes lower than that of the d-shell and further decreases across the lanthanide series. However, this fall is not monotonous. The monotony is violated when the second half of the f shell starts to fill. For Gd<sup>3+</sup> and Lu<sup>3+</sup>, the f shell lies deep below the d shell (see Figure 1.24). Thus, the sesquioxides of these three rare earths (La, Gd and Lu) are characterized by the highest band gaps (defined by the distance between the O 2p and the RE 5d shell). When it is not above and not too far below the d shell, the f shell plays an active role in the determination of the gap. In other words, if the f-

band is situated in the forbidden gap, then  $E_g$  is determined either by the p-f gap (if the f shell is empty) or by the f-d gap (if the f shell is partially filled<sup>16</sup>). Although the f shell can determine the optical gap, its localized nature of its electron states should forbid thinking of it as a band. However, it turns out that hybridization with the 5d and 2p states introduces a band-like character [202].

The low 4f binding energy of some rare earths (namely Ce, Tb and Pr) leading to the lowest band gap values can be qualitatively explained as follows. Both Ce<sup>3+</sup> and Tb<sup>3+</sup> ions have one electron in excess with respect to the most stable  $f^0$  and  $f^7$  configurations. Pr<sup>3+</sup> has two excess electrons with respect to the  $4f^0$  configuration, but its 4f electrons have the same binding energy as those of Tb (see Figure 1.24) and have therefore a similar behavior. The small binding energy of f electrons results in a relatively low energy of the  $4f^n-4f^{n-1}5d^1$  transition. In particular, the binding energy of the ground state of the 4f shell is small enough that this level lies above the valence band and determines the gap. It is interesting to notice that when this happens, studying the absorption edge is equivalent to studying the density of states of the 5d band. In fact, due to the inner nature of the f shell, f-d transitions occur from very localized ground states. Therefore, there is no convolution with a large valence band.

In the case of CeO<sub>2</sub>, the distance between the valence band (O 2p) and the conduction band (Ce 5d) has been experimentally found in the 5.5–6.5 eV range [203, 204]. Inside the CeO<sub>2</sub> gap there is an empty Ce 4f state ( $4f^0$ ), which is narrow and localized in stoichiometric ceria [205]. The f shell being empty, its distance from the valence band is referred to in the literature as the optical gap, and its value is 3.6 eV [206].

Not all interesting properties of CeO<sub>2</sub> originate from its non-stoichiometry and many technological applications can benefit of its unique electronic properties related to the band structure. For example, the electronic behavior of CeO<sub>2</sub> is of considerable interest in that the 4f electron in Ce is thought to be at the borderline of exhibiting localized and band-like behavior.

The conventional knowledge on lanthanides suggests that CeO<sub>2</sub> contains Ce<sup>4+</sup> ions with a configuration of localized  $4f^0$  states. The large band gap ensures insulating behavior. Ce<sub>2</sub>O<sub>3</sub>, on the other hand, is formally constituted by Ce<sup>3+</sup> ( $f^1$ ) ions. A partially occupied 4f band normally result in a certain metallic behavior. However, due to the localized nature of 4f states, it is expected that both materials are insulating.

This simple picture cannot explain why the 4f electronic levels of Ce present band-like behavior. If, however, the bonding laid between the ionic and the covalent description through hybridization, it could be indeed described by band structure. The band-like character is added to the 4f band through mixing with the O 2p and Ce 5d states.

A theoretical approach using the HSE hybrid functional theory has been proposed by Hay *et al.* [205]. The distribution of the electronic states around the Fermi level is reported in Figure 1.28a for both CeO<sub>2</sub> and Ce<sub>2</sub>O<sub>3</sub>. Their work shows that all three bands are a hybrid of O 2p, Ce 4f and Ce 5d states. The prevalent component is indicated in the figure. For Ce<sub>2</sub>O<sub>3</sub>, the occupied 4f states split from the rest of the 4f band and create a gap of 3.2 eV to the rest of the 4f states and to the 5d states. Since f-f transitions are dipole forbidden, an optical measurement of the band gap will detect principally the f-d gap. This value is higher than the value measured by Prokofiev *et al.* (2.4 eV) [201]. The band gap of CeO<sub>2</sub> is given by the p-f transitions. The f band is split into two bands that are 3.3 eV and 3.5 eV away from the valence band, respectively. These values are close to the previously reported value of 3.6 eV.

The most popular model describes CeO<sub>2</sub> as mixed-valence: the valence at the Ce site fluctuates between Ce<sup>3+</sup>,  $4f^1(v)$ , with a vacancy (v) in the valence states of oxygen 2p and Ce<sup>4+</sup>,  $4f^0$  [202, 207-212].

<sup>16</sup> The empty f states are superimposed with the d states, but they do not determine the gap due to the forbidden nature of f-f transitions.

The configuration interaction between the two valences best describes the electronic structure of the system.

Strictly, Ce<sub>2</sub>O<sub>3</sub> and CeO<sub>2</sub> should be written as Ce<sub>2</sub>O<sub>3</sub><sup>\*</sup> and CeO<sub>2-x</sub> to indicate that it is not possible to form stoichiometric crystals. Experimental evidence of the mixed valence can be found in the analysis of the of the 3d photoemission spectra [213]. In Ce<sub>2</sub>O<sub>3</sub><sup>\*</sup>, Ce in the ground state is in the almost trivalent state. In CeO<sub>2-x</sub>, it is in the 3+ and 4+ mixed-valence state with 4f electron occupation around 0.4-0.5. This mixed valence is characteristic of other rare earth oxides (Tb, Pr) and explains their particularly rich phase diagrams.

Experimental evidence of this type of band structure has been reported by Askrabic *et al.* [214] for nanocrystalline CeO<sub>2</sub>. Nanostructured CeO<sub>2</sub> tends to release more oxygen than bulk CeO<sub>2</sub> due to the increased surface-to-volume ratio and the electrons left behind when oxygen vacancies are created can be either localized on the Ce<sup>4+</sup> ions or captured by oxygen vacancies. The localization of electrons on the Ce<sup>4+</sup> ions is followed by the reduction of Ce<sup>4+</sup> ions to Ce<sup>3+</sup> ions and partial filling of the 4f band. Partial filling of the 4f band introduces some occupied 4f states in the band gap between the full O 2p and the empty 4f (4f<sup>0</sup>5d<sup>1</sup>) bands. These states lie close to the O 2p valence band [215, 216], as shown in Figure 1.28b. In other words, CeO<sub>2</sub> presents a certain Ce<sub>2</sub>O<sub>3</sub> character due to the presence of some Ce<sup>3+</sup> sites.

In this work, CeO<sub>2</sub> will be deposited in thin films. The behavior of these films is expected to be in-between the bulk and the nanocrystals.

It is interesting to study CeO<sub>2</sub> as photon-converting layer because of its good compatibility with silicon-based optoelectronics. In contrast to rare-earth doped oxide phosphors such as Y<sub>2</sub>O<sub>3</sub>, RE doping into CeO<sub>2</sub> in view of luminescence has been relatively less studied. CeO<sub>2</sub> is a promising host material for photon management because of its good thermal and chemical stability and low phonon energy (465 cm<sup>-1</sup> ≈ 58 meV) [125, 126]. In addition, the ionic radius of trivalent lanthanide ions is very close to that of Ce<sup>4+</sup> (~90 pm) [217].

When a trivalent lanthanide substitutes a Ce<sup>4+</sup> ion, the symmetry of the lattice site is lowered [218, 219]. In particular, two oxygen vacancies replacing e.g. atoms 1 and 2 in Figure 1.27 could reestablish the six-fold coordination of trivalent lanthanides (see Figure 1.22). This event is particularly probable due to the high concentration of oxygen vacancies related to the unavoidable presence of Ce<sup>3+</sup> ions.

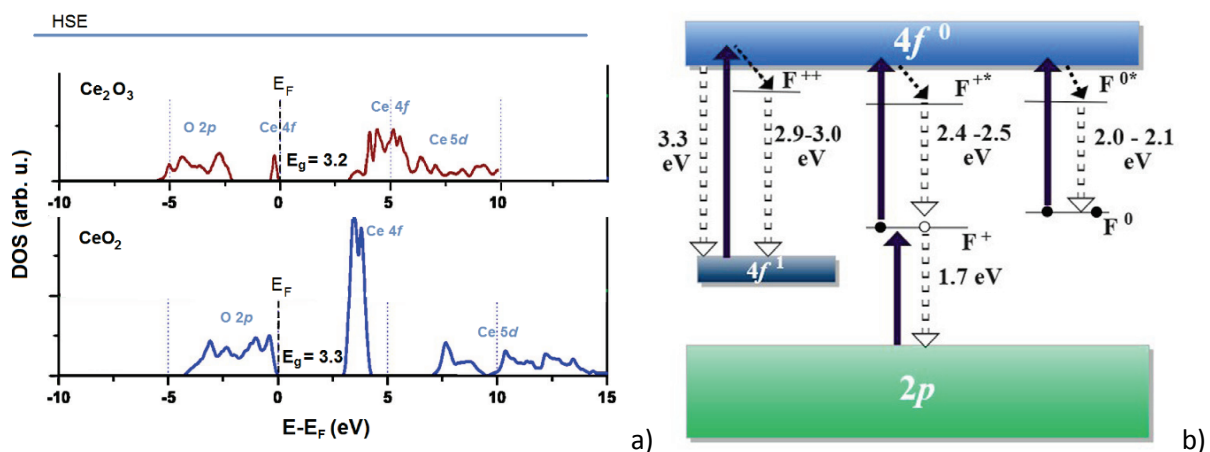


**Figure 1.28** – a) Density of states (DOS) for the ground state of Ce<sub>2</sub>O<sub>3</sub> and CeO<sub>2</sub> calculated using the HSE functional theory [205]. b) Illustration of radiative electronic transitions in nanocrystalline CeO<sub>2</sub> samples [214].

Recently, the UC properties have been investigated by Wu *et al.* [220] in three-dimensionally ordered macroporous CeO<sub>2</sub>: Er<sup>3+</sup>, Yb<sup>3+</sup>, while the structural and luminescent properties of CeO<sub>2</sub>:Eu<sup>3+</sup> and

CeO<sub>2</sub>:Sm<sup>3+</sup> thin films have been investigated by Fujihara *et al.* [221] and by Wang *et al.* [Li, 2013 #476] in CeO<sub>2</sub>/Sm<sub>2</sub>O<sub>3</sub> multilayers.

Tetravalent cerium ions (Ce<sup>4+</sup>) have no 4f electron. This implies that CeO<sub>2</sub> can be a promising photoluminescence host material because of strong light absorption through the charge transfer (CT) from O<sup>2-</sup> to Ce<sup>4+</sup> in the UV-blue region of the spectrum. If efficient energy transfer to the lanthanide dopant occurs, CeO<sub>2</sub> can be a good host for photon conversion.

This host is also appropriate for solar cell applications as anti-reflection coating on silicon solar cells, given its high transparency to visible light ( $E_g = 3.6$  eV [127]), and the refractive index around 2.

Using a rare earth oxide as host instead of ZnO is more expensive. If 1% RE doping of ZnO led to a cost of 0.001 \$/m<sup>2</sup>, the cost of 100 nm of CeO<sub>2</sub> is expected to be about 100 times higher, i.e. 10 cents/m<sup>2</sup>. More precise calculation using the density of CeO<sub>2</sub> (7.3 g/cm<sup>3</sup>) and the volume to obtain the weight per square meter of solar cell indicated that 100 nm of CeO<sub>2</sub> cost 7.3 cents/m<sup>2</sup> for CeO<sub>2</sub> powder bought at 100 \$/Kg. Fortunately, the ideal thickness for anti-reflection coating properties is only 60 nm.



## 2 EXPERIMENTAL TECHNIQUES

### 2.1 Thin film deposition techniques

#### 2.1.1 Sputtering

Due to the large ionic radius of REs, insertion of these ions into ZnO can be quite a difficult task. For this reason, physical deposition techniques like sputtering should provide better dopant insertion compared to chemical approaches.

The principle of reactive sputtering allowing the growth of oxides from a metallic target is illustrated in Figure 2.1. A high vacuum is created in the sputtering chamber, where the substrate is placed in front of the target. Argon gas is then inserted in the chamber and a voltage is applied between the substrate and the target. At the breakdown voltage, which depends on the pressure, electrons flow from the cathode and are accelerated by the electric field. When this current passes through the neutral Ar atoms, it ionizes part of them. In the process, more free electrons are created that can be further accelerated and can ionize other atoms. A dynamic equilibrium is reached between the ionization and the recombination processes.  $\text{Ar}^+$  ions are then accelerated towards the target, where they can pull out some metal atoms (the emission of one atom results from several impacts). Since the desired film is an oxide, oxygen gas is added in the chamber to react with the metal. The compound can be formed on the target surface, in-flight or on the substrate depending on the process parameters and metal oxidation energy.

When argon ions hit the target, they tend to be neutralized by taking an electron from the target. In the case of metal targets, these electrons can be replaced by other electrons from the underlying cathode. The use of an alternate voltage (usually a radiofrequency, RF) is necessary in the case of insulating targets, but is also possible in the case of metallic targets.

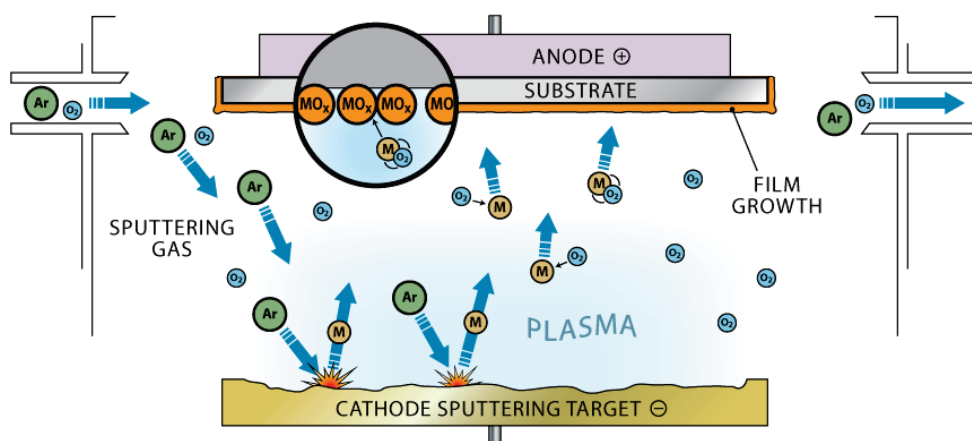
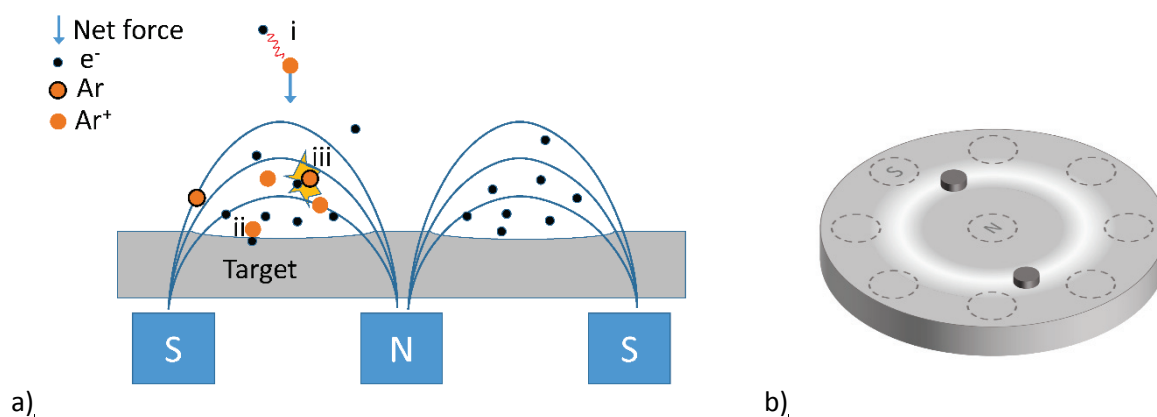


Figure 2.1 – Working principle of reactive sputtering

A magnetic field around the target can highly increase the efficiency of the sputtering process. Argon atoms ionized by the voltage (i) are accelerated by the net force and neutralize on the target (ii). With the magnetic field lines disposed as shown in Figure 2.2, a high concentration of electrons is maintained close to the surface. The high kinetic energy of these electrons is sufficient to ionize the argon atoms

(iii), so that they are attracted again onto the target. The combination of the radiofrequency with the magnetic field is called “magnetron”.



**Figure 2.2** – a) Working principle of magnetron sputtering and b) placement of the RE metal discs on the zinc target in our sputtering system. The dashed circles represent the position of the magnets under the target. The white zone indicates where sputtering prevalently occurs due to the magnetic field.

All ZnO films prepared for this work have been deposited by RF magnetron reactive sputtering using an *Orion3* sputtering system by AJA international. In this system, up to three targets can be placed and allow confocal sputtering. A distance-to-substrate of 12 cm provided good uniformity over a surface of about 2". All targets were pure 2" metallic Zn targets. Doped films have been obtained by placing small discs of metallic REs as shown in Figure 2.2b. To avoid contamination, several targets have been used for the different rare earths. Co-doping has been achieved by co-sputtering from two targets.

Two massflows ensured the desired gas flows and the pressure in the chamber was maintained by an electrovalve with feedback control in front of the turbomolecular pump. The deposition pressure was fixed at 3.4 mTorr and the RF power at 50 W, values that ensured reasonable growth rates and good film quality.

The Ar gas flow has been varied between 8 and 16 sccm and the oxygen flow between 1.5 and 5 sccm. The substrate temperature was varied between 15 °C (temperature of the substrate holder cooled with water) and 400 °C by two halogen lamps located behind the sample holder.

Since the pressure in the chamber is maintained constant, the gas flow ratio is the key parameter and not the absolute value of the gas flows. However, since the Ar gas enters the chamber close to the target, while oxygen enters close to the substrate, this is valid up to a certain limit. In the range explored in this work, this approximation proved to be valid. For example, a gas flow ratio of 16:4 gives the same results of a gas flow of 8:2. Therefore, in the results the ratios will be often indicated instead of the absolute flows.

### 2.1.2 Pulsed laser deposition (PLD)

Another physical deposition technique is pulsed laser deposition (PLD). The working principle of PLD is illustrated in Figure 2.3 and is based on focusing a high-power UV laser on a target of the desired material. The high energy transferred to the target is sufficient to pull off and ionize the atoms of the target's surface. A plasma plume is formed perpendicular to the target and the atoms start to deposit on the substrate placed in front. A galvanometric motor coupled with two mirrors moves the laser beam so that a certain surface can be swept on the target. The laser source was a KrF excimer laser with a frequency of 10 Hz and a power of 25 mJ. Films grown by PLD usually maintain the stoichiometry of the

target, but a gas flow can be added in the chamber to react with the plasma and change the film properties. The substrate was heated by a resistance and rotated at 5 rpm to increase uniformity of the deposited layer.

An advantage of PLD over the sputtering technique is that the deposition can be easily performed from home-made, sintered, small targets. Among the reasons behind the choice to deposit  $\text{CeO}_2$  and  $\text{CeO}_2\text{:RE}$  thin films by PLD is the very short preparation time of the targets and the higher cost of  $\text{CeO}_2$  sputtering targets compared to that of pure Zn targets. The sintering procedure will be given in paragraph 2.2.

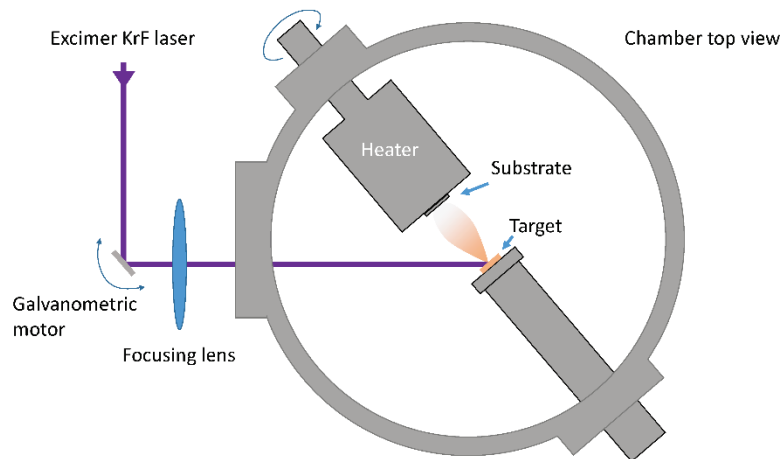


Figure 2.3 – Working principle of PLD

PLD cannot be scaled up for industrial applications, but it is very useful for lab tests and can provide good insertion of dopants like the sputtering technique.

In order to investigate the properties of undoped and doped  $\text{CeO}_2$  films, several parameters have been changed such as the deposition temperature and the oxygen pressure during deposition. Since these layers should be compatible with solar cells, most samples have been grown at temperatures below 600 °C. The highest tested oxygen pressure is  $5 \cdot 10^{-3}$  mbar. Square silicon substrates of 1 cm<sup>2</sup> have been used.

## 2.2 Powder preparation and PLD target sintering

In this work, several RE oxide powders have been used. Since the rare earths have to be inserted into oxide hosts, the study of the structural and optical properties of pure RE oxides is particularly useful. In addition, these oxides are necessary in the preparation of PLD targets.

Except for  $\text{CeO}_2$  (Sigma Aldrich®, 99.95% pure) and  $\text{Pr}_2\text{O}_3$  (Alfa Aesar®, 99.9% pure), all other oxides have been prepared starting from RE salts. These salts have been thermally decomposed in air using tubular furnaces.  $\text{Yb}_2\text{O}_3$  was prepared by decomposing Yb-oxalate ( $\text{Yb}_2(\text{C}_2\text{O}_4)_3$ ) in air at 700 °C during 1 h, as suggested by Hussein and Balboul [223]. The oxalate has been prepared by mixing a solution of Yb-acetate ( $\text{Yb}(\text{C}_2\text{H}_3\text{O}_2)_3 \cdot x\text{H}_2\text{O}$ , Sigma Aldrich®, 99.999% pure) with a solution of oxalic acid. The precipitate was then dried overnight at 50 °C before annealing.

In the case of  $\text{Nd}_2\text{O}_3$ , Nd-nitrate hexahydrate ( $\text{Nd}(\text{NO}_3)_3 \cdot 6 \text{H}_2\text{O}$ , Fluka®, 99.9% pure) has been decomposed at several temperatures up to 1200 °C.  $\text{Nd}_2\text{O}_3$  from Sigma Aldrich® (99.9% pure) was also available. Such high temperatures were reached using a Lenton® furnace.

The preparation of  $\text{CeO}_2\text{:RE}$  PLD targets was carried out by solid state reaction of the oxides from the stoichiometric mixture of the elemental oxide powders. The exact weight ratio between  $\text{CeO}_2$  and the rare earth sesquioxide have been calculated in order to attain the desired nominal concentration  $x$  (with

respect to the Ce content). 4 g of powders pressed in a mold with diameter of 26 mm give after sintering about 18 mm x 2 mm round targets for PLD. Once the powders have been weighted, they are carefully mixed in a mortar by adding few ml of ethanol and then dried. The powders are then pressed in the mold at 100 bars during 5 minutes and let dry overnight at 50 °C. The next day, the pellets were placed into the Lenton® furnace where the temperature was increased up to 1400 °C at 1.6 °/min, followed by a dwell of 10 h at 1400 °C and slow cooling down to room temperature.

## 2.3 Annealing of ZnO thin films

ZnO thin films have been annealed in a quartz tubular furnace by Carbolite Ltd using argon, oxygen and nitrogen constant gas flows. The procedure with which the samples are placed in the furnace is very important. In particular, the steepness of the temperature ramps can deeply change the annealing effects. For temperatures up to 700 °C, annealing was performed as follows. The sample was placed into a quartz annealing boat and entered in the furnace on position 2 of Figure 2.4. After 30 s, the boat is pushed to position 3. The cap seals the tube during step 3. Before extraction, the boat was stopped in position 2 during 60 s and then in position 1 during 30 s. The annealing times reported in this work are the sum of all these steps. Afterwards, the boat was extracted, the sample removed and cooled in air.

For annealing temperatures above 700 °C, the insertion step in position 2 was of 60 s and the extraction time in 2 and 3 were of 90 s and 60 s, respectively.

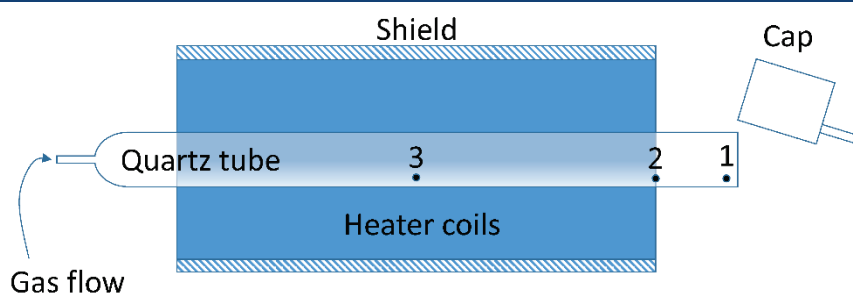


Figure 2.4 – Section view of a quartz tubular furnace.

## 2.4 Thin film characterization techniques

### 2.4.1 Structural and morphological characterization

In this work, structural information has been obtained by X-ray diffraction (XRD) and morphological characterization by different microscopies such as atomic force microscopy (AFM), transmission electron microscopy (TEM) and scanning electron microscopy (SEM). Additional information on the film properties and in particular that associated to the dopant has been obtained by Rutherford backscattering spectroscopy (RBS) and near-edge X-ray absorption spectroscopy (NEXAFS). The following paragraphs are dedicated to the description of these techniques and to the specific instrumentation used in this work.

#### *X-ray diffraction (XRD)*

In 1913, English physicists Sir W.H. Bragg and his son Sir W.L. Bragg developed a relationship to explain why the cleavage faces of crystals appear to reflect X-ray beams at certain angles of incidence ( $\theta$ ). This observation is an example of X-ray wave interference, commonly known as X-ray diffraction (XRD), and

was direct evidence for the periodic atomic structure of crystals postulated for several centuries. Figure 2.5 illustrates its principle. The variable  $d$  is the distance between atomic layers in a crystal, and the variable  $\lambda$  is the wavelength of the incident X-ray beam;  $n$  is an integer. In crystals, atoms are disposed in a regular lattice and atomic planes are separated by distances that are comparable to X-ray radiation wavelengths. Therefore, when an incoming electromagnetic wave hits the crystal, interference phenomena are likely to occur. In particular, constructive interference occurs when the difference in optical path between the two reflections ( $2d \sin \theta$ ) is a multiple of the wavelength. Bragg's relation then reads

$$n\lambda = 2d \cdot \sin \theta$$

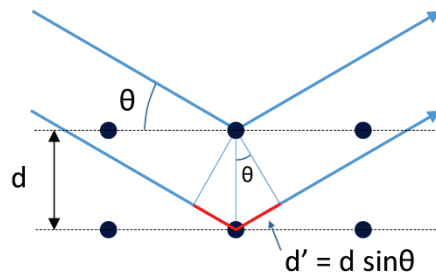


Figure 2.5 – Interference between two reflections from adjacent atomic planes.

If a constant wavelength is used, the angle  $\theta$  can be varied and the position of the constructive interference peak gives the interplanar distance (or  $d$ -spacing). Since there are several families of planes in a lattice, a diffraction pattern usually contains several peaks. Each peak in the pattern is associated with a family of planes  $\{h\ k\ l\}$ <sup>17</sup>. Details about the calculation of  $d$ -spacings from the diffraction angles are given in [Appendix C](#).

It is very important to calculate the lattice parameters, because in real crystals they depend on the defects. Compressive and tensile stress caused by impurities will affect the volume of the unit cell and provide information on the defect population.

The most common X-ray diffraction configuration is the so-called “ $\theta$ - $2\theta$ ” (or Bragg-Brentano) configuration (Figure 2.6). The detection angle is measured with respect to the incident beam direction and is therefore  $2\theta$ . With this setup, only the families of planes parallel to the sample surface are investigated. In a single crystal, this corresponds to a single family of planes, i.e. the measured diffraction pattern is made of a single peak (and its higher orders).

Sometimes real crystals are deformed and the planes are slightly bent. This means that constructive interference can be obtained also at small angles from the normal. Information about the bending can be obtained by oscillating the sample in the symmetric (with respect to the sample surface) configuration of the  $\theta$ - $2\theta$  scan. In real materials, each Bragg angle  $\theta_{hkl}$  has a certain distribution in  $\omega$ . This is the principle of  $\omega$ -scan (or “rocking curve”).

For polycrystalline materials with randomly oriented crystallites<sup>18</sup>, a simple  $\theta$ - $2\theta$  scan provides information about all  $d$ -spacings and the concept of  $\omega$ -scan becomes meaningless.

With thin films, the situation is more complicated. They can be made of either a single crystal, of randomly oriented crystallites or of partially oriented crystallites (textured, i.e. aligned along one

<sup>17</sup> The Miller indices  $h$ ,  $k$  and  $l$  determine a family of lattice planes orthogonal to a direction  $[h, k, l]$  in the basis of the reciprocal lattice vectors.

<sup>18</sup> Crystallites are small regions of the material in which the material is in single crystalline form. Crystallites must not be confused with grains or particles. Each grain is usually made of several crystallites.

direction). We will show further that crystallites in ZnO films have a preferential orientation and that the preferential orientation is perpendicular to the sample surface. In this case, the diffraction pattern will show only one peak, just like the single crystal, and the  $\omega$ -scan acquires a new meaning. Assuming that crystal plane bending is negligible because strain is relaxed at grain boundaries, an  $\omega$ -scan gives direct information about the tilt distribution of the crystallites around the preferential direction.

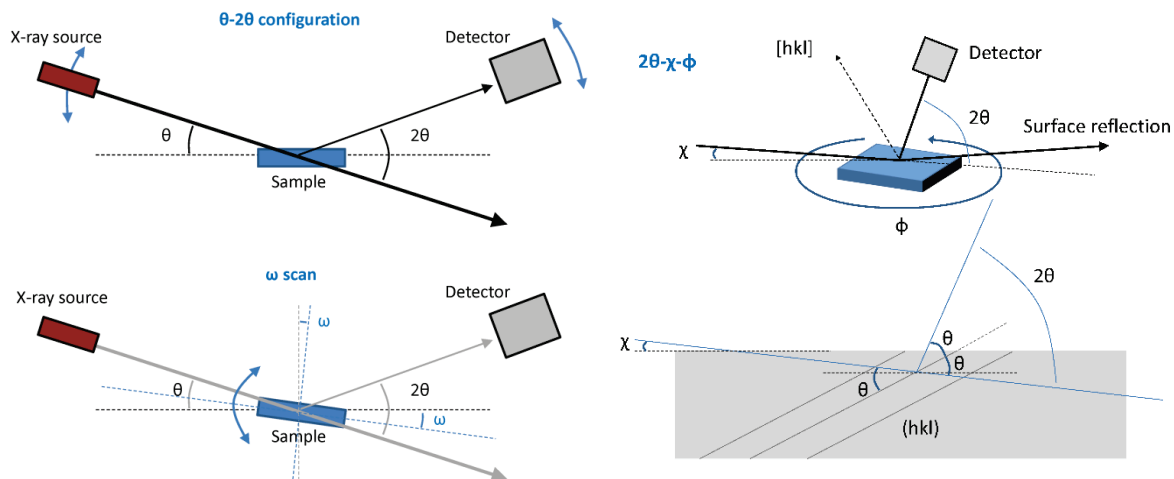


Figure 2.6 -  $\theta$ - $2\theta$ ,  $\omega$ -scan and  $2\theta$ - $\chi$ - $\phi$  configurations

The existence of an epitaxial relation with the substrate when the  $\theta$ - $2\theta$  scan evidences the existence of a preferential orientation along the growth direction can be verified by using another asymmetric configuration, the  $2\theta$ - $\chi$ - $\phi$  configuration. In this configuration, also schematized in Figure 2.6, the detection angle  $2\theta$  is fixed at the Bragg angle of one of the family of planes that are tilted with respect to the substrate surface. Then, the incidence angle is varied and the sample is rotated so that a mapping of the angular distribution of these planes is obtained. Due to the preferential direction along the growth direction, reflection from a different family of planes is detected only at a certain angle  $\chi$ . If an epitaxial relation exists, the reflection is detected only at certain  $\phi$ s. Otherwise, a ring is observed.

A  $\theta$ - $2\theta$  scan of a polycrystalline material can also provide information about the size of the crystallites. In the following, some qualitative considerations are presented to show how this is possible.

Let's suppose that the angle  $\theta$  is such that the path difference for rays scattered by the first and second planes is only a quarter wavelength. These rays do not cancel one another but simply interfere to form a beam of smaller amplitude than that formed by two rays which are completely in phase. However, the rays scattered by the second and third planes would also be a quarter wavelength out of phase. This means that the rays scattered by the first and third planes are exactly half a wavelength out of phase and would completely cancel one another. Similarly, the rays from the second and fourth planes, third and fifth planes, etc., throughout the crystal, are completely out of phase. The result is destructive interference and no diffracted beam is observed.

This is an extreme example. If the path difference between rays scattered by the first two planes differs only slightly from an integral number of wavelengths, then the plane scattering a ray exactly out of phase with the ray from the first plane will lie deep within the crystal. If the crystal is so small that this plane does not exist, then complete cancellation of all the scattered rays will not result. It follows that there is a connection between the amount of "out-of-phaseness" that can be tolerated and the size of the crystal.

In an infinite, perfect single crystal illuminated by a perfectly monochromatic parallel beam, and if the beam intensity is constant through the lattice, constructive interference occurs only at Bragg angles and

the diffraction pattern is expected with Dirac comb features. If this is the case, the experimental line width is given by the instrumental broadening.

In a real crystal, none of these conditions are completely fulfilled. In particular, when the periodicity is interrupted after only few hundred atomic planes, the broadening due to the finite size is usually much larger than other broadenings. In 1918, Scherrer [224] developed an equation that can be used to determine the coherence length along one crystal direction from the peak width

$$D_{hkl} = \frac{K\lambda}{\beta_{hkl} \cos \theta_{hkl}}$$

where  $K$  is a dimensionless shape factor close to unity<sup>19</sup>,  $\beta$  the full width at half maximum (FWHM),  $\lambda$  the wavelength of the incident radiation and  $2\theta$  the Bragg angle. This coherence length can be interpreted as the average (apparent) crystallites size. In GIXRD, the instrumental broadening is much larger and the determination of a correct value of the crystallites size becomes a difficult task.

More information about the XRD technique can be found in the book of Cullity [225].

In this work, several samples have been analyzed, ranging from powders (RE oxides) to preferentially oriented polycrystalline CeO<sub>2</sub> and ZnO films.

Powders and pellets have been measured using a Siemens D5000® X-ray diffractometer or a Bruker D8 ADVANCE® X-ray diffractometer, both equipped with a monochromatic Cu K $\alpha_1$  incident radiation ( $\lambda = 0.154056$  nm).

The structural properties of thin films were analyzed by means of a Rigaku SmartLab® X-ray diffractometer equipped with a monochromatic source (Ge(220)x2) delivering a Cu K $\alpha_1$  incident beam (45 kV, 200 mA,  $\lambda = 0.154056$  nm). This instrument allows precise alignment with the film surface, thus reducing the possible zero shift induced by a sample tilt. The alignment is usually automatically performed by moving the sample up and down and by changing  $\omega$  at  $\theta = 0$ . For the films grown on Si(100), the alignment can be also performed on the 400 peak of Si.

### ***Transmission electron microscopy (TEM)***

Transmission electron microscopy (TEM) is a microscopy technique in which an electron beam is transmitted through an ultra-thin sample. An image is formed from the interaction of the electrons with the local electronic potential of the sample. The image is magnified and focused onto an imaging device, such as a fluorescent screen, a photographic film, or a CCD camera.

TEMs are capable of imaging at a significantly higher resolution than light microscopes, owing to the small de Broglie wavelength of electrons accelerated by high voltages (200 kV in our case).

The most common mode of operating a TEM is the bright field imaging mode. In this mode the contrast formation, when considered classically, is formed directly by the diffusion of electrons in the sample. Thicker regions of the sample, or regions with a higher atomic number will appear dark, whereas regions with no sample (or light elements) in the beam path will appear bright – hence the term “bright field”. When crystalline samples are analyzed, a “dark field” mode exists opposed to the bright field. In this mode, the detector is placed at a certain angle with respect to the transmitted beam and analyzes one of the diffracted beams due to interference with a given family of crystal planes of the sample. In fact, when the sample is crystalline, it acts as diffraction grating and the image on the screen is composed of a series of spots or rings. A selected-area (electron) diffraction (SAED) pattern provides information on the (local) structural properties of the sample.

<sup>19</sup> The exact value of  $K$  is in fact a function of the crystal (diffracting unit) shape, indices of the diffraction plane, definition of line breadth  $\beta$  and definition of average crystallites size  $D$  (Fava, R.A., Polymers - Part B: Crystal Structure and Morphology. Methods of Experimental Physics. Vol. 16. 1980, New York: Academic Press).

The capabilities of TEM can be further extended by additional stages and detectors. For example, a TEM can be modified into a scanning transmission electron microscope (STEM). In this mode the electron beam, which is not parallel anymore but convergent on the sample, moves across (rasters) the sample to form the image. Modern TEMs include aberration correctors.

All information (structural and morphological) obtained by TEM has to be considered as local, given the small observation area.

The samples dedicated to TEM observation need to be very thin, so that electrons can be transmitted through. In the case of powders, it is sufficient to have grains with small diameter dispersed on a carbon membrane. The observation of thin films is more complicated as they are deposited on a thick substrate. Preparing thin films for TEM observation needs a long, painstaking procedure that involves polishing and, sometimes, ion bombardment.

Two procedures have been used in this work to prepare the samples for the cross-section view and the plan view. The first involves the use of an Allied Multiprep<sup>®</sup> for the whole preparation procedure and the second uses a Gatan Precision Ion-beam Polishing System (PIPS) for the final sample thinning. Both procedures start with a small square sample of about 2x2 mm<sup>2</sup>, such as that depicted in Figure 2.7a (bottom). For the cross section observations, an intermediate step is necessary. The sample is cut in two equal parts with a dicing saw and the two parts are stuck together on the film face with epoxy resin, as illustrated in Figure 2.7a (top). In this way, the film is protected during polishing and the number of observable regions is doubled. The samples are then polished with diamond discs in the Multiprep until a thickness of about 40 μm has been reached (see Figure 2.7a). The next steps are different for the two procedures. In one procedure, the sample is put in a Gatan Precision Ion-beam Polishing System (PIPS) and thinned using an Ar<sup>+</sup> beam (accelerated at 5 kV and hitting the sample with an angle of 5°) until a hole appears between the two faces in the middle. The bombardment is very slow, so that local heating is reduced. On the two sides of the hole, a small area thin enough for TEM observation is formed.

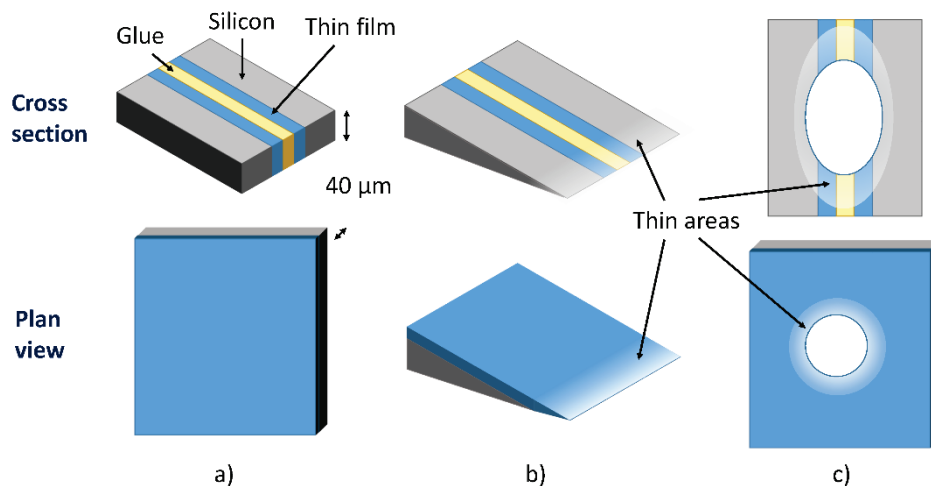


**Figure 2.7** – a) TEM sample precursor for cross section (top) and plan view (bottom). b) Samples ready for TEM observation using b) the “wedge” configuration obtained with the Multiprep and c) the “hole” configuration obtained using ion milling. These figures are not in scale.

In the other procedure, the sample is polished further, but with a small tilt. This creates a wedge sample that is very thin on one side. The results of both procedures for the cross section and plan view are shown in Figure 2.7b and c.

All TEM observations on ZnO have been performed using a JEOL 2100F microscope Cs-corrected at the probe level, with a point-to-point resolution of 2.2 Å.

### ***Scanning electron microscopy (SEM)***

A scanning electron microscope (SEM) is a type of electron microscope that produces images of a sample by scanning its surface with a focused beam of electrons. The electrons interact with atoms in the sample, producing various signals that can be detected and analyzed to extract information about the sample's surface topography and composition.

The types of signals produced by a SEM include secondary electrons (SE), back-scattered electrons (BSE), characteristic X-rays, light (cathodoluminescence) (CL), specimen current and transmitted electrons. The most common imaging mode detects the secondary electrons emitted by atoms excited by the electron beam. Since the signal results from interactions of the electron beam with atoms at or near the sample surface (after few collisions, SE are not able to leave the sample), the amount of surface "seen" by the electron beam is very important. Therefore, the contrast in the secondary electron image (SEI) is created by sharp features and tilts on the sample surface.

Back-scattered electrons (BSE) are beam electrons that are reflected from the sample by elastic scattering. BSE are often used in analytical SEM along with the spectra made from the characteristic X-rays, because the intensity of the BSE signal is strongly related to the atomic number (Z) of the specimen. BSE images (COMPO) can provide information about the distribution of different elements in the sample. Characteristic X-rays are emitted when the electron beam removes an inner shell electron from the sample, causing a higher-energy electron to fill the shell and release energy. These characteristic X-rays are used to identify the composition and measure the abundance of elements in the sample.

Magnification in a SEM can be controlled over a range of up to 6 orders of magnitude from about 10 to 500,000 times. Unlike optical and transmission electron microscopes, image magnification in the SEM is not a function of the power of the objective lens. SEMs may have condenser and objective lenses, but their function is to focus the beam to a spot, and not to image the sample.

Assuming that the display screen has a fixed size, higher magnification results from reducing the size of the raster on the specimen, and vice versa. Due to the very narrow electron beam, SEM micrographs have a large depth of field yielding a characteristic three-dimensional appearance useful for understanding the surface morphology of a sample.

All measurements have been performed using a JEOL 6700F scanning electron microscope (SEM).

### ***Atomic force microscopy (AFM)***

AFM is a technique allowing to analyze the morphology of relatively flat surfaces and to extract quantitative information. For this purpose, a cantilever with a sharp tip (probe) at its end is used to scan the specimen surface. When the tip is brought into proximity of the surface, forces between the tip and the sample lead to a deflection of the cantilever. Typically, the deflection is measured using a laser spot reflected from the top surface of the cantilever into an array of photodiodes. Other methods that are used include optical interferometry, capacitive sensing or piezoresistive AFM cantilevers. In most cases a feedback mechanism is employed to adjust the tip-to-sample distance by maintaining a constant force between the tip and the sample. This avoids potential damage caused by a collision with the surface.

In order to have topographic information, the AFM can be operated mainly in two modes: static (also called contact) mode and dynamic (non-contact or "tapping") mode, where the cantilever is vibrated above the surface close to its resonance frequency. The interaction with the surface causes the amplitude of the oscillation to decrease and the topography image is reconstructed from the feedback movement necessary to keep the amplitude constant. This method minimizes the risk of damage to the surface and the tip compared to the contact mode.

Both AFM and SEM provide detailed images of the sample surface. Although AFM presents some disadvantages compared to SEM, such as the small scan area (below few tenths of microns) and depth range, it can give a precise measurement of the surface roughness.

All measurements presented in this work have been performed in tapping mode using a Veeco® Nanoscope Dimension 3100 AFM microscope.

### ***Rutherford backscattering spectroscopy (RBS)***

RBS is generally used to determine some structural properties and the composition of materials by measuring the backscattered ions of a beam of high energy ions (typically protons or alpha particles) impinging on a sample. In this work, RBS has been used to obtain information about the composition of the films, in particular the RE concentration.

In the first approximation, Rutherford backscattering can be described as an elastic (hard-sphere) collision between a light high-kinetic-energy particle from the incident beam and a stationary heavy particle located in the sample (the target). The energy of backscattered ions carries information about the mass of the atoms in the target and the depth at which the collision occurred. The good knowledge of the energy loss phenomena of charged ions in matter allows precise interpretation of the data. Surprisingly, this can be done quite well using classical physics.

When a sample is bombarded with a beam of high energy particles, the vast majority of particles are implanted into the material and do not escape. This is because the diameter of an atomic nucleus is on the order of  $10^{-15}$  m while the spacing between nuclei is on the order of  $10^{-10}$  m. A small fraction of the incident particles do undergo a direct collision with a nucleus of one of the atoms in the upper few micrometers of the sample. The conservation of momentum and kinetic energy implies that the energy of the scattered projectile is reduced because part of it is transferred to the target. The heavier is the target atom, the smaller is the energy loss (less momentum is transferred to the target atom) and the higher is the energy of the backscattered particle, which asymptotically approaches the incident particle energy. This means that RBS has good mass resolution for light elements, but poor mass resolution for heavy elements. Since more momentum is transferred to light atoms, fewer ions are backscattered at high angles and can leave the sample. Therefore, the sensitivity of the RBS technique to light atoms is poor (low signal).

While large-angle scattering only occurs for ions that scatter off target nuclei, inelastic small-angle scattering can also occur with the sample electrons. This results in a gradual decrease of the number of ions which penetrate more deeply into the sample, so that backscattering off interior nuclei occurs with lower "effective" incident energy. The amount by which the ion energy is lowered after passing through a given distance is referred to as the stopping power of the material and is dependent on the electron distribution. The same amount of energy will be lost on the way back to the sample surface. The stopping power increases with the atomic number  $Z$  of the target. This energy loss varies continuously with respect to the travelled distance, assuming a constant density of atoms. This allows depth resolution of the element proportions. Since the backscattered ion signal only depends on the number of collisions and not to on the interval between them, correct estimation of the depth requires that the density of the material is known. A typical RBS spectrum is shown in Figure 2.8.

Detectors to measure backscattered energy are usually silicon surface barrier detectors, a very thin layer (100 nm) of p-type silicon on an n-type substrate forming a p-n junction. Ions that reach the detector lose some of their energy to inelastic scattering from the electrons, and some of these electrons gain enough energy to overcome the band gap between the semiconductor valence and conduction bands. This means that each ion incident on the detector will produce some number of electron-hole pairs which is dependent on the energy of the ion. These pairs can be detected by

applying a voltage across the detector and measuring the current, providing an effective measurement of the ion energy.

The measurements were carried out at room temperature using a  $^4\text{He}^{2+}$  particles beam with an energy between 2 and 3 MeV. A Van de Graaff particle accelerator provided the necessary 4 MV accelerating voltage.

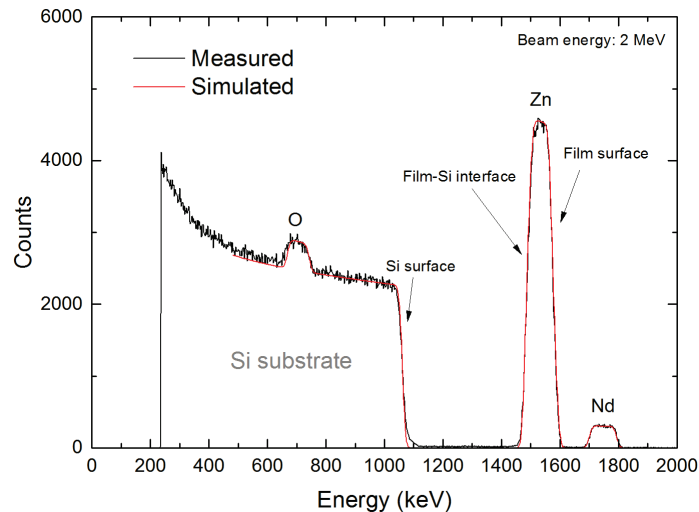


**Figure 2.8** – Measured and simulated RBS spectrum of a 100 nm ZnO:Nd (1.6%) sample on silicon substrate.

### ***Near-edge X-ray absorption fine-structure spectroscopy (NEXAFS)***

NEXAFS spectroscopy refers to the absorption fine structure close to an absorption edge, about the first 30 eV above the actual edge. This region usually shows the largest variations in the X-ray absorption coefficient and is often dominated by intense, narrow resonances. NEXAFS is very sensitive to the bonding environment of the absorbing atom and is therefore very useful to obtain information about the valence of a particular element and about the defects.

Complementary to the related X-ray photoemission spectroscopy (XPS) technique, where the photon energy is fixed and the electron intensity is measured as a function of electron kinetic energy, in NEXAFS the X-ray energy is scanned and the absorbed X-ray intensity is measured. NEXAFS spectra can be recorded in different ways. The most common methods are transmission and fluorescence/electron yield measurements. The transmission technique requires thin foils, while the fluorescence or electron yield techniques, called total fluorescence yield (TFY) and total electron yield (TEY) respectively, can be used for conventional samples. The absorbed X-ray intensity is not measured directly in TFY and TEY, but rather the fluorescence photons or photoelectrons that are created by the absorbed X-rays. In the case of TEY, X-rays are absorbed through excitations of core electrons to empty states above the Fermi level. The created holes are then filled by Auger decay (dominant in the soft X-ray region over X-ray fluorescence). The intensity of the emitted primary Auger electrons is a direct measure of the X-ray absorption process and is used in so called Auger electron yield (AEY) measurements, which are highly surface sensitive, similar to XPS. As they leave the sample, the primary Auger electrons create scattered secondary electrons which dominate the total electron yield (TEY) intensity. The TEY cascade involves several scattering events and originates from an average depth. Electrons created deeper in the sample lose too much energy to overcome the work function of the sample and therefore do not contribute to the TEY. Detection of the TEY signal is accomplished by measuring the electron charge that leaves the

sample during the absorption process. The sampling depth in TEY measurements is typically a few nanometers, while it is often less than 1 nm for AEY measurements. As stated above, the fluorescence signal is weaker than the electron signal in the soft X-ray range. However, the sampling depth is larger because X-rays can easily escape from the sample. The total fluorescence yield (TFY) mode is therefore more adapted to investigate the “bulk” of our thin films.

For a more detailed discussion, please refer to the book of Stöhr [226].

NEXAFS spectroscopy was performed by Paul Bazylewski in the group of Gap Soo Chang at the University of Saskatchewan using the Resonant Elastic-Inelastic X-ray Scattering (REIXS) beamline of the Canadian Light Source. The TEY spectra were obtained at a 45° angle of incidence and were normalized to the incoming photon flux recorded by Au mesh. Measurements were intensity normalized to a constant background.

### ***Atom-probe tomography***

Atom Probe Tomography (APT or 3D Atom Probe) is one of the few material analysis technique offering extensive capabilities for both 3D imaging and chemical composition measurements at the atomic scale (around 0.1-0.3nm in depth and 0.3-0.5nm lateral resolution). Since its early developments, Atom Probe Tomography has contributed to major advances in materials science.

The sample is prepared in the form of a very sharp tip. The cooled tip is biased at high DC voltage (5-20 kV). The very small radius of the tip and the High Voltage induce a very high electrostatic field (tens V/nm) at the tip surface, just below the point of atom evaporation. Under laser or HV pulsing, a few atoms are evaporated from the surface, by field effect (near 100% ionization), and projected onto a Position Sensitive Detector (PSD) with a very high detection efficiency.

The detector allows to simultaneously measure:

- the Time Of Flight of the ions: measuring the time between the laser flash and the arrival on the PSD allows to determine the  $m/q$  (mass over charge) ratio.
- the (X,Y) position of the ion impact on the detector: measuring the X-Y position and the order of arrival of the ions on the PSD allows to reconstruct the original position of the atoms on the tip.

By repeating this sequence, the atoms are progressively removed from the tip, and a 3D image of the material can be reconstructed at the atomic scale.

AP measurements were performed on our samples by Rodrigue Lardé at GPM-Materials Research Group of the University of Rouen (France). For such analyses, some silicon pillars were picked off from the wafer, mounted on a stainless steel fine tip needle with conductive epoxy glue, and tip-shaped using a focused Ga ion beam (30 kV).

The tips were analyzed by laser-assisted wide-angle tomographic atom probe(LAWATAP) from CAMECA at 80 K in an ultrahigh vacuum chamber at a pressure of  $10^{-9}$  mbar. The femtosecond laser pulse system used was an amplified ytterbium-doped laser (AMPLITUDE SYSTEM s-pulse) with a 350 fs pulse length and a 342 nm wavelength.

## **2.4.2 Optical characterization**

### ***Spectrophotometry***

UV-vis-NIR spectrophotometry is a widespread technique to analyze transmittance ( $T$ ) and reflectance ( $R$ ) of different kind of samples. Absorbance can be calculated as  $1-R-T$ . When this technique is applied to thin films, the data must be interpreted more carefully. First, the sample is non-uniform because it includes at least the substrate on which the film is deposited. The measured data will correspond to

those of the whole sample and not of the thin film alone. Second, interference can play an important role in shaping the measured curves.

The basic principle of this technique consists in sending monochromatic light on the sample and in analyzing the reflected or transmitted light. Usually, transmittance measurements are performed at normal incidence, while reflectance measurements are performed at  $8^\circ$  from the normal for obvious technical reasons. At such a small angle, the reflectance is not very different from that measured at normal incidence. With a special setup, however, the reflectance at higher angles can also be measured.

Regardless of the sample, a certain amount of the impinging light is diffused in all direction. With a detector placed at  $-8^\circ$ , only specular reflectance can be detected. The small solid angle of the detector can be increased using an integration sphere, i.e. a white cavity that reflects diffused light until it reaches the detector.

All the measurements of this work have been performed with a LAMBDA 950 UV/vis/NIR spectrophotometer from Perkin-Elmer. A deuterium lamp and a tungsten halogen lamp provided excitation wavelengths between 190 nm and 3300 nm. The detection was ensured by a photomultiplier for the UV-visible part of the spectrum and by a PbS detector for the infrared part. An integration sphere of 150 mm was available for diffuse reflectance measurements.

A schematic view of the spectrophotometer is illustrated in Figure 2.9. All blocks are oversimplified.

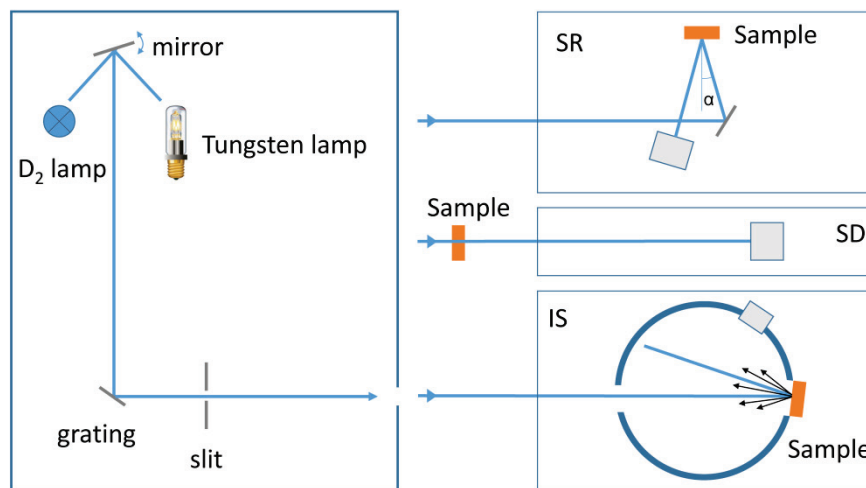


**Figure 2.9** – Schematic view of a spectrophotometer. The light source is directed onto a monochromator (grating) and a small wavelength region is selected by a slit. Then, the light enters one of the three detection modules, i.e. the integrating sphere (IS), the specular reflectance (SR) or the standard transmittance (SD) module. In this last case, the sample is placed outside the detector module. The grey box represents the detector.

Contrarily to the photoluminescence setup described in the next paragraph, the detection in a spectrophotometer is usually not wavelength-selective. This fact must be taken into consideration when interpreting the spectra of photon converting layers.

### ***Photoluminescence spectroscopy***

Luminescence is the property of materials to emit photons following an external excitation. If the external excitation consists of photons, the process is called photoluminescence (PL). Other excitation mechanisms involve electron beams (cathodoluminescence), electric fields and currents (electroluminescence) and high energy particles (radioluminescence).

In photoluminescence, the excitation process consists in the excitation of electrons to higher energy states. These electrons typically undergo various relaxation processes and in some cases photons can be

re-radiated. The period between absorption and emission can be extremely short: it ranges from the femtosecond-regime up to milliseconds.

Several variations of photoluminescence exist, including photoluminescence excitation (PLE) spectroscopy and time-resolved photoluminescence (TRPL). PLE is a method where the emission is detected as a function of the excitation photon energy. TRPL is a method where the sample is excited with a light pulse and then the decay in photoluminescence with respect to time is measured.

Photoluminescence is an important technique for measuring the purity and crystalline quality of semiconductors and for quantification of the amount of disorder present in a system. In fact, defects and impurities often introduce electronic states in the band gap associated with radiative transitions.

In a typical PL experiment, a semiconductor is excited with a light-source that provides photons with energy larger than the band gap energy. When electrons are excited high in the conduction band, the carrier temperature initially decreases quite fast via emission of optical phonons. This is quite efficient due to the comparatively large energy associated with optical phonons and their rather flat dispersion, allowing for a wide range of scattering processes under conservation of energy and momentum. Once the carrier temperature decreases below the value corresponding to the optical phonon energy, acoustic phonons dominate the relaxation. Here, cooling is less efficient due their dispersion and small energies and the temperature decreases much slower beyond the first tens of picoseconds.

PL can also be a key measurement for quantum dots, where the semiconductor bands are quantized and radiative transitions can occur from the excited states of the conduction band if the distance between the levels is higher than the phonon energy.

In the case of optically active centers (such as the rare earths) embedded into a host, PL allows studying the activation and the spectral properties of these centers in the specific host as well as the transfer properties from/to the host.

The two setups used in this work are illustrated in Figure 2.10. High-power UV excitation was provided either by a pulsed frequency-tripled neodymium-doped yttrium aluminium garnet (Nd-YAG) laser (355 nm) or a continuous-wave He-Cd laser (325 nm). The Nd-YAG laser pulse width, frequency and power were of 10 ns, 20 kHz and 100 mW, respectively. The maximum He-Cd laser power was ~10 mW. A tunable laser was also available, but the tuning process was too long to use it as a source in PLE measurements.

Low-power excitation was provided by a broad-spectrum Energetiq® EQ-99FC laser-driven light source (LDLS™). The peculiarities of this lamp are the extremely flat spectrum profile and the relatively high power in the UV region, where conventional lamps are weak.

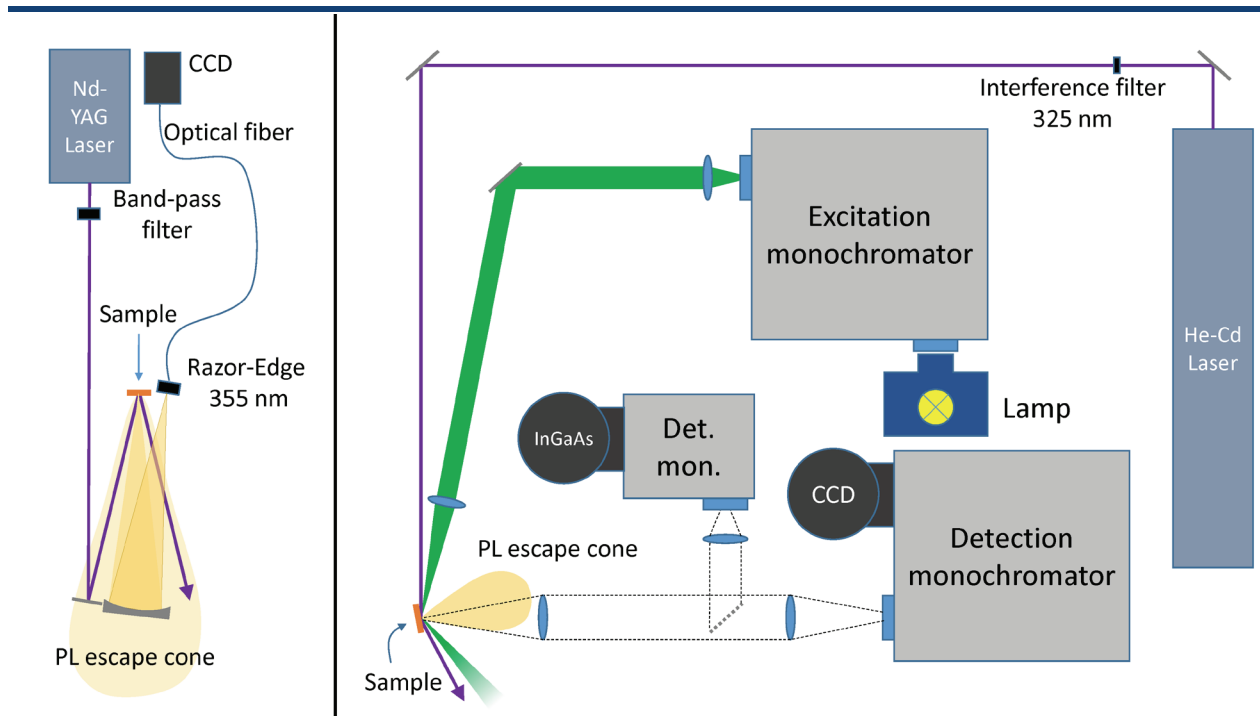


**Figure 2.10** – The two setups used for PL and PLE experiments.

The PL signal after excitation with the Nd-YAG laser was collected by means of a concave mirror into an optical fiber and analyzed by a CCD (left setup in Figure 2.10) at room temperature.

The PL signal after excitation with the He-Cd laser or with the lamp was recorded by means of an N<sub>2</sub>-cooled CCD camera or a N<sub>2</sub>-cooled InGaAs detector (right setup in Figure 2.10). Low-temperature PL was measured at about 4 K using an Oxford MG11 cryostat (not shown in Figure 2.10). Particular attention was paid to eliminate parasitic luminescence coming from the environment and from the excitation by using a set of filters. The spectra presented here have been corrected for the filter and lamp emission, as well as for the detector response.

When this technique is applied to thin films, it is important to collect the signal within the escape cone mentioned in paragraph 1.4.3. For good DC properties, this cone should be small and the setup must be built more carefully.

### ***Raman spectroscopy***

Raman spectroscopy is a nondestructive characterization technique that allows precise measurement of the vibrational modes of a material. This technique is based on inelastic scattering, or Raman scattering, of a monochromatic laser light from the sample. Part of the scattered light has different energy (higher or lower) resulting from the interaction with phonons. Not all vibrational modes interact with light and those who do not are called “silent” modes. Raman can operate in *resonant mode*, when the excitation photon energy corresponds to an electronic transition in the material and *non-resonant mode*, when the material is transparent to this light.

Raman spectra were obtained using a confocal dispersive Raman microprobe-LabRam Aramis from Horiba Jobin-Yvon Co. equipped with a YAG ( $\lambda = 532 \text{ nm}$ ) laser excitation source. The power was minimized to 9 mW to avoid any deformation of the structure due to laser heating. The spectrometer resolution is lower than  $1 \text{ cm}^{-1}$  and the data were collected in the  $200\text{-}1000 \text{ cm}^{-1}$  range.

### Ellipsometry

Ellipsometry is an optical technique for surfaces and thin films analysis. It is based on the measurement of the change in polarization state of a monochromatic light beam caused by the reflection on the material surface or the transmission through the material. With an appropriate optical model it is then possible to obtain the thickness and the electrical (dielectric constants) or optical (refractive index) properties of the material. The measured parameters are the so-called ellipsometric angles  $\Psi$  and  $\Delta$ . These are related to the complex Fresnel reflection coefficients  $r_s$  and  $r_p$  for light polarized parallel and perpendicular to the surface. The fundamental equation of ellipsometry reads:

$$\rho = \frac{r_p}{r_s} = \tan \Psi e^{i\Delta}$$

where

$$\tan \Psi = \frac{|r_p|}{|r_s|} \quad (0^\circ \leq \Psi \leq 90^\circ)$$

$$\Delta = \delta_p - \delta_s \quad (0^\circ \leq \Delta \leq 360^\circ)$$

Figure 2.11 illustrates the working principle of ellipsometry and a scheme of the HORIBA UVISEL™ Lt M200 FGMS (210–880 nm) spectroscopic ellipsometer used in this work. The oblique incidence ( $\phi > 0$ ) is very common, since it leads to pronounced changes in the polarization of incident light upon reflection from the sample. For isotropic samples, currents driven along the surface ( $s$  waves) or perpendicular to it ( $p$  waves) are different. For anisotropic samples, measurable changes of polarization state can occur even at normal incidence. In general, the white light of a xenon lamp is passed through a linear polarizer before it hits the sample surface. Polarization must not be in the same plane of the two light beams. After the reflection, a photoelastic modulator (PEM) induces a modulation of the state of polarization that means that the ellipticity of the polarization varies as a function of time. In this work, the modulator used is based on the photoelastic effect: stress is applied to a silica bar so that its optical properties are modified. In its equilibrium state, the modulator is optically isotropic with one index of refractive index, and becomes birefringent (with two indices) under mono-axial stress. The phase retardation between the two components is known. The transducer is tuned to the resonance frequency of the optical element along its long dimension, determined by its length and the speed of sound in the material. An alternate voltage is applied to the transducer to vibrate the optical element through stretching and compressing which changes the birefringence of the transparent material. Because of this resonant character, the birefringence of the optical element can be modulated to large amplitudes, but also for the same

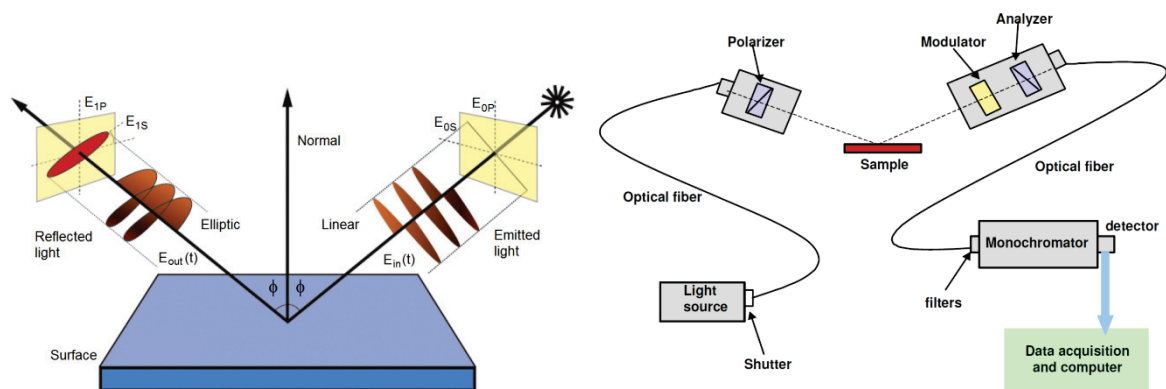


Figure 2.11 – a) Working principle of ellipsometry and b) scheme of a spectral ellipsometer.

After the reflection, a photoelastic modulator (PEM) induces a modulation of the state of polarization that means that the ellipticity of the polarization varies as a function of time. In this work, the modulator used is based on the photoelastic effect: stress is applied to a silica bar so that its optical properties are modified. In its equilibrium state, the modulator is optically isotropic with one index of refraction, and becomes birefringent (with two indices) under mono-axial stress. The phase retardation between the two components is known. The transducer is tuned to the resonance frequency of the optical element along its long dimension, determined by its length and the speed of sound in the material. An alternate voltage is applied to the transducer to vibrate the optical element through stretching and compressing which changes the birefringence of the transparent material. Because of this resonant character, the birefringence of the optical element can be modulated to large amplitudes, but also for the same

reason, the operation of a PEM is limited to a single frequency, and most commercial devices manufactured today operate at about 50 kHz. The advantages of the photoelastic modulation are: very fast acquisition, high accuracy and working frequency far from ambient noise sources.

The outgoing signal is passed through a monochromator and detected by a photomultiplier. The measured intensity of a phase-modulated ellipsometer can be written as:

$$I(t) = I[I_0 + I_s \sin(\delta_0 + A_m \sin \omega t) + I_c \cos(\delta_0 + A_m \sin \omega t)]$$

with the amplitude of modulation  $A_m$  and the frequency of modulation  $\omega$ .  $I$  is a pre-factor (lamp intensity, sample reflectivity, transmission of optical elements), which is omitted during later calculations.  $\delta_0$  is the rest-birefringence of the modulator. The factors  $I_0$ ,  $I_s$  and  $I_c$  contain the azimuth of the polarizer P, the modulator M and the analyzer A in respect to the plane of incidence and the ellipsometric angles  $\psi$  and  $\Delta$ . Measurements have been performed in the configuration where  $M = 0^\circ$  and  $A = 45^\circ$ . In this case, the relation between  $I_s$  and  $I_c$  and the ellipsometric angles is:

$$I_s = \sin 2\Psi \sin \Delta$$

$$I_c = \sin 2\Psi \cos \Delta$$

It is necessary to create a model of the sample to determine the sample parameters ( $n$ ,  $k$ , and  $d$ ). Once the model is built, calculated data must be fitted to the experimental data and the best match between the two sets has to be found. The user has to evaluate the best-fit model in order to decide whether the predictive model is physically reasonable and whether the different parameters are unique and not correlated.

When the thickness of the film is greater than about four times the penetration depth, the film can be treated as a substrate because only a negligible part of the light is reflected from the interface and reaches the detector.

In this case the thickness cannot be determined and the measured data give directly the optical constants  $n$  and  $k$ . In the case of a deposited film on a substrate, the part of light which is transmitted cannot be ignored as it is the case for a bulk material because it is reflected on the film-substrate interface. Moreover, multiple reflections are likely to occur (see Figure 2.12).

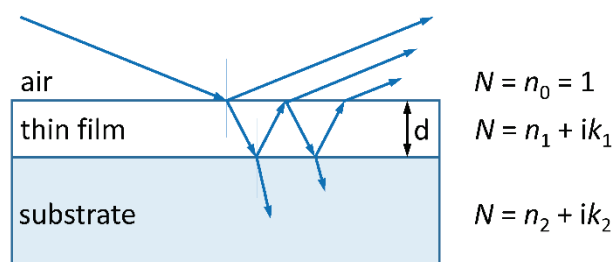


Figure 2.12 – Multiple reflections in thin films.

The two measured quantities  $I_s$  and  $I_c$  are not sufficient to give the value of three incognita ( $n$ ,  $k$ , and  $d$ ). However, most thin films are transparent in a certain spectral region ( $k = 0$ ). Since  $d$  is independent of  $\lambda$ ,  $n(\lambda)$  and  $d$  can be successfully determined in the transparent region. Then,  $d$  can be fixed and  $n$  and  $k$  can be fitted over the whole range. If  $k \neq 0$  on the whole spectrum, a second measurement in a different configuration is necessary to determine the three parameters.

Among all dispersion formulas that have been tested, the Adachi-new Forouhi (AnF) dispersion formula provided a good fit for both ZnO and CeO<sub>2</sub>. Using this formula, Kang *et al.* could measure the small optical anisotropy of ZnO [227].

This model is a combination of the model developed by Forouhi and Bloomer [228, 229], called “New Amorphous” in the DeltaPsi® software, and a modification of the dispersion formula developed by Adachi [230]. The New Amorphous dispersion formula was developed to describe the band-to-band absorption of amorphous semiconductors and can be regarded as a single oscillator above a certain energy band gap below which there is no absorption. For crystalline semiconductors dielectrics and metals, several peaks can be observed and more than one oscillator should be used. The Adachi dispersion formula is mainly applied to transitions appearing in semiconductors near the band gap and is therefore more adapted to describe the several critical points characteristic of crystalline materials. In the AnF dispersion formula, two additional oscillators have been added to the “New amorphous” dispersion.

It must be emphasized that  $E_g$  value obtained by ellipsometry is not the optical band gap, but only the value from which  $k = 0$  if  $E \leq E_g$ . The difference between the two can be seen in Figure 2.13, where the value usually taken as optical gap is named  $E_g^{opt}$ . The approximation  $k = 0$  if  $E \leq E_g$  is not physically realistic because it does not take into account the band tail states. Therefore, the value  $E_g$  has poor physical meaning.

More information about the absorption coefficient and band gap determination will be given in [Appendix D](#).

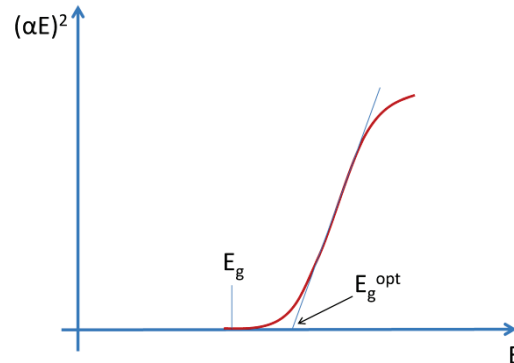


**Figure 2.13** – Discrepancy between the values of the optical band gap as measured with a Tauc plot of the absorption coefficient for an amorphous semiconductor and the value given by the model.

### ***Solar cell quantum efficiency***

The external quantum efficiency (EQE) calculates the number of electron-hole pairs generated per incident photon. The setup used to measure the (EQE) consists of a light source (Xenon lamp) and a filter wheel with 41 filters that select different wavelengths between 300 nm and 1200 nm. Instead of the photon flux, the setup measures the ratio between the current produced on the sample cell by monochromatic light and the current generated in a reference detector at the same wavelength.

Since not all the incoming light reaches the active part of the solar cell (mainly due to the cell reflectance and to the parasitic absorbance of the window layers), the EQE is not the best parameter to evaluate the efficiency of the active part of the cell. The internal quantum efficiency (IQE) can be calculated from the EQE as  $IQE = EQE/(1-R)$  where R is the reflectance at the corresponding wavelength.

This parameter bypasses the reflectance differences and is therefore more indicated to represent the efficiency of the active part of the cell and in most cases it is not important to consider the absorption of the window layers. When dealing with sensitized down-shifting and down-converting layers, however, differences in the efficiency of the cell are searched exactly in the region where the window layer absorbs. It is difficult to separate the differences in the absorbance due to a different absorption coefficient or layer thickness from those due to photon conversion. Unfortunately, precise evaluation of the absorbance is a very difficult task and could not be subtracted from the IQE curves presented in this work.

### 2.4.3 Electrical characterization

The most common method for measuring resistivity is the four-point probe method. In the most simple case, when the probes are aligned, a small constant current is passed through the outer two probes and the voltage is measured between the inner two probes (see Figure 2.14a). However, the measurement of the resistivity only gives the product of the mobility ( $\mu$ ) and carrier concentration. To measure each parameter directly, the most-common method uses the Hall effect. In semiconductors, this measurement also provides the main type of carrier ( $n$  or  $p$ ). The Hall effect is named after the scientist who made the discovery in 1879, E.H. Hall [231], and is based on the Lorentz force acting on charge carriers moving in a magnetic field.

The Hall effect in a semiconducting bar crossed by a current perpendicular to the magnetic field is illustrated in Figure 2.14b. The Lorentz force accumulates the carriers on one side of the sample so that a voltage is created (the Hall voltage  $V_H$  is the voltage at which the electric force on the carriers counterbalances the Lorentz force).

The Hall voltage in a semiconducting bar like that of Figure 2.14b is expressed by

$$V_H = R_H IB$$

with the Hall constant  $R_H$  and the Hall factor  $r_H$  expressed by

$$R_H \cong \frac{r_H}{e} \frac{\mu_p^2 p - \mu_n^2 n}{(\mu_p p - \mu_n n)^2}$$

$$r_H \equiv \frac{\langle \tau_m^2 \rangle}{\langle \tau_m \rangle^2}$$

where  $\tau_m$  is the mean free time between two scattering processes averaged for the two types of carriers,  $\mu_{n,p}$  the carrier mobility,  $n$  and  $p$  the carrier density and  $e$  the elementary charge. This equation for  $R_H$  is valid only under the assumption that  $\mu B \ll 1$ . The sign of  $R_H$  indicates the main carrier type.

When the conduction is dominated by one type of carrier, say  $n$  type, the equation is largely simplified as

$$R_H = \frac{1}{en}$$

The Hall mobility is defined as the product of the Hall constant and the conductivity

$$\mu_H = \sigma |R_H|$$

and is related to the drift mobility by

$$\mu_H = r_H \mu$$

In order to determine both the mobility  $\mu$  and the bulk carrier density, a combination of a resistivity measurement and a Hall measurement is needed, together with accurate measurement of the sample

thickness ( $d$ ). The resistivity can be determined using either a four-point probe (Figure 2.14a) or van der Pauw measurement technique (Figure 2.14b). In both cases, ohmic contacts are needed.

The advantage of the van der Pauw technique is that it can be done by the same setup as that for the Hall measurement, but in a different measurement configuration. In the case of thin film on a square substrate, the contacts are usually placed as in Figure 2.14c. In the van der Pauw technique, the current is applied to two adjacent contacts and the voltage is detected between the other two. In the Hall measurement, a current is applied between opposite contacts (1 and 3 in the figure), a voltage is detected between the other two opposite contacts (2 and 4).

Because Hall voltages are typically quite small, averaging techniques are critical to obtaining accurate mobility results. To obtain more precise results, the recommended technique involves a combination of reversing source current polarity, sourcing on additional terminals, and reversing the direction of the magnetic field.

The electrical properties of thin films were investigated at room temperature using an ECOPIA Hall-effect measurement system.

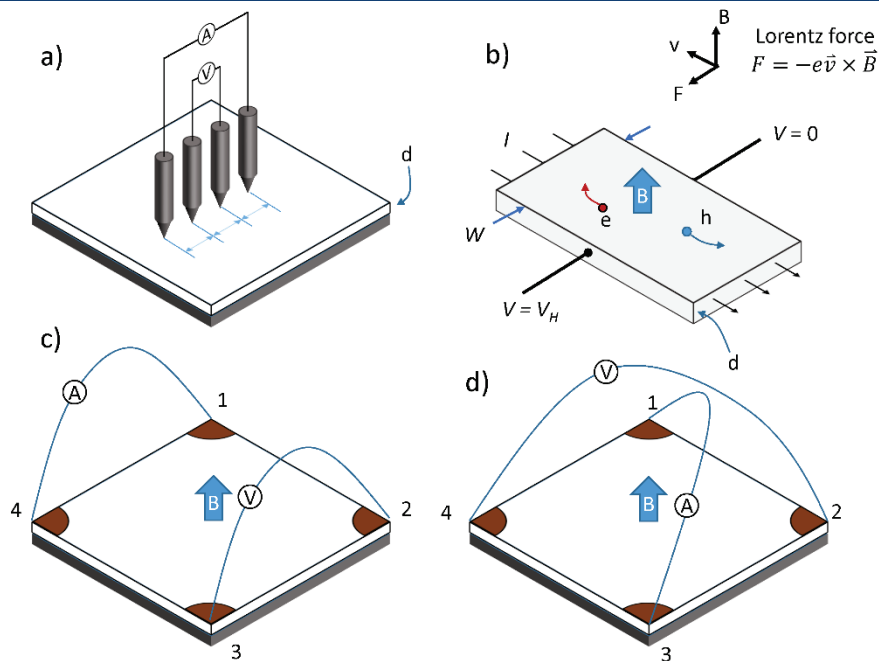


**Figure 2.14** – a) In line four-point-probe resistivity configuration. b) Hall effect on a semiconducting bar. c) Van der Pauw resistivity measurement (one of the eight possible configurations) and d) Hall effect measurement configuration for thin films on insulating substrate.

---

## Results and discussion - Overview

The results of this work are organized in three main chapters. Chapter 3 reports the results obtained with RE-doped ZnO films and is divided in four sections.

In the first part of Chapter 3, the reader is introduced to the structural and morphological properties of undoped and RE-doped sputtered ZnO films (Section 3.1). The section has not been thought to be an exhaustive analysis of sputtered films, as the research work has been often driven by the optical properties of the films. The choice to present the structural and morphological results and the optical results in separate sections has been motivated by the will to give a compact, coherent view of these results. In the next sections, however, the main structural results are shortly recalled when needed.

Section 3.2 is a brief section dedicated to describe the basic optical properties of ZnO films (refractive index, reflectance, ...) in order to confirm that these layers are suited for anti-reflection coating (ARC) applications on silicon solar cells. Small doping levels such as those used in this work are expected to have little effect on the basic optical properties of ZnO, which means that the ARC properties should be maintained with doping. Besides the ARC properties, ZnO is also used for its TCO properties. In most cases, efficient conduction is obtained by doping the film with trivalent Al, but ZnO often possesses non-negligible intrinsic conduction properties. Section 3.3 is also a brief section describing the electrical properties of our ZnO films and the effect of doping with trivalent rare earths.

In the third part of this chapter (section 3.4), the photon-converting properties of these films will be tested by using photoluminescence measurements. Unlike the structural properties and the refractive index, the PL results strongly depend on the rare earth and are therefore divided into three separate sections (3.4.2 for Yb, 3.4.3 for Pr and 3.4.4 for Nd).

Chapter 4 describes the results obtained with CeO<sub>2</sub>. The investigation of this material is still at a preliminary stage, but the results are very interesting and deserved a small chapter in this work. Since the films have been obtained by PLD using homemade pellets and the quality of the films depends on that of the pellets, the properties of the pellets will be presented first (section 4.1). The properties of the films are reported in section 4.2.

Some results obtained on the RE-oxide powders will be presented throughout the last two chapters and not in a separate chapter.

Chapter 5 reports the results obtained when the most promising films are integrated on solar cells.



## 3 RESULTS AND DISCUSSION: ZINC OXIDE

ZnO is an n-type semiconducting oxide widely investigated as a low-cost transparent conductive oxide for optoelectronic and solar cell applications. Embedding rare earth ions in ZnO can add photon management properties

This chapter will investigate the properties of Yb-, Pr- and Nd-doped ZnO films deposited by the sputtering technique. All these rare earths potentially present efficient NIR emission just above the band gap of silicon. If Yb can only lead to down-shifting due to its single excited level, Pr and Nd could also lead to down-conversion. The combination of Pr and Yb is also particularly promising for cooperative down-conversion.

### 3.1 Structural and morphological properties of sputtered ZnO

The aim of this section is to present the structural and morphological properties of sputtered RE-doped ZnO and has been thought in view of photon conversion. Therefore, only a limited number of experimental conditions are reported, which led to interesting luminescence properties of the films. In most cases the structural properties of the doped films are very similar to those of undoped ZnO, that has been deposited (and annealed) in the same conditions to have a reference. In the following, the results on doped and undoped ZnO will be alternatively reported, selected with respect to their clarity.

The deposition parameters that have a larger influence on the PL are the deposition temperature and gas flow ratio. The Ar/O<sub>2</sub> gas flow ratio during deposition proved to be a very critical parameter, having a deep influence on the film morphology and RE insertion and activation. In particular, only a narrow range around a value of 4 is suitable for photon converting applications. Therefore, most results will be reported for this value.

Section 3.1.1 is dedicated to the structural analysis using the XRD technique. The effect of the deposition and annealing temperature are reported in terms of crystallites size and lattice parameter along the growth direction, i.e. the two parameters easily accessible from a  $\theta$ -2 $\theta$  scan. The information that can be obtained from this data is particularly important to understand the evolution of the optical properties with respect to the structural quality achieved during deposition or obtained using post-deposition treatments.

Section 3.1.2 reports the TEM, SEM and AFM morphological investigations. These observations provide additional information on the film structure and morphology in the direction perpendicular and parallel to the growth direction. Besides the film structure and morphology, it is important to obtain information about the stoichiometry, spatial distribution and oxidation state of the dopant. Both TEM and SEM can provide some information on the film composition by analyzing the characteristic X-rays of the different chemical elements following a core electron expulsion from the atoms under the electron beam. However, due to the small RE concentration and the small amount of material (100 nm of film), quantitative estimation of the film stoichiometry is not possible using reasonable acquisition times. In addition, the information obtained is an average over the whole film thickness.

Quantitative data about the RE concentration profile as a function of the depth can be obtained by RBS, to which the first part of section 3.1.4 is dedicated. However, this technique offers no clue about the lateral distribution and the concentration value is an average over the lateral size of the ion beam (~1 mm). This means that non-uniform local distribution (e.g. clusters) are not detected by RBS. The 3D

distribution of dopant is very difficult to obtain and requires sophisticated, time-consuming techniques. In order to exclude the formation of clusters and aggregates, atom probe tomography has been performed on three selected samples and the results are reported in the second part of section 3.1.4.

The last key information in order to study the optical activation of REs in ZnO regards their oxidation state. To this purpose, NEXAFS investigation is reported in section 3.1.5.

### 3.1.1 XRD data and structural properties of the films

Figure 3.1a shows the typical  $\theta$ - $2\theta$  XRD diffraction patterns of ZnO thin films deposited at different temperatures with an Ar/O<sub>2</sub> gas flow ratio of 16:4. XRD data show that sputtered ZnO thin films present the expected hexagonal wurtzite structure and a strong texture along the [002] direction, i.e. most crystallites have the c-axis perpendicular to the substrate surface. This oriented growth occurs for all investigated conditions. The crystallites are so well oriented, that a single diffraction peak emerges from a  $\theta$ - $2\theta$  scan. In the case of doped films, no RE (Yb, Pr, Nd) oxide peaks have been observed in the detection limit of the XRD technique. For high deposition temperatures, two other peaks are observed at high angles, originating from the same family of planes: the ZnO (004) peak and the (006) peak (not reported here).

If a preferential orientation has been detected for all films, the quality of the crystallites orientation, as well as the peak intensity, width and position change with the deposition parameters. These quantities can be related to some physical properties of the lattice. The peak width is related to the crystallites size, while the angular position depends on the compressive/tensile stress created by defects. The crystallites size along the [002] direction calculated using Scherrer's formula and the lattice parameter calculated from the angular position are reported in Figure 3.1b-c-d for undoped and RE-doped films as a function of the deposition temperature.

As a result of the larger amount of energy available to atoms and molecules for diffusion during growth, the average crystallites size along the [002] direction increases with the deposition temperature for both doped and undoped samples. At 400 °C, the values approach a third of the total thickness of the film (100 nm). It is interesting to notice that there is no appreciable difference between doped and undoped samples. As it will be shown further, this is not true when samples are annealed.

Along with the increase of the crystallites size, the lattice stress decreases, as indicated by the lattice parameter approaching its bulk value  $c = 5.207 \text{ \AA}$  (represented by a horizontal dashed line in Figure 3.1b-c-d). Values above the bulk value indicate generally a compressive stress, such as the stress generated by interstitial atoms. Values below the bulk value are related to tensile stress, such as that produced by oxygen and zinc vacancies. Other sources of stress in a lattice are impurities and dopants. In the case of undoped ZnO, this decrease of the  $c$  parameter with the deposition temperature suggests the existence of defects, such as oxygen and zinc in interstitial position, which are progressively healed when the deposition temperature is increased. This happens also in doped samples. Moreover, if the large RE ions were in substitutional position, one would expect a larger compressive stress to appear. However, except for high Yb doping, the behavior is quite ambiguous. A possible explanation can be that when REs substitute a small divalent ion like Zn<sup>2+</sup>, they usually create stress- or charge-compensating defect around them.

Figure 3.1 proves that the deposition temperature has a strong effect on the film growth. However, thermal energy can be also provided after the deposition. Undoped, Yb-doped and Pr-doped samples have been annealed in different atmospheres (Ar, O<sub>2</sub>, N<sub>2</sub>) during 10 to 40 min.

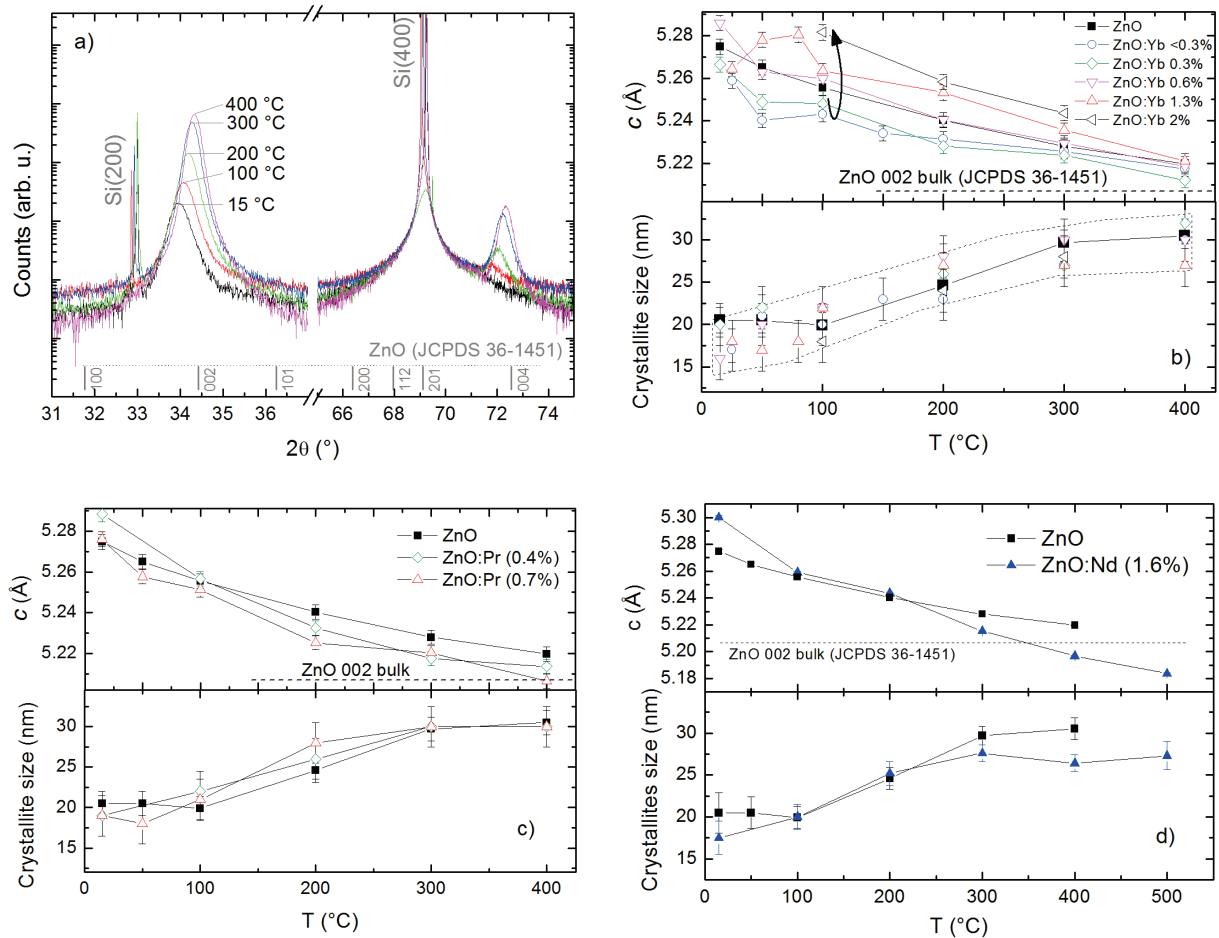


**Figure 3.1** – a) Typical  $\theta$ - $2\theta$  XRD diffraction patterns of ZnO thin films as a function of the deposition temperature and b), c), d) crystallites size and the lattice parameters calculated using Scherrer's and Bragg's formulas for undoped, Yb-, Pr- and Nd-doped films.

The effect of the post-deposition (ex-situ) annealing temperature on the crystallites size and lattice parameter of undoped and Yb(2%)-doped films is reported in Figure 3.2a-b for samples annealed in Ar during 10 min. With or without dopant, the lattice parameter approaches the bulk value and eventually stabilizes at a slightly lower value for temperatures above 800 °C. However, there is a substantial difference from the point of view of the crystallites size. For the undoped samples, it increases continuously with the annealing temperature up to 1000 °C. For the doped sample, it remains stable up to 800 °C and then almost doubles for higher temperatures. This might indicate that a certain type of Yb-related defects, which cannot be healed by annealing up to 800 °C, somehow “pins” the grain boundaries and prevents grain growth. However, the lattice can relax inside the crystallites (e.g. by defect migration towards the grain boundaries and occupation of vacancies by interstitial atoms), as indicated by the decrease of the lattice parameter.

There is evidence that the reason behind the crystallites size increase above 800 °C is related to Yb diffusion to the film/Si interface. In particular, the RBS measurements performed on annealed samples indicates that Yb starts to migrate towards the interface already at 700 °C. This might be related to the formation of zinc silicates ( $\text{Zn}_2\text{SiO}_4$  and  $\text{ZnSiO}_3$ ) evidenced by XRD for the sample annealed at 1000 °C. These results are not shown here, because outside the scope of this work.

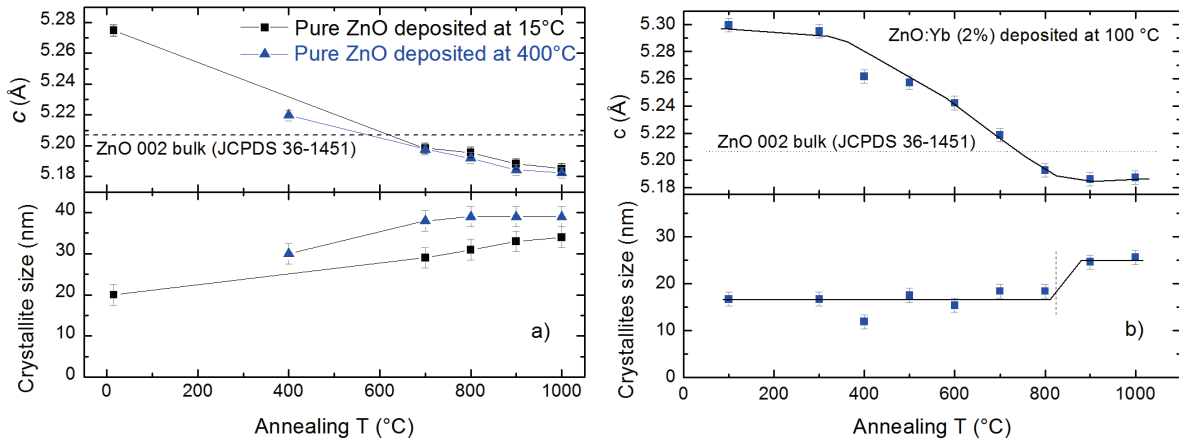


**Figure 3.2** - Effect of the annealing temperature on the crystallites size and *c* lattice parameter of undoped (a) and Yb(2%)-doped (b) ZnO thin films deposited at different temperatures and annealed during 10 min in Ar atmosphere. The first experimental point of each set corresponds to the “as deposited” value. The plain black lines are a guide for the eye.

A closer look to Figure 3.2a, which presents the lattice parameter and crystallites size of pure ZnO deposited at 15 °C and 400 °C, reveals that the lattice parameter follows the same curve by increasing the annealing temperature. This suggests that the final value of the lattice parameter depends only on the highest temperature seen by the sample, during or after the deposition. In other words, annealing at high temperature would smooth out the differences in stress due to the deposition temperature. This does not hold for the crystallites size, which depends on the deposition temperature.

To get more insight, Yb-doped and undoped samples have been prepared at different temperatures and annealed at 700 °C in Ar during 10 min. The lattice parameter and crystallites size are reported in Figure 3.3. For both doped and undoped ZnO, the lattice parameter reaches a certain value just below the bulk value, regardless of the deposition temperature. From the point of view of the crystallites size, however, doped and undoped samples behave differently. For undoped ZnO, annealing induces an increase of the crystallites size for all deposition temperatures, while for the Yb(1.3%)-doped samples deposited at low temperature, the crystallites size is unchanged. This suggests that the Yb-related defect pinning the grain boundaries is only formed at low deposition temperatures.

Contrarily to the lattice parameter, the final crystallites size after annealing depends on the deposition temperature. In order to exclude the possibility that this is related to the short annealing time (10 min), some doped samples have been annealed for up to 40 min. The results are also reported in Figure 3.3 and show no difference with respect to shorter annealing times.

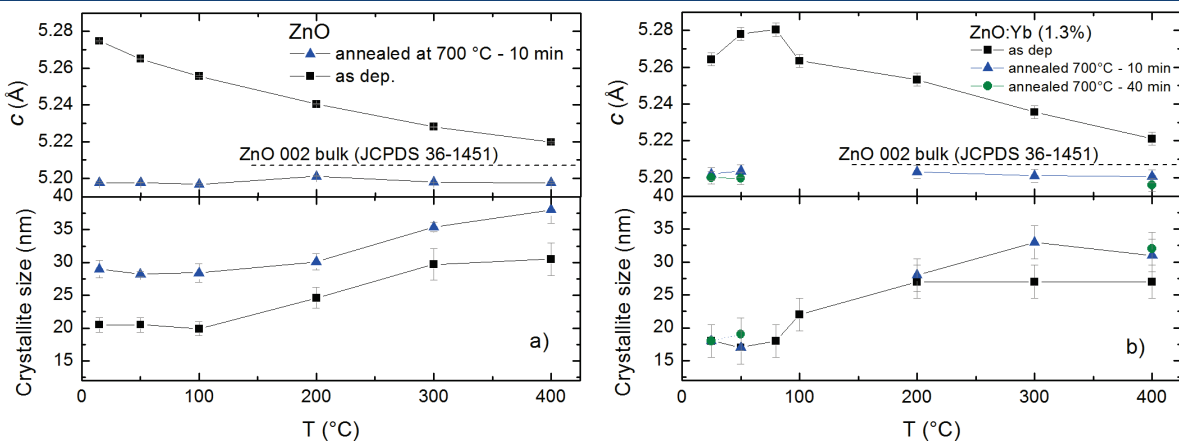


**Figure 3.3** - Influence of the deposition temperature on the crystallites size and *c* lattice parameter of undoped (a) and Yb(1.3%)-doped (b) ZnO thin films after annealing at high temperature (700 °C) during 10 min in Ar atmosphere.

The short annealing time needed to reach stable values of the film properties and the fact that the lattice stress point of view using high deposition temperatures is equivalent to perform in-situ annealing on the growing film explains why the samples have not been annealed at temperatures below or equal to the deposition temperature. This is particularly true in our case, where deposition times of 20-40 min are needed to reach film thicknesses of 100 nm and post-deposition cooling takes about 90 min.

As for the other annealing gases, it turned out that the final lattice parameter and crystallites size only depend on the annealing temperature and not on the atmosphere. This suggests that the defects inducing the stress and healed by annealing are either not related to oxygen atoms or that the atomic diffusion during the short annealing time is limited. The choice to present only the results obtained in Ar atmosphere is motivated by the larger number of investigated conditions. In general, however, not all the film properties are independent of the annealing gas. When needed, like in the case of the Pr luminescence, XRD data related to a different atmosphere will be added to support the explanation.

The results of annealing on the lattice parameter and crystallites size of Pr-doped films is equivalent to that of Yb-doped films and has been not reported. Nd-doped samples have not been annealed at all.

The deposition temperature and the thermal treatments also modify the orientation of the crystallites. Figure 3.4a shows a rocking curve ( $\omega$ -scan) around the (002) peak of undoped ZnO deposited at RT and 400 °C, and deposited at RT but annealed at 700 °C during 10 min. The use of high deposition temperatures constitutes the most effective way to obtain a strong texture, where most of the crystallites are oriented within 2-3° with respect to the normal to the surface. Annealing can also improve the orientation, but the final distribution is not as narrow as that reached with high deposition temperatures. Figure 3.4a is representative of all samples, although  $\omega$ -scans of doped ZnO have slightly wider peaks. Figure 3.4a also confirms that even samples deposited at room temperature are textured. There are very few crystallites tilted more than 15° from the normal.

So far, only the film properties along the growth direction have been presented. Although other techniques are more appropriate to investigate the structure and morphology in other directions, XRD can provide one more qualitative information, i.e. if there is a preferential direction also in these directions. In particular, the film could have an epitaxial relation with respect to the substrate. In other words, the film would be a single crystal with crystallites only slightly tilted with respect to each other and all oriented in the same direction with respect to the substrate (which is a single crystal). A  $2\theta$ - $\chi$ - $\phi$  scan of the (105) diffraction peak is reported in Figure 3.4b and shows that the crystallites are randomly twisted around the c-axis.

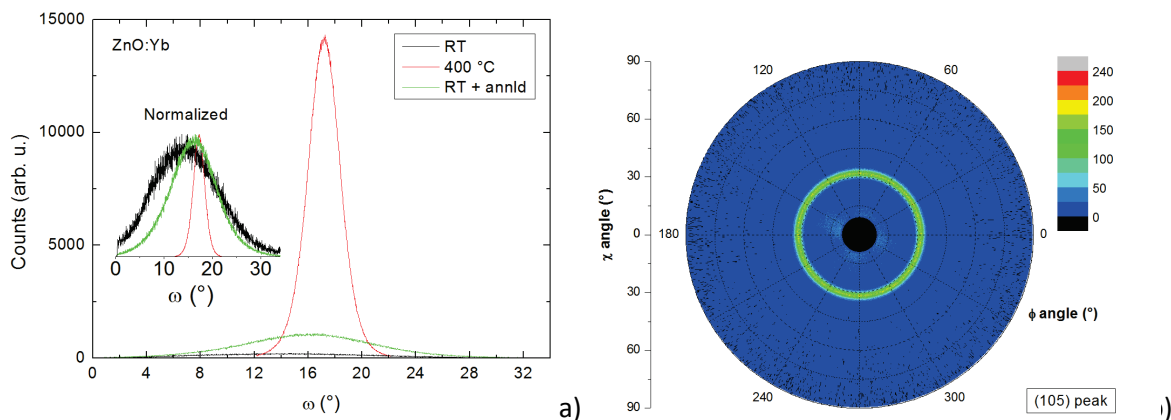


**Figure 3.4** - a)  $\omega$ -scan around the (002) peak of undoped ZnO deposited at RT and 400 °C, and deposited at RT but annealed at 700 °C during 10 min and b) pole figure ( $2\theta$ - $\chi$ - $\phi$  scan) of the (105) peak of a ZnO:Yb (1.3%) sample deposited at 400 °C.

From the XRD data, it is clear that the preparation condition of the films do not modify the film texture (the  $\theta$ - $2\theta$  scans show only the {002} peak family and the  $\omega$ -scans small tilt values for these crystal planes). However, some deposition parameters, such as the temperature and the gas flow ratio, and ex-situ annealing have a non-negligible effect on the grain size and lattice parameter. In the following paragraphs, the microscopy data show how the morphology of the film is modified. In particular, they affect the surface roughness, as well as the film density and uniformity.

### 3.1.2 TEM observations

In order to have a deeper insight into the crystalline structure and the influence of the deposition temperature, TEM analysis has been performed on several samples. Figure 3.5 shows the cross section of two samples of ZnO:Yb (1.3%) deposited at 200 °C and 400 °C. Low-resolution images show that both layers are homogeneous and have a thickness of about 90 nm. In both cases, a columnar growth is observed. The columns seem to extend over the whole film thickness.

The film deposited at 400 °C shows a much larger surface roughness and column width than those of the sample grown at 200 °C. A thin (< 2 nm) amorphous layer of native silicon oxide is always present between the substrate and the film. The presence of this layer is unavoidable due to the presence of oxygen in the sputtering chamber and rules out any possibility of epitaxial relation with the substrate.

High-resolution (HR) cross-section TEM has been performed and a detail of the interface is reported as inset in Figure 3.5. The ZnO crystallites grow by stacking of the (002) atomic planes along the growth direction. However, a continuity of the ZnO (002) planes across the grain boundaries is observed, which confirms that individual crystallites are only twisted with respect to each other around the growth direction. It is important to point out that these planes appear to be slightly bent in some points, probably due to structural defects such as edge dislocations and grain boundaries.

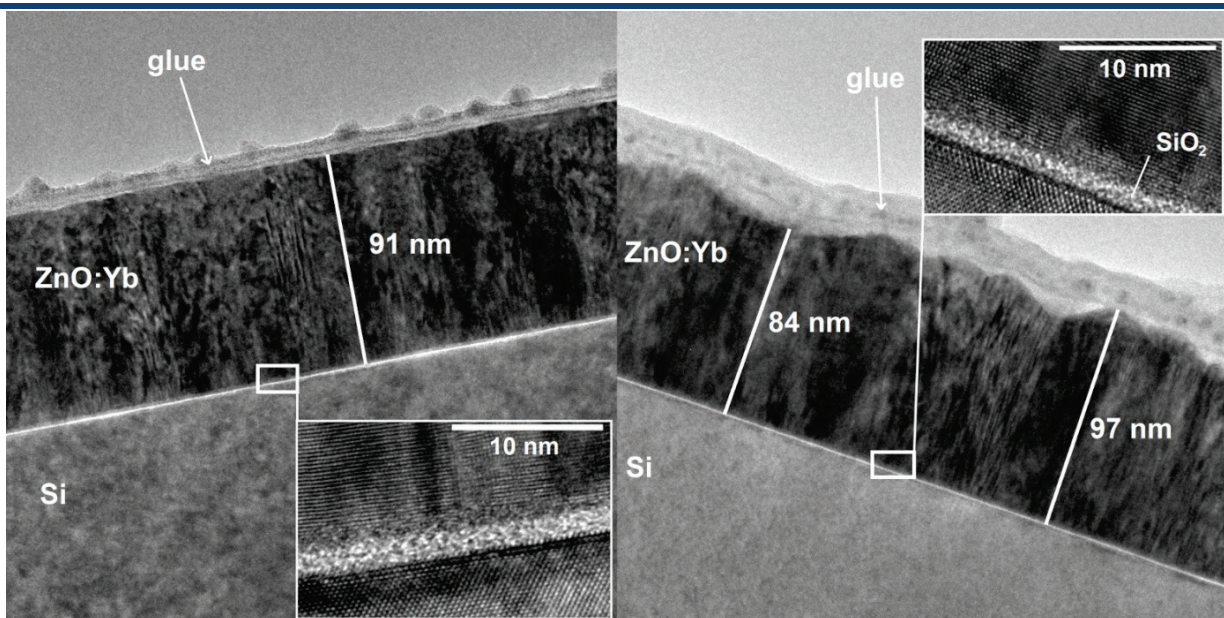


**Figure 3.5** – Cross section TEM image and HR-TEM interface detail of ZnO:Yb (1.3%) samples deposited at 200 °C (left) and 400 °C (right).

Figure 3.6a reports a typical SAED pattern of a ZnO film cross section. The absence of diffraction rings is characteristic of single crystals or of polycrystalline materials with a preferential orientation perpendicular to the electron beam. The strong elliptic shape of the ZnO (002) spots compared to the circular spots of silicon is due to the small tilt distribution of the c-axis with respect to the growth

direction. A SAED pattern such as that of Figure 3.6a, where the spots of the film are aligned with those of the substrate might suggest an epitaxial relation. However, the pole figure presented above and the thin oxide layer show that this is not the case. The alignment is essentially due to the fact that the films are deposited on Si(100) and that the images are observed in zone axis, which means that the sample is tilted until a clear 2D pattern due to Si can be seen. In addition, the observed region contains mostly ZnO crystallites with a particular orientation with respect to the substrate surface. Figure 3.6b and c are dark field images obtained by using the (002) reflection and the (1-10) reflection which is at 90° from the first. The fact that the whole film is bright when using the (002) reflection confirms the strong preferential orientation, while the very small bright area using a different reflection confirms the random twist around the c-axis.

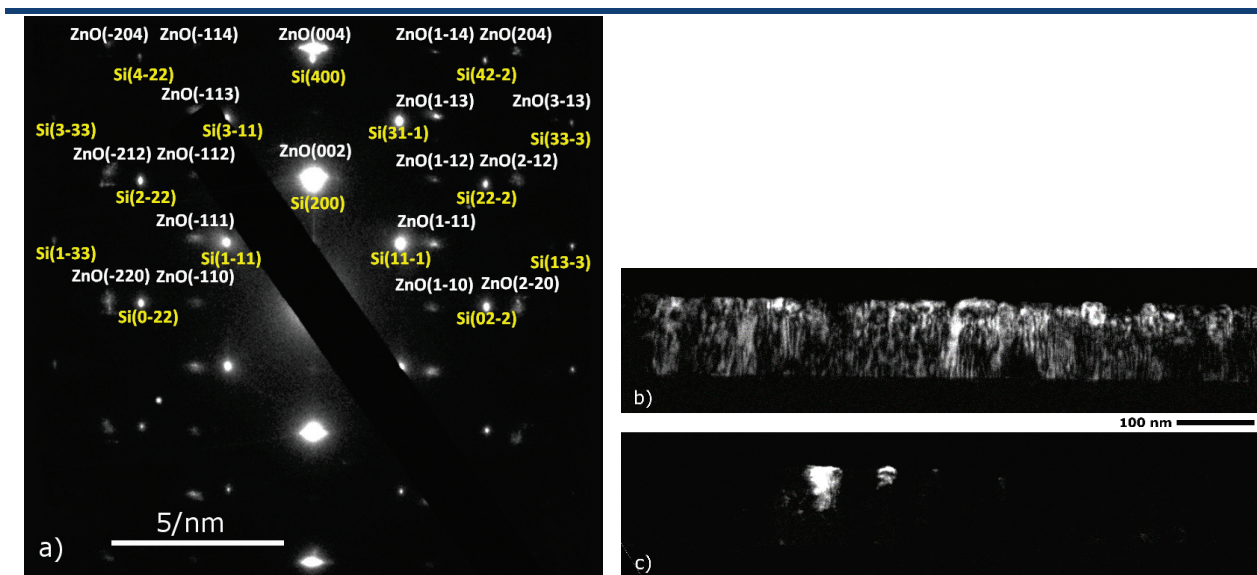


**Figure 3.6** – Cross section SAED pattern of undoped ZnO deposited at 400 °C (a) and dark field (b) (002) and (c) (1-10) reflection.

A plan view can give a direct representation of the twist, but requires a sample thickness lower than the crystallites size. Only if this condition is fulfilled it is possible to distinguish the crystal planes without blurring or unwanted moiré fringes<sup>20</sup>. Undoped samples deposited at 400 °C have large crystallites size along the growth direction (~30 nm) and are therefore well suited for this observation. A plan-view HR image of an undoped ZnO thin film deposited at 400 °C is reported in Figure 3.7a. Figure 3.7b shows the same sample, but at higher magnification, in order to provide a clearer view of the atomic ordering. The grain boundaries are sharp and the crystal planes are parallel within each crystallite, but have different orientation from one crystallite to the other. The SAED pattern is also shown in Figure 3.7c. Contrarily to the cross section image, the pattern presents the rings characteristic of a polycrystalline material. However, the fact that the main reflections are those from planes containing the c axis ( $hk0$ ) reveals the preferential orientation. In particular, two of the main diffraction rings are missing, the (101) and the (002).

The plan view of an undoped ZnO sample deposited at 200 °C is reported for comparison in Figure 3.7d. Here, the crystallites are small and the electron beam crosses several crystallites with different orientations. The result is a blurred image constellated with moiré patterns. The corresponding

<sup>20</sup> Moiré fringes are image artifacts (interference patterns) produced by two superposed regular patterns, in this case produced by two families of planes tilted with respect to each other and belonging to two different crystallites. The combination of the two patterns produces a regular variation of the image contrast and gives the illusion that a third pattern exists.

diffraction image is shown in the inset. The rings are more continuous with respect to the sample deposited at 400 °C due to the higher number of crystallites, but the presence of the same diffraction rings indicates that crystallites are still well oriented along the c-axis.

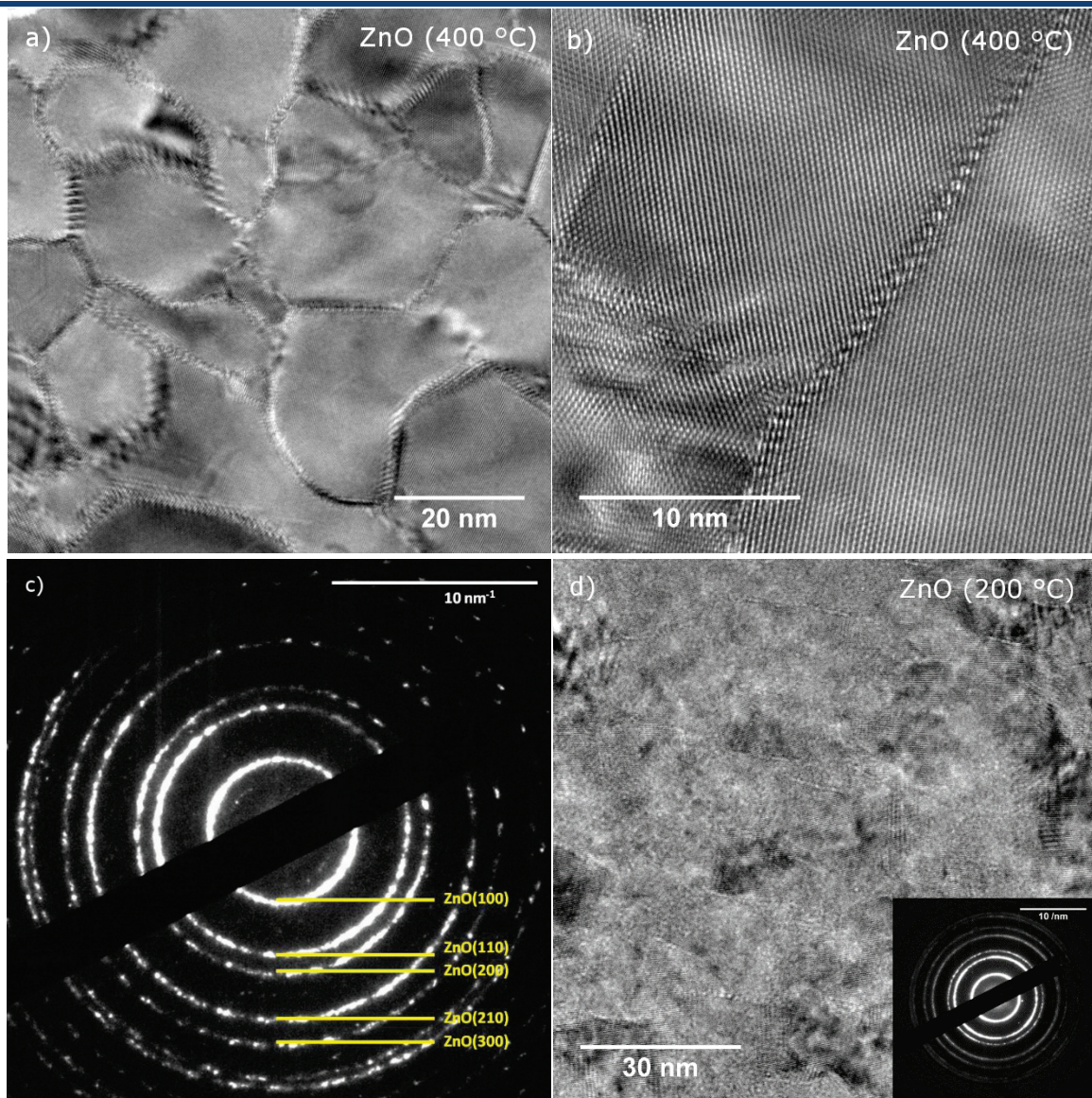


**Figure 3.7** – Plan views at different magnifications of a pure ZnO film deposited at 400 °C (a) and (b). Corresponding SAED pattern showing the polycrystalline nature of the sample (c). Plan view of a pure ZnO film deposited at 200 °C with corresponding SAED pattern.

TEM images are very useful to investigate the structural and morphological properties of the films, but give a very local view of the sample. With SEM images, a qualitative but effective idea of the general sample surface morphology can be obtained.

### 3.1.3 Morphology of the films

SEM micrographs illustrate particularly well the effect of the Ar/O<sub>2</sub> gas flow ratio during deposition. Figure 3.8 shows the results for ZnO:Yb (2%) thin films deposited at 100 °C and Ar/O<sub>2</sub> gas flow ratio between 4 and 8. A small ratio (below 4) is necessary in order to have uniform and dense ZnO(:RE) films. We found out that for gas flow ratios above 10 (not shown here), ZnO forms a powder that can be easily scratched away from the substrate.

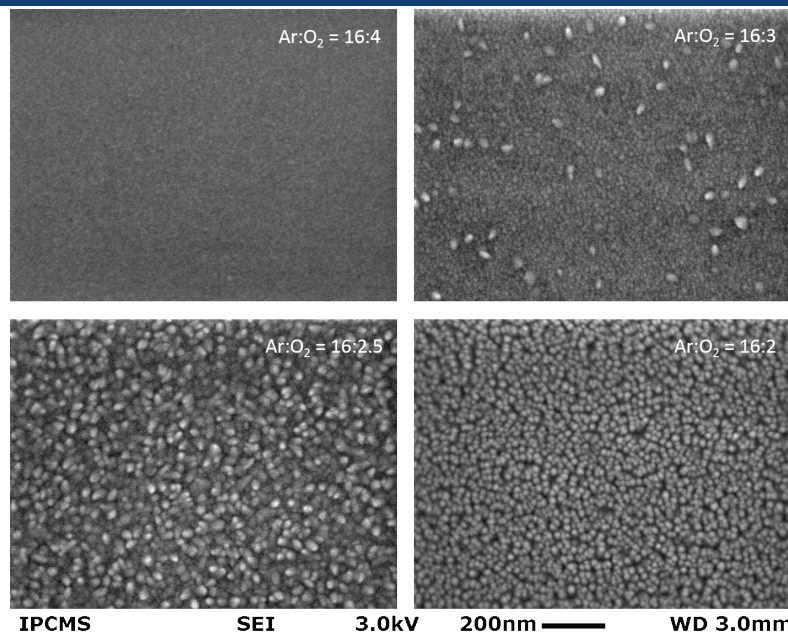


**Figure 3.8** - SEM micrographs recorded on a 100 nm ZnO:Yb (2%) film illustrating the effect of the Ar/O<sub>2</sub> gas flow ratio on the film morphology. The films were deposited at 100 °C.

Since small Ar/O<sub>2</sub> flow ratios also improve the RE insertion (as it will be shown in section 3.1.4), a ratio of 4 has been chosen for all samples shown in this work. The influence of the deposition temperature on the morphology is illustrated in Figure 3.9. In this case, all films are dense and uniform, but the surface roughness strongly depends on the temperature.

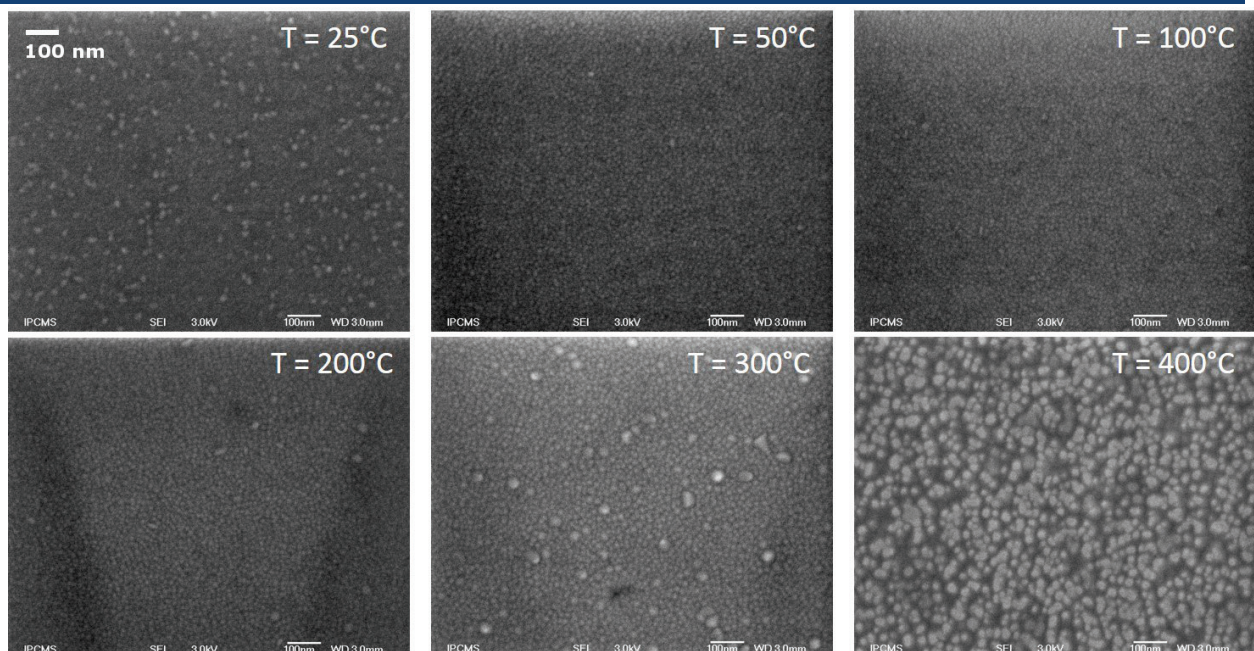


**Figure 3.9** - SEM micrographs illustrating the effect of the deposition temperature on the film morphology. ZnO:Yb (1.3%) sample is taken as an example.

Cross section TEM and SEM images give a qualitative view of the surface roughness. Quantitative information on the surface roughness can be obtained by AFM. Figure 3.10 reports the AFM image of undoped and Yb-doped ZnO deposited at RT and 400 °C, and deposited at RT but annealed at 700 °C in Ar atmosphere during 10 min.

The AFM data confirm the results given by TEM about the deposition temperature: depositing a sample at high temperature allows the formation of larger grains and leads to high surface roughness.

AFM data also shows that the grain size increases with annealing for undoped samples, while it remains roughly the same for doped samples. This might be the cause of the crystallites size pinning suggested by XRD data.

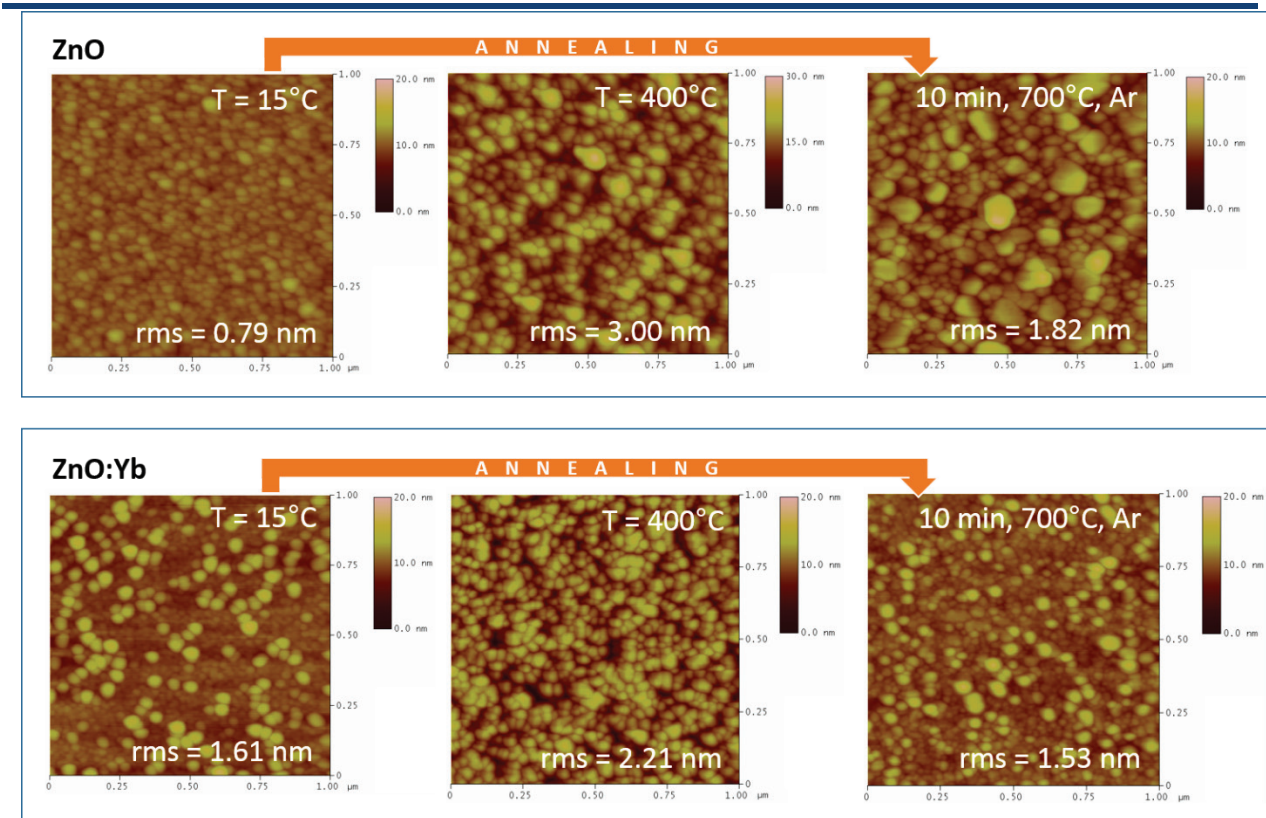


**Figure 3.10** – The effect of the deposition temperature and annealing on the surface morphology of ZnO and ZnO:Yb (2%) as shown by  $1 \times 1 \mu\text{m}^2$  AFM images. The roughness values are also indicated.

### 3.1.4 Rare earth distribution in ZnO films

RBS can be used to determine the distribution of the elements along the growth axis. If the distribution is constant, the stoichiometry of RE-doped ZnO films can be determined.

All RE concentrations presented in this work are effective atomic concentrations as determined by simulating the RBS spectra using in-house software. The RE concentration is evaluated with respect to the zinc content, so that the material can be written as  $\text{Zn}_{1-x}\text{O}_y\text{RE}_x$ . The reason behind this choice is that an accurate determination of the oxygen content is quite difficult by common techniques such as RBS or EDX (energy dispersive X-ray spectroscopy).

A typical RBS spectrum of sputtered RE-doped ZnO and the relative simulation are presented in Figure 3.11a. The dopant concentration along the growth direction is uniform for all deposition temperatures and is independent of the temperature up to 400 °C. In the case of Yb, annealing above 700 °C showed some migration of the rare earth towards the silicon interface. Again, this can be related to the formation of zinc silicates evidenced by XRD.

Despite the problems in the determination of the oxygen content, it is worth noting that all spectra are better simulated with  $y \approx 1.1$ . The presence of some excess oxygen in the films is also suggested by

photoluminescence (as it will be shown further), and is compatible with the small Ar:O<sub>2</sub> ratio used during deposition. This oxygen excess does not exclude the presence of a small concentration of oxygen vacancies, as most of the extra oxygen is in interstitial position.

Figure 3.11b and c show how strongly the RE concentration depends on the oxygen flow during deposition. At a ratio of 16:5 the concentration is almost five times that obtained at a ratio of 16:2. It is not clear, though, if this difference is due to the larger amount of oxygen available during deposition or simply to the fact that more oxygen in the chamber slows down the growth process, allowing RE ions to be better inserted in ZnO. For this reason, the growth rate is also reported in Figure 3.11b-c.

From the point of view of the rare earth insertion, ratios below 4 should be preferred. However, this leads to very long deposition times. The ratio of 4 and the resulting deposition time of about 40 min used in this work provide reasonable RE concentrations (>1%) in order to study the luminescence.

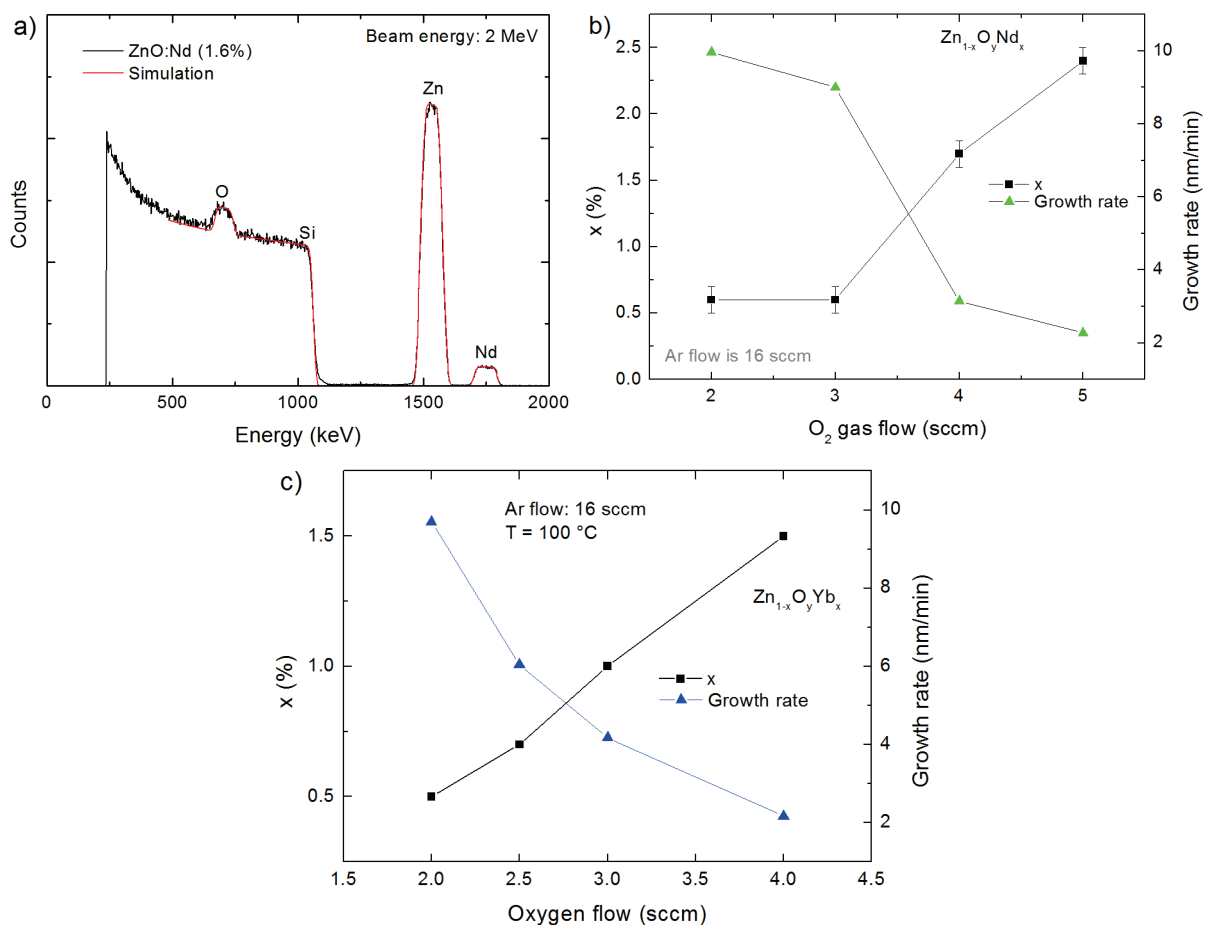


**Figure 3.11** – a) Experimental and simulated RBS spectra of a ZnO:Nd (1.6%) film of 100 nm and variation of the RE content and of the growth rate with the oxygen gas flow used during deposition in the case of Nd (b) and Yb (c) doping.

RBS only gives the 1D distribution of the rare earth along the growth direction. In order to check the 3D distribution of the dopant, it is necessary to use a more sophisticated (and time consuming) technique.

Atom-probe tomographic measurements have been performed on two Yb-doped ZnO samples deposited at 15 °C and 400 °C and on one of the Yb-doped samples annealed at 700 °C. These measurements have been carried out by Rodrigue Lardé in the frame of a collaboration with the GPM group at the University of Rouen (France). In all three cases, the distribution of Yb in the film is very homogeneous. Figure 3.12 reports the results obtained on the sample deposited at 15 °C and 400 °C. In the investigated volume, no Yb cluster has been observed and the distribution of Yb atoms is very close

to a uniform, random distribution described by the Poisson equation. However, due to the small investigated volume, clustering cannot be completely excluded.

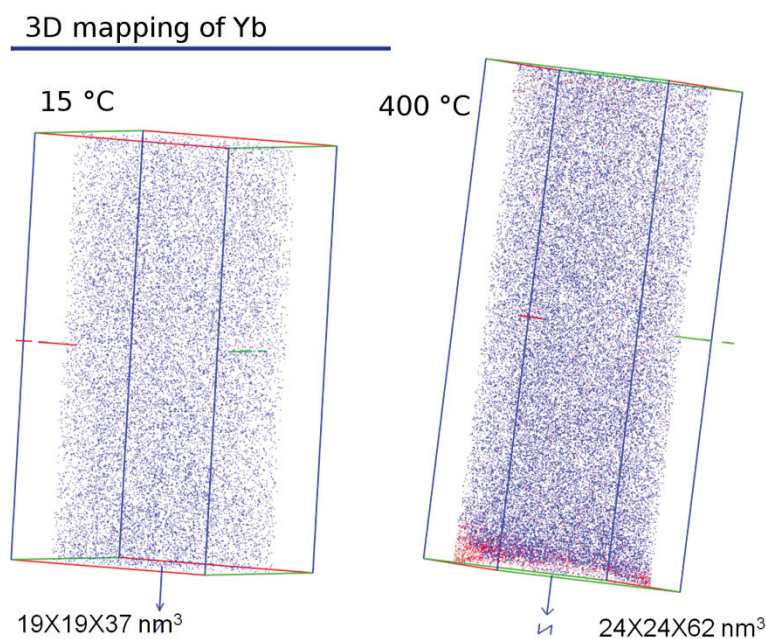


**Figure 3.12** – Atom-probe tomographic 3D mapping of Yb in ZnO thin films deposited at 15 °C and 400 °C. The red dots are silicon atoms. Some are situated within the film because in some cases the analysis crosses the ZnO/Si interface.

### 3.1.5 NEXAFS data of ZnO(:RE) films

Thanks to NEXAFS measurements, information about the valence and the local environment of the different elements can be obtained. NEXAFS spectroscopy was performed by Paul Bazylewski in the frame of a collaboration with the group of Gap Soo Chang at the University of Saskatchewan (Canada).

Figure 3.13a-b-c show the O K (1s) XAS (TEY) spectra of selected RE-doped ZnO films (Yb, Pr and Nd, respectively) deposited at different temperatures. The O K XAS (TEY) spectrum of undoped ZnO deposited at 100 °C is reported for reference. The effect of annealing in Ar at 700 °C during 10 min is also shown for Yb-doped films. The curves have been artificially shifted for clarity.

The intensity of the shoulder peaks (their positions are marked by vertical lines in Figure 3.13a-b-c) is related to the concentration of oxygen vacancies. As it can be observed, Yb-doped films present a higher oxygen vacancy concentration with respect to undoped ZnO, suggesting that Yb might attract some oxygen from neighboring lattice sites. However, annealing in Ar at 700 °C restores the vacancy concentration to the undoped value. The deposition temperature has little influence on the oxygen vacancy concentration.

Pr- and Nd-doped samples have the same oxygen vacancy concentration of undoped ZnO, except for the ZnO:Nd sample deposited at 400 °C, which presents a lower oxygen vacancy concentration.

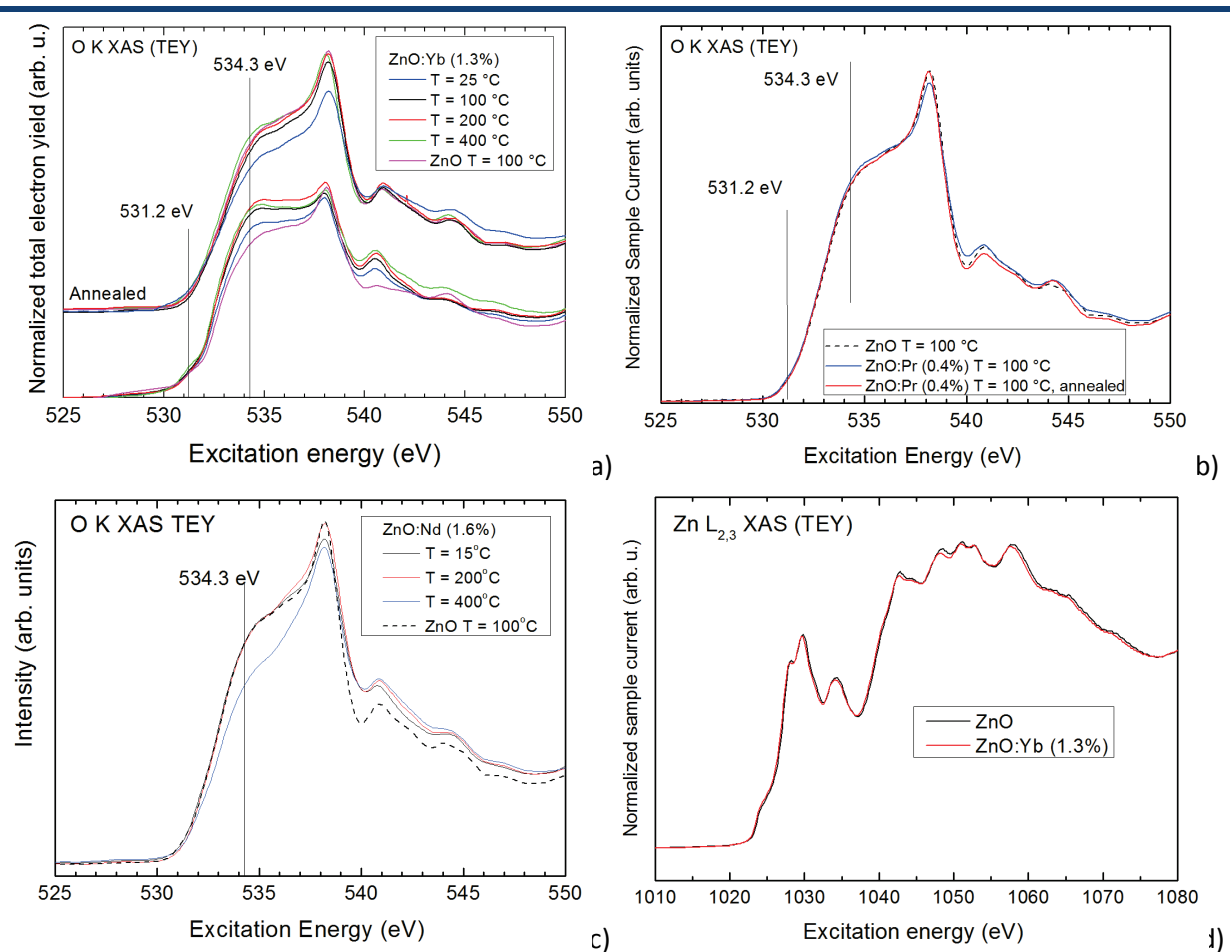


**Figure 3.13** - O 1s XAS (TEY mode) of a) ZnO:Yb, b) ZnO:Pr and c) ZnO:Nd films as a function of the deposition temperature and/or annealing in Ar during 10 min at 700 °C. The curves in a) have been artificially shifted to improve clarity. d) The Zn L<sub>2,3</sub> XAS (TEY mode) of an undoped and an Yb-doped film.

The Zn L<sub>2,3</sub> XAS (TEY) spectrum was also measured for all samples. Figure 3.13d compares the typical signal of a doped sample with the reference undoped ZnO. The signals are very similar without significant changes in peak locations or intensity, which means that the Zn lattice is not significantly perturbed by doping.

It is important to point out that TEY measurements only sound the first few nanometers of the film and that the oxygen vacancy concentration might not be the same deep in the film. Measurements in TFY mode of the O 1s XAS spectra have been performed to investigate the “bulk” of the film. Figure 3.14a reports the O 1s XAS (TFY) spectra of Yb-doped ZnO films deposited at different temperatures and Figure 3.14b those of Nd-doped ZnO films. It is clear that the oxygen vacancy concentration deep in the film is comparable with that of undoped ZnO and that the differences observed above are a surface effect.

Besides the oxygen and zinc edges, the RE M<sub>4,5</sub> edge has been also measured. Unfortunately, the fluorescence signal of REs is too weak to perform TFY measurements. Only TEY data will be reported, which means that the results cannot be safely extended to the whole film.

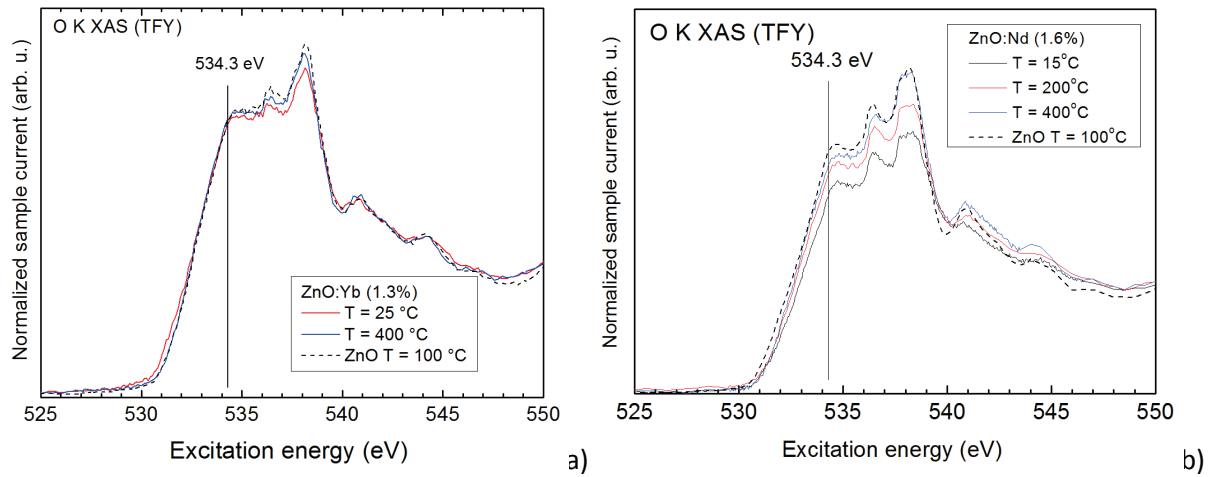


**Figure 3.14** - O 1s XAS (TFY mode) of a) ZnO:Yb, b) ZnO:Nd films as a function of the deposition temperature.

Figure 3.15a-b reports the Yb  $M_5$  XAS spectra of ZnO:Yb films deposited at different temperatures and annealed in Ar at 700 °C during 10 min. The measurements are normalized to a background at 1580 eV. The two graphs present the same data with different normalizations.

Comparison with  $Yb_2O_3$  indicates that the main peak at 1520.6 eV is associated to  $Yb^{3+}$ . The variation of the peak intensity represents the variation of the  $Yb^{3+}$  concentration in the proximity of the sample surface.

The sample deposited at 400 °C has an unusual behavior after annealing. Since the peak shifts to lower energy than  $Yb_2O_3$  and it comes from unoccupied states, some  $Yb^{3+}$  could donate some extra charge to its local environment, so that the oxidation state is something like  $Yb^{3.5+}$ , but not as high as  $Yb^{4+}$ . Alternatively, since TEY sounds only the sample surface, the difference can be explained by a damaged surface or contaminant in the measurement spot. The different background evidenced in Figure 3.15b supports this idea. In any case, Yb is still definitely mostly in 3+ oxidation state, as indicated by the presence of a single peak.

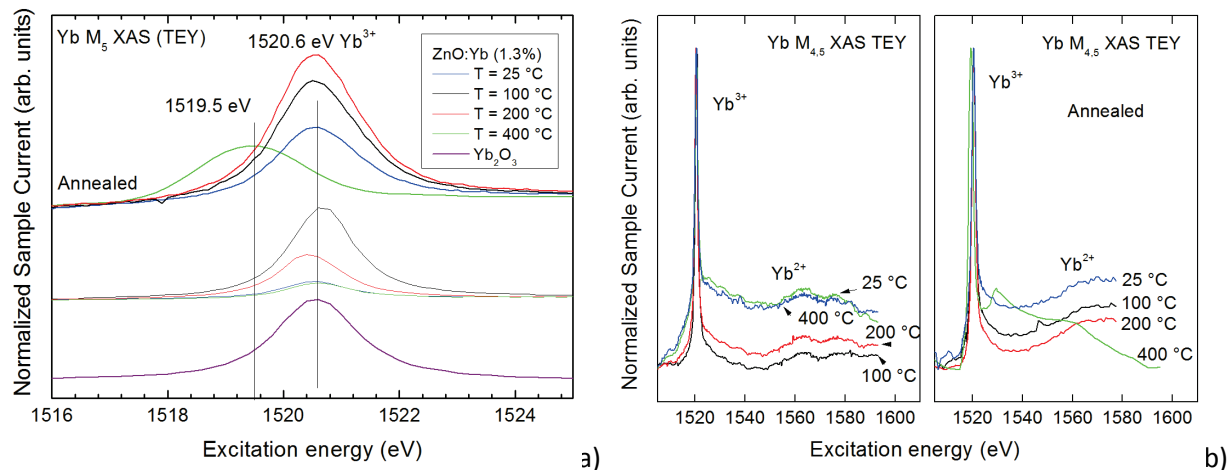


**Figure 3.15** - Yb  $M_{4,5}$  XAS (TEY) of ZnO:Yb films deposited at different temperatures and annealed in Ar at 700 °C during 10 min. The measurements are normalized to a background at 1580 eV. The two graphs present the same data with different normalizations: a) the curves in each group (annealed and as deposited) are normalized with each other and to the background signal, but not between the two groups, b) the curves are normalized with respect to the peak intensity at 1520.6 eV.

The reason why  $Yb^{3+}$  presents a single peak can be resumed as follows [232, 233]. The  $M_{4,5}$  edge corresponds to  $3d \rightarrow 4f$  transitions. The number of possible  $3d^9 4f^{14}$  final states is quite small at the edges of the rare earth series and it is further reduced by the  $\Delta J$  selection rules. The initial state for  $Yb^{3+}$

is  $4f^{13}$  and has  $L = 3$  and  $S = 1/2$ . The two possible values of  $J$  are  $5/2$  and  $7/2$  and the ground state is that with  $J = 7/2$  according to Hund's rule. The  $^4F_{5/2}$  state has an energy difference with the ground state of approximately 1.3 eV due to spin-orbit coupling (see Figure 1.21). The final state, after 3d absorption, is  $3d^9 4f^{14}$ , with term symbols  $^2D_{3/2}$  and  $^2D_{5/2}$ . The energy difference between these two terms due to the spin-orbit coupling is 49 eV. However, in the XAS spectrum, only the  $^2D_{5/2}$  line (corresponding to the  $M_5$  edge) is present, since the  $^2D_{3/2}$  term cannot be reached from the  $^4F_{7/2}$  ground state because of the  $\Delta l$  selection rules. The presence of a crystal field partially relaxes the selection rules, so that a small  $M_4$  edge is expected at about 50 eV above the  $M_5$  edge. It is worth notice that transitions to both final states are possible from the  $^4F_{5/2}$  excited initial state, but that at room temperature very few atoms are in the excited state.

Figure 3.15b presents the spectra with the intensity normalized to the  $M_5$  peak. The small and wide peak around 1570 eV could be the  $M_4$  edge, but the vertical shift must have a different explanation.

A possible explanation involves the presence of  $Yb^{2+}$ . For  $Yb^{2+}$ , the initial state is a full f shell. In this case, no sharp multiplet features should be observed, but rather an edge jump without sharp peaks. Figure 3.15b shows that the samples deposited at 25 °C and 400 °C have a larger edge jump and larger overall background signal. This might indicate a greater concentration of  $Yb^{2+}$  close to the film surface and is consistent with the loss of intensity in the  $Yb^{3+}$  feature when the spectra are normalized to the background signal. This difference in  $Yb^{2+}$  concentration is maintained after annealing, except for the sample deposited at 400 °C, which presents a different spectrum.

For Pr and Nd, the number of possible  $3d^9 4f^{n+1}$  final states is larger than for Yb and several lines are expected. The Pr  $M_{4,5}$  XAS of a typical ZnO:Pr samples before and after annealing in Ar at 500 °C during 10 min is shown in Figure 3.16a. The same spectrum for the Yb-Pr codoped sample is also reported. All samples present non-negligible amounts of  $Pr^{4+}$  with the same proportions to  $Pr^{3+}$ .

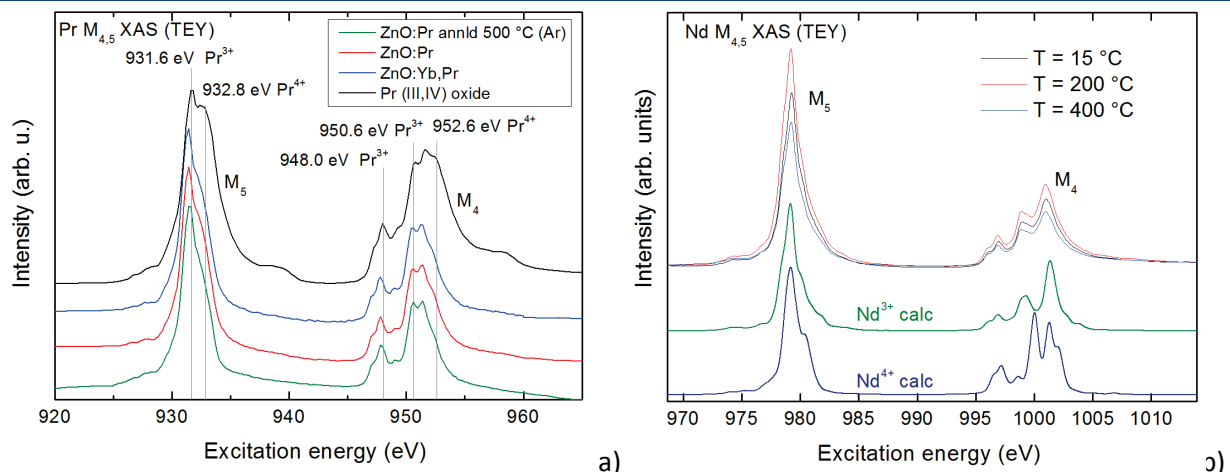


**Figure 3.16** – a) Pr  $M_{4,5}$  XAS (TEY) of a typical ZnO:Pr samples before and after annealing in Ar at 500 °C during 10 min. The same spectrum for the Yb-Pr codoped sample is also reported. The spectrum of Pr (III, IV) oxide is reported for reference. b) Nd  $M_{4,5}$  XAS (TEY) for samples deposited at different temperatures and *ab initio* edge calculations for  $Nd^{3+}$  and  $Nd^{4+}$ .

The Nd  $M_{4,5}$  XAS (TEY) spectra are reported in Figure 3.16b for samples deposited at different temperatures. All samples present the same spectrum. *Ab initio* calculations show that this spectrum corresponds to the 3+ oxidation state. Calculations have been performed without considering the crystal field effect. The good agreement between measured and calculated data proves that this is a good approximation when dealing with inner shells, such as the 3d and 4f shells.

### 3.1.6 Concluding remarks

The structural and morphological investigations showed that RF-sputtering starting from pure Zn target provides highly-oriented polycrystalline ZnO thin films in all investigated conditions. In particular, the preferential growth along the [002] direction is conserved in doped samples. No evidence of rare earth oxide or parasitic phases have been observed, except for samples annealed at temperature as high as 1000 °C.

Oxygen scarceness during deposition leads to poor insertion rates of the rare earth. In particular, it is possible that a certain amount of the extra oxygen is needed to balance the charge of the RE<sup>3+</sup> ion enters the lattice directly during growth. Nevertheless, insertion of up to 2 % of rare earth ions in ZnO films has been successfully obtained by magnetron reactive sputtering and no clustering has been observed.

Both deposition temperature and annealing temperature affect the crystalline structure, as indicated by the structural (lattice parameter and crystallites size) and morphological (roughness, grain size) investigations. These data indicate that there are several kinds of defects. In particular, for low deposition temperatures we evidenced the existence of a RE-related defect that inhibits grain growth.

RBS and tomography showed that the rare earths are uniformly distributed in the film, but they do not give any information about where the RE ions are situated in the lattice. Even the lattice parameter obtained from XRD did not show a clear shift that might indicate RE insertion in substitutional position (except in the case of Yb).

The analysis of the O 1s (K) XAS indicated that the oxygen vacancy concentration close to the film surface of RE-doped ZnO films presents some variations with respect to undoped films and the analysis of the RE M<sub>4,5</sub> edge revealed that oxidation states other than 3+ exist in ZnO. This information will offer some clue in interpreting some of the PL properties described in the next sections.

More information on the films can be obtained by studying their optical properties. In the next section, the basic optical properties of RE-doped ZnO films will be presented. With “basic” optical properties we mean those properties that characterize the “bulk” nature of the films (band gap, optical constants, ...), as opposed to the “local” optical properties of the dopants (RE photoluminescence) that will be presented in details in section 3.4.

## 3.2 Basic optical properties of ZnO(:RE) films

Doping a material might strongly alter its optical properties. In particular, doping might have an effect on the refractive index and on the density of states at the band edge, two very important parameters when dealing with transparent windows for solar cells.

As stated in the introduction, the negative effects of a poor refractive index matching or a wrong band gap values can quickly overwhelm the positive effect of photon conversion. In particular, refractive index matching with silicon is crucial in order to reduce the escape cone and to keep the reflectance at small levels. On the other hand, the band gap value is important when matrix-sensitized photon conversion is used. In this case, the absorption cross section of the matrix above the gap is as important as the band gap value itself.

In this section, the data of the complex refractive index of ZnO will be presented in two different ways. Below 400 nm (i.e. where ZnO absorbs), the variation of the extinction coefficient is more interesting than that of the refractive index. Therefore, the absorption edge as a function of the different preparation parameters will be reported. Above 400 nm, refractive index matching is crucial for good ARC properties. Thus, the analysis will be done from this point of view.

It turns out that in the investigated conditions, the variation of the gap value is much less impressive than the variation of the absorption edge just above its value. For this reason, the absorption edges will be presented in the following and the exact values of the gap will not be reported. However, the choice to present the absorption edges as Tauc plots allows extracting some visual information about the gap. One more reason not to focus on the band gap values is that the Tauc law cannot be applied to determine the optical band gap in presence of excitonic features. In fact, if the excitonic feature is strong, the measured value corresponds more to the excitonic absorption than to the band-to-band absorption. From the point of view of sensitized photon conversion, however, both absorptions are important.

Figure 3.17a reports the absorption edge of undoped ZnO films deposited at different temperatures. It can be seen that the deposition temperature has a clear effect on the electronic states at the band edges. Higher deposition temperatures produce steeper absorption edges due to a more important excitonic feature. A similar behavior is observed in case of annealing, whose effect on the absorption edge of ZnO films is shown in Figure 3.17b-c for two different deposition temperatures. It is interesting to notice that above 800 °C, the absorption cross section of ZnO is strongly reduced, while the band gap value remains constant.

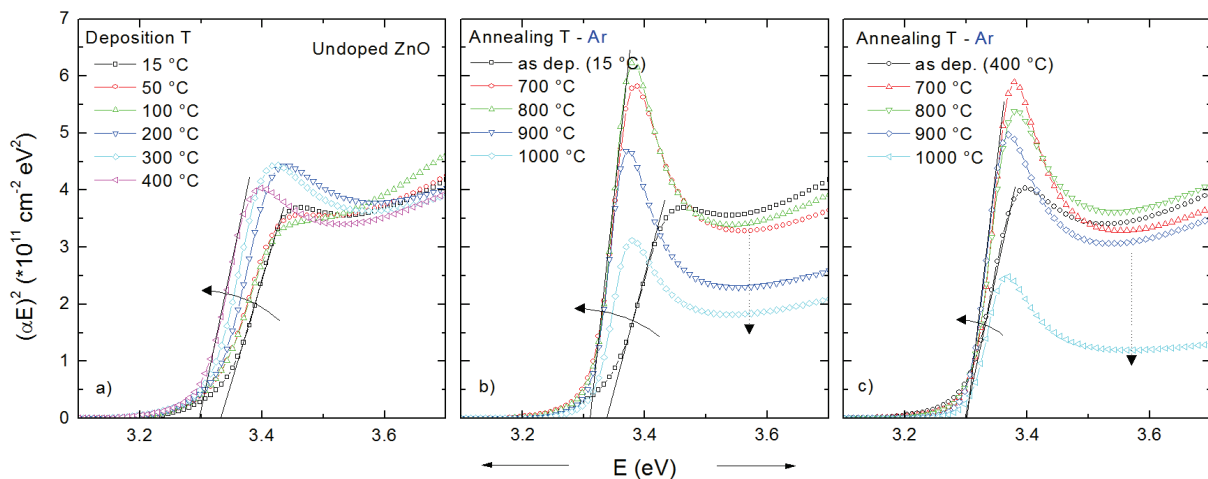


**Figure 3.17** – a) Effect of the deposition temperature on the absorption edge of undoped ZnO films. b-c) Effect of the annealing temperature on the absorption edge of an undoped ZnO films deposited at 15 °C and 400 °C.

Figure 3.18a,c shows that a similar effect is observed on Yb-doped films with two main differences: the excitonic peak is less pronounced and the decrease of the absorption cross section with high annealing temperatures is stronger. In this case, annealing in oxygen gas was also tested and the results are reported in Figure 3.18b. From the point of view of the absorption edge, using Ar or O<sub>2</sub> as annealing gas makes no substantial difference.

For Pr- and Nd-doped films, fewer annealing conditions have been tested. The variation of the absorption edge with the deposition temperature and annealing gas (for Pr only) are reported in Figure 3.19a-c. In this case, high deposition and annealing temperature decrease the band gap, while the steepness of the edge is not deeply altered.

Figure 3.20 illustrates the effect of the RE (Yb, Pr, Nd) concentration on the absorption edge. As the concentration increases, the excitonic feature disappears and the edge becomes smoother.

All these data show that modifying the preparation condition changes the shape of the absorption edge between 3.3 and 3.5 eV. These changes can be attributed in part to a modification of the band gap

value, but mostly to the variation of the excitonic feature. All films remain highly transparent below 3.2 eV and strongly absorbent above this value.

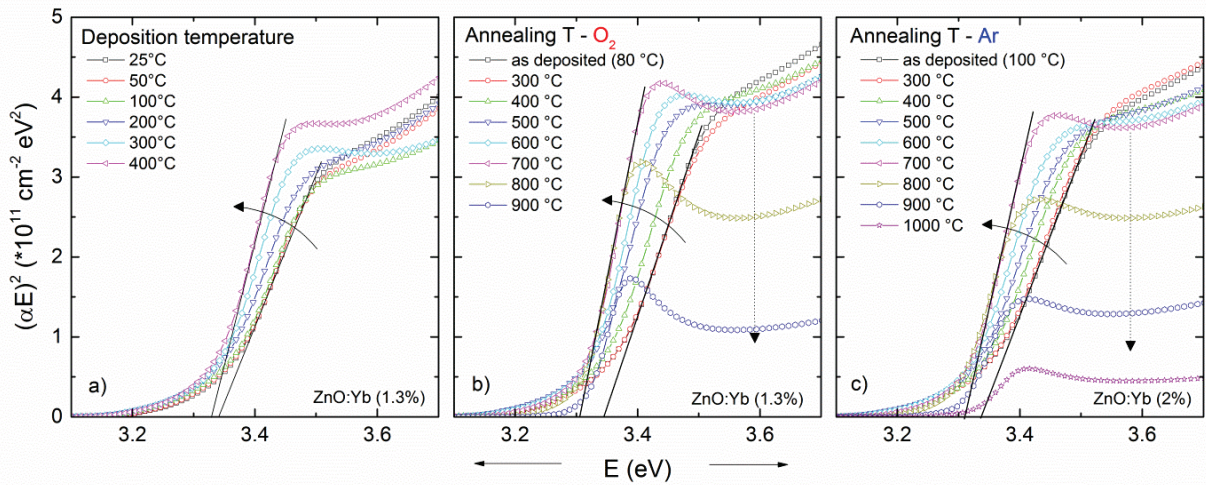


Figure 3.18 - a) Effect of the deposition temperature on the absorption edge of Yb-doped ZnO films. b-c) Effect of the annealing temperature on the absorption edge of an Yb-doped ZnO films deposited at 15 °C and 400 °C.

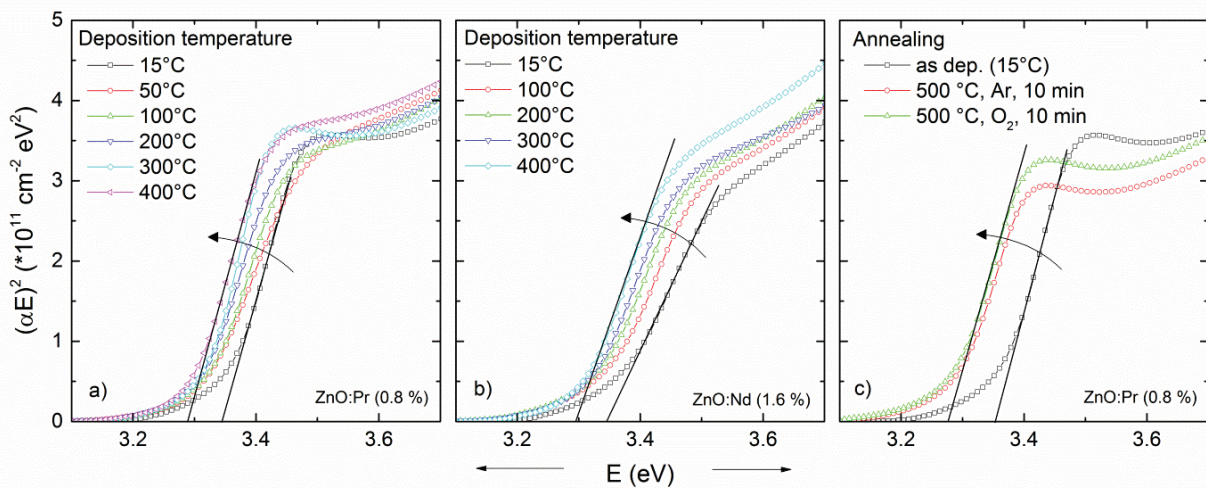


Figure 3.19 – Effect of the deposition temperature on the absorption edge in the case of a) Pr-doped and b) Nd-doped films. The effect of annealing ZnO:Pr (0.8 %) films at 500 °C in argon and oxygen atmospheres is reported in figure c).

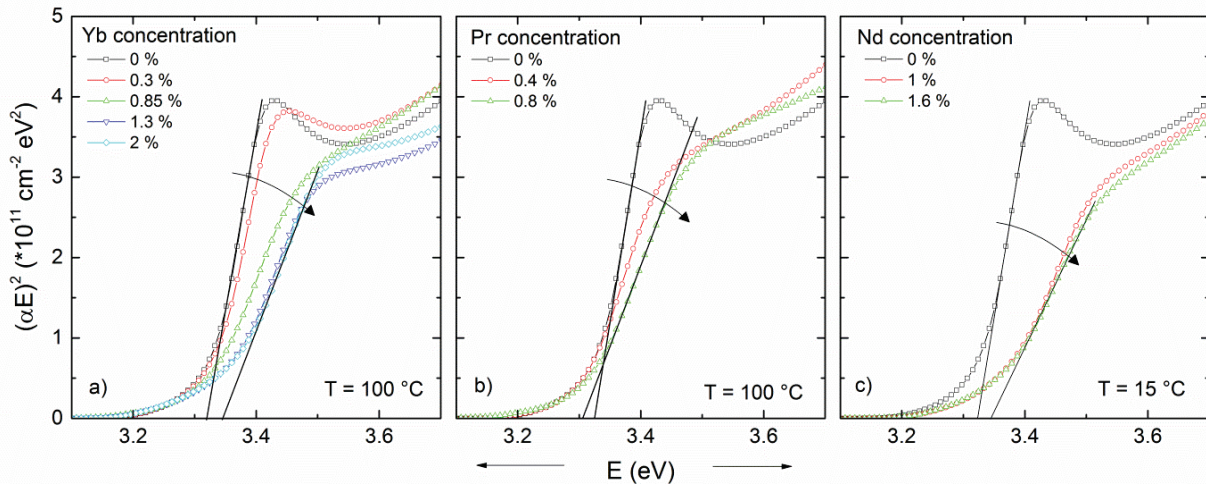
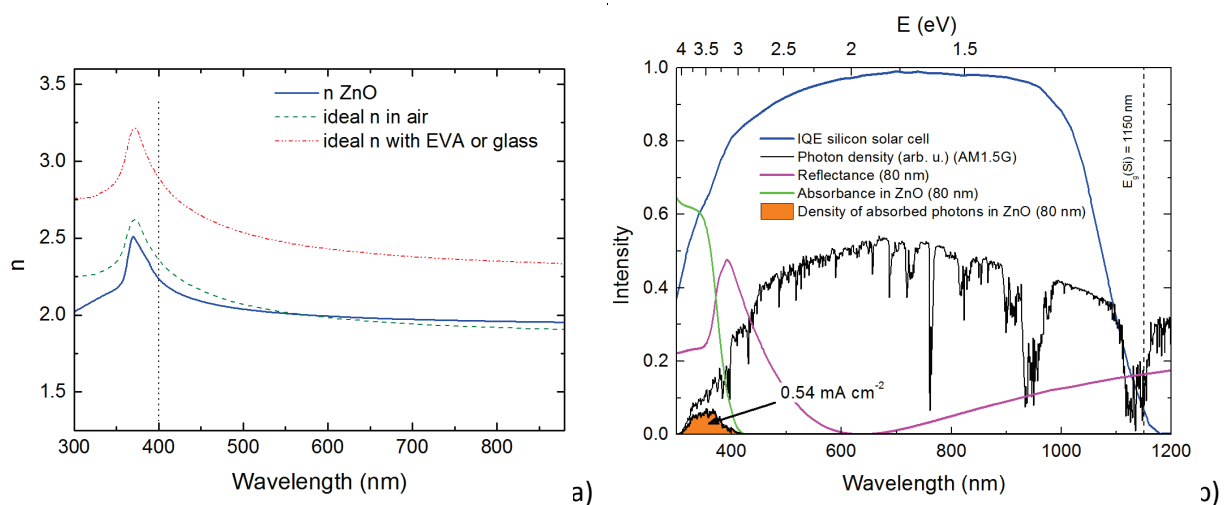


Figure 3.20 – Effect of the RE concentration on the absorption edge in the case of a) Yb, b) Pr and c) Nd.

In the transparent region, the value of the refractive index must be kept under control. It turns out that the refractive index of ZnO above 400 nm is practically unchanged by doping, deposition temperature or annealing, which means that adding photon management properties by doping with rare earths maintains the good ARC properties of ZnO.

Figure 3.21a reports the typical refractive index of ZnO as a function of the photon wavelength. Also indicated are the ideal refractive indices for optimal ARC properties, calculated as  $n_{ideal} = \sqrt{n_{Si}n_{IM}}$  (IM for incoming medium), in the case of a solar cell in air or with an encapsulant of refractive index 1.5 (i.e. glass or ethylene vinyl acetate, EVA). It is clear that ZnO presents optimal ARC properties when air is the incoming medium<sup>21</sup>. This means that the reflectance can be decreased to zero in the regions of destructive interference. Since the photon density of the solar spectrum is not uniform, neither is the spectral response of the solar cell, it is essential to select where to apply destructive interference and decrease the reflectance conveniently.



**Figure 3.21** – a) Typical refractive index of ZnO as a function of the photon wavelength obtained by fitting ellipsometric data. Also indicated are the ideal refractive indices for optimal ARC properties. b) The reflectance and the absorbance of a typical ZnO film of 80 nm. An example of IQE of silicon solar cell and the photon density in the solar spectrum are reported for reference. The additional current added to that of the solar cell by ideal DS is also indicated.

This region can be selected by choosing the appropriate thickness. For this purpose, the average reflectance over the whole spectral range as a function of the film thickness can be calculated. A more accurate estimation of the optimal thickness can be obtained by averaging the reflectance over the photon density and the IQE of a silicon solar cell. With this precaution, the optimal ZnO film thickness for ARC properties has been calculated to be about 80 nm. Unfortunately, less than 50 % of the light below 400 nm is absorbed by 80 nm of ZnO, thus limiting the energy available for downshifting or down-conversion. Figure 3.21b illustrates these concepts. If all photons absorbed by ZnO were downshifted and absorbed by Si,  $0.54 \text{ mA/cm}^2$  of current would be added to the total current of the cell. This value must be doubled in case of ideal DC.

The use of air as incoming medium also decreases the cone loss of the converted light (see Figure 1.12), reducing the cone aperture from about  $90^\circ$  in the case of glass to about  $60^\circ$  in the case of air. The lost PL intensity calculated with respect to the isotropic PL emission is then reduced from 18% to 7%<sup>22</sup>.

<sup>21</sup> If air or vacuum exist between the glass (or EVA) and the solar cell, then ZnO remains a good ARC.

<sup>22</sup> Values calculated using a wavelength in the near infra-red.

### Concluding remarks

The analysis of the complex refractive index proved two things. First, it proved that modifying the preparation condition changes the shape of the absorption edge between 3.3 and 3.5 eV. These changes can be attributed in part to a modification of the band gap value, but mostly to the variation of the excitonic feature. All films remain highly transparent below 3.2 eV and strongly absorbent above this value. Second, in the transparent region, RE-doped ZnO films have interesting ARC properties when air is the incoming medium. In addition, an upper limit for sensitized DS and DC has been established.

So far, it has been proved that RE-doped ZnO grown by sputtering forms high-quality uniform films with good ARC properties. However, most applications of ZnO films, including solar cells, require electrical conductivity of the film. High structural quality in a material whose conducting properties are based on intrinsic defects is not necessarily a good thing. The electrical properties of our ZnO films will be briefly discussed in the next section.

## 3.3 Electrical properties of ZnO:RE films

n-type intrinsic conductivity of ZnO is related to oxygen vacancies or OH groups (when ZnO is grown by solution-based approaches). However, the concentration of intrinsic defects is usually too low and extrinsic defects must be created by doping. Doping binary materials like ZnO is not as simple as doping silicon. Embedding alien atoms in the lattice often creates several compensating defects whose effects on the conduction cannot be foreseen. In the case of REs, the binding energy of 4f electrons is too large and they cannot be promoted to the conduction band by the thermal energy. Therefore, the presence of the 3+ valence state is possible only when the extra electron is shared in chemical bonding (e.g. with interstitial oxygen). However, embedding REs in ZnO might create some other defect that helps the conduction, such as oxygen vacancies. Table 3.1 reports the electrical properties of selected ZnO films measured by Hall effect at room temperature.

**Table 3.1** - Electrical properties of selected RE-doped ZnO films measured by Hall effect at room temperature. The conductivity of a good ZnO:Al sample deposited in the same sputtering chamber is reported for reference.

| Sample         | T (°C) | GFR <sup>a</sup> | Substrate | Annealed<br>(T / gas) | Carriers<br>(cm <sup>-3</sup> ) | Resistivity<br>(Ω cm) | Mobility<br>(cm <sup>2</sup> V <sup>-1</sup> s <sup>-1</sup> ) |
|----------------|--------|------------------|-----------|-----------------------|---------------------------------|-----------------------|--|
| ZnO:Yb (2 %)   | 300    | 16:4             | Glass     | -                     | $-1.4 \cdot 10^{14}$            | $4.6 \cdot 10^3$      | 10.5   |
| ZnO:Yb (0.3 %) | 15     | 16:4             | Quartz    | 700 °C / Ar           | $-5.7 \cdot 10^{20}$            | $1.4 \cdot 10^{-2}$   | 0.942  |
| ZnO:Nd (1.6 %) | 300    | 16:4             | Glass     | -                     | $-1.6 \cdot 10^{13}$            | $1.1 \cdot 10^4$      | 39.8   |
| ZnO:Nd (1.6 %) | 400    | 16:4             | Glass     | -                     | $-6.1 \cdot 10^{17}$            | 1.2                   | 8.4  |
| ZnO:Nd (1.6 %) | 15     | 16:2             | Glass     | -                     | $-1.2 \cdot 10^{20}$            | $1.4 \cdot 10^{-2}$   | 3.69   |
| ZnO:Al (2 %)   | 400    | -                | Glass     | -                     | $-7.9 \cdot 10^{20}$            | $3.6 \cdot 10^{-4}$   | 21   |

<sup>a</sup> Gas flow ratio

Most of the films (including the undoped films) were too resistive and could not be measured, but some interesting information can be obtained from the samples that could be measured. All samples proved to have n-type conductivity. In the case of Yb-doped samples, only samples deposited at high temperature were sufficiently conductive to be measured. Comparison with an Al-doped film deposited starting from an AZO target indicates that the conduction properties of Yb-doped samples are low. Only annealing at high temperature allows reaching acceptable values. Curiously, the mobility value is smaller than that of samples deposited at 300 °C. This might be because the annealed sample was deposited at room temperature. Also for Nd-doped films, only samples deposited at relatively high temperatures

present a weak conductivity, the others being too resistive. In all cases, the mobility values are correct and the small conductivity is due to a small number of carriers. This is probably due to the high crystalline quality of the layers observed above and in particular the reason behind the small number of carriers must be the oxygen-rich atmosphere in the sputtering chamber that prevents the creation of oxygen vacancies.

Table 3.1 shows that decreasing the oxygen gas flow to 2 sccm during deposition strongly increases the conductivity, so that even samples deposited at room temperature present acceptable values. Unfortunately, good intrinsic conductivity and RE insertion and activation require different deposition conditions.

In any case, it turned out that embedding trivalent REs in ZnO does not lead to the formation of electrically active defects.

#### **Concluding remarks**

The conduction properties of our ZnO layers are certainly related to the crystalline quality. More than the crystalline order, the presence of excess oxygen during growth seems to explain the high resistivity of the films. High temperatures during deposition or annealing might favor the creation of oxygen vacancies and restore a certain conduction.

In conclusion, RE-doped ZnO films present good structural and ARC properties, but the poor electrical conduction might prevent their application as TCOs. Codoping with REs and Al might be a solution, but its effect on the photon converting properties has not been investigated yet.

In the next sections, the study of the photoluminescence will show if the RE ions are optically active in the films and if the sensitized photon conversion processes are likely to occur. From the optical point of view, the high quality and the excess oxygen might be an advantage.

## **3.4 Luminescence properties of ZnO(:RE) films**

### **3.4.1 Introduction**

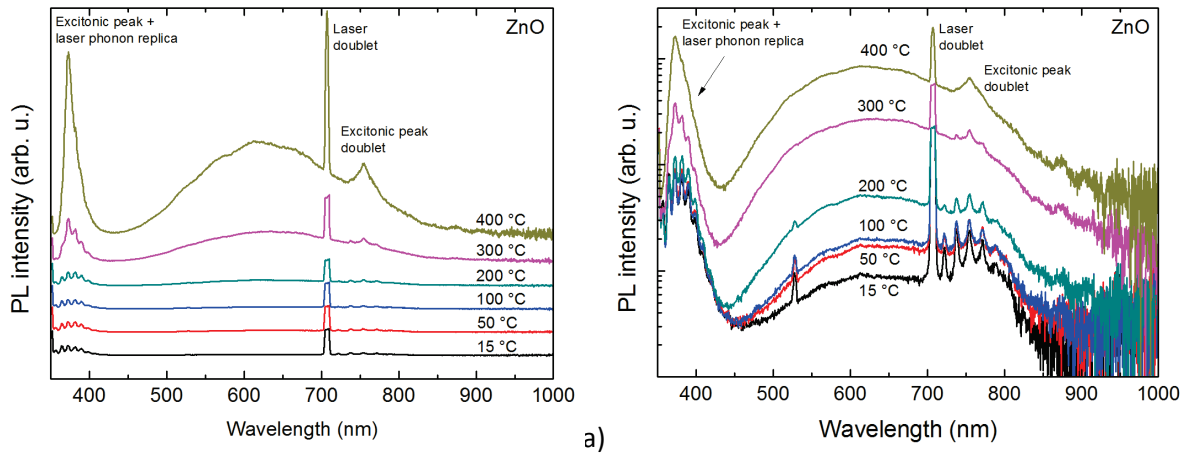
Before studying the PL properties of rare earths embedded in ZnO, it is important to study the PL properties of ZnO itself. In fact, as stated in section 1.6, ZnO already presents interesting downshifting properties via native defects.

Figure 3.22 illustrates the effect of the deposition temperature on the PL spectrum of undoped ZnO films resulting from 355 nm (Nd-YAG) laser excitation. Figure 3.22a shows that both the excitonic emission and the defect-related emission increase with the deposition temperature. This result appears to be quite contradictory. On the one hand, the increase of the excitonic peak is supported by the study of the absorption edge and can be explained by the increase of the crystalline quality shown by XRD. On the other hand, the increase of the defect-related emission seems to indicate poorer film quality. The most probable explanation, supported by the fact that the emission shape (see Figure 3.22b) does not change, is that the radiative defect population is the same for all deposition temperatures (and probably also decreases). What happens at higher deposition temperature is that the non-radiative defect population strongly decreases, thus boosting the exciton lifetime and its chances to reach radiative defects.

It can be noticed that the defect band appears like a single wide band centered at 620 nm and that no emission band appears at 500 nm (the green band associated with oxygen deficiency). This is consistent with the fact that our layers are rich in oxygen, as suggested by RBS data.

The fringes superimposed with the excitonic peak are the Raman replica of the laser beam, distanced by the longitudinal optical (LO) phonon energy in ZnO (71.6 meV). The observation of intense replica of

only LO phonon modes is typical of bulk ZnO [234] and attests the good crystalline quality of our sputtered ZnO.



**Figure 3.22** – a) PL spectra of undoped ZnO films as a function of the deposition temperature. The spectra are artificially shifted for clarity. b) The same spectra in logarithmic scale, but without artificial shift.

Figure 3.23a reports the effect of ex-situ annealing in Ar atmosphere during 10 min on the PL spectrum of undoped ZnO deposited at 400 °C under 355 nm laser excitation. Just like for high deposition temperatures, annealing at high temperature has a similar effect on the ZnO emission bands, i.e. both bands increase. The excitonic emission continuously increases with annealing temperatures up to 1000 °C, contrarily to the defect-related emission band, which increases up to 800 °C and then decreases.

Although the increase of the excitonic emission can be justified by the strong excitonic feature in the absorption edge, such a strong increase in the intensity is unusual. Indeed, the same samples studied under 325 nm (He-Cd) laser excitation generate a much weaker excitonic emission (see Figure 3.23b). Also, the intensity ordering of the bands with respect to the annealing temperature is different.

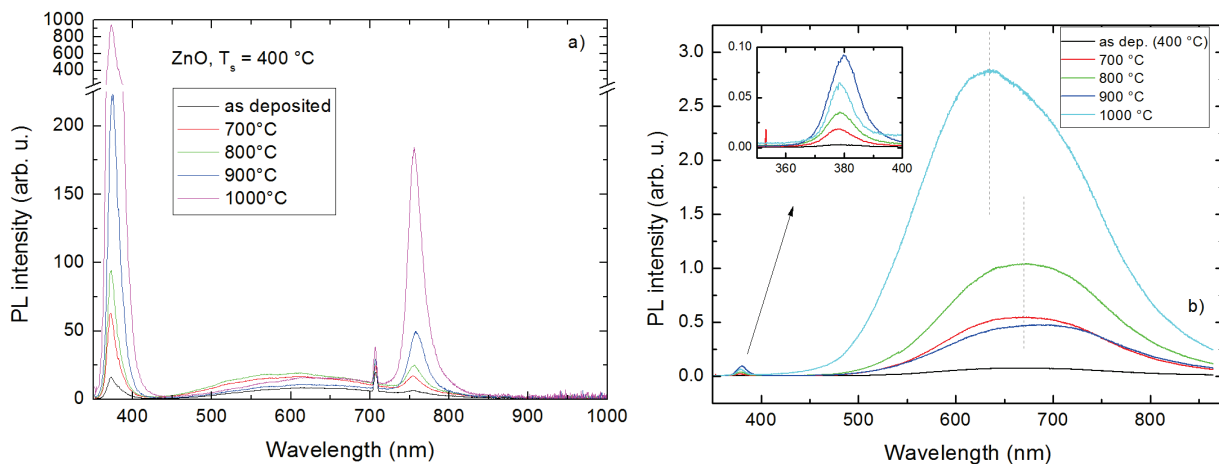


**Figure 3.23** - Effect of ex-situ annealing in Ar atmosphere during 10 min on the PL spectrum of undoped ZnO deposited at 400 °C, resulting from a) 355 nm (Nd-YAG) and b) 325 nm (He-Cd) laser excitation.

Many possible origins of these differences have been investigated. After all possible explanations due to the different experimental setup (optical blocks, excitation power, ...) have been excluded, the only explanation left seems to be the following: the 355 nm (Nd-YAG) excitation is so close to the excitonic peak, that direct excitation of excitonic states occurs, which results in anomalous excitonic emission.

Direct pumping of excitonic states also alters the defect-related recombination probability, depending on how efficiently the excitonic states are pumped.

By observing Figure 3.23b, it is interesting to notice that the defect-related band maximum is shifted towards higher energies due to annealing at 1000 °C. For the same temperature, the excitonic emission starts to decrease. The decrease of the excitonic peak might be related to the smaller absorption coefficient observed in Figure 3.17c.

This effect of anomalous excitonic emission is much weaker for lower temperatures and can be neglected in the range of the investigated deposition temperatures. Therefore, the results in Figure 3.22 are considered to be acceptable.

### 3.4.2 Yb-doped ZnO

Considering the energy levels of all lanthanides, as shown in Dieke's energy level diagram (see Figure 1.21), it is immediately evident that the energy level structure of  $\text{Yb}^{3+}$  is ideally suited for photon conversion applications in c-Si solar cells. The  $\text{Yb}^{3+}$  ion has a single excited state denoted by the term symbol  $^2F_{5/2}$  approximately 1.3 eV above the  $^2F_{7/2}$  ground state, which is just above the band gap of silicon (1.125 eV or  $9074 \text{ cm}^{-1}$ ).

The typical PL spectrum of ZnO:Yb films is shown in Figure 3.24a as a function of the deposition temperature. With respect to the emission of ZnO, a NIR infrared band appears. The reason why more than one peak are observed is the crystal field splitting of the two electron states of the  $\text{Yb}^{3+}$  ion when this is embedded in ZnO. The fact that the Yb emission is not superimposed with the emission of ZnO allows separate integration of the signals. Figure 3.24b shows the integrated PL spectra as a function of the deposition temperature and Yb concentration.

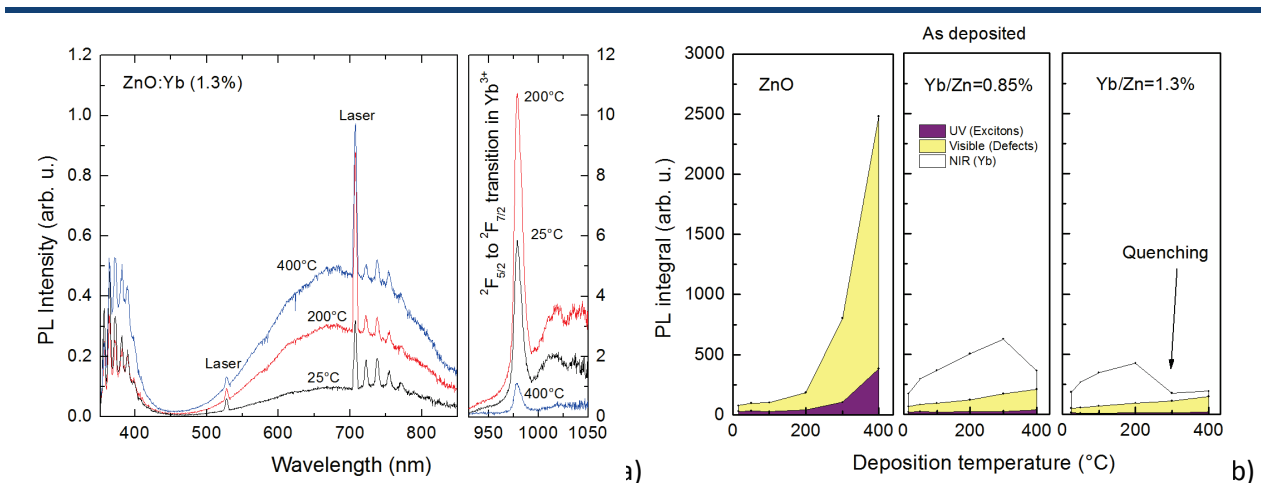


**Figure 3.24** – a) Typical emission spectrum of ZnO:Yb films deposited at different temperatures and excited by the 355 nm line of the YAG laser. b) Integrated PL spectra as a function of the deposition temperature and Yb concentration.

By observing the intensity of the different contribution to the total PL, the following picture can be drawn. Up to 200 °C, the addition of Yb to the films simply adds an intense NIR band to the spectrum of undoped ZnO. In films grown at such low temperatures, the concentration of non-radiative defects is quite high and recombination occurs at a small distance from the excitation. Thus, recombination on Yb ions is not in competition with radiative recombination on ZnO defects. At higher deposition temperatures, the distance travelled by excitons before recombining increases and the presence of Yb ions strongly reduces the intrinsic luminescence of ZnO. Unfortunately, either the radiative recombination process on Yb ions is less efficient than that on ZnO defects or the insertion of Yb creates some non-radiative defects, so that the total PL is drastically lowered. In addition, quenching of Yb

emission is observed for high deposition temperatures, especially for higher Yb concentration. This effect is not related to Yb clustering, as shown by atom probe tomography, but might be related to Yb sites that are not optically active. NEXAFS measurements showed some variations of the  $\text{Yb}^{3+}$  concentration close to the film surface, but this might not be the case deep in the film.

In order to investigate further the origin of these variations with the temperature, the films have been annealed at temperatures up to 1000 °C in Ar and  $\text{O}_2$  atmospheres. Figure 3.25a-e reports the effect of the annealing temperature and gas on the PL.

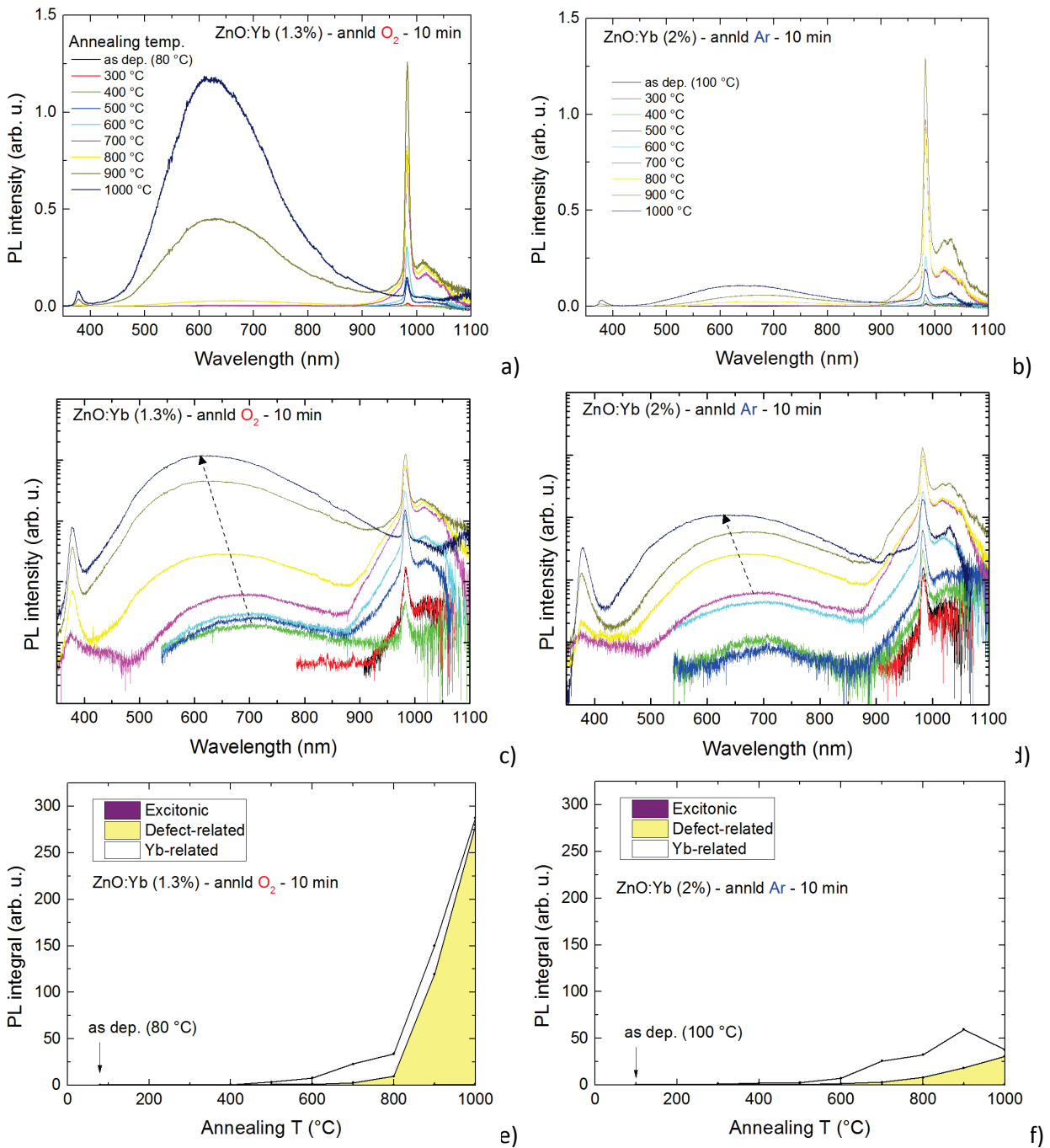


**Figure 3.25** – a-b) Effect of the annealing temperature and gas on the PL emission spectra under 325 nm He-Cd laser excitation. c-d) The same spectra in logarithmic scale. e-f) PL integral as a function of the annealing temperature and gas.

Up to 800 °C there is no substantial difference between the two annealing gases. Above this temperature, the increase in the defect-related PL is much more important using oxygen gas. It is

important to notice that the defect related band maximum shifts towards higher energies (as indicated by the dashed arrows in Figure 3.25c-d), like for undoped ZnO.

Again, 400 °C seems to induce Yb-PL quenching in some cases. The reason behind this is still unclear and the low intensity of the signals in a region where the correction factor is important due to the low CCD response prevents us from drawing any quantitative conclusion. In addition, the results of the PL emission intensity using Nd-YAG laser excitation (see Figure 3.26) are not totally compatible with those described above. For high annealing temperatures, the direct excitation of excitonic states strongly favors excitonic recombination, thus artificially decreasing the other types of contributions. Yb-related PL quenching at 400 °C is observed for both annealing gases and as deposited Yb-PL appears higher. However, the results for the two excitations seem to agree in the intermediate region (500-800 °C), where the signals are relatively strong and excitonic absorption not too intense.

Despite these discrepancies, it can be pointed out that annealing above 400 °C substantially improve both the Yb- and defect-related emissions, probably due to a strong decrease of the non-radiative defect population.

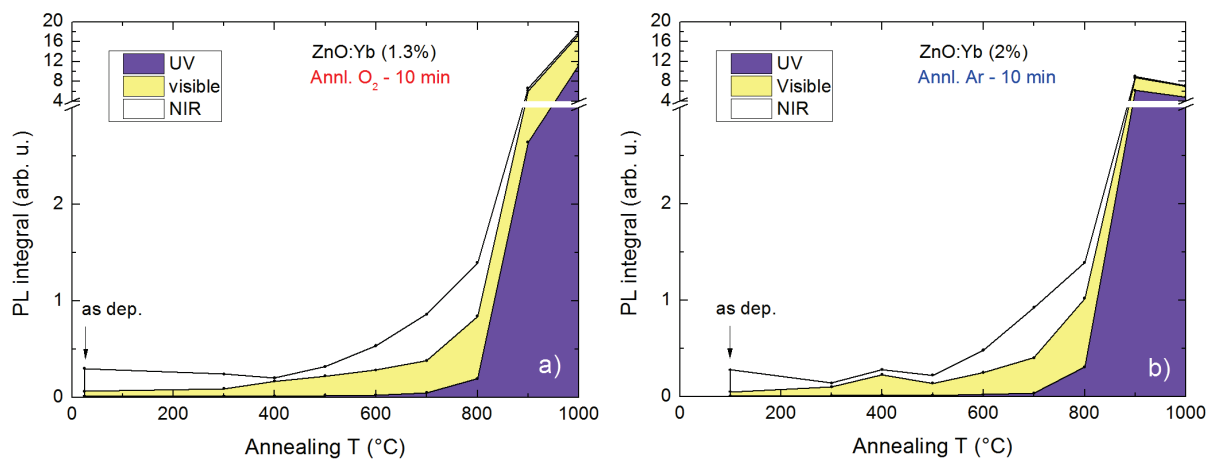


**Figure 3.26** - PL integral as a function of the annealing temperature in a) O<sub>2</sub> and b) Ar gas atmosphere measured under 355 nm Nd-YAG laser excitation.

For solar cell applications, too high temperatures cannot be used for two reasons: they increase the production cost and they degrade the solar cell. Therefore, the lowest temperature generating an intense Yb-related PL (700 °C) has been chosen for further investigation. The results of annealing at 700 °C in Ar during 10 min are presented in Figure 3.27 for films grown at different temperatures and with different Yb concentrations. The dashed curves indicate the total PL integral before annealing (see Figure 3.24b). For undoped samples, annealing at 700 °C generates a strong increase of the PL. The differences due to the deposition temperature are smoothed out, although a monotonic increase of the defect-related PL is still observed. The oscillations in the UV band will not be discussed, as the samples were excited using the Nd-YAG laser.

In the case of the doped samples, the total PL does not reach values as high as those of undoped ZnO. However, an increase of the PL compared to as-deposited samples is observed. This increase is particularly strong for the deposition temperatures that led to the worst results before annealing, so that the same samples now present the highest PL.

Both the total PL and the Yb-related PL decrease when the Yb concentration is increased above 1%. This sets an upper limit for photon converting applications of Yb-doped ZnO. XRD data provide more information about this limit. The fact that the lattice parameter increases continuously with doping from 0.3 to 2 % suggests that the amount of Yb substituting Zn ions in the host matrix increases continuously,

and therefore, the solubility limit of Yb in ZnO is not yet reached. Thus, the upper limit of the PL must have a different origin. One possibility is that there is not enough interstitial oxygen to activate more than a certain number of Yb ions.

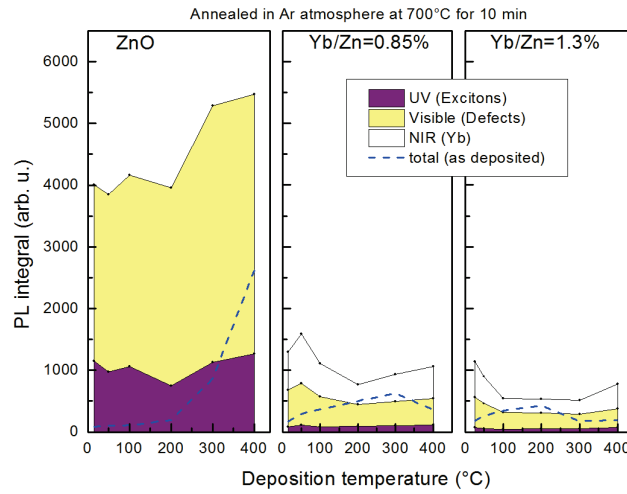


**Figure 3.27** – Effect of annealing on the PL intensity of ZnO:Yb films deposited at different temperatures and with different Yb concentrations. The dashed curves indicate the total PL integral before annealing. The samples were excited using the Nd-YAG.

Figure 3.28a represents in 2D what happens to the Yb emission when the deposition temperature and the Yb concentration are varied. Figure 3.28b presents the results after annealing. It can be seen that after annealing the best results are obtained for ZnO films deposited at low temperature and with an Yb concentration around 0.8 %. A second maximum is observed at high temperature, but the absence of experimental points in this region makes this observation more uncertain.

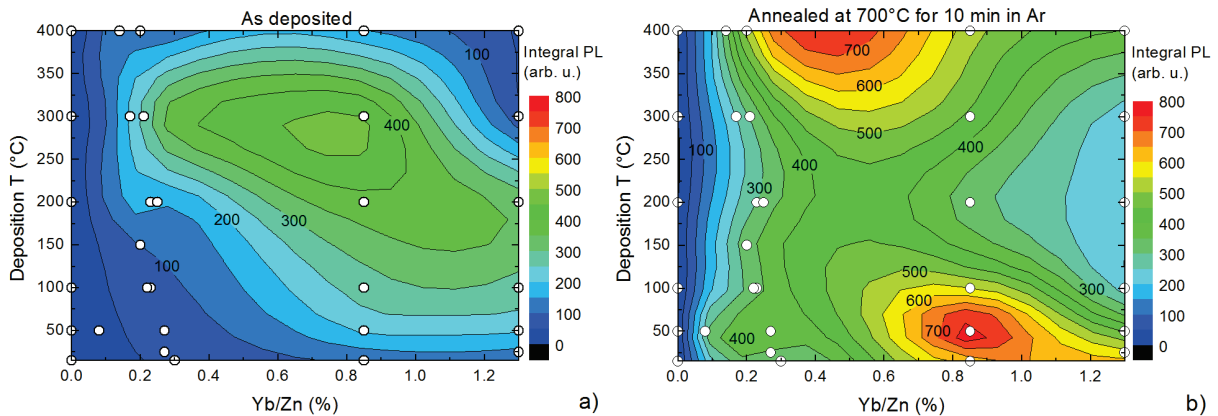


**Figure 3.28** - Integral Yb-related PL intensity as a function of the deposition temperature and Yb concentration (a) for as-deposited samples and (b) after annealing in Ar atmosphere for 10 min at 700 °C. The white dots are the experimental points.

So far, a lot has been said about how the preparation conditions change the luminescence of the film and the variations have been attributed to changes in the defect population. It has been assumed that UV excitation of ZnO produced electron-hole pairs and that these carriers would somehow transfer their energy to radiative (and non-radiative) defects. In the following, two very important points will be discussed, i.e. the transfer mechanism and the fine structure of the  $^2F_{5/2} \rightarrow ^2F_{7/2}$  transition of  $Yb^{3+}$ , due to the crystal field of ZnO.

In order to study the transfer mechanisms, excitation dependent PL has been performed on undoped and Yb-doped ZnO films. The results for films deposited at 400 °C and annealed during 10 min at 700 °C

in Ar are reported in Figure 3.29. By comparison with the ZnO absorption coefficient, it is clear that in both cases radiative recombination occurs after excitation of ZnO. The weaker excitonic feature in the PLE spectrum probably originates from the fact that thin film interference smoothes out the absorption peak, as indicated by the absorbance curve. The decrease of the PL intensity for smaller excitation wavelengths is in contrast with the increasing absorption in the film. Unfortunately, quantitative estimation of the absorption edge or of the quantum efficiency from PLE data is not possible due to the fact that only radiative recombination is detected.

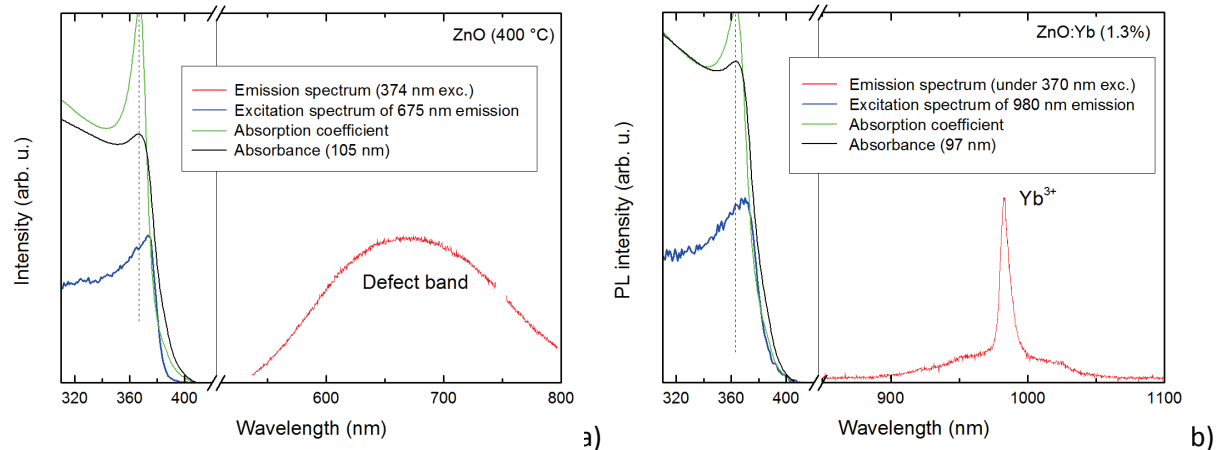


**Figure 3.29** – Excitation spectrum of the defect-related PL of an undoped ZnO film and of the Yb-related PL of a ZnO:Yb (1 %) film deposited at 400 °C and annealed at 700 °C. The absorption coefficient and the absorbance calculated using the transfer matrix method [235, 236] are reported for reference (not in scale).

Figure 3.30a illustrates the possible mechanisms leading to radiative recombination. An electron is excited to the conduction band, where it relaxes to the excitonic state (dashed horizontal line) by fast non-radiative phonon emission. Then, the exciton can recombine radiatively on a deep level trap. Since the shape of the defect band undergoes only minor changes for all investigated temperatures, the width of the band (FWHM  $\sim 0.4$  eV) must be due to several stable configurations of the same defect in ZnO (e.g. interstitial oxygen) and to the contribution of phonons.

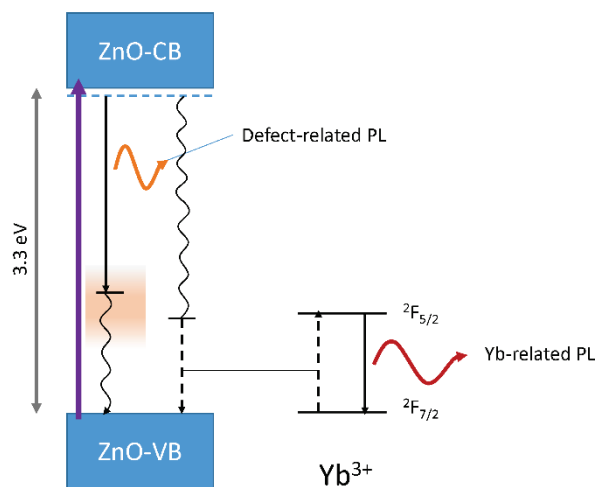


**Figure 3.30** – Possible mechanisms leading to radiative recombination after excitation of ZnO.

$\text{Yb}^{3+}$  emission following excitation of ZnO can only occur if part of the energy is transferred to the 4f electron and excites it to the  ${}^2F_{5/2}$  state. This transfer can occur via dipole-dipole interaction from a

transition which is resonant or close to resonance with the transition of  $\text{Yb}^{3+}$ . Given the high value of the gap of ZnO, this transfer can only occur via lattice defects. However, these defects must be close to the Yb lattice site because of the small range of the interaction. The observed strong Yb-related emission indicates that many Yb ions find themselves close enough to these defects. This suggests that we are probably dealing with defects associated with the presence of  $\text{Yb}^{3+}$ . In order to have a 3+ valence in ZnO, the presence of excess oxygen is necessary in the surrounding of the Yb ion. If the excess oxygen in the films concentrates around Yb ions, this might explain the observed PL quenching due to doping. This picture where the defect-related emission and the transfer to  $\text{Yb}^{3+}$  ions occurs from the same defect band is illustrated in Figure 3.30a. Due to the different lattice environment of the interstitial oxygen related to the presence of Yb, relaxation to the defect level might occur non-radiatively. However, many other transfer mechanisms are possible and the location of the ZnO intrinsic defects has not been unequivocally determined.

As stated at the beginning of this paragraph, the Yb-related emission is composed of several peaks (the strongest of which is situated at about 980 nm) due to the crystal field splitting. Figure 3.31 reports the deconvolution of the  $\text{Yb}^{3+}$  emission spectrum of a typical ZnO:Yb film at room temperature (a) and low temperature (4 K) (b). Up to ten (Gaussian) components are necessary to deconvolute the emission spectrum at room temperature and it is difficult to distinguish between fundamental electronic levels and vibronic components. On the other hand, the emission spectrum at low temperature is composed of only four peaks that can be easily identified and associated to transitions between the  $(2J+1)/2$  Stark components of the  ${}^2F_{7/2}$  multiplet<sup>23</sup>. Unfortunately, at this temperature there is no thermal energy to populate the higher states of the  ${}^2F_{5/2}$  multiplet. The emission associated to these states can be tentatively identified in the RT emission spectrum, although their position is less sure with respect to the ground state multiplet. This is due to the fact that the smooth high energy part of the emission must also contain the symmetric counterpart of the vibronic components. If peaks 6 and 8 can be easily identified as vibronic components due to their symmetric nature around peak 7, the other vibronic components do not have an intense high energy twin. Peak 9 and 10 do not correspond to any of them and were therefore ascribed to fundamental electronic transitions. The energy of the phonon modes in ZnO can help identifying these vibronic peaks. In particular, peak 1 and 4 correspond to the  $E_2^{\text{high}}$  (52 meV [237, 238]) phonon replica of peak 7 and peak 3 corresponds to the  $A_1(\text{LO})$  (71.6 meV) replica of the same peak. The fact that two vibronic components (3 and 4) are superimposed with the electronic level explains why these peaks are much more intense in the RT spectrum with respect to the first electronic level (peak 5). Peak 2 could not be attributed to any specific vibronic mode around peak 7.

If Yb is oxidized to its 3+ state by interstitial oxygen, the ion will tend to recreate the octahedral configuration of the sesquioxide. Therefore, it is interesting to compare the crystal field splitting in ZnO with that of  $\text{Yb}_2\text{O}_3$ . In the cubic phase, the Yb atoms occupy two octahedral sites; 8 atoms in positions with three-fold inversion symmetry  $C_{3i}$ , and 24 atoms in positions with two-fold symmetry  $C_2$ . Both sites have lower symmetry than that of the ideal  $C_{4v}$  site. For the  $C_{3i}$  site, two oxygen atoms are missing across the body diagonal, while for the  $C_2$  site they are missing across a face diagonal. Both sites induce a full Stark degeneracy lift of the 4f levels. Since the  $C_2$  sites are statistically prevalent (3:1), and transitions originating at these sites are forced electric dipole allowed, they should dominate the observed spectra [239].

---

<sup>23</sup> The non-vanishing signal below peak 3 is probably due to the correction related to the low CCD response in this region.

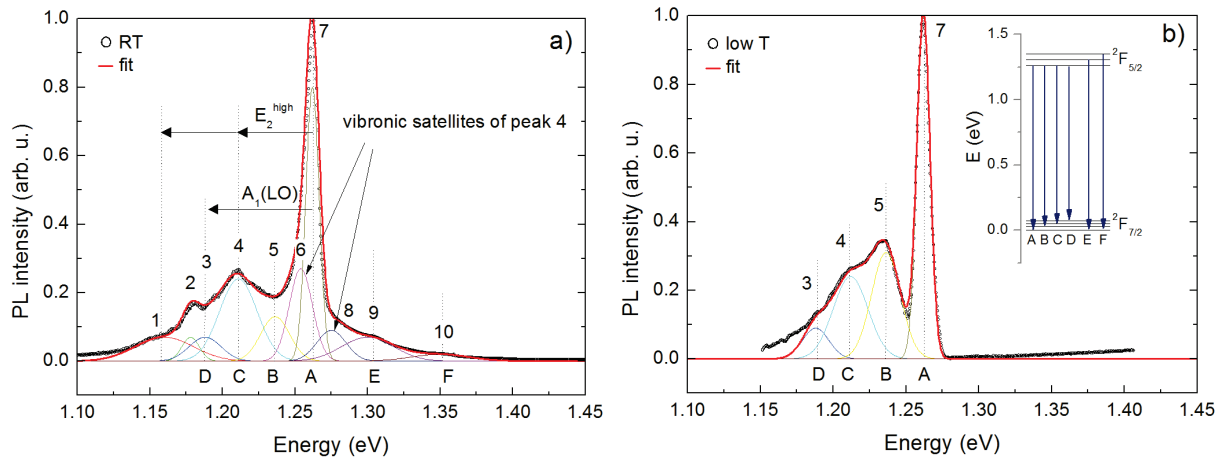


**Figure 3.31** – a) RT and b) low T emission spectrum of  $\text{Yb}^{3+}$  of a typical ZnO:Yb film, normalized with respect to the main peak. Transitions between the  $(2J+1)/2$  Stark components of the two  $\text{Yb}^{3+}$  levels are indicated in the inset.

Figure 3.32 compares the absorption spectrum of  $\text{Yb}_2\text{O}_3$  powder obtained from diffuse reflectance with the emission spectrum of a ZnO:Yb film. Temporarily neglecting how the levels have been identified, it can be seen that the position of the electronic levels is not the same. This confirms that there is no Yb oxide in the film and shows that the electronic environment is still far from that of the sesquioxide. The larger Stark splitting of the levels in the oxide indicates that the symmetry in ZnO must be higher than  $C_2$ . This means that the charge-compensating defects around the rare earth in ZnO do not strongly decrease (and might actually also increase) the  $C_{3v}$  symmetry of Zn sites.

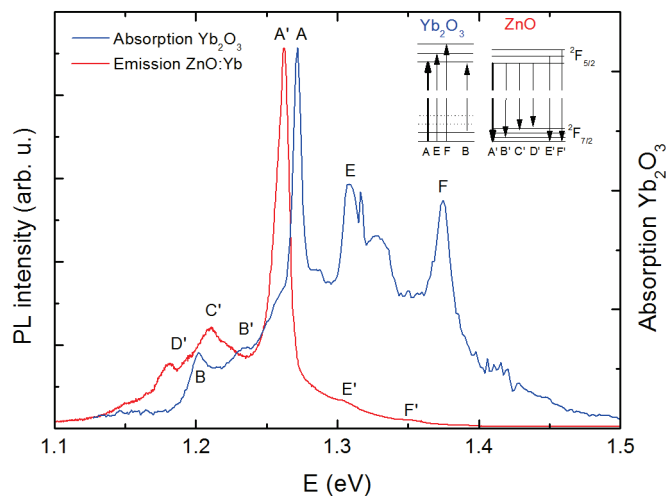


**Figure 3.32** – Absorption spectrum of  $\text{Yb}_2\text{O}_3$  calculated from the diffuse reflectance of the powder. The emission spectrum of a ZnO:Yb film is reported for reference and the electronic transitions are indicated.

Despite the relatively strong intensity of the electronic transitions, their identification among the satellite structure created by interaction with phonons can be difficult. The fact that vibronic peaks are symmetric with respect to the involved electronic level helps identification. Therefore, in Figure 3.33a the absorption spectrum has been divided into two parts centered around the main absorption peak (A), which can be easily identified as the transition between the  $^2F_{7/2}$  and the  $^2F_{5/2}$  ground states. Figure 3.33b reports the non-resonant Raman spectrum of the powder, where the principal modes have been indicated as suggested in refs. [239, 240]. These modes are also indicated in Figure 3.33a and help identifying the observed transitions.

The B transition is possible thanks to thermal population of the first excited state of the  $^2F_{7/2}$  multiplet and should normally disappear at low temperature [239]. The F transition must be an electronic transition, because there is no phonon mode at such a high energy. The E electronic transition is superimposed with a vibronic peak, but the high intensity confirms the presence of the electronic transition. The origin of the peak marked by a question mark is less sure. In their detailed discussion about the origin of this peak, Schugar *et al.* [239] seem to forget one possibility, i.e. that this peak is a vibronic peak constructed around the fundamental F peak. Given the perfect matching with the  $T_g+A_g$  phonon mode and the presence of a weak symmetric peak at 0.14 eV, this explanation might actually be the most probable.

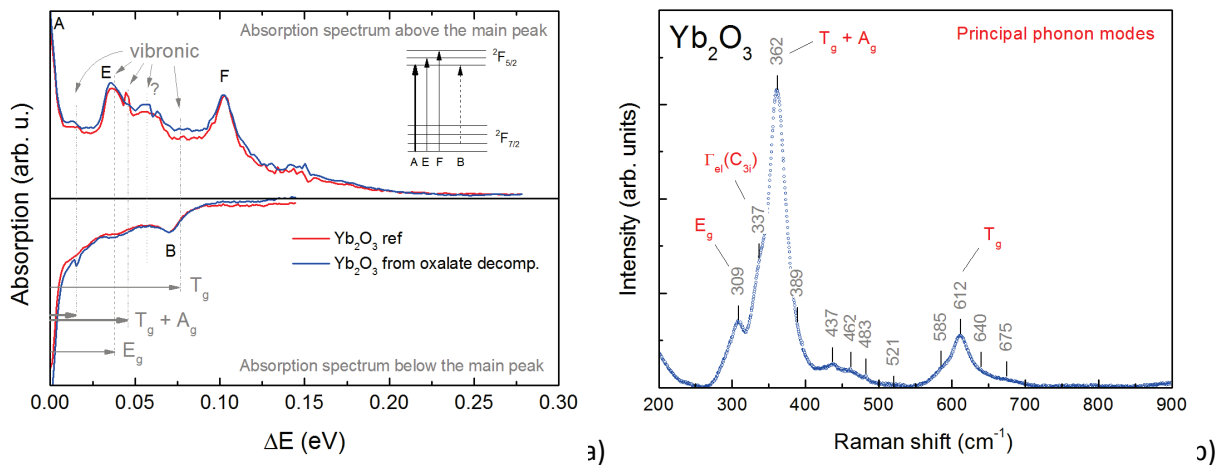


**Figure 3.33** – a) Symmetric view of the absorption spectrum of  $\text{Yb}_2\text{O}_3$  around the main peak at 975 nm. b) Raman spectrum of  $\text{Yb}_2\text{O}_3$  powder obtained using the 532 nm line of a YAG laser.

#### Concluding remarks on ZnO:Yb films

Emission from  $\text{Yb}^{3+}$  ions can be successfully induced by indirect excitation of ZnO, indicating that energy transfer occurs. The strong variations of this emission with the deposition and annealing temperature have been mainly attributed to changes in the amount of non-radiative defects. As this amount decreases, the transfer efficiency is improved.

Due to the large mismatch between the ZnO band gap and the energy distance between the two RE levels, energy transfer must occur via a certain defect level in the gap. The relatively high efficiency of this transfer and the short range of dipole energy transfer indicate that this defect must be quite abundant in the film and located close to the Yb site. The fact that Yb must attract some extra oxygen to be oxidized to its 3+ state suggests that transfer might occur via a defect related to interstitial oxygen.

In addition, even if direct excitation of  $\text{Yb}^{3+}$  ions was not possible due to the very small energy distance between the levels of the (single) excited state multiplet, the crystal field splitting of the  $\text{Yb}^{3+}$  levels in ZnO has been determined by combining RT and low T emission with Raman information. With this information, an experimental energy band diagram of  $\text{Yb}^{3+}$  in ZnO has been successfully drawn. Comparison with the Stark effect in  $\text{Yb}_2\text{O}_3$  indicates that the environment of  $\text{Yb}^{3+}$  in ZnO is different from that of  $\text{Yb}_2\text{O}_3$ . This confirms that there is no Yb oxide in the film. The larger Stark splitting of the levels in the oxide indicates that the symmetry must be higher than  $C_2$ . This means that the charge-compensating defects around the rare earth in ZnO do not strongly decrease (and might actually also increase) the  $C_{3v}$  symmetry of Zn sites.

### 3.4.3 Pr-doped ZnO

While Pr-doped crystals have already been widely investigated [241-245] and found their main application in lasers, only few reports exist on Pr-doped ZnO [165, 169, 246]. In particular, no report has been found on Pr-doped ZnO thin films. This is surprising, since the energies of the  $^3P_0$  and  $^3H_4$  excited states of  $Pr^{3+}$  are potentially well suited for DC in silicon solar cells.

This section is focused on the luminescence properties of ZnO:Pr films and the structural results have been presented in the previous section. However, some important informations like crystallites size (obtained using Scherrer's formula) and lattice parameter along the growth direction, calculated on the (002) peak, are recalled in Table 3.2 for a selected set of samples. These data are accompanied by the band gap values obtained from a Tauc plot of ellipsometric data and some quantitative analysis on the main Pr-related PL emission peak. These data will help interpret the PL emission spectra. The  $c$  parameter approaching the bulk value, the decreasing PL peak width and the band gap values decreased by the excitonic feature observed at high temperatures are clear indicators of improved crystalline order.

**Table 3.2** - Lattice parameter, crystallites size, band gap values and 630 nm peak area and width (FWHM) of selected ZnO:Pr (0.9%) samples.

| Deposition T | Annealing T / gas       | $c$ (Å)    | Cryst. size (nm) | Tauc gap (eV) | Peak area <sup>a</sup> | Peak width (meV) |
|--------------|-------------------------|------------|------------------|---------------|------------------------|------------------|
| 15 °C        | /                       | 5.2761(11) | 18.3 ± 1.3       | 3.349(5)      | 1                      | 11.6 ± 0.3       |
| 200 °C       | /                       | 5.2253(6)  | 26.8 ± 1.3       | 3.300(5)      | 1.44                   | 9.7 ± 0.3        |
| 400 °C       | /                       | 5.2065(3)  | 29.0 ± 1.3       | 3.289(5)      | 1.89                   | 8.0 ± 0.3        |
| 15 °C        | 500 °C / O <sub>2</sub> | 5.225(3)   | 18 ± 3           | 3.277(5)      | 1.76                   | 8.8 ± 0.3        |
| 15 °C        | 500 °C / Ar             | 5.217(2)   | 18 ± 3           | 3.282(5)      | 0.44                   | 8.8 ± 0.3        |

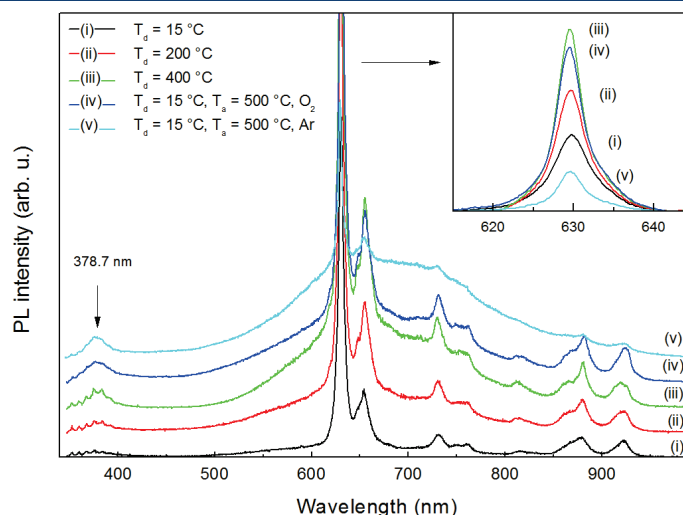
<sup>a</sup> The peak area of the sample deposited at 15°C is taken as reference.

Figure 3.34 presents the UV-to-NIR PL emission spectrum (under laser excitation at 325 nm) of the same set of samples. A small peak related to excitonic recombination is found at  $379 \pm 1$  nm ( $3.272 \pm 0.008$  eV).

The increase of the excitonic peak with the deposition temperature is consistent with the improvement of crystalline order, as indicated by the  $c$  value approaching the theoretical value of 5.2066 Å.

A comparison between the excitonic emission band center and the band gap values of Table 3.2 clearly indicates that the optical absorption is dominated by excitonic features at high deposition temperatures and after annealing.

The wide emission band between 500 and 800 nm is the usual defect-related emission band. Compared to Yb-doped ZnO, this band is more severely quenched by doping. This means that either Pr ions seize a greatest number of interstitial oxygen atoms, thus decreasing their relative emission, or that embedding Pr ions creates non-radiative defects in ZnO. An increase of the defects band and excitonic peak with the deposition and annealing temperature, i.e. with the crystalline order, is still observed, indicating that intrinsic non-radiative recombination paths are reduced.



**Figure 3.34** - Room temperature emission spectra under He-Cd 325 nm laser excitation of ZnO:Pr (0.9 %) films prepared at different deposition temperatures and after annealing. The inset provides a closer picture of the main  $\text{Pr}^{3+}$  emission peak, without the contribution of the defect band.

The narrow intense peaks superimposed to the wide visible band are attributed to radiative transitions of excited  $\text{Pr}^{3+}$  ions (precise identification of the peaks will be given further in the text). This proves the optical activation of Pr inside the ZnO matrix and the feasibility of the transfer, because no  $\text{Pr}^{3+}$  level exists that can be directly excited by the laser. A closer look on the main  $\text{Pr}^{3+}$  emission peak is provided in the inset of Figure 3.34 and the integrated area of the peak is reported in Table 3.2. It can be noticed that the area almost doubles from 15 °C to 400 °C and by annealing at 500 °C in oxygen atmosphere, but barely decreases to half of its value due to annealing in argon atmosphere. The Pr emission changes could be due to different transfer efficiency from ZnO and/or different amount of active  $\text{Pr}^{3+}$  ions. However, the interpretation of these changes is not straightforward. The good crystalline quality and the low Pr-related emission efficiency of samples annealed in Ar show that the peak intensity is not strictly related to the crystallites size and the lattice parameter. On the other hand, it is important to note that the peak width always decreases together with the stress, as indicated by the  $c$  values.

It is important to point out that the position, the number and the relative intensity of the different Pr emission lines are the same before and after annealing and independent of the deposition temperature.

In the coming paragraphs, the attention will be focused on the Pr-related emission and the luminescence of the ZnO host will be neglected. The  $\text{Pr}^{3+}$ -like emission recorded under laser excitation is that coming from indirect excitation of Pr ions. However, although the emission is that characteristic of  $\text{Pr}^{3+}$  ions, it does not mean that Pr is in its 3+ form in ZnO. In fact, two mechanisms can be at the origin of the emission. The first mechanism involves electron-hole pairs recombination in the vicinity of  $\text{Pr}^{3+}$  ions transferring part of their energy to the 4f electron. This type of recombination could be induced by the perturbation of the crystal field due to the Pr ion itself or some interstitial oxygen. In the second mechanism, a  $\text{Pr}^{4+}$  ion acts as an acceptor and is temporarily reduced to an excited state of  $\text{Pr}^{3+}$ . In this case, the excited state must be situated within the band gap. Since  $\text{Pr}^{4+}$  is detected by NEXAFS, further investigation is needed in order to understand which is the real mechanism.

In order to attempt direct excitation of Pr ions and thus have deeper insight in the transfer mechanisms, the PL spectrum was recorded as a function of the excitation wavelength before and after annealing. The excitation was varied between 350 nm (above the ZnO band gap) and 515 nm (below the expected value of the  $^1\text{H}_4 \rightarrow ^3\text{P}_0$  transition of  $\text{Pr}^{3+}$  [65]). Measurements have been performed at low temperature in order to reduce phonon-related widening of the lines and phonon-assisted non-radiative recombination. Narrow and intense absorption lines were therefore observed, corresponding to direct

excitation of  $\text{Pr}^{3+}$ . The emission mechanism based on  $\text{Pr}^{3+}$  ions is then confirmed, although some emission due to the reduction of  $\text{Pr}^{4+}$  to  $\text{Pr}^{3+}$  cannot be excluded.

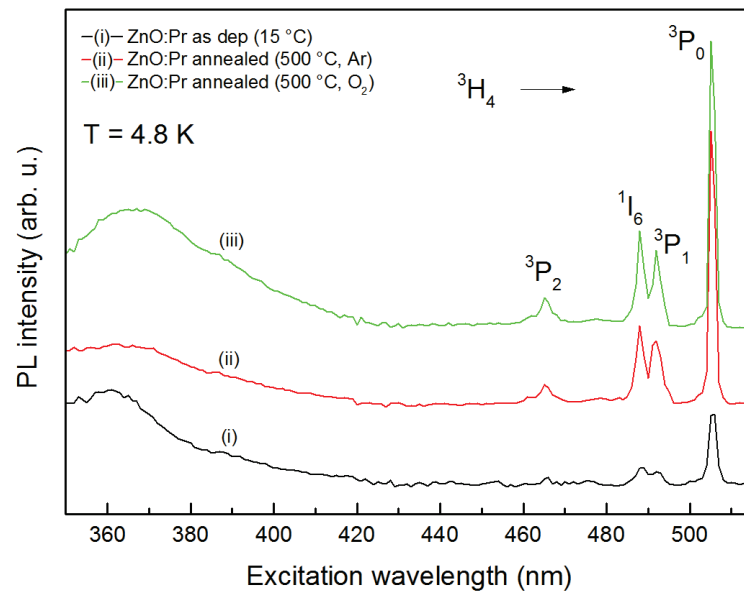


**Figure 3.35** - Low temperature excitation spectra of the main emission line of  $\text{Pr}^{3+}$  in ZnO before and after annealing. The integrated emission intensity was considered. The sample annealed in  $\text{O}_2$  is underestimated due to slightly smaller excitation power.

Figure 3.35 shows the low temperature PL excitation spectrum (PLE) of the main emission line (630 nm) before and after annealing. The other lines present exactly the same excitation spectrum and are therefore not reported.

$\text{Pr}^{3+}$  excited levels are found at 505, 492, 488 and 465 nm, identified as transitions from the fundamental state to the  $^3\text{P}_J$  multiplet and  $^1\text{I}_6$  level. Direct excitation activates the same  $\text{Pr}^{3+}$  emission lines observed in Figure 3.35 with the same relative intensity. This can be understood only by assuming that all radiative transitions take place from the  $^3\text{P}_0$  level. This conclusion is supported by the fact that direct excitation of this level generates the most intense emission. Room temperature PLE has been attempted and weak absorption from the  $^3\text{P}_0$  level has been detected at 505 nm, thus indicating that the temperature of the lattice does not modify the  $\text{Pr}^{3+}$  energy levels.

Under indirect excitation, the evolution of the emission intensity with annealing is compatible with the results reported in Figure 3.34. On the other hand, the emission under direct excitation improves for both annealing atmospheres. This means that the reason behind the weak emission of samples annealed in Ar under indirect excitation must be ascribed to weaker transfer and not to fewer active sites. The fact that an oxygen-rich atmosphere is necessary for high transfer efficiencies suggests that the transfer might be due to some oxygen-related defects in ZnO.

The smooth increase of the  $\text{Pr}^{3+}$  emission intensity at the ZnO absorption edge might appear in contrast with the steep absorption of a direct semiconductor like ZnO, especially at low T. A possible explanation could be that weak absorption due to band tail states and exciton creation is compensated by higher transfer efficiency to  $\text{Pr}^{3+}$  ions compared to excitation of free electrons with high k value. Again, quantitative estimation of the absorption edge or of the quantum efficiency from PLE data is not possible due to the fact that only radiative recombination is detected. In Figure 3.36, the low temperature emission spectrum under direct excitation is compared with that under indirect excitation at low T (curves ii) and RT (curve iii) for the sample annealed in  $\text{O}_2$ . The purpose is to tentatively identify the  $\text{Pr}^{3+}$  levels at the origin of the emission lines. Transitions from the  $^3\text{P}_0$  excited level to the  $^1\text{G}_4$ ,  $^3\text{F}_4$ ,  $^3\text{F}_3$ ,

$^3F_2$ ,  $^3H_6$  underlying levels and to the fundamental state  $^1H_4$  could be easily identified. Contrarily to all other emission lines, the  $^3P_0 \rightarrow ^1H_4$  emission line is only visible at low temperature. This suggests that the  $^3H_4$  level could be very close to the valence band of ZnO, as predicted by Dorenbos and van der Kolk [105]. At high temperatures, the extension of the band tail states might create a competitive recombination path.

No emission line could be attributed to the  $^3P_0 \rightarrow ^3H_5$  transition or to the emission from the  $^1D_2$  intermediate level. Two small emission peaks (situated at 1.53 and 1.61 eV and labeled by \*), together with one of the peaks in the  $^1G_4$  multiplet, could not be identified. The peak at 1.53 eV is visible on all samples, but only at RT, while that at 1.61 eV is only visible at low T.

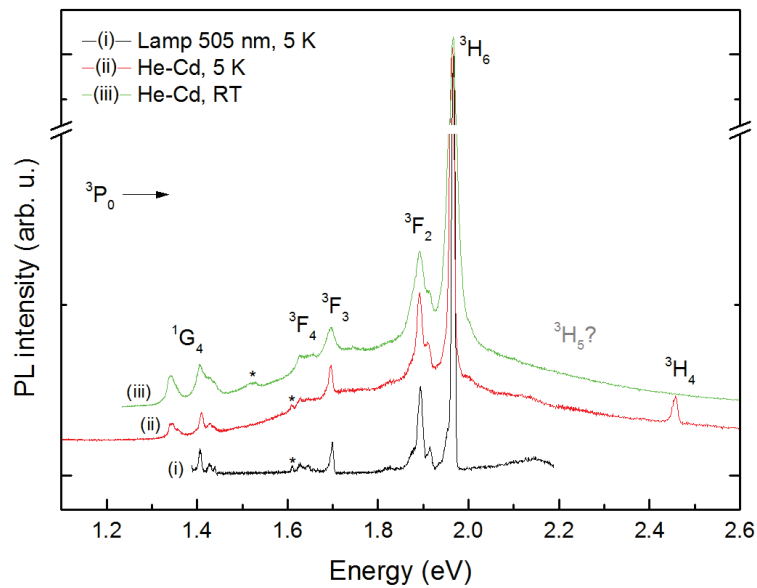


**Figure 3.36** - PL spectra of ZnO:Pr (0.9%) sample under direct and indirect excitation at low T and RT. The spectra are normalized with respect to the intensity of the 630 nm emission line.

The degeneracy of each level is  $2J+1$  and can be totally or partially lifted by an electric field (Stark effect) such as the crystal field of the host material. The lift can be total only if  $J$  is integer and the symmetry of the environment very low. It can be noted from Figure 3.36 that each level is indeed composed of a group of emission lines. Since the  $^3P_0$  level is non-degenerate, the number of lines in each group at low T must correspond to the number of the  $2J+1$  levels of the destination level for which the degeneracy is removed and for which the radiative transition probability from the  $^3P_0$  level is non-negligible.

The large Stark splitting of some levels indicates that the crystal field is quite strong and the symmetry quite low. This can be understood if we keep in mind the large ionic radius of the rare earth compared to that of Zn. In fact, doping ZnO with  $Pr^{3+}$  means that the large  $Pr^{3+}$  ions, with an effective ionic radius (Pauling) of 99 pm in octahedral coordination [217] such as in  $Pr_2O_3$ , should enter the tetrahedral sites of  $Zn^{2+}$  (60 pm [217]) in ZnO. Besides the large splitting of the levels, the ionic radius difference could also induce oxidation to the  $Pr^{4+}$  state, which has a radius of 85 pm in octahedral coordination [217].

Due to the small distance between the levels in the crystal field of ZnO, radiative transitions from the  $^3P_{1,2}$  and  $^1I_6$  levels to lower levels are encompassed by non-radiative phonon-related transitions. For this reason, it is not possible to construct a complete energy diagram from the emission spectrum alone. The information contained in the excitation spectrum of Figure 3.35 is essential to draw a more complete energy level diagram.

Figure 3.36 also provide key information on the transfer mechanism. Due to a different crystal field,  $\text{Pr}^{3+}$  and a temporarily reduced  $\text{Pr}^{4+}$  must have slightly different energy levels. The fact that the emission spectrum is the same under direct and indirect excitation proves that energy transfer from ZnO to  $\text{Pr}^{3+}$  is the dominant emission mechanism. In addition, if the fundamental state of  $\text{Pr}^{3+}$  is just above the valence band as suggested above, the electron trapped by  $\text{Pr}^{4+}$  is more likely to fall to the fundamental state of  $\text{Pr}^{3+}$ , where it recombines with a hole from the valence band.

Coming back to the purpose of Pr-doping of ZnO, i.e. to obtain DC, it turns out that none of the two transitions interesting for DC on silicon solar cells presents an intense emission line. This means that the crystal field of ZnO does not provide a good term mixing to effectively break the selection rules for these transitions. One possible solution is to combine Pr with a second RE having levels that are in resonance with two  $\text{Pr}^{3+}$  transitions and potentially lead to DC through a cooperative process. With reference to Dieke's diagram,  $\text{Yb}^{3+}$  is one of the best candidates and many research groups devoted much effort to the study of the Yb-Pr couple [186, 247-250]. Motivated by the interesting results obtained in ceramic glasses and other materials, co-doping with Pr and Yb has been tested in ZnO films.

Figure 3.37a illustrates the possible energy transfer mechanism from ZnO to  $\text{Pr}^{3+}$  and the cooperative DC process between Yb and Pr. Unlike the case of charge transfer, in the case of energy transfer the alignment of the levels with the bands of the host is uninteresting. The fundamental states of  $\text{Pr}^{3+}$  and  $\text{Yb}^{3+}$  have been arbitrarily aligned to the top of the valence band. If the calculations performed by Dorenbos and van der Kolk are correct [105], this might be the effective situation for  $\text{Pr}^{3+}$ . The orange arrow indicates the radiative emission observed from ZnO defects and attributed to interstitial oxygen.

Since transitions from the  $^3\text{P}_0$  levels are observed using indirect excitation, the energy transfer must excite electrons beyond this level. The position in the gap of defect levels due to interstitial oxygen is not compatible with the transfer to or above the  $^3\text{P}_0$  level. The mechanism suggested in Figure 3.37a involves the presence of an oxygen vacancy defect (usually leading to green luminescence) close to the  $\text{Pr}^{3+}$  ion, from which energy transfer occurs thanks to the resonance with the  $^3\text{P}_j$  multiplets. This kind of defect was not observed in undoped and Yb-doped ZnO films, but it might be created to stabilize the insertion of Pr.

Figure 3.37b presents for the first time the 4f states energy level diagram of  $\text{Yb}^{3+}$  and  $\text{Pr}^{3+}$  ions in ZnO. The energy levels of  $\text{Pr}^{3+}$  and  $\text{Yb}^{3+}$  in  $\text{LaCl}_3$  [65] are reported for comparison.

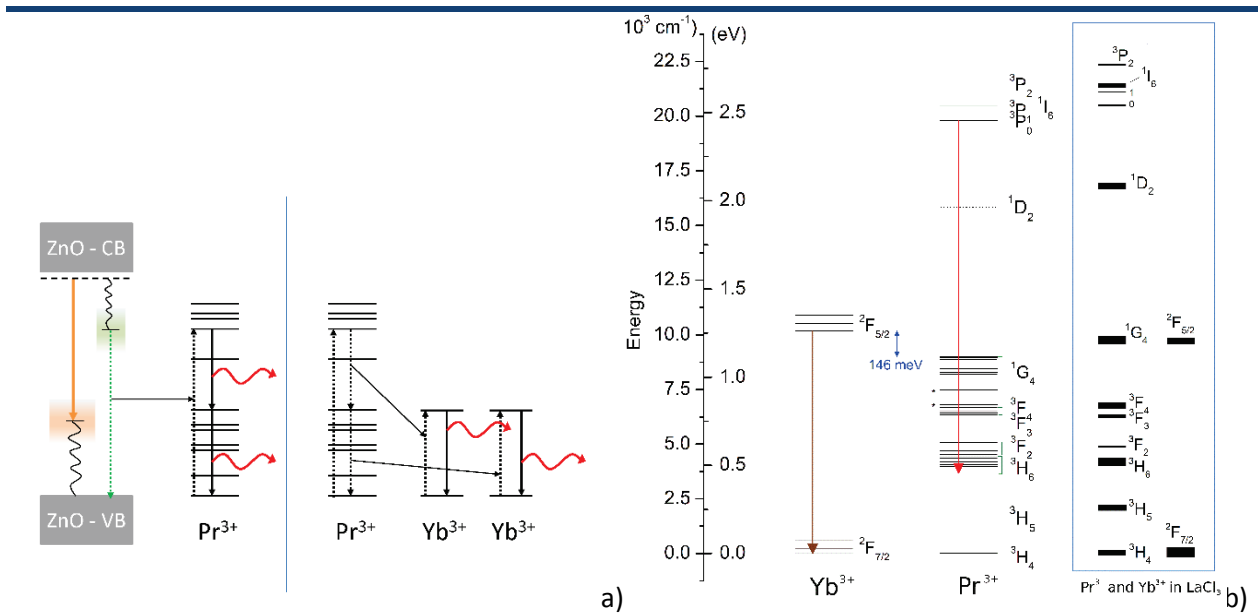


**Figure 3.37** – a) Possible energy transfer mechanism from ZnO to  $\text{Pr}^{3+}$  and the cooperative DC process between Yb and Pr. b) Energy level diagram of  $\text{Pr}^{3+}$  and  $\text{Yb}^{3+}$  in ZnO. The width of the levels does not correspond to the experimental line width or intensity. The brackets group the lines attributed to a specific level and the arrows indicate the principal emission line. The energy levels of the ions in  $\text{LaCl}_3$  are reported for comparison. The thickness of each level represents the total crystal field splitting in  $\text{LaCl}_3$ .

If the luminescent ions occupy substitutional position, then the energy diagram of Figure 3.37b is that of  $\text{Yb}^{3+}$  and  $\text{Pr}^{3+}$  in the tetrahedral  $\text{Zn}^{2+}$  site of ZnO, probably modified by charge compensating defects. Depending on the type of energy transfer (exchange, radiative, ...), the distance between the ions can be an important parameter. The low rare earth concentration, in particular that of Yb that should be twice that of Pr for good DC properties, might therefore contribute to decrease the DC efficiency.

In cooperative transfer, resonance between transitions is also important, although phonon-assisted non-resonant transfer may occur. Figure 3.37b clearly shows the poor resonance conditions between the  ${}^2\text{F}_{7/2} \rightarrow {}^2\text{F}_{5/2}$  transition in  $\text{Yb}^{3+}$  and the  ${}^3\text{P}_0 \rightarrow {}^1\text{G}_4$ ,  ${}^1\text{G}_4 \rightarrow {}^1\text{H}_4$  transitions in  $\text{Pr}^{3+}$ .

It turns out that in ZnO, 146 meV separate the  ${}^2\text{F}_{5/2} \rightarrow {}^2\text{F}_{7/2}$  transition from the  ${}^1\text{G}_4 \rightarrow {}^3\text{H}_4$  transition (corresponding to approximately two times the optical phonon energy of 72 meV) and phonon-assisted energy transfer may occur. At the same time, the energy of only one phonon separates the Yb transition from the upper  ${}^3\text{P}_0 \rightarrow {}^1\text{G}_4$  transition. However, the probability of these two multi-step processes should be rather low.

To test the cooperative down-converting properties of the Yb-Pr couple, direct laser excitation of the  ${}^3\text{P}_0$  level of  $\text{Pr}^{3+}$  was used on ZnO:Yb,Pr films at room temperature. Figure 3.38a reports the NIR emission spectrum of a ZnO:Pr,Yb film under 505 nm laser excitation delivered by a tunable laser. As expected, intense emission from  $\text{Pr}^{3+}$  ions has been detected. However, a small emission peak appears at 980 nm, where Yb emission is expected. A comparison with the emission of a ZnO film doped only with Yb shows that this peak must arise from the excitation of some ZnO defect or by a two-photon absorption process in ZnO. This means that either there is no transfer to  $\text{Yb}^{3+}$  or the non-resonant transfer efficiency is very low. An alternative explanation could be that Yb is not optically active in presence of Pr. This hypothesis is ruled out by the fact that Yb emission similar to that previously reported is detected following indirect excitation of the host (see Figure 3.38b).

If on the one hand the efficiency of phonon-assisted transfer is low, on the other hand multi-phonon relaxation might explain why some transitions between  $\text{Pr}^{3+}$  energy levels are suppressed. As a rule of

thumb, transitions as large as five times the phonon energy can be bridged by multi-phonon relaxation. This can explain why the highest excited levels,  $^3P_1$ ,  $^1I_6$  and  $^3P_2$ , do not radiatively relax to some lower-lying level state when directly excited, but rather relax to the  $^3P_0$  that can further radiatively emit. This can also explain the absence of emission related to the  $^1G_4 \rightarrow ^3H_4$  transition.

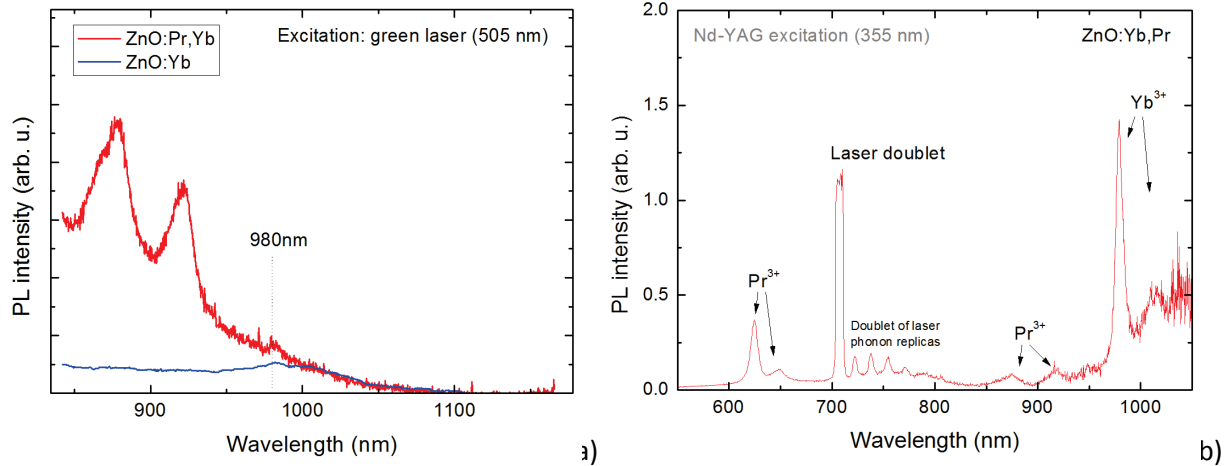


**Figure 3.38** – a) NIR emission spectra of ZnO:Pr,Yb and ZnO:Yb films under 505 nm laser excitation. b) Visible and NIR emission spectrum of a ZnO:Pr:Yb film excited by the 355 nm line of a YAG laser.

#### Concluding remarks on ZnO:Pr films

Luminescent transitions of Pr<sup>3+</sup> ions could be excited directly and indirectly through the ZnO matrix, indicating the optical activation of the RE and the feasibility of the energy transfer. For ZnO:Pr films, indirect excitation is expected to be more favorable due to the wide absorption cross section of ZnO and low concentration of Pr. However, the emission intensity under direct excitation is higher, suggesting that the transfer efficiency is low. This result is supported by the fact that the PL signals are typically lower than those recorded for Yb-doped and undoped ZnO films.

Moreover, the weak emission intensity of the  $^3P_0 \rightarrow ^1G_4$  transition and the absence of the  $^1G_4 \rightarrow ^3H_0$  transition indicate that the DC efficiency of ZnO:Pr<sup>3+</sup> films is low. Finally, co-doping with Yb, which could potentially lead to cooperative DC, did not provide better results due to the low resonance between the energy levels induced by the crystal field of ZnO.

However, by combining the information obtained from the study of the PL and PLE spectra, an almost complete energy level diagram of Pr<sup>3+</sup> ions in the ZnO crystal field has been drawn.

#### 3.4.4 Nd-doped ZnO

As stated in the introductory section, three kind of optical losses affect single junction solar cells, namely thermalization, transparency, and low blue response. In the frame of photon management, the three processes available are down-shifting (DS), down-conversion (DC) and up-conversion (UC). The specific loss can be targeted by choosing the appropriate host and RE.

Doping ZnO with Nd ions is particularly interesting due to the rich level structure of Nd<sup>3+</sup>, which is potentially suited for recovering all three optical losses. Although some work exists on Nd-doped ZnO thin films [177, 180, 251, 252], no extensive investigation of the luminescence properties has been performed yet.

Table 3.3 recalls the lattice parameter and crystallites size values for ZnO:Nd thin films deposited in different conditions. The structural investigations have shown that the crystalline quality improves at

high deposition temperatures, leading to larger crystallites and decreasing the compressive stress in the film.

At the same time, the gas flow ratio used during deposition strongly affects the Nd insertion in the film and the lattice structural properties. In particular, by increasing the oxygen gas flow from 2 to 5, an abrupt change in the crystal properties is observed. This change is probably related to the higher Nd concentration obtained with higher oxygen flows, which leads to smaller grains and higher compressive stress created by the large Nd ions.

These structural values will be particularly useful for the interpretation of the PL data.

**Table 3.3** - Lattice parameter and crystallites size for ZnO:Nd thin films deposited at different temperatures with an Ar/O<sub>2</sub> gas flow ratio of 16:4 and deposited at 15 °C but with different gas flow ratios.

| T (°C)<br>(Ar:O <sub>2</sub> = 16:4) | Cryst. size<br>(nm) | c (Å)           | Ar:O <sub>2</sub> ratio<br>(T = 15 °C) | Cryst. size<br>(nm) | c (Å)           |
|--------------------------------------|---------------------|-----------------|--|---------------------|-----------------|
| 15                                   | 17.5 ± 1.9          | 5.3002 ± 0.0015 | 16:5                                   | 16.7 ± 1.7          | 5.3232 ± 0.0015 |
| 100                                  | 20.0 ± 1.5          | 5.2590 ± 0.0009 | 16:4                                   | 17.5 ± 1.9          | 5.3002 ± 0.0015 |
| 200                                  | 25.2 ± 1.4          | 5.2436 ± 0.0006 | 16:3                                   | 22 ± 3              | 5.2248 ± 0.0014 |
| 300                                  | 27.6 ± 1.1          | 5.2154 ± 0.0003 | 16:2                                   | 25 ± 4              | 5.2331 ± 0.0014 |
| 400                                  | 26.4 ± 1.0          | 5.1968 ± 0.0004 |  |                     |                 |
| 500                                  | 27.3 ± 1.7          | 5.1838 ± 0.0006 |  |                     |                 |

In the previous sections, very few results have been reported regarding the different gas flows. This decision was motivated by the strong variation of the rare earth concentration and of the growth rate, which complicate the possibility of a coherent study of the film properties as a function of a different deposition parameter. In addition, the plasma instabilities at very low oxygen flows limit the range of available gas flow ratios. Nonetheless, the abrupt change in the structural parameters observed between the gas flows 16:3 and 16:4 matches some key differences in the PL spectra and might help interpreting the rich emission pattern observed. Figure 3.39 reports the main NIR emission band under 325 nm He-Cd laser excitation of ZnO:Nd films deposited using the two above-mentioned gas flows.

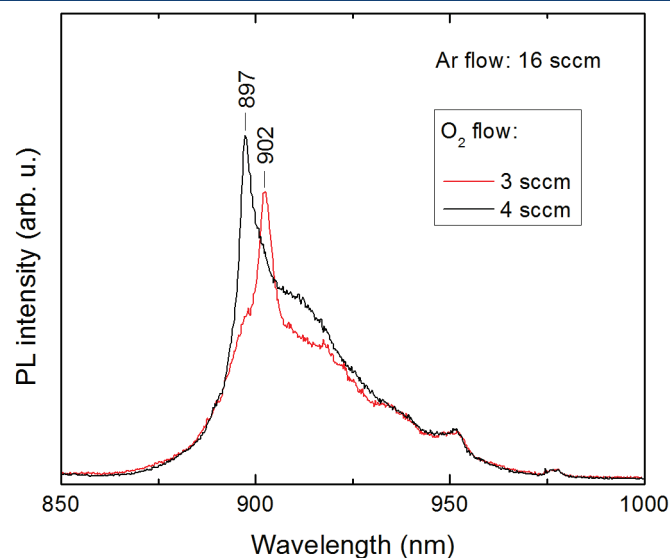


**Figure 3.39** – Main NIR emission band under 325 nm He-Cd laser excitation of ZnO:Nd films deposited using an Ar/O<sub>2</sub> gas flows of 16:3 and 16:4.

This band is composed of several peaks that will be discussed with more details below in the text, but it is interesting to notice that most intense peak switches from that at 902 nm to that at 897 nm in

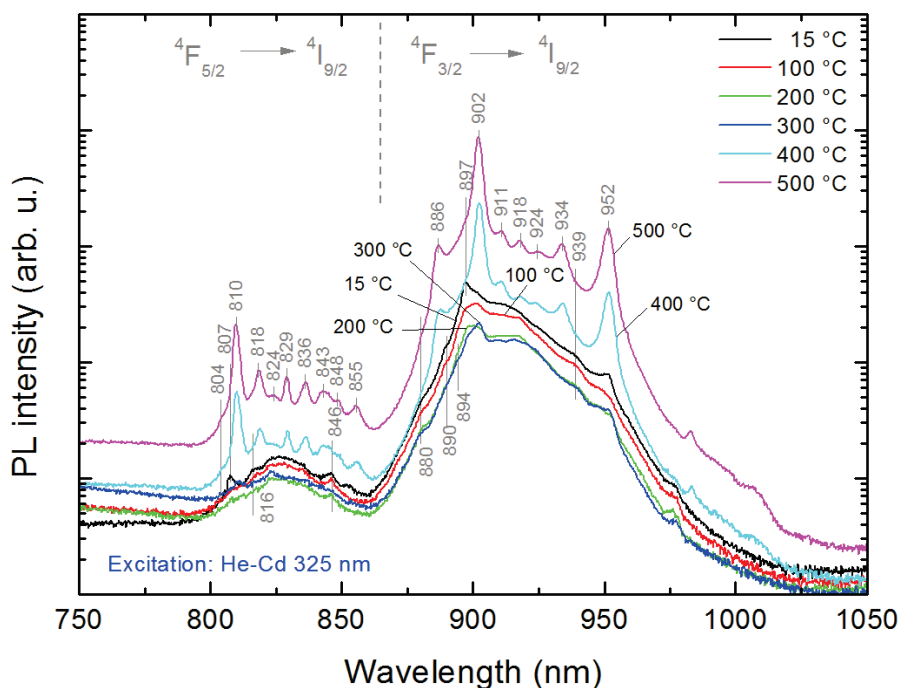
correspondence with the change in the structural parameters. This suggests that two slightly different lattice sites for Nd in ZnO exist with similar emission efficiency under indirect excitation. Since the Zn lattice sites are all equivalent in the wurtzite crystal, the matrix must be non-stoichiometric around the Nd ions. This is compatible with the existence of charge-compensating defects due to the higher valence of the rare earth.

Figure 3.39 also shows that the intensity of the two bands under indirect excitation of the host is approximately the same, despite the very different Nd content. This can be interpreted as an experimental evidence that efficient transfer from ZnO occurs only toward a small fraction of Nd ions, especially those associated with a particular configuration of charge-compensating defects.

The effect of the deposition temperature on the Nd-related PL is even more impressive. Figure 3.40 shows the near infra-red (NIR) emission spectra under 325 nm laser excitation of ZnO:Nd (1.6%) thin films deposited at different deposition temperatures. The main group of emission lines is the group reported above and is centered at 920 nm. This group is usually attributed to the  ${}^4F_{3/2} \rightarrow {}^4I_{9/2}$  transitions of  $Nd^{3+}$  [253, 254]. A second, less intense group appears around 820 nm and can be attributed to the  ${}^4F_{5/2} \rightarrow {}^4I_{9/2}$  transitions. No emission related to  $Nd^{3+}$  has been detected below 700 nm. One explanation could be that energy transfer from ZnO only excites the lowest levels of  $Nd^{3+}$ . Alternatively, given the large number of excited states above the  ${}^4F_{3/2}$  level and the quite large phonon energy of ZnO, non-radiative relaxation processes might occur when the electron is excited to higher states. These spectra, recorded by the CCD camera, cover the spectral range useful for solar cell applications. However, lower infrared emission of ZnO:Nd thin films could be useful for other optoelectronic devices. A more extended range will be studied further in the text.

It is interesting to note in Figure 3.40 that the shape and intensity of the emission spectra do not present major changes up to a deposition temperature of 300 °C (except for a slight decrease of the intensity). At 400 °C, the overall emission increases and some of the peaks become particularly strong. A similar pattern has been obtained by Liu *et al.* [254] for Nd-doped ZnO nanocrystals annealed at 400 °C. Although not all the individual peaks are well defined, it is clear that these bands contain more than the five peaks expected for the crystal field splitting of the  ${}^4I_{9/2}$  level. Liu *et al.* [254] attributed the rich pattern to several active sites for  $Nd^{3+}$  in the ZnO lattice. New evidence presented in this work allows deeper insight in the different active sites. For this reason, the approximate position of the peaks that could be distinguished is also indicated in Figure 3.40.

First of all, a closer look to Figure 3.40 shows that practically all the peaks that become so intense at 400 °C are already there for lower temperatures, but very small. This means that several active sites exist even at low deposition temperatures and that either high temperatures promote the creation of a particular site or that the energy transfer to this site is improved.



**Figure 3.40** – NIR PL emission spectra of ZnO:Nd thin films deposited at different temperatures. Two bands associated to radiative transitions between the  ${}^4F_{5/2}$  and  ${}^4F_{3/2}$  excited states to the  ${}^4I_{9/2}$  fundamental state multiplet can be distinguished. The approximate position of the individual lines is also indicated.

This abrupt change in the PL cannot be ascribed to a change in the structural properties, given the smooth variations of the lattice parameter and crystallites size with the deposition temperature. On the other hand, the fact that the most intense of the “new” peaks is situated at 902 nm, exactly where the main emission peak was observed when less oxygen was introduced in the chamber, might not be a coincidence. Higher temperatures might supply enough energy so that Nd ions can attract some extra oxygen from neighboring lattice sites, thus leaving the host poorer in oxygen, a situation that is similar to that created by a smaller oxygen flow. For some reason, the transfer efficiency for this second type of Nd sites must be higher. This might be related to the position in the ZnO band gap of defects related to oxygen vacancies.

Additional information can be obtained by studying the excitation spectrum of the PL emission, *i.e.* by looking at the evolution of the PL emission intensity when the excitation wavelength is varied.

Wide range (300-800 nm) PL excitation spectra (PLE) of ZnO:Nd emission have been recorded at room temperature. For simplicity, only the PLE of selected emission lines is reported. The PLE of the most intense emission peak, situated at 902 nm, is reported in Figure 3.41 for three deposition temperatures. The smooth excitation spectrum below 400 nm follows the typical absorption edge of ZnO and gives an experimental proof that energy transfer occurs from the host to Nd ions.

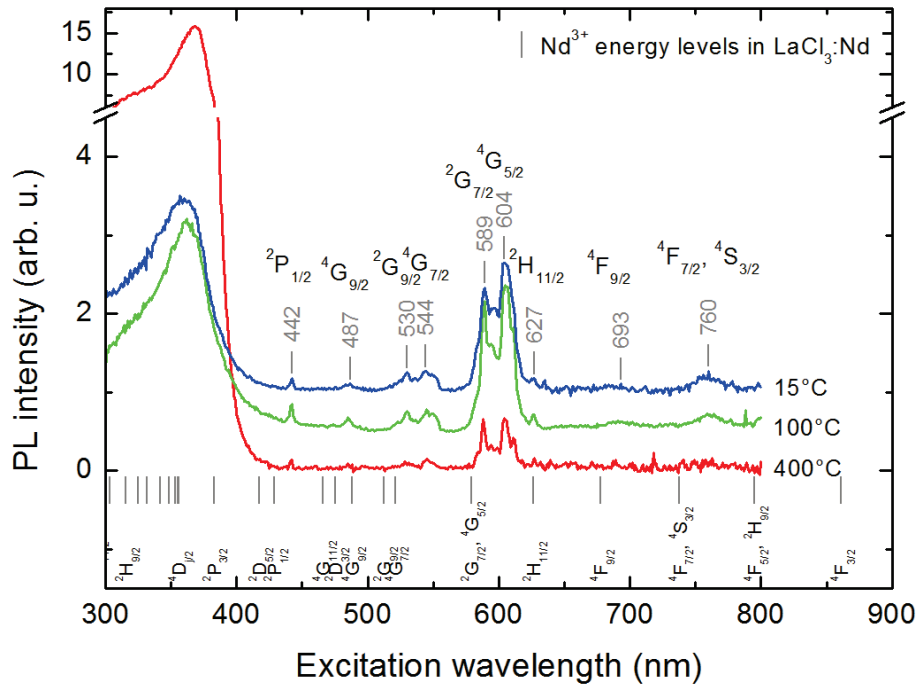


**Figure 3.41** - Room temperature PL excitation spectra of the 902 nm emission line of ZnO:Nd thin films deposited at different temperatures. The electronic level configuration of Nd<sup>3+</sup> in LaCl<sub>3</sub>:Nd crystals is reported for comparison [65].

This means that excitons and electrons, while recombining across the gap or through some lattice defect in the neighborhood of Nd ions, can transfer some energy to 4*f* electrons of Nd<sup>3+</sup>, which are then promoted to an excited state. In this case, the highest accessible excited state of Nd<sup>3+</sup> is limited by the band gap value or the amplitude of the defect-related transition.

Figure 3.41 also shows that Nd<sup>3+</sup> emission can be obtained even by using excitation energies below the band gap value of ZnO (*i.e.* above 400 nm). In this case, the excitation is distributed in several relatively narrow peaks centered at 442, 487, 530, 544, 589, 604, 627, 693 and 760 nm. A comparison with the electronic level configuration of Nd<sup>3+</sup> in LaCl<sub>3</sub>:Nd crystals indicates that these peaks correspond to direct excitation of Nd<sup>3+</sup>. It is interesting to note that almost all levels of Nd<sup>3+</sup> in ZnO are red-shifted with respect to those in LaCl<sub>3</sub> and present a stronger Stark-splitting, evidencing the strong crystal field experienced by Nd<sup>3+</sup> in the ZnO lattice in agreement with what previously reported in the last sections in Yb- and Pr-doped ZnO. The peak position is very close to that of Nd<sup>3+</sup> in ZnO nanocrystals [254].

No RE absorption level is observed above the ZnO band gap because of the strong absorption cross section of ZnO that absorbs most of the light and decreases the intensity available for RE excitation.

The spectra of Figure 3.41 show that energy transfer from the host is efficient enough for the emission to be higher than that resulting from direct excitation. Moreover, the wide absorption region of ZnO increases the advantage of indirect excitation. It is however difficult to quantify the real efficiency of this process.

Compared to the samples prepared at lower temperatures, the excitation efficiency of the sample deposited at 400 °C appears to be different. In particular, for this sample, the emission intensity is higher under indirect excitation and lower under direct excitation.

Figure 3.42 illustrates more clearly what happens on the whole  $4F_{3/2} \rightarrow 4I_{9/2}$  emission band. Here, the emission of a sample deposited at 100 °C is compared with that of the sample deposited at 400 °C in the case of direct and indirect excitation.

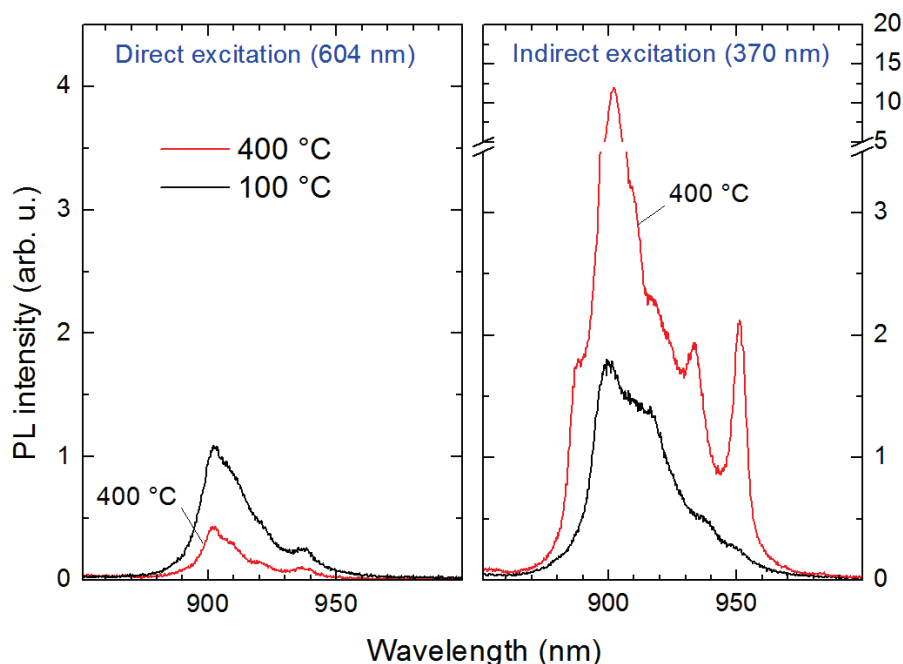


**Figure 3.42** - Room temperature PL emission under direct (604 nm) and indirect (370 nm) excitation for ZnO:Nd thin films deposited at 100 °C and 400 °C.

In the case of the sample deposited at low temperature, the shape of the PL spectrum presents only small changes between direct and indirect excitation. The intensities of the two emissions are also comparable. A possible explanation could be that the limiting factor is the emission yield from this active site, rather than the transfer efficiency, but it could also be a coincidence. It is interesting to notice that in the case of the sample deposited at 400 °C, the emission spectrum under direct excitation is exactly the same as that of the sample deposited at low temperature, but with lower intensity. On the other hand, the spectrum under indirect excitation reproduces the results of Figure 3.41. This means that the Nd site activated at high temperature cannot be efficiently directly excited. Another interesting result is that direct excitation of higher excited states produces the same emission bands in the infrared as indirect excitation. This supports the hypothesis that non-radiative relaxation occurs until the electron reaches the  $^4F_{3/2}$  state.

Although a complete deconvolution of the bands is quite a difficult task, more information can be obtained by recording the emission at a very low temperature, where the contribution of phonons is reduced.

Figure 3.43 reports the emission spectra recorded at RT and 15 K for the samples deposited at 15 °C and 400 °C. Indeed, many transitions are suppressed at such a low temperature. In particular, the whole  $^4F_{5/2} \rightarrow ^4I_{9/2}$  emission band disappears. This fact can be explained if we assume that these transitions can only occur following a phonon-assisted process. The fact that the energy separating the  $^4F_{5/2}$  level from the  $^4F_{3/2}$  level is approximately the energy of two longitudinal optical phonons in ZnO (72 meV) supports this hypothesis.

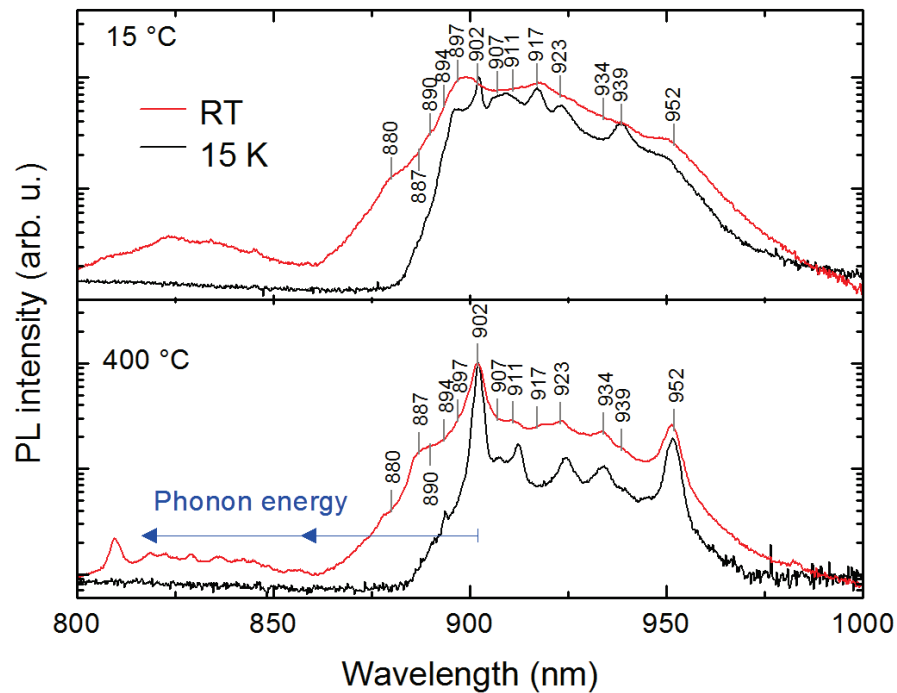


**Figure 3.43** - Normalized emission spectra of the samples deposited at 15 °C and 400 °C following He-Cd laser excitation and recorded at RT and at 15 K.

Additional information can be obtained if the detection range is extended in the infrared region, where the other two main emission lines of  $\text{Nd}^{3+}$  are expected [253, 255]. These lines are commonly attributed to the  ${}^4\text{F}_{3/2} \rightarrow {}^4\text{I}_{11/2}$  and  ${}^4\text{F}_{3/2} \rightarrow {}^4\text{I}_{13/2}$  transitions of  $\text{Nd}^{3+}$ .

In Figure 3.44, wide-range low-temperature emission spectra of samples deposited at 15 °C and 400 °C under laser excitation is reported. The three line groups commonly attributed to the  ${}^4\text{F}_{3/2} \rightarrow {}^4\text{I}_j$  transitions can be identified. However, these transitions alone cannot account for the rich pattern observed. In fact, even for the sample deposited at 15 °C, the simplest deconvolution of each group requires no less than 15 Gaussian peaks, which is more than twice the maximum multiplicity  $(2J+1)/2$  of the  ${}^4\text{I}_j$  levels after the degeneracy lift due to the Stark effect in the ZnO crystal field. The maximum multiplicity could be theoretically doubled due to the multiplicity of the  ${}^4\text{F}_{3/2}$  level, but similarly to what has been observed for Yb, the population of these levels should be reduced at such a low temperature. However, some of the lines observed in Figure 3.43 (those visible at slightly shorter wavelength than 902 nm for the spectrum recorded at room temperature) could be due to a non-negligible population of these levels.

This can indeed be interpreted as a proof that several active sites for  $\text{Nd}^{3+}$  exist in ZnO. However, due to the large superposition of the different emission patterns, the separation of the different contributions is a very difficult task even at such low temperatures.

Deeper insight in the energy level structure of  $\text{Nd}^{3+}$  and in the energy transfer from ZnO can be obtained by means of low temperature PLE measurements. The low temperature PL spectra under selected excitations are reported in the inset of Figure 3.45 for the sample deposited at 15 °C. Under indirect excitation (360 nm), the spectrum presents a rich pattern of emission lines. Up to seven emission lines can be clearly seen, but not all seven can be directly excited at the same time. The peaks at 895 nm and 916 nm present a different excitation spectrum. The PLE spectra performed on the 895, 902 and 916 nm emission lines are presented in Figure 3.45.

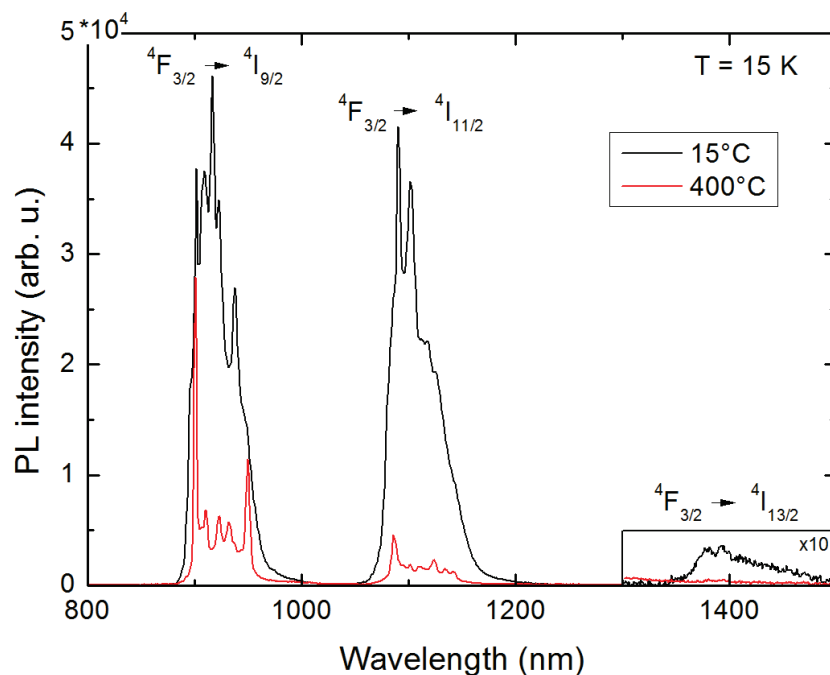


**Figure 3.44** - Low temperature PL emission spectra of samples deposited at 15 °C and 400 °C under He-Cd (325 nm) laser excitation. Due to the small intensity of the band at 1400 nm, its intensity has been artificially increased to improve clarity.

The peak at 895 nm can also be induced by direct excitation, but from different  $\text{Nd}^{3+}$  levels. This suggests that this peak is not part of the  ${}^4F_{3/2} \rightarrow {}^4I_{9/2}$  group. The fact that it can be observed following direct excitation of the  ${}^4G_{5/2}$  and/or  ${}^4G_{7/2}$  levels might suggest that this peak originates from a transition between an excited state situated between these levels and the  ${}^4F_{3/2}$  level to one of the  ${}^4I_j$  multiplets. The other intense emission peak can be found at 916 nm. It seems that this peak can be excited only indirectly, just as the intense peaks described above. The weak peaks in the excitation spectrum are probably derived from the convolution with the surrounding peaks. The reason why this peak can only be excited indirectly is not clear yet.

The PLE spectrum of the 902 nm emission line clearly shows that some of the direct excitation peaks disappear at low temperatures. This might be due to a different crystal field sensed by the Nd ions at such a low temperature, that alters the wavefunction mixing. Alternatively, it might indicate that phonons may play an important role in direct excitation.

The comparison between the PLE spectra recorded at 895 nm and 902 nm shows that the  ${}^2G_{7/2} / {}^4G_{5/2}$  group splits in at least 9 lines, exceeding the maximum total multiplicity of these two levels. This rules out the explanation given above involving different transition of the same ion and supports the hypothesis of a third active site for  $\text{Nd}^{3+}$ .

At this point, it is important to understand why some emission lines should only be excited by energy transfer from the host.

In the case of the lines emerging at high deposition temperature, their presence in all emission groups suggests that the emission takes place from the  ${}^4F_{3/2}$  energy level of a  $\text{Nd}^{3+}$  ion. A different lattice site could explain the slightly different emission pattern, but the absence of  $\text{Nd}^{3+}$  absorption levels in the PLE spectra of these lines must be taken into account. Two types of transfer are possible from the host, leading to  $\text{Nd}^{3+}$  emission. Either one 4f electron of a  $\text{Nd}^{3+}$  ion is excited by non-radiative energy transfer to a higher level or one electron from the conduction band of the host is trapped by  $\text{Nd}^{4+}$ , which temporarily reduces to the 3+ state.  $\text{NdO}_2$  is unstable in ambient conditions and therefore a pure 4+ state is unlikely to be present [256, 257]. However, some  $\text{Nd}^{3+}$  ions could lose some more charge (e.g. to

interstitial oxygen) to form an intermediate state. Ions in such a state could be temporarily reduced to the 3+ state by trapping one electron from the host.

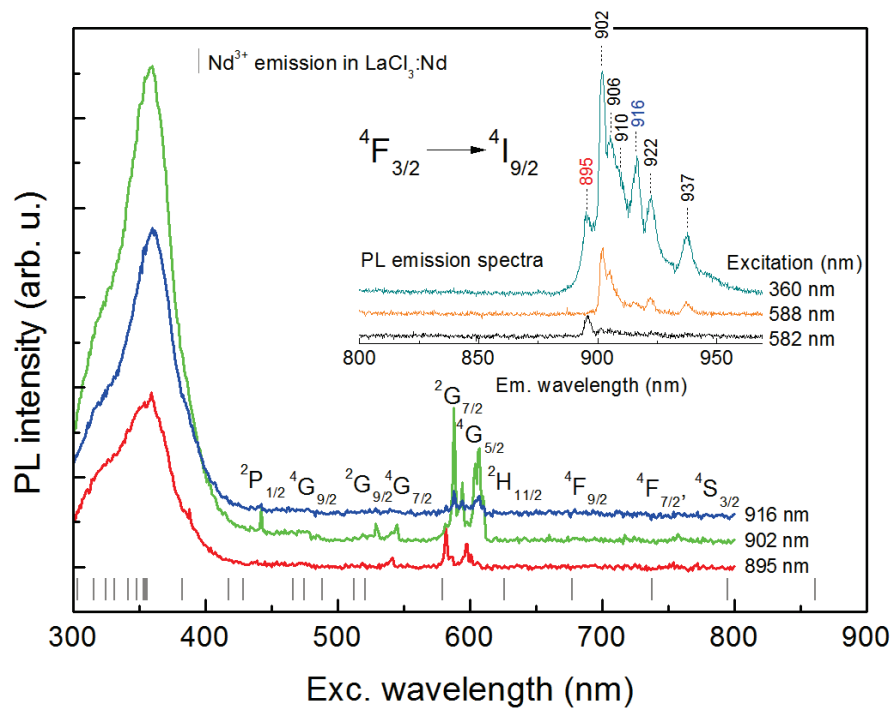


**Figure 3.45** - Low temperature (3.2 K) PL excitation spectra of the emission lines at 895, 902 and 916 nm on ZnO:Nd (1%) thin films deposited at 15 °C. Inset: low temperature PL emission spectra of ZnO:Nd (1%) under different excitations.

Since the presence of Nd<sup>4+</sup> requires a different crystal field, the slightly different emission pattern observed could be explained. This would explain also the absence of direct excitation. In fact, all excited states of Nd<sup>4+</sup> are highly energetic [258], which means that these ions can only be excited by far UV light illumination.

However, the observed signals could also be explained by a second Nd site whose valence state is 3+. If the number of sites is small, but the transfer mechanism is particularly efficient, both the absence of strong direct excitation and the high emission intensity under indirect excitation can be explained.

NEXAFS measurements of the ZnO:Nd have shown that the greatest part of the Nd ions is in the 3+ state in the proximity of the film surface. However, if there was a small amount of ions in a different oxidation state, e.g. one to one hundred Nd ions, even this sophisticated technique would not detect it. In addition, the Nd concentration is too low to allow detection in TFY mode, and the oxidation state in the proximity of the surface might be different from that in the bulk of the film.

In conclusion, both explanations suggest the existence of a small number of active sites with high transfer efficiency from the host. Unfortunately, such small concentrations push many techniques to their physical limits, which makes the interpretation of the optical data quite difficult.

In Figure 3.46, the information obtained by the study of PL and PLE spectra is summarized. The direct excitation peaks and emission peaks of Nd<sup>3+</sup> which could be attributed with the highest confidence are indicated by the arrows.

Due to the complex nature of the absorption and emission spectra, it was not possible to reconstruct a complete energy level diagram of Nd<sup>3+</sup> in ZnO. However, valuable information has been obtained concerning the origin of the observed transitions. In particular, the three transfer mechanisms which might be responsible for the energy transfer from the host are drawn on the right side of Figure 3.46.

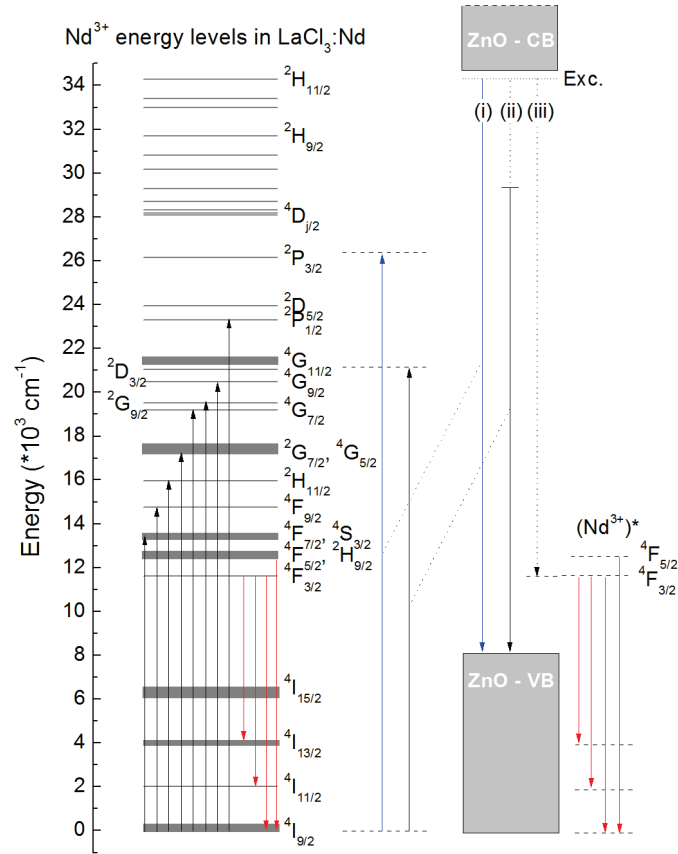


**Figure 3.46** - Observed radiative transitions of  $\text{Nd}^{3+}$  in ZnO and possible energy transfer mechanisms from the host. The energy levels of  $\text{Nd}^{3+}$  in  $\text{LaCl}_3$  are reported for reference

Mechanism (i) represents the ideal case when band-to-band or exciton recombination transfer all the energy to one  $4f$  electron of  $\text{Nd}^{3+}$ . In mechanism (ii), the energy transfer occurs through some localized defect state within the band gap. Mechanism (iii) accounts for the emerging features observed at high deposition temperature and involves electron trapping by  $\text{Nd}^{4+}$  ions. In particular, the case when the electron is trapped by the lowest excited state in the gap. Although the exact position of Nd levels with respect to the ZnO bands has never been measured experimentally, theoretical calculations indicate that the fundamental state of  $\text{Nd}^{3+}$  is situated at about 1 eV below the top of the valence band [105]. If this was the case, then the lowest level in the gap would be exactly the level from which the emission takes place.

If the explanation of the new patterns relies on the existence of several  $\text{Nd}^{3+}$  active sites, then several (ii)-type processes occur. Figure 3.47 illustrates better the two transfer types (electronic and energetic) and the two defect levels that could explain the existence of two different  $\text{Nd}^{3+}$  active sites. The orange defect band in the gap might be the usual defect band behind the orange emission of sputtered ZnO films and the green band could be the band associated with oxygen vacancies that so often leads to green emission in ZnO.

One last point should be emphasized, regarding the variation of the band gap with the deposition temperature observed in section 3.2. A variation of the gap could change the resonance condition between the levels of the host and the RE and explain a strong increase in the PL. However, since the PL only occurs from the  ${}^4\text{F}_{3/2}$  and the  ${}^4\text{F}_{5/2}$  levels, the same emission pattern would be expected. The change in the relative emission intensity of the peaks exclude this hypothesis and favors the explanation based on several active sites of Nd.

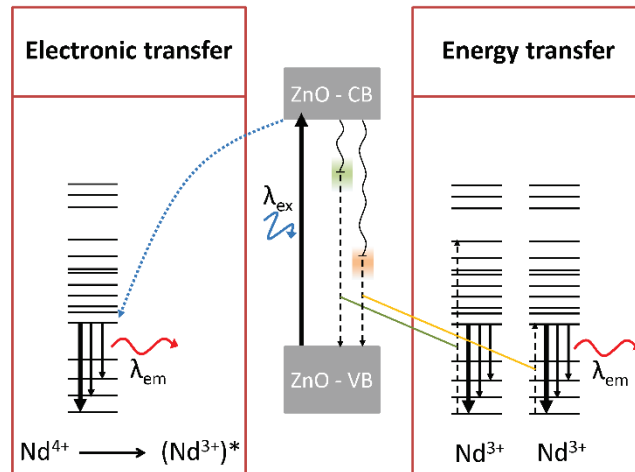


**Figure 3.47** – Schematic illustration of the two types of transfer (electronic and energetic) and possible defect bands behind the two  $\text{Nd}^{3+}$  active sites.

Further insight in the  $\text{Nd}^{3+}$  transitions in an oxide matrix like ZnO can be obtained by studying pure  $\text{Nd}_2\text{O}_3$ . Therefore,  $\text{Nd}_2\text{O}_3$  powders have been produced by calcination of Nd-nitrate at high temperature. Figure 3.48a shows that depending on the calcination temperature, different crystal phases can be obtained (prevalently cubic up to 800 °C and hexagonal above 1000 °C). The crystallites size also increases along with the temperature, as indicated by the narrowing of the PL peaks. The different crystal phases also have different vibration modes, as indicated by the Raman spectra of Figure 3.48b. Therefore, different patterns of emission lines are expected, both because of the different  $\text{Nd}^{3+}$  lattice sites and the different phonon energies.

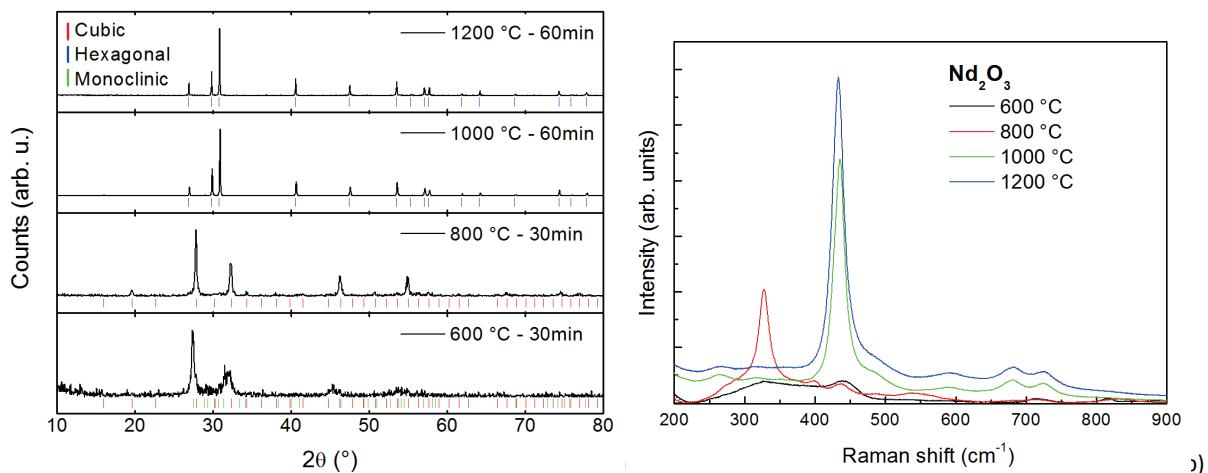


**Figure 3.48** – a) XRD patterns and b) non-resonant Raman spectra of  $\text{Nd}_2\text{O}_3$  powders obtained by calcination of Nd-nitrate at different temperatures.

Figure 3.49 reports the absorption spectra of the powders, as obtained by the measurement of diffuse reflectance, and compares them to the energy level diagram of  $\text{Nd}^{3+}$  in  $\text{LaCl}_3$  and the PLE of the 902 nm emission in ZnO. By analyzing the spectra of the powders, several considerations can be made. The different phases have different band gaps and the smaller grains produced at lower calcination temperature smooth out the absorption edge by increasing the internal reflections. The  $\text{Nd}^{3+}$  absorption lines are narrower (due to the improved crystalline order) and the relative intensity of the peaks is different for high calcination temperatures.

Since an integration sphere has been used to detect the diffuse reflectance, the appearance of strong absorbance bands indicates that a great part of the light is absorbed and not re-emitted. However, the relative intensity of the bands should not be regarded as indicative of the emission efficiency, as it also depends on the absorption cross section. This low emission efficiency suggested by the intensity of the absorption lines can be attributed to a quenching effect related to the high concentration of Nd ions. The emitted light from a  $\text{Nd}^{3+}$  ion is re-absorbed by neighboring ions until non-radiative recombination occurs.

The position of the peaks in the oxide is clearly different from that in the chloride as all peaks are shifted towards lower energies. The position of the peaks in the PLE signal of our ZnO:Nd films is very close to that of the peaks in the oxides, except that all peaks are further shifted towards lower energies. Curiously, the intensity of the peaks is not the same and indicates that  ${}^4\text{F}_{3/2} \rightarrow {}^4\text{I}_{9/2}$  emission is particularly efficient by excitation of the  ${}^2\text{G}_{7/2}$  and/or  ${}^4\text{G}_{5/2}$  multiplets. This could indicate that a direct optical transition between one of these levels and the  ${}^4\text{F}_{3/2}$  level occurs and that Nd might act as down-converter. Unfortunately, such a transition is outside the detection range of our setup (and has too low energy to be absorbed by Si).

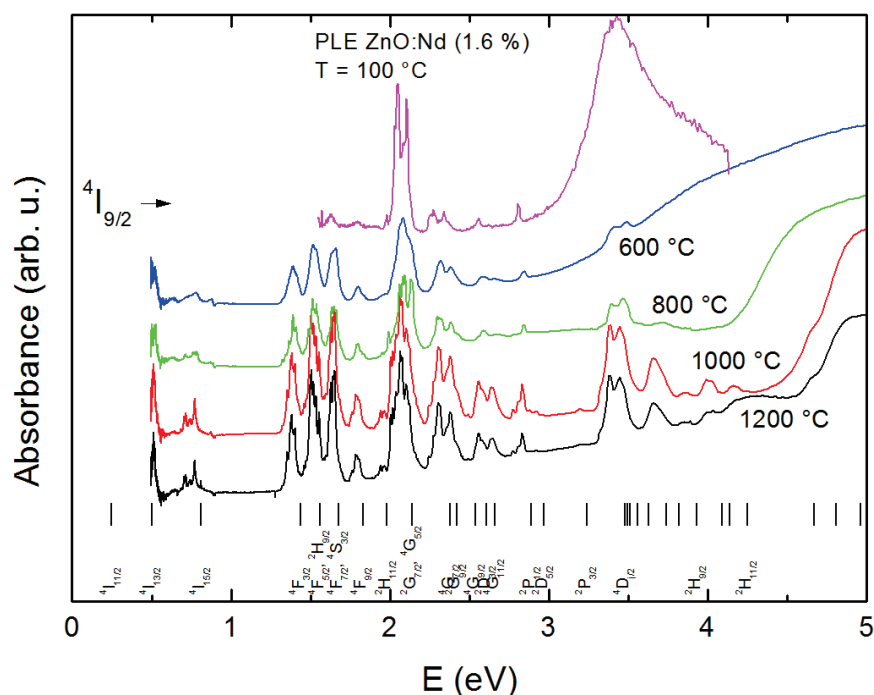


**Figure 3.49** - Absorption spectra of  $\text{Nd}_2\text{O}_3$  powders, as obtained by the measurement of diffuse reflectance. The energy level diagram of  $\text{Nd}^{3+}$  in  $\text{LaCl}_3$  and the PLE of the 902 nm emission in ZnO are reported for comparison.

#### Concluding remarks on ZnO:Nd films

The presence of optically active Nd ions has been confirmed by PL measurements at all deposition temperatures and efficient IR emission of  $\text{Nd}^{3+}$  in ZnO has been evidenced.

Due to the very rich nature of the  $\text{Nd}^{3+}$  energy level structure, interpretation of the luminescence signals is not straightforward. If the structural information does not offer a clue to the problem, the combination of PL and PLE analysis performed on a wide spectral range and down to cryogenic temperatures allowed identification of several transitions related to Nd ions in ZnO and valuable information has been obtained about their origin.

Three emission groups have been attributed to the  ${}^4F_{3/2} \rightarrow {}^4I_1$  emission of  $\text{Nd}^{3+}$  ions and one to the  ${}^4F_{5/2} \rightarrow {}^4I_{9/2}$  transition. A closer look to the emission spectra showed that several additional emission lines are present, compared to those expected from the spectroscopic level multiplicity. Some of these lines strongly increase for deposition temperatures above 400 °C.

These lines have been attributed to a different active site for Nd and several transfer mechanisms have been proposed. The fact that these intense lines emerge from all emission groups and that no absorption from  $\text{Nd}^{3+}$  is visible in their excitation spectra suggests two possible explanations. Either this emission involves  $\text{Nd}^{3+}$  ions that are slightly more oxidized, or a small amount of ions are in a second active site of  $\text{Nd}^{3+}$ , for which the transfer from the host is particularly efficient. The small concentrations involved challenge the most sensitive analysis techniques and hampers the selection of one single transfer mechanism.

The similarities between the emission of films deposited at lower oxygen flows and that of films deposited at high temperature led us to the hypothesis made at the beginning of this section, which stated that oxygen vacancies might be responsible for the emission at 902 nm. The low efficiency of direct excitation of these sites suggested a small population of active sites, which might explain why in NEXAFS measurements of the O K edge no appreciable variation of the shoulder related to oxygen vacancies has been observed.

Some additional features, such as the emission peaks at 916 nm and 895 nm, are more difficult to explain. The presence of a third active site and an additional transition from a higher level of  $\text{Nd}^{3+}$  might be at the origin of these peaks.

Regarding the possible applications of Nd-doped ZnO films on silicon solar cells, several assertions can be made. No evidence of down conversion was observed in the frame of the investigated parameters, although some results might indicate a DC process producing a photon well below the band gap of Si. However, the high transfer efficiency from the host observed in certain samples proves that Nd-doped ZnO can find applications as an efficient downshifter. Unfortunately, at least half of the emitted light falls outside the spectral region useful for Si-based solar cells.

### 3.4.5 Concluding remarks

As shown in section 3.1, the three different rare earths (Yb, Pr and Nd) susceptible to lead to DS and DC processes useful for silicon solar cells have been successfully inserted in ZnO films deposited by magnetron reactive sputtering. The structural investigations showed that the quality of the films and the existence of a strong preferential direction are not strongly affected by the RE insertion. On the other hand, the film quality depends on the deposition temperature and the insertion rate on the oxygen flow during growth. In all cases, the rare earth are uniformly distributed in the films. Section 3.2 showed that these films have interesting ARC properties and established an upper limit for sensitized photon conversion and section 3.3 indicated that our films have poor electrical properties, probably due to the high amount of oxygen in the film.

What emerges from section 3.4 is that all three rare earths are optically active in all the films and that this is certainly related to the oxygen content in the films. How the insertion rate is bound to the oxygen flow during deposition indicates how sensitive rare earths are to this element. Oxygen-related defects are called to explain most of the observed differences in the PL, which are hardly explained by the observed trends in the structural parameters of the films. Unfortunately, a correct estimation of the oxygen content and of the amount of oxygen related defects is very hard even with very sophisticated techniques like NEXAFS. This is probably due to the fact that we are dealing with a very small population of defects, whose effects on the optical activity of rare earths are particularly strong.

One of the most important achievements is that the emission of all three rare earths can be stimulated by indirect excitation of the host, thus offering a potential solution to recover the parasitic absorption of the ZnO layer. Most of the ions are in the 3+ state, which suppose the existence of charge compensating defects in the lattice.

Different transfer mechanisms have been proposed for the different rare earths. This might appear quite arbitrary. However, it has been shown that each rare earth behaves quite differently with the deposition temperature and with annealing. Since these parameters affect the defect population, it is probable that the transfer mechanism is different for the different rare earths.

In the case of Yb, it turned out that the preparation parameters can deeply change the emission intensity and this phenomenon has been attributed to different transfer efficiencies from the host. The observed trends are compatible with changes in the non-radiative defect concentration and in the amount of interstitial oxygen.

In the case of Pr, the preparation parameters have a weaker influence on the emission intensity. Moreover, the overall emission efficiency is weaker than in the case of Yb. Non-negligible amounts of Pr<sup>4+</sup> and an energy transfer from a different type of defect could explain this low efficiency.

Codoping with Yb and Pr has been also tested, in view of potential down-converting properties. To bypass the low transfer efficiency from the host, Pr<sup>3+</sup> ions have been directly excited by a laser and the NIR PL has been recorded. The absence of Yb-related emission suggests that the DC properties of this RE pair is low in ZnO. Two main reasons have been stretched out to explain this low performance: the poor resonance conditions and the large Stark splitting of the Pr<sup>3+</sup> levels induced by the crystal field of ZnO, which favor non-radiative recombination paths.

In the case of Nd, at least two transfer mechanisms have been observed and associated to two different active sites for Nd ions. Despite the large number of transitions involved, the careful study of the PL and the PLE allowed obtaining some information on these two sites. The largest part of Nd ions in the film seems to be associated to one site, related to Nd<sup>3+</sup>, for which the transfer efficiency from the matrix is low. High deposition temperatures favor the formation of a second active site (already present even at room temperature). Although the part of Nd ions in this second site is still minor, this site is characterized by a more efficient energy transfer from the host.

Of the three rare earths, Nd is the only one that offers reasonable down shifting efficiencies at relatively low temperatures (400 °C) compatible with certain solar cell technologies. Therefore, a ZnO:Nd (1.6 %) film deposited at 400 °C has been selected for a test on solar cells. The results will be presented in Chapter 5.

## 4 RESULTS AND DISCUSSION: CERIUM OXIDE

Although CeO<sub>2</sub> is not an intrinsic n-type semiconductor like ZnO, this material possesses a large band gap and an appropriate refractive index for ARC properties on silicon. The large ionic radius of Ce ions should favor the insertion of the large RE ions, thus repelling the concentration quenching limit.

The work on CeO<sub>2</sub> is not as extensive as that on ZnO and only few deposition conditions have been tested, based on some preliminary work carried out at IPCMS and driven by the purpose of applying the film to solar cells. The aim of this chapter is to report the observed properties of RE-doped and undoped CeO<sub>2</sub> thin films prepared by PLD. Since the films are obtained from lab-made pellets, the properties of the pellets will be briefly reported at the beginning of this section to help understanding the properties of the films.

### 4.1 RE-doped CeO<sub>2</sub> pellets

#### 4.1.1 Structural and morphological properties of CeO<sub>2</sub> pellets

The preparation of CeO<sub>2</sub>(:RE) PLD targets was carried out by solid state reaction of a stoichiometric mixture of the elemental oxide powders. The indicated concentrations are the nominal concentrations because the measurements of the concentration of elements that are so close in the periodic table is quite difficult by common techniques like RBS and EDX.

Figure 4.1 reports the XRD patterns of the pellets after sintering at 1400 °C and that of the CeO<sub>2</sub> powder.

All peaks can be attributed to the cubic CeO<sub>2</sub> structure. No spurious phases or dopant oxide peaks are observed, although the doped pellets are obtained by mixing CeO<sub>2</sub> with the RE oxide. This is probably due to the low RE concentration.

Information about the crystal quality of the pellets can be obtained by calculating the crystallites size and lattice parameter. The values of the peak positions corrected by the zero shift caused by the different thickness of the pellets were obtained by least square method using all the peaks in the spectrum. The lattice parameter of the pellets calculated using Bragg's law is 5.414(2) Å independently of the doping type and level. The values of the crystallites size calculated using Scherrer's formula on the (111) peak are reported in Figure 4.2.

Due to the sintering process, the crystallites of the pellets are much larger than those in the powder. In particular, the crystallites in the undoped pellet seem to be slightly larger than those in the doped pellets.

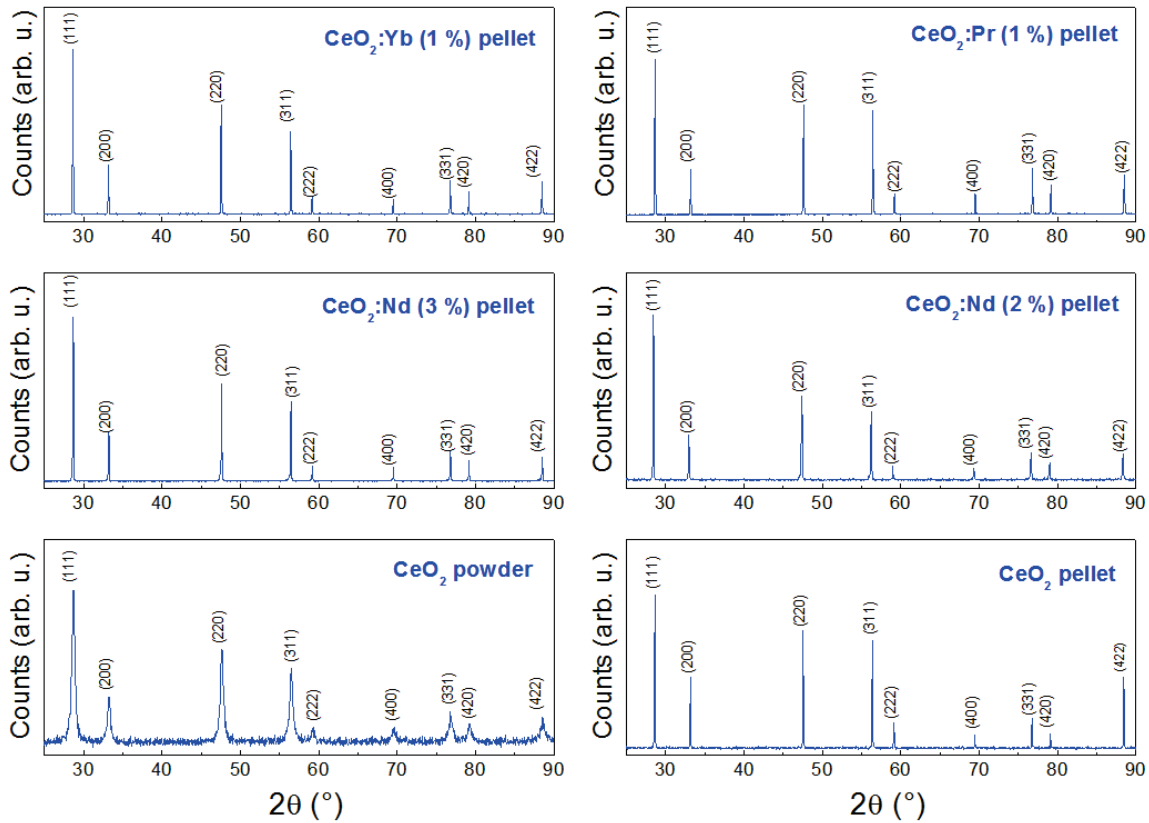


Figure 4.1 – XRD patterns of the CeO<sub>2</sub> powder and of the pellets (doped and undoped) after sintering at 1400 °C.

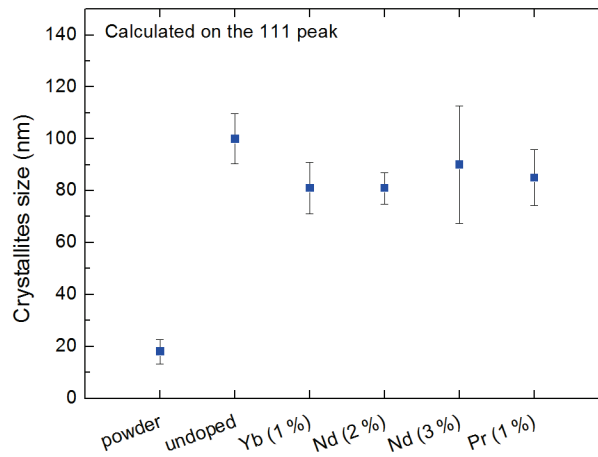
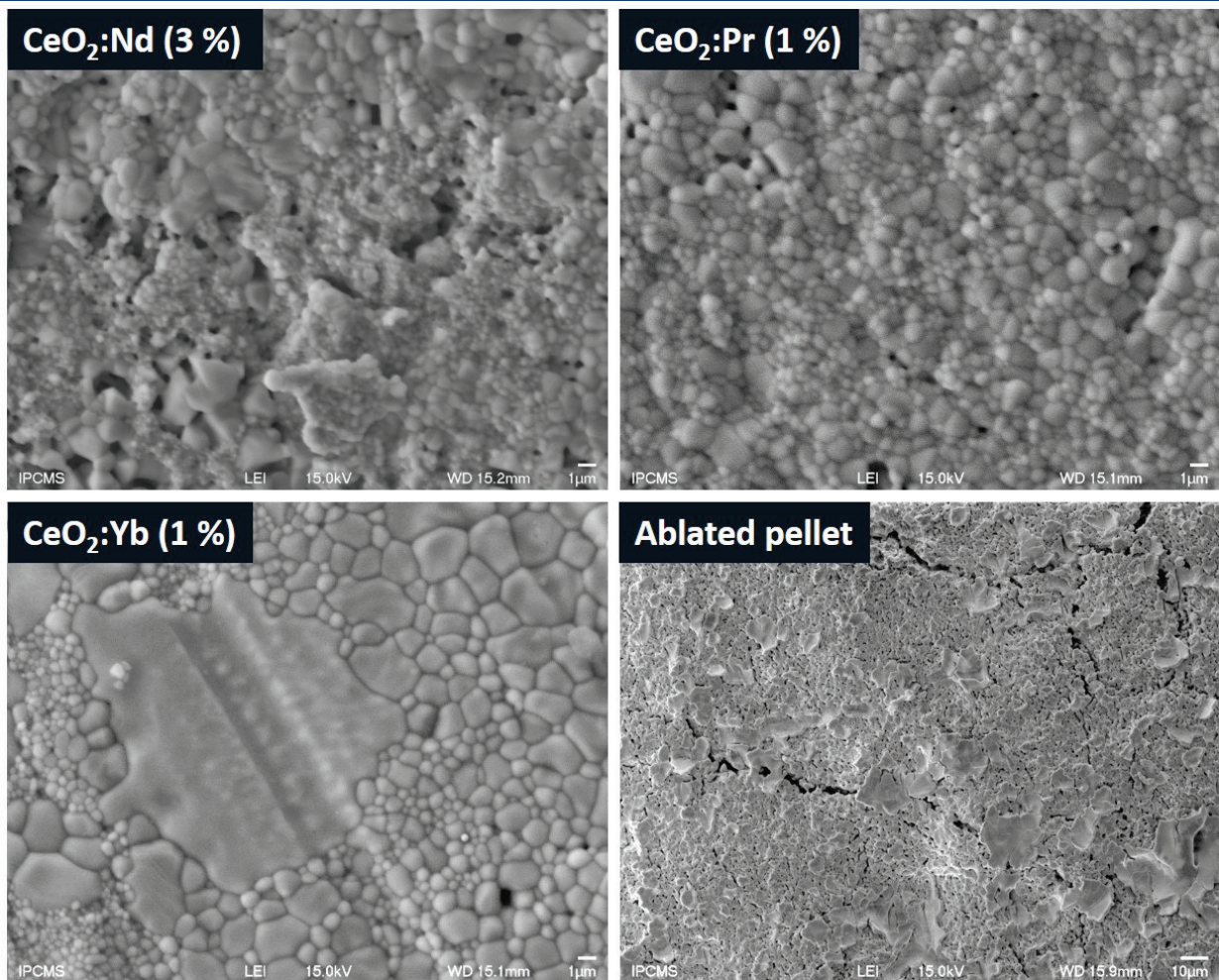


Figure 4.2 – Calculated values of the crystallites size of CeO<sub>2</sub> pellets after sintering at 1400 °C. The crystallite size of the powder is reported for reference.

Due to annealing at such a high temperature, some grains are expected to coalesce. An idea of the morphology of the target can be obtained by SEM (see Figure 4.3). Most pellets appear as a compact aggregate of particles with an average size of about 1 μm. Only the Yb-doped pellet appears more compact than the others. The different aspect of the Yb-doped pellet could be due to the lower melting point of Yb (824 °C against 935 °C for Pr and 1010 °C for Nd) that favors the diffusion. For comparison, the melting point of Ce is 795 °C. Unfortunately, due to the very similar atomic number between Ce and the other rare earths, it is not possible to determine if some RE oxide grains are still present after sintering.

After ablation, the appearance of flakes indicates that the surface of the pellet has melted under the highly energetic laser pulses.



**Figure 4.3** – SEM images of several CeO<sub>2</sub>:RE pellets. The image of a typical pellet surface after ablation is also reported (in this case with 3 % of Nd).

#### 4.1.2 Optical properties of CeO<sub>2</sub> pellets

The first optical observation on the pellets can be made by the naked eye. Contrarily to the snowy white CeO<sub>2</sub> powder, after sintering all pellets acquire an intense copper-like color. This color is the characteristic color of Ce<sub>2</sub>O<sub>3</sub> and is due to the small band gap (2.4 eV) of this oxide. However, no trace of Ce<sub>2</sub>O<sub>3</sub> has been observed in the XRD spectra. Only the measurement of the diffuse reflectance will allow discriminating if this color is due to the presence of Ce<sup>3+</sup> or to the emission from some impurities or intrinsic defects in CeO<sub>2</sub>. Figure 4.4 reports the absorbance curves calculated from the diffuse reflectance of the pellets and of the CeO<sub>2</sub> powder. The absorbance of the powder is not sharp as expected from a direct band gap material and it extends below 3.6 eV. The high amount of surface in the powder and the associated high number of internal reflections might explain this behavior. For the pellets, the absorbance band extends well below the typical absorption edge of CeO<sub>2</sub>. In particular, three wide absorbance features are observed for wavelengths below 600 nm. This justifies the reddish color of the pellets. Besides the CeO<sub>2</sub> band gap absorption, two additional absorbance bands can be distinguished at about 520 nm (2.4 eV) and 380 nm (3.26 eV). A closer look to the curves indicates that these new bands are already present in the powder, but very weak. Since 2.4 eV is the band gap value of Ce<sub>2</sub>O<sub>3</sub> reported by Prokofiev *et al.* [201], this band could be related to this oxide. This means that some

oxygen is lost during sintering even if the process occurs in air. However, if the sesquioxide is really present in the pellets, the absence of the relative XRD peaks must be explained. One possibility is that the amount of Ce<sub>2</sub>O<sub>3</sub> is very small. The reason why a strong absorption band can be created despite the small amount of this oxide could be that CeO<sub>2</sub> is transparent to visible light. The increased penetration depth in the pellet increases the amount of Ce<sub>2</sub>O<sub>3</sub> material “seen” by this light.

As for the band centered at 380 nm (3.26 eV), it matches very well with the f-d transitions of isolated Ce<sup>3+</sup> ions in CeO<sub>2</sub>, as shown by Askrabic *et al.* [214].

Figure 4.4 also shows that strong absorption bands related to 4f transitions of RE<sup>3+</sup> ions are observed in the case of Nd- and Yb-doped pellets. The absence of such absorption bands in the Pr-doped pellet indicates that this rare earth must be in its 4+ state, favored by the presence of Ce<sup>4+</sup>.

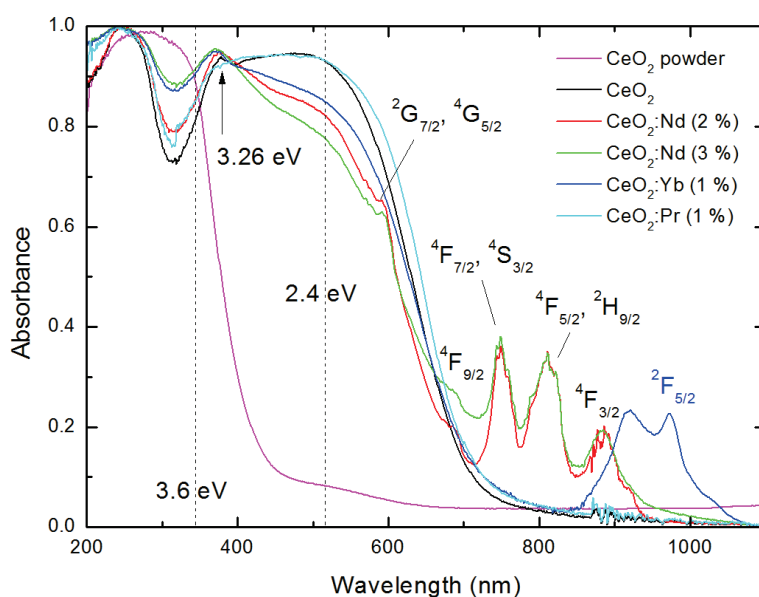


**Figure 4.4** - Absorbance spectra calculated from the diffuse reflectance of the pellets and of the CeO<sub>2</sub> powder. The transitions excited state relative to the RE<sup>3+</sup> absorption bands are indicated for Nd and Yb.

PL and PLE spectra have been recorded in order to see if the dopant is already optically active in the pellets. Figure 4.5a-b show the PL emission spectra of the CeO<sub>2</sub> pellets under 325 nm laser excitation.

Several strong emission bands can be observed, composed of a large number of narrow peaks. Since none of these peaks can be attributed to Ce ions or to CeO<sub>2</sub>, indirect excitation of the dopants by energy transfer from the host must occur. The two emission bands in the infrared range can be easily attributed to Nd<sup>3+</sup> and Yb<sup>3+</sup>, but the emission band in the visible region cannot be attributed to these rare earths. This band is attributed to Sm<sup>3+</sup> [259], which must exist in the CeO<sub>2</sub> powder as impurity. Nd<sup>3+</sup> must also be present as impurity in the powder, as its signal is visible in all spectra. Given the high purity of the powder (99.95 %), their concentration must be very small (< 0.05 %). Still, intense PL signals are recorded, indicating that almost all ions must be optically active and that the energy transfer from CeO<sub>2</sub> is very efficient.

The fact that the peaks are so narrow indicates a small distortion of the lattice sites and that the phonon broadening is weak. The large number of peaks indicates the existence of several active sites. For instance, the greatest part of the Nd<sup>3+</sup> ions could still be in Nd<sub>2</sub>O<sub>3</sub> particles and only a small fraction has migrated in CeO<sub>2</sub>.

More insight in the transfer mechanisms can be obtained by the analysis of the PLE spectra of the RE<sup>3+</sup> emission. Figure 4.6 reports the PLE spectra of the strongest emission lines of Yb<sup>3+</sup> and Nd<sup>3+</sup>. In the spectrum of Nd-doped CeO<sub>2</sub>, several absorption bands are observed.

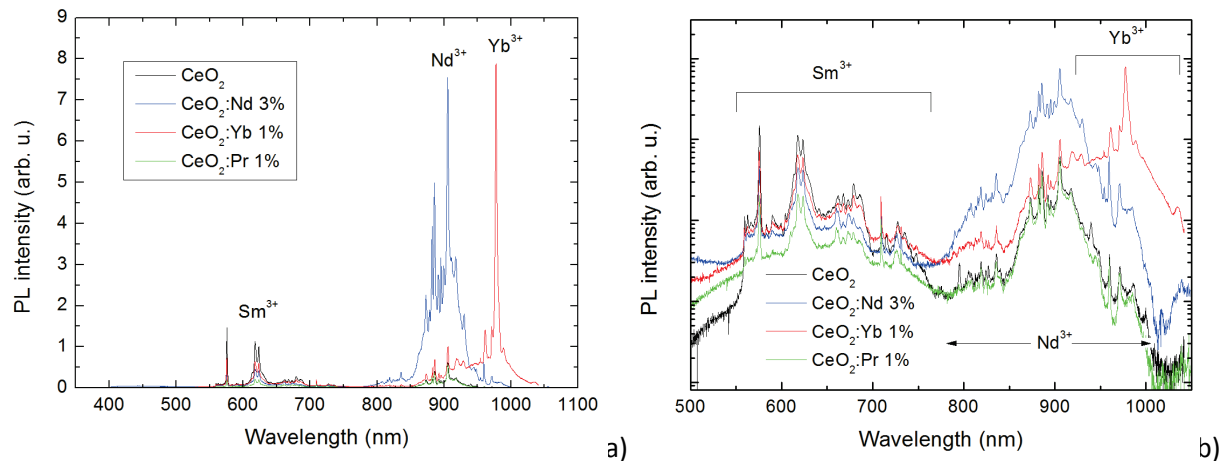


**Figure 4.5** - PL emission spectra of the doped and undoped CeO<sub>2</sub> pellets under 325 nm laser excitation in a) linear and b) logarithmic scales.

The PLE bands around 600 nm and 800 nm correspond to direct excitation of Nd<sup>3+</sup> ions, while the intense peak at 380 nm is attributed to indirect excitation of the host. Curiously, indirect excitation only occurs by exciting the absorption feature observed at 3.26 eV, which had been ascribed to isolated Ce<sup>3+</sup> ions. This suggests that Nd<sup>3+</sup> and Yb<sup>3+</sup> ions are situated close to isolated Ce<sup>3+</sup> ions, from which efficient transfer occurs. An oxygen vacancy created to balance the charge when trivalent Nd and Yb ions replace Ce<sup>4+</sup> ions might explain the presence of Ce<sup>3+</sup> in the vicinity of the RE.

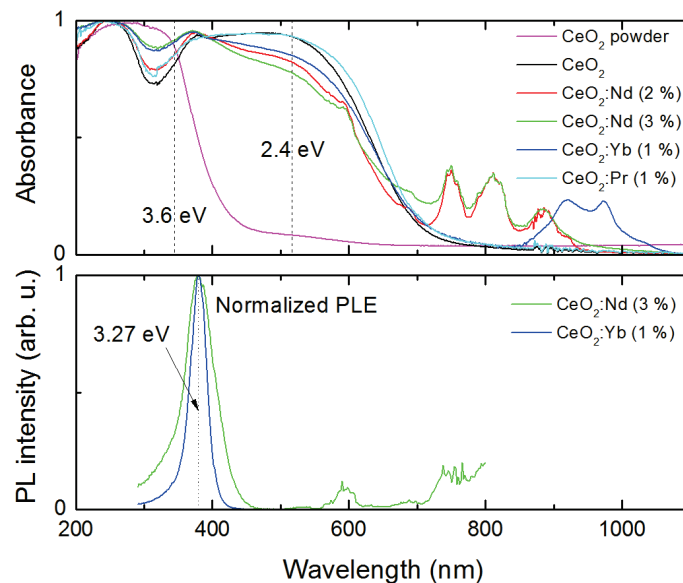


**Figure 4.6** - PLE spectra of the main emission line of Yb<sup>3+</sup> and Nd<sup>3+</sup>. The absorbance spectra of the pellets and the powder are reported for reference.

### Concluding remarks

The structural analysis on the pellets showed that the rare earths do not modify the typical structure of CeO<sub>2</sub>. They have, however, a small effect on the crystallites size.

The different color observed for the pellets after sintering is due to the appearance of two absorption bands below the band gap of CeO<sub>2</sub>. One of these bands, centered at 3.26 eV, revealed to be the band from which the energy transfer to the rare earth impurities occurs. This band has been attributed to isolated Ce<sup>3+</sup> ions in CeO<sub>2</sub>. The other band is probably related to Ce<sub>2</sub>O<sub>3</sub>.

Strong absorption bands have been also observed arising from direct absorption of the trivalent dopant ions.

Since the pellets proved to be of good quality and the presence of the dopants has been confirmed, they have been used as targets for PLD from which RE-doped CeO<sub>2</sub> films have been deposited. The structural and optical properties of these films will be the topic of the next sections.

## 4.2 RE-doped CeO<sub>2</sub> thin films

### 4.2.1 Structural and morphological properties of CeO<sub>2</sub> thin films

The preliminary study on RE-doped CeO<sub>2</sub> films indicated that high deposition temperatures have a positive effect on the emission. The presence of a low pressure of oxygen gas in the chamber is also recommended. Since the highest possible temperature for our test cells is 400 °C due to the aluminum contacts, CeO<sub>2</sub> thin films have been deposited at 400 °C in 10<sup>-3</sup> mbar of O<sub>2</sub> gas atmosphere. The laser source was a KrF excimer laser with a frequency of 10 Hz and a power of 25 mJ. The substrate was heated by a resistance and rotated at 5 rpm to increase uniformity of the deposited layer.

In the following, the results on Pr-doped CeO<sub>2</sub> films will be omitted as no Pr optical activity has been observed neither in the pellet nor in the films.

Figure 4.7 shows the XRD patterns of about 100 nm of film deposited on silicon substrate. All peaks can be attributed to CeO<sub>2</sub> and the films are clearly polycrystalline. The crystallites size calculated on the (111) peak using Scherrer's formula is 13 ± 2 nm for all films.

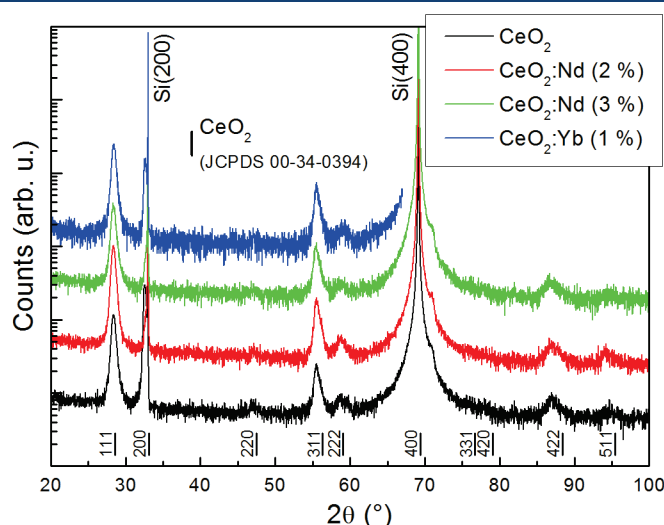


**Figure 4.7** - XRD patterns of undoped and RE-doped CeO<sub>2</sub> thin films deposited at 400 °C.

The diffractograms show two preferential directions for the growth of CeO<sub>2</sub> along the [111] and [311] axes, corresponding to the situation where the most dense crystal planes grow parallel to the substrate surface. This type of preferential direction is usual in thin films grown on flat substrates (even amorphous). The very low intensity of one of the most intense peaks observed in the pellets, namely the (220) peak, seems to confirm the existence of this partial orientation of the crystallites. On the other hand, the (200) peak is present with an intensity that is comparable to that of the (111) peak.

The existence of a preferential growth direction perpendicular to the (002) planes must have a different explanation. The very good matching of the lattice parameter between silicon ( $a = 5.4307$  Å)

and CeO<sub>2</sub> ( $a = 5.4113 \text{ \AA}$ ) could favor epitaxial growth. This epitaxial relation is quite unexpected, as the silicon wafers should be covered by a thin layer of amorphous native SiO<sub>2</sub>.

It is possible, however, that this thin amorphous layer presents some holes where local epitaxy can occur. It is not excluded that these holes are created by Ce ions that pump part of the oxygen inside the film.

Unfortunately, the superposition with the peaks of silicon prevents a clear view on the peaks of CeO<sub>2</sub> crystals that could have an epitaxial relation with the substrate. In particular, this rules out the use of  $2\theta$ - $\chi$ - $\phi$  scans to determine the orientation of the crystallites in plane with the substrate. It is possible, however, that with higher deposition temperatures this epitaxial relation is improved and easier to detect.

More information can be obtained by TEM observation of the cross section of the film. Figure 4.8 reports the HR-TEM cross section image of a CeO<sub>2</sub>:Nd (2%) film deposited on Si (100) substrate. Only in few regions of the film, the lattice planes can be clearly distinguished. In the rest of the film, blurred areas alternate with moiré patterns, indicating that the electron beam crosses several crystallites. The polycrystalline nature of the film indicated by XRD data is confirmed and the calculated average value of the crystallites size (13 nm) is compatible with TEM observations.

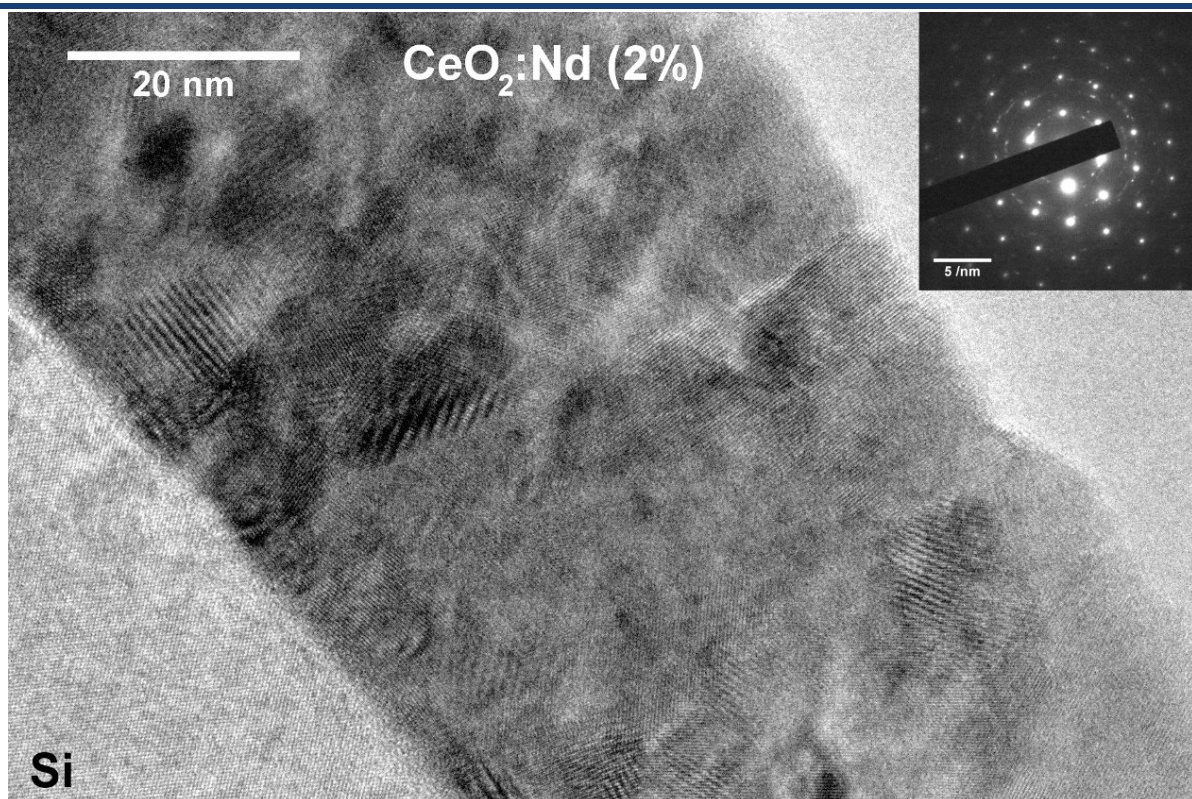


**Figure 4.8** – TEM image of the cross section of a CeO<sub>2</sub>:Nd (2%) film deposited on Si (100) substrate. The SAED pattern relative to the observed area is reported in the inset.

The SAED pattern is composed of a regular pattern produced by the silicon substrate and of pale irregular circles that come from the film, which means that the film is polycrystalline. However, the small observed area gives no clue about the partial orientation of the films observed in the XRD patterns.

This type of information can be obtained by dark field observations, where the spatial distribution of the crystallites with a certain orientation can be observed. This is done by selecting one or few spots in the SAED pattern. Figure 4.9 illustrates the DF images of the films obtained by observing the first two

reflections (111 and 200) along the growth direction and in a direction that is almost in plane. The two images show that the crystallite shape and size are quite different in the two directions. In particular, the crystallites seem to be well oriented along the growth direction in the first half of the film (close to the silicon surface) and then lose this orientation in the second half.

The absence of (220) peak along the growth direction is confirmed by TEM. In fact, this peak corresponds to the third diffraction ring, which is not visible along the growth direction (above point 1 in the SAED pattern).

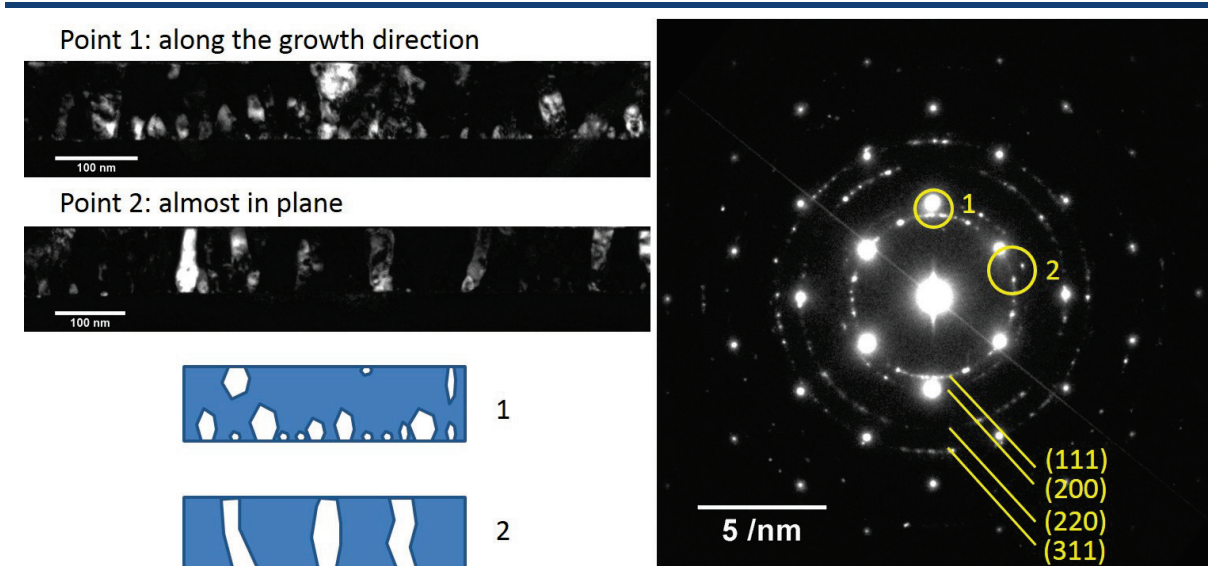


**Figure 4.9** – Dark field TEM images of a CeO<sub>2</sub>:Nd (2%) film deposited on Si (100) substrate. The complete SAED pattern of the observed area is also reported, in which the spots selected for the SAED pattern are indicated.

### Concluding remarks

CeO<sub>2</sub> films grown on silicon substrates are polycrystalline, but present several preferential orientations of the crystallites. Two orientations are those expected from films grown on flat surfaces, as the film tends to grow with the most dense crystal planes parallel to the substrate surface. The other direction suggests the existence of a local epitaxial relation with the substrate. Further investigation is needed in order to shed light on this point.

In any cases, TEM images indicate that the films thickness is uniform and that the surface roughness is acceptable.

### 4.2.2 Basic optical properties of CeO<sub>2</sub>(:RE) thin films

In the introductory section, it was stated that the optical properties of CeO<sub>2</sub> thin films are well suited for application as anti-reflection coating on silicon solar cells. This statement was mainly based on the properties (band gap and refractive index) of bulk CeO<sub>2</sub>, but nanostructures and doping might strongly alter the optical properties.

As stated in the introduction, the negative effects of a poor refractive index matching or a wrong band gap values can quickly overwhelm the positive effect of these conversion layers.

In particular, refractive index matching with silicon is crucial in order to reduce the escape cone and to keep the reflectance at small levels. On the other hand, the band gap value is important when matrix-sensitized photon conversion is used. In this case, the absorption cross section of the matrix above the gap is as important as the band gap value itself.

Figure 4.10a reports the refractive index and absorption coefficient of the CeO<sub>2</sub> films as a function of the photon wavelength. It turns out that both the refractive index and the extinction coefficient of CeO<sub>2</sub> are practically unchanged upon doping. The refractive index value in the transparent region (2.5) and the calculated band gap value using Tauc's law (3.75 eV) are slightly higher than usually reported values for CeO<sub>2</sub> thin films (3.31-3.6 eV).

Figure 4.10b compares the refractive index of the typical CeO<sub>2</sub> film with the ideal refractive index for optimal ARC properties, calculated as  $n_{\text{ideal}} = \sqrt{n_{\text{Si}}n_{\text{IM}}}$  (IM for incoming medium), in the case of a solar cell in air or with an encapsulant of refractive index 1.5 (i.e. glass or ethylene vinyl acetate, EVA). It is clear that ZnO presents optimal ARC properties when glass is the incoming medium. This means that the reflectance can be decreased to zero in the regions of destructive interference. Since the photon density of the solar spectrum is not uniform, neither is the spectral response of the solar cell, it is essential to select where to apply destructive interference and decrease the reflectance conveniently. This region can be selected by choosing the appropriate thickness. For this purpose, the average reflectance over the whole spectral range as a function of the film thickness can be calculated. A more accurate estimation of the optimal thickness can be obtained by averaging the reflectance over the photon density and the IQE of a silicon solar cell. With this precaution, the optimal CeO<sub>2</sub> film thickness for ARC properties has been calculated to be about 60 nm. If all photons absorbed by CeO<sub>2</sub> were downshifted and absorbed by Si, 0.22 mA/cm<sup>2</sup> (0.27 mA/cm<sup>2</sup> with EVA or glass) of current would add to the total current of the cell. This value must be doubled in case of ideal DC, but is less than half the value predicted for ZnO. The higher band gap is responsible for this lower photon-converting potential. In addition, the use of glass as incoming medium increases the cone loss from 3.7% to 10%.

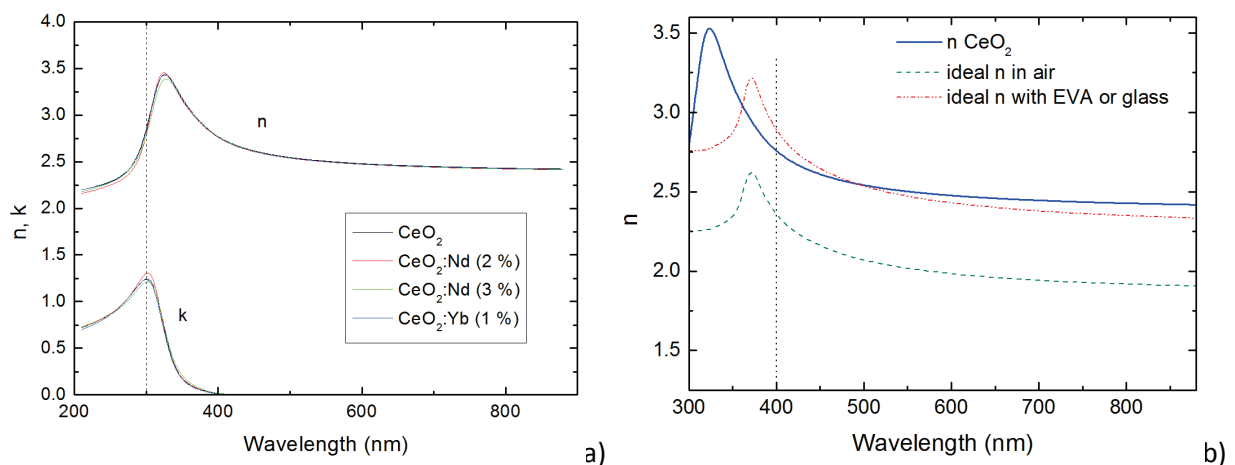


**Figure 4.10** – a) Refractive index and extinction coefficient of undoped and doped CeO<sub>2</sub> films as a function of the light wavelength. b) Typical refractive index of CeO<sub>2</sub> films compared with the ideal refractive indices calculated for air and glass as incoming media.

### Concluding remarks

So far, it has been proved that uniform RE-doped CeO<sub>2</sub> films with good ARC properties can be grown by PLD. An upper limit for sensitized DS and DC has been established. The low conductivity prevents the use of CeO<sub>2</sub> films as TCO, but if the photon converting properties are good, these layers can be used as a functionalized ARC and even combined with a TCO in a double layer structure. In the next paragraph, the photon management properties of rare earth doped CeO<sub>2</sub> films will be investigated.

### 4.2.3 Luminescence properties of RE-doped CeO<sub>2</sub>

Since the 4f shell in CeO<sub>2</sub> is empty, no optical activity is expected from the host, except that originating from lattice defects and band gap recombination. Infrared emission might occur, due to the presence of Ce<sup>3+</sup> in non-stoichiometric lattice, but the photon energy is too low to be considered for solar cell applications. Figure 4.11a-b show the PL emission spectra of undoped and RE-doped CeO<sub>2</sub> under 325 nm laser excitation. No appreciable emission due to the host is observed, compared to the strong emission originating from RE impurities. Like for the pellets, the emission spectra are composed of many lines, although the relative intensity of the lines is not the same. For example, the Yb-related emission is much weaker compared to Nd-doped films with respect to the emission observed from the relative pellets. The width of the lines is smaller than that of Nd and Yb in ZnO.

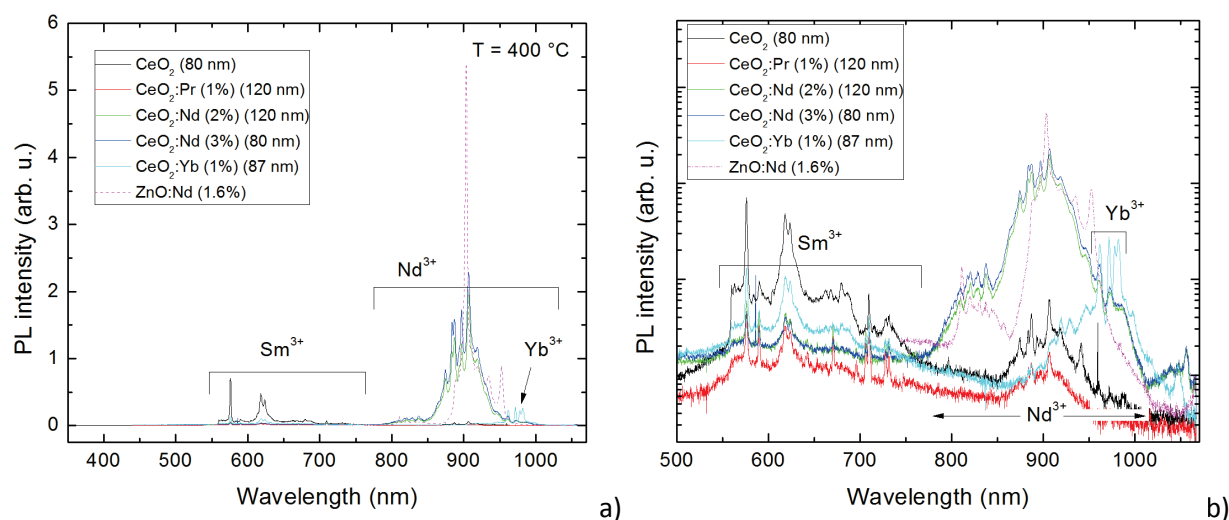


**Figure 4.11** – PL emission spectra in a) linear scale and b) log scale of undoped and RE-doped CeO<sub>2</sub> thin films under 325 nm He-Cd laser excitation. The PL of a ZnO:Nd thin film deposited at the same temperature (400 °C) is reported for reference.

A closer look to the emission spectra allows identifying the multiplets behind the observed transitions, but low temperature PL measurements would be necessary to separate the Stark components from the vibronic satellites. Figure 4.12a reports the visible emission spectrum of Sm<sup>3+</sup> and the position of the emission lines from the <sup>4</sup>G<sub>5/2</sub> level to the lower levels in LaCl<sub>3</sub>. Compared to the emission in the chloride, the emission of Sm<sup>3+</sup> in CeO<sub>2</sub> is red shifted of approximately 80 meV. This means that the <sup>4</sup>G<sub>5/2</sub> level is closer to the fundamental state.

The weaker spin-orbit splitting is typical of the oxide hosts and has been already observed for the rare earth oxides and for ZnO. Figure 4.12b reports the NIR emission spectrum of Nd<sup>3+</sup> in CeO<sub>2</sub> films. The two main emission groups observed in ZnO films and originating from transitions between the <sup>4</sup>F<sub>J</sub> multiplets to the ground state are also observed in CeO<sub>2</sub> films. The Yb<sup>3+</sup> emission spectrum is not reported because of the single excited state multiplet and of the superposition with the emission spectrum from unwanted Nd<sup>3+</sup> impurities.

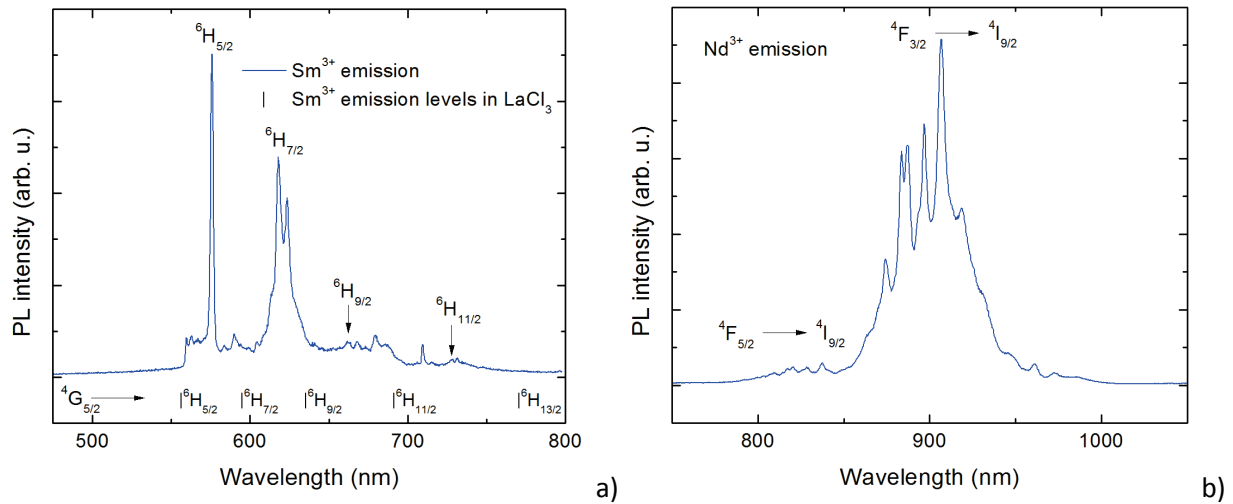


**Figure 4.12** – Emission spectra of a) Sm<sup>3+</sup> and b) Nd<sup>3+</sup> in CeO<sub>2</sub> thin films under 325 nm He-Cd laser excitation. The emission levels of Sm<sup>3+</sup> in LaCl<sub>3</sub> are reported for reference [65].

Although the PL emission spectra under UV excitation are similar to those of the pellets, the transfer mechanisms could be different. In fact, the extinction coefficient suggests that the absorption spectra of the films are different from those of the pellets. More information on the energy transfer mechanisms can be obtained by measuring the PLE. Figure 4.13a reports the PL and PLE spectra of Sm<sup>3+</sup> ions in undoped CeO<sub>2</sub> and those of Nd<sup>3+</sup> ions in CeO<sub>2</sub>:Nd (2%). In both cases, the emission mainly originates from the indirect excitation of the host and no appreciable direct excitation peaks are observed. Figure 4.13b compares the PLE with the absorption coefficient and confirms the observation made with the pellets, i.e. that the indirect excitation occurs only by exciting some electronic states below the absorption band related to CeO<sub>2</sub>. However, the center of the band is blue shifted with respect to the pellets and depends on the rare earth (343 nm for Nd and 357 nm for Sm), suggesting that different resonances are involved in the transfer mechanisms.

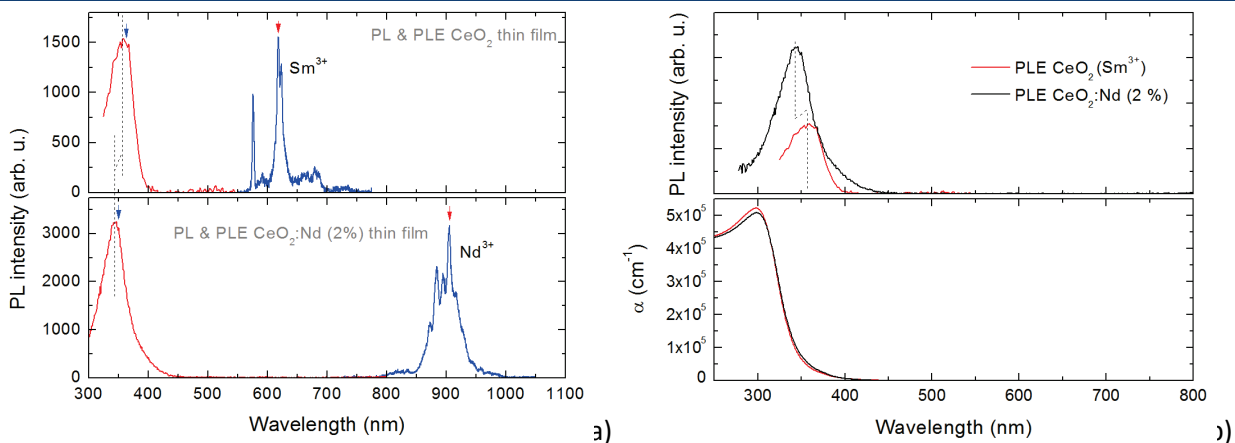


**Figure 4.13** – a) PL (blue) and PLE (red) spectra of Sm<sup>3+</sup> and Nd<sup>3+</sup> in CeO<sub>2</sub> films. b) PLE spectra of Sm<sup>3+</sup> and Nd<sup>3+</sup> in CeO<sub>2</sub> films and relative absorption coefficient calculated from the  $k$  values.

### Concluding remarks

In conclusion, in the few explored deposition conditions good-quality CeO<sub>2</sub> films have been grown on silicon substrates by PLD. All films are polycrystalline, but showed signs of partial orientation of the film.

The study of the complex refractive index showed that the rare earths do not modify the optical properties of the films and that good ARC properties are obtained when glass or EVA are used as

incoming medium. An upper limit for sensitized DC and DS processes has been calculated and turned out to be smaller than for ZnO.

Intense PL signals have been recorded from some layers by exciting the host, indicating that efficient transfer occurs to the rare earth impurities. This and the fact that no emission has been observed under direct excitation of the rare earths suggest two things: that the local environment in CeO<sub>2</sub> does not lead to a strong wavefunction mixing (and therefore the cross section of the 4f transitions is small) and that the transfer efficiency must be quite high. Of the three rare earths used (Nd, Yb, Pr), the most promising is Nd, with an emission as intense as that from Nd-doped ZnO. No emission has been detected from Pr-doped films. All the multiplets behind the observed emission lines have been identified.

Unwanted emission from rare earth impurities present in the powder complicates the analysis of the emission spectra and the association of all the lines to the respective multiplets.

In particular, intense emission is observed originating from Sm<sup>3+</sup> ions. The fact that a concentration lower than 0.05 % generates a signal almost as intense as that recorded from 3 % of Nd suggests that the transfer efficiency should be particularly high towards Sm<sup>3+</sup> ions. Sm-doped CeO<sub>2</sub> thin films are therefore very promising not only as downshifters, but also in screens and lighting applications.

## 5 CONVERTING LAYERS TESTED ON SOLAR CELLS

The main purpose of this work was to find efficient down-converting or down-shifting layers for solar cells applications by combining transparent hosts with rare earth ions. Thin films of two different hosts and doped with several rare earth ions have been tested on silicon substrates and relatively intense PL signals have been collected. Despite these promising results, quantitative estimation of the conversion efficiency or quantum yield of these films require very sophisticated setups and can be very tricky. Therefore, the best way to know the efficiency of these layers is to test them directly on solar cells. Simple in-house 1 cm<sup>2</sup> p-type Si solar cells have been selected as the best suited to test the films. The structure of the cell is illustrated in Figure 5.1. Since most films are poorly conductive, all films have been deposited on top of the metal fingers so that the carrier extraction is ensured.

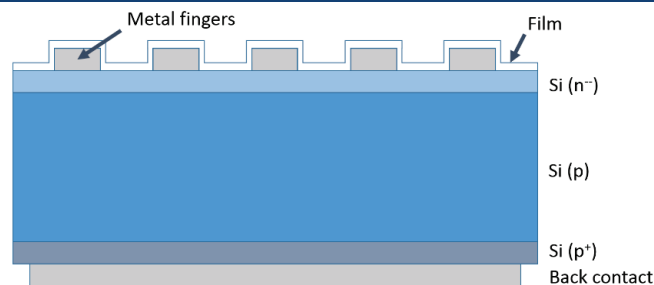


**Figure 5.1** – Schematic illustration (out of scale) of the solar cells used to test the photon converting properties of the films.

Compared to the best available silicon solar cells, the spectral response of our cells is quite low in the near infrared, close to the silicon band gap. This means that carriers generated deep in the cell are not efficiently collected. Figure 5.2 compares the internal quantum efficiency (IQE)<sup>24</sup> of our cells with that of a good silicon solar cell and situates the (best) emission spectra of Nd and Yb in ZnO with respect to the response of the cell. Although the integrated emission intensity is quite similar, the Nd emission is more efficiently absorbed by our cells.

Due to the aluminum contacts of our cells, the maximum temperature at which the films can be deposited is 400 °C. Therefore, undoped and RE-doped CeO<sub>2</sub> and ZnO films (80 - 100 nm) have been deposited on the cells at 400 °C. Figure 5.3 reports the internal quantum efficiency of the cell without film, of the cells with the undoped films and of the cells with the films that presented the highest luminescence (i.e. the Nd-doped films). In the UV part of the spectrum, the absorbance of the film reduces the spectral response of the cell. However, if part of the absorbed light was downshifted or downconverted, the spectral response of the cells with doped films should be higher than that of the cell with the undoped film and might be even higher than that of the cell without the film, given the poor surface passivation. The fact that doping does not increase the UV response reveals that the conversion efficiency is still too low to be detected.

<sup>24</sup> Number of generated carriers per absorbed photon.

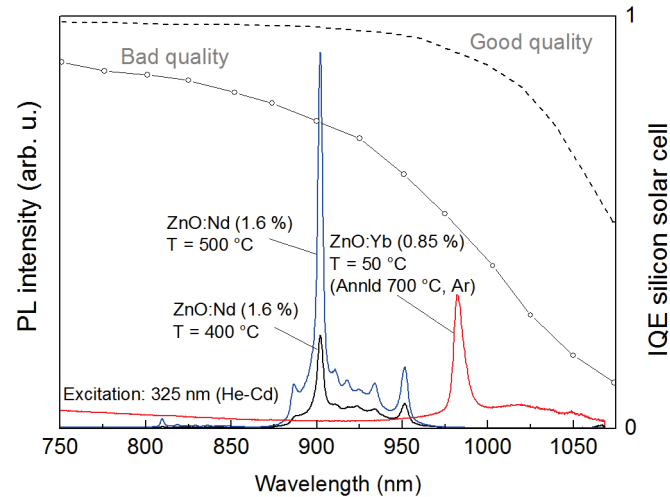


**Figure 5.2** – NIR Internal quantum efficiency of our cell and of a good cell in the market. The emission spectra of Nd and Yb in ZnO are reported for reference.

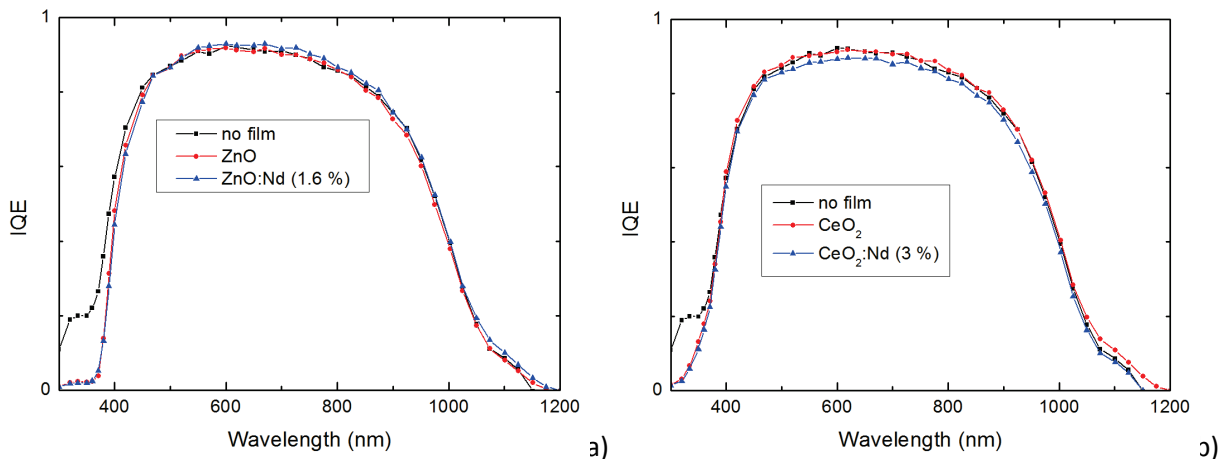


**Figure 5.3** – Internal quantum efficiency of our test cells with and without the a) ZnO:Nd and b) CeO<sub>2</sub>:Nd photon converting films.

### Concluding remarks

The most promising RE-doped ZnO and CeO<sub>2</sub> layers have been tested on silicon solar cells, but no improvement in the cell efficiency has been detected. Looking back to the results of the PL, several findings might have anticipated these negative results.

In the PLE spectra of doped ZnO films, for example, the emission under indirect excitation of the host was always comparable with that of direct excitation of the quite small concentration of RE ions. This suggested that the low photon conversion efficiency could be mainly ascribed to losses in the transfer process from the host. These losses might be due to resonance problems between the transitions and/or to competitive recombination paths. In addition, the inefficient transfer mechanism from ZnO to the rare earth ions was also indicated by the much higher emission efficiency from ZnO defects observed when the film was annealed at very high temperature (the absorbance in the film being comparable).

Similar observations can be done for doped CeO<sub>2</sub> films. For example, comparable emission intensities have been recorded from < 0.05 % of Sm and 3 % of Nd, suggesting that the transfer mechanism that excites Nd<sup>3+</sup> ions is not so efficient.

# 6 CONCLUSIONS AND PERSPECTIVES

One of the principal limits of present-day silicon solar cells is related to the intrinsic optical losses linked to use of a single junction. A promising approach that might recover these losses is to use photon-converting layers and adapt the solar spectrum to the semiconductor. This field of research has been very active in the past years and countless number of materials and geometries have been proposed. Rare earths are the key elements of most of these systems, due to their outstanding optical properties related to the partially filled f shell.

Embedding rare earth ions in transparent oxides that can be used as transparent windows on the cell is conceptually the simplest configuration. In this way, the structure of the solar cell is not modified. If the host is completely transparent, the photon conversion must rely only on the rare earth ions and their 4f transitions. However, the small absorption cross section of 4f levels is not well suited to convert a wide region of the spectrum and a reasonable absorption requires high amounts of rare earths. Due to concentration quenching, doping cannot be increased above a certain level, which means that the only way to have a large amount of rare earths is to use a thick host. If, however, an absorbing host or a sensitizing ion could transfer the absorbed energy to the rare earth, a smaller amount of material would be necessary. In the case of down-converting (DC) and down-shifting (DS) materials, which are developed to recover the thermalization losses associated with the absorption of high energy photons by a low band gap material like Si, an absorbing host can be used as sensitizer, provided that this host is transparent to the red-shifted light. For DC purposes, the layer should be placed in front of the cell and should possess a band gap value ranging between twice the gap of silicon (2.25 eV) and the highest energetic photons of the solar spectrum. The typically large absorption cross section of the host allows using thinner layers. When thin films are placed in front of the solar cell, a good refractive index matching is also required due to interference effects. The reflectance losses due to a wrong refractive index can easily cancel the positive effect of photon conversion.

The objective of this work was to investigate the photon converting properties of RE-doped transparent oxides in view of potential application on silicon solar cells. The choice of the host materials, ZnO and CeO<sub>2</sub>, has been mainly driven by the fact that ZnO is a low-cost and promising TCO and CeO<sub>2</sub> a material with a smaller ionic radius mismatch with respect to the rare earth ions. These two materials have band gaps that are significantly higher than the ideal value of 2.25 eV, thus limiting the part of the spectrum that can be down-converted. However, the refractive index matches very well that of the cell. To prepare the films, two different physical vapor deposition techniques have been used, namely sputtering and pulsed laser deposition (PLD). With these techniques, relatively high doping levels have been reached together with a uniform dopant distribution in the films.

Our sputtered ZnO films are polycrystalline and have the typical wurtzite structure. Independently of the deposition conditions, most crystallites have the c-axis oriented along the growth direction.

Three rare earths (Yb, Pr and Nd) have been successfully inserted in ZnO despite the large ionic radius mismatch and the different valence. All rare earths are optically active in the film and sensitized photon conversion through energy transfer from the host proved to be possible. In order to evaluate the possible resonances between rare earth levels that potentially lead to DC, the energy level diagram of the rare earth in the ZnO lattice is needed. However, none of these diagrams can be found in the literature. The use of powerful and very carefully optimized PL and PLE measurement setups has led to

the determination of an almost complete energy level diagram of all three rare earths in ZnO. This allowed for example understanding why the promising Pr-Yb couple is not suited for DC in ZnO.

Although all three rare earths are optically active in ZnO and can be indirectly excited through the host, the transfer efficiency strongly depends on the film properties. For example, Yb-doped films perform best after annealing at 700 °C, while Nd-doped films perform best when deposited at high temperature. The compositional and structural properties have been studied with very powerful techniques, such as very sensitive thin-film-dedicated X-ray diffraction, TEM microscopy, atom probe tomography and near-edge X-ray absorption fluorescence spectroscopy (NEXAFS). The picture arising from these data is unable to give a satisfying explanation of all the observed changes in the PL, but several advances have been made in the understanding of the transfer processes. For example, the transfer mechanisms seem to be related to the charge-compensating defect created around the trivalent rare earth ion, such as interstitial oxygen and oxygen vacancies. In the case of Yb, the observed trends in the PL are compatible with changes in the non-radiative defect concentration and in the amount of interstitial oxygen. In the case of Pr, the preparation parameters have a weaker influence on the emission intensity. Moreover, the overall emission efficiency is weaker than in the case of Yb. Non-negligible amounts of Pr<sup>4+</sup> and an energy transfer from a different type of defect could explain this low efficiency.

In the case of Nd, at least two transfer mechanisms have been observed and associated to two different active sites for Nd ions. Despite the large number of transitions involved, the careful study of the PL and PLE spectra allowed obtaining some information on these two sites. The largest part of Nd ions in the film seems to be associated to one site, related to Nd<sup>3+</sup>, for which the transfer efficiency from the matrix is low. High deposition temperatures favor the formation of a second active site (already present even at room temperature). Although the part of Nd ions in this second site is still minor, these ions are characterized by high-efficiency energy transfer from the host.

The CeO<sub>2</sub> layers deposited by PLD are polycrystalline and present few preferential orientations. XRD data show that two preferential orientations are due to the natural growth mechanisms of films on flat surfaces. The third preferential orientation suggests the presence of an epitaxial relation with the silicon substrate. Indeed, TEM data show that certain crystallites in the proximity of the silicon surface are oriented. This is probably due to the very similar lattice parameters of Si and CeO<sub>2</sub>, but it is not clear how this epitaxy is possible, given that a thin amorphous SiO<sub>2</sub> layer should exist on the substrate.

Not all rare earths used are optically active in the films. In particular, Pr showed no emission even under direct excitation, which suggests that the substitution of Ce<sup>4+</sup> ions favors the formation of Pr<sup>4+</sup>. Also the emission of Yb ions appears to be quite weak. Even considering the lower concentration, the transfer to Yb<sup>3+</sup> ions seems to be less efficient than that to Nd<sup>3+</sup> ions and, curiously, both transfer mechanisms seem to be less efficient than the transfer to Sm<sup>3+</sup> ions, which exist as impurity in the CeO<sub>2</sub> powder.

All considerations about the efficiency in this work are purely qualitative and are based on the relative intensity of the recorded signals using the same measurement setup. Quantitative estimation of the efficiency of these processes is a very difficult task and can be attempted only using more sophisticated setups including an integrating sphere. Therefore, the easiest way to test these layers is to apply them on solar cells and to measure the spectral response. If the layers work, an increase of the response of the cell is expected upon doping with respect to the undoped layers, in the region where the film absorbs. The cells that have been chosen in this work are simple Si p-n junctions with a back-surface field and metal contacts, upon which the film has been deposited.

By analyzing the data of the internal quantum efficiency, it turned out that even the most promising down-shifting layers (in both cases the Nd-doped films) have no positive effect on the cell efficiency with respect to the undoped films. This suggests that the absolute transfer efficiency from the host to the

rare earth ions is rather low. The reasons behind this low transfer efficiency can be innumerable and the difficulty of achieving efficient DS and DC has been already explained in the introductory section. In brief, it can be said that the ideal photon converting material has many requirements that are not easily met in real systems. One of the main reasons is that even in the simplest case, the photon conversion process is a multistep process that involves resonances between electronic transitions. In addition, unless a single rare earth is charged for the whole process, these transitions are usually separated in space and often require the interaction with phonons. The efficiency of all these processes is far from ideal and can easily damp the total efficiency of several orders of magnitude.

Despite the negative results, the study of these systems is fundamental to understand how the best photon-converting layer should be build, what materials should be used, in which geometry and if these processes are really suited for solar cell applications. The fact that these layers must enter the solar cell structure without decreasing the cell efficiency impose a trade-off between many parameters and shortens the list of available materials. For example, ZnO and CeO<sub>2</sub> have an appropriate refractive index to be used as anti-reflection coatings, but the large band gap limits the maximum current gains in the case of DC to 0.54 and 0.22 mA/cm<sup>2</sup>, respectively. For comparison, the extra current made available by DC using an ideal absorber is around 9.7 mA/cm<sup>2</sup> and increases the efficiency of the cell of about 10 % points. This means that ideal DC using these hosts can only lead to an increase of the cell efficiency smaller than 1 % point. When non-ideal transfer mechanisms are considered, the efficiency gain is further reduced.

In conclusion, RE-doped transparent oxide films are a viable low-cost solution for obtaining photon-converting layers that can be applied on solar cells. This work proves that the efficiencies reached by doping ZnO and CeO<sub>2</sub> with Yb, Pr and Nd are not sufficient to observe an increase of the solar cell efficiency. Other hosts and luminescent species are waiting to be tested and the fact that these materials are attractive for other fields of technology, such as screens and lighting, should encourage to continue the research towards other materials even if the possibility of application in solar technology are scarce.



## APPENDIX A - Russell-Saunders term symbols

In quantum mechanics, the Russell-Saunders notation describes the angular momentum quantum numbers of a multi-electron atom, assuming an LS coupling.

In this notation (also called *spectroscopic notation*),  $S$  is the total spin quantum number,  $J$  the total angular momentum quantum number and  $L$  is the total orbital momentum quantum number.

The nomenclature for  $L$  derives from the spectroscopic lines corresponding to s, p, d, f orbitals ( $l = 0, 1, 2, 3$ , respectively): sharp, diffuse, principal, fundamental.

|            |          |          |          |          |          |          |          |          |            |
|------------|----------|----------|----------|----------|----------|----------|----------|----------|------------|
| <b>L =</b> | <b>0</b> | <b>1</b> | <b>2</b> | <b>3</b> | <b>4</b> | <b>5</b> | <b>6</b> | <b>7</b> | <b>...</b> |
|            | <b>S</b> | <b>P</b> | <b>D</b> | <b>F</b> | <b>G</b> | <b>H</b> | <b>I</b> | <b>K</b> | <b>...</b> |

The combination of an  $S$  value and an  $L$  value  $^{2S+1}L$  is called a *term*, the combination of  $S$ ,  $L$  and  $J$  is called a *level* and the combination of  $S$ ,  $L$ ,  $M$  and  $M_J$  is called a *state*. The ground state level is predicted by Hund's rules<sup>25</sup>.

*Example: the ground state of fluorine*

The electronic configuration is  $1s^2 2s^2 2p^5$ . Full shell must be discarded, so that only the partially filled p shell is considered. The p shell has three orbitals ( $m_l = 1, 0, -1$ ) that can hold up to 6 electrons. The ground state configuration is given by the Pauli exclusion principle:

|                         |                         |           |           |
|-------------------------|-------------------------|-----------|-----------|
|                         | <b><math>m_l</math></b> |           |           |
|                         | <b>+1</b>               | <b>0</b>  | <b>-1</b> |
| <b><math>m_s</math></b> | <b>↑↓</b>               | <b>↑↓</b> | <b>↑</b>  |

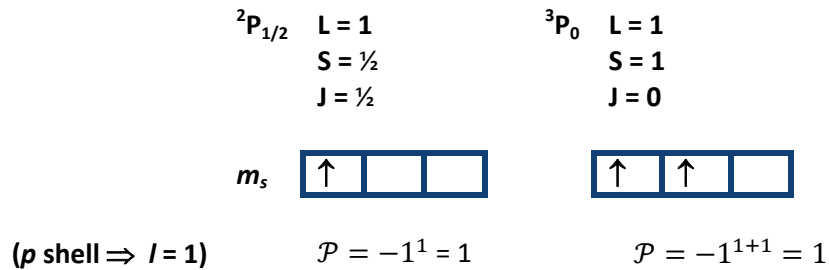
The overall  $S$  is calculated by adding the  $m_s$  values ( $S = \frac{1}{2} + \frac{1}{2} + \frac{1}{2} - \frac{1}{2} - \frac{1}{2} = \frac{1}{2}$ ) and the overall  $L$  is calculated by adding the  $m_l$  values ( $L = 1 + 0 - 1 + 1 + 0 = 1$ ) for each electron. The calculation of  $J$  depends on the shell occupation. If less than half the shell is occupied,  $J$  takes its minimum value  $J = |L - S|$ . If it is more than half filled, it takes the maximum value  $J = |L + S|$  and if it is half filled,  $L = 0$  and  $J = S$ . Thus, in the case of fluorine, the ground state is  $^2P_{3/2}$ .

The parity of a term symbol is calculated as  $\mathcal{P} = -1^{\sum l_i}$ , where  $l_i$  is the orbital quantum number of each electron. Only electrons in odd orbitals (p, f, ...) contribute to the total parity. An odd number of electrons in an odd orbital will make an odd term symbol.

<sup>25</sup> Hund's rules should not be used to predict the order of states other than the ground state.

---

Example: parity of the ground state of the two smallest occupations of the p shell



${}^2P_{1/2}$  has odd parity, while  ${}^3P_0$  has even parity

---

Excited states are formed when the electrons are distributed in the p shell in a different configuration with respect to that of lowest energy. For example, the ground state of the  $2p^2$  configuration is  ${}^3P_0$ . If the two electrons both have  $m_l = +1$  (both electrons in the first case  $\begin{array}{|c|} \hline \uparrow \downarrow \\ \hline \end{array}$ ), the spectroscopic term associated with the excited level is  ${}^1D_2$ . The fact that these levels have different  $L$  values might induce to think that the two states have different parity. However, as long as the number of the electrons in the p shell is not modified, parity is unchanged because related to  $l_i$ .

The electric dipole operator being an odd operator, radiative transition between excited states of the same shell are dipole-forbidden.

---

## APPENDIX B - The 32 crystallographic point groups

In crystallography, a crystallographic point group is a set of symmetry operations, like rotations or reflections, that leave a central point fixed while moving other directions and faces of the crystal to the positions of features of the same kind. For a periodic crystal (as opposed to a quasicrystal), the group must also be consistent with maintenance of the three-dimensional translational symmetry that defines crystallinity. The point groups are denoted by their component symmetries. There are a few standard notations used by crystallographers, mineralogists, and physicists.

In Schönflies notation, point groups are denoted by a letter symbol with a subscript. The symbols used in crystallography mean the following:

- $C_n$  (for cyclic) indicates that the group has an  $n$ -fold rotation axis.  $C_{nh}$  is  $C_n$  with the addition of a mirror (reflection) plane perpendicular to the axis of rotation.  $C_{nv}$  is  $C_n$  with the addition of a mirror plane parallel to the axis of rotation.
- $S_{2n}$  (for Spiegel, German for mirror) denotes a group that contains only a  $2n$ -fold rotation-reflection axis.
- $D_n$  (for dihedral, or two-sided) indicates that the group has an  $n$ -fold rotation axis plus  $n$  twofold axes perpendicular to that axis.  $D_{nh}$  has, in addition, a mirror plane perpendicular to the  $n$ -fold axis.  $D_{nd}$  has, in addition to the elements of  $D_n$ , mirror planes parallel to the  $n$ -fold axis.
- The letter  $T$  (for tetrahedron) indicates that the group has the symmetry of a tetrahedron.  $T_d$  includes improper rotation operations,  $T$  excludes improper rotation operations, and  $T_h$  is  $T$  with the addition of an inversion.
- The letter  $O$  (for octahedron) indicates that the group has the symmetry of an octahedron (or cube), with ( $O_h$ ) or without ( $O$ ) improper operations (those that change handedness).

Due to the crystallographic restriction theorem,  $n = 1, 2, 3, 4, \text{ or } 6$  in 2- or 3-dimensional space.

Table B1 reports the 32 crystallographic point groups expressed in the Schönflies and Hermann-Mauguin notations. The symmetry order is indicated by the letter  $g$  and represents the number of symmetry axes or planes. The group with maximal symmetry is the cubic  $O_h$  group.

The groups important for crystal symmetry are mostly related to the cyclic groups  $C_g$ , where the generating element  $a$  represents a rotation about a fixed axis through an angle  $h/g$ , and the group consists of  $a$  and all its powers up to  $ag = e$ . All cyclic groups are Abelian. For crystal symmetry, only  $C_1, C_2, C_3, C_4,$  and  $C_6$  occur. All the non-cubic crystallographic groups are simple extensions of the cyclic group, which are obtained by adding to the elements of the cyclic group one or more generating elements  $b, c$  of order 2. The geometrical significance of these additional elements is a rotation about a twofold axis, a reflection at a symmetry plane, or an inversion. Always  $b^2 = e$ .

**Table B1** – The 32 crystallographic point groups (18 different groups). The symmetry increases

|  | S <sup>a</sup> | HM <sup>b</sup>   | Order (g) | Center of symmetry | Isomorphism                 |
|--|----------------|-------------------|-----------|--------------------|-----------------------------|
| <b>Triclinic</b>                           |                |                   |           |                    |                             |
| 1  | $C_1$          | 1                 | 1         |                    |                             |
| 2  | $C_i = S_2$    | $\bar{1}$         | 2         | v                  | $C_2$                       |
| <b>Monoclinic</b>                          |                |                   |           |                    |                             |
| 3  | $C_2$          | 2                 | 2         |                    |                             |
| 4  | $C_s = C_{1h}$ | M                 | 2         |                    | $C_2$                       |
| 5  | $C_{2h}$       | 2/m               | 4         | v                  | $D_2 = C_2 \times C_2$      |
| <b>Orthorombic</b>                         |                |                   |           |                    |                             |
| 6  | $D_2 = V$      | 222               | 4         |                    | $C_2 \times C_2$            |
| 7  | $C_{2v}$       | mm2               | 4         |                    | $D_2 = C_2 \times C_2$      |
| 8  | $D_{2h} = V_h$ | 2/m 2/m 2/m       | 8         | v                  | $C_2 \times C_2 \times C_2$ |
| <b>Trigonal (rhombohedral)<sup>c</sup></b> |                |                   |           |                    |                             |
| 9  | $C_3$          | 3                 | 3         |                    |                             |
| 10   | $C_{3i} = S_6$ | $\bar{3}$         | 6         | v                  | $C_2 \times C_2 \times C_2$ |
| 11   | $D_3$          | 32                | 6         |                    |                             |
| 12   | $C_{3v}$       | 3m                | 6         |                    | $D_3$                       |
| 13   | $D_{3d}$       | 32/m              | 12        | v                  | $D_6$                       |
| <b>Tetragonal</b>                          |                |                   |           |                    |                             |
| 14   | $C_4$          | 4                 | 4         |                    |                             |
| 15   | $S_4$          | $\bar{4}$         | 4         |                    | $C_4$                       |
| 16   | $C_{4h}$       | 4/m               | 8         | v                  | $C_4 \times C_2$            |
| 17   | $D_4$          | 422               | 8         |                    |                             |
| 18   | $C_{4v}$       | 4mm               | 8         |                    | $D_4$                       |
| 19   | $D_{2d} = V_d$ | $\bar{4} 2m$      | 8         |                    | $S_{4v} = D_4$              |
| 20   | $D_{4h}$       | 4/m 2/m 2/m       | 16        | v                  | $D_4 \times C_2$            |
| <b>Hexagonal</b>                           |                |                   |           |                    |                             |
| 21   | $C_6$          | 6                 | 6         |                    |                             |
| 22   | $C_{3h}$       | $\bar{6} = 3/m$   | 6         |                    | $S_6, C_6$                  |
| 23   | $C_{6h}$       | 6/m               | 12        | v                  | $C_6 \times C_2$            |
| 24   | $D_6$          | 622               | 12        |                    |                             |
| 25   | $C_{6v}$       | 6mm               | 12        |                    | $D_6$                       |
| 26   | $D_{3h}$       | 6m2               | 12        |                    | $D_6$                       |
| 27   | $D_{6h}$       | 6/m 2/m 2/m       | 24        | v                  | $D_6 \times C_2$            |
| <b>Cubic</b>                               |                |                   |           |                    |                             |
| 28   | $T$            | 23                | 12        |                    | $A_4$                       |
| 29   | $T_d$          | $\bar{4} 3m$      | 24        |                    | O                           |
| 30   | $T_h$          | 2/m $\bar{3}$     | 24        | v                  | $T \times C_2$              |
| 31   | $O$            | 432               | 25        |                    | $\pi_4$                     |
| 32   | $O_h$          | 4/m $\bar{3} 2/m$ | 48        | v                  | $O \times C_2$              |

<sup>a</sup> S = Schönflies symbols

<sup>b</sup> HM = Hermann-Mauguin (International) symbols

<sup>c</sup> Trigonal and rhombohedral are often confused with each other. However, crystals in the rhombohedral lattice system are always in the trigonal crystal system, but some crystals such as quartz are in the trigonal crystal system but not in the rhombohedral lattice system.

## APPENDIX C – d-spacings and lattice constants

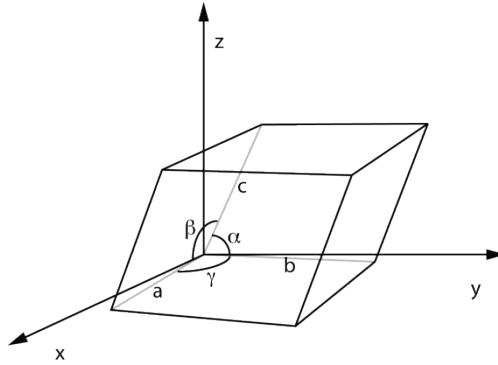


Figure C1 - Lattice unit cell in the most general case

The  $d$ -spacings are related to the lattice parameters ( $a, b, c$ ) forming the unit cell of the lattice. In the most general case, in which the lattice unit cell has no square angle (see Figure C1), the following relation holds

$$\begin{aligned} \mathbf{d}_{hkl}^* \cdot \mathbf{d}_{hkl}^* &= (h\mathbf{a}^* + k\mathbf{b}^* + l\mathbf{c}^*)(h\mathbf{a}^* + k\mathbf{b}^* + l\mathbf{c}^*) = \\ &= h^2 a^{*2} + k^2 b^{*2} + l^2 c^{*2} + 2hka^*b^* \cos \gamma^* + 2klb^*c^* \cos \alpha^* + 2lhc^*a^* \cos \beta^* \end{aligned}$$

thus

$$\begin{aligned} \frac{1}{d_{hkl}^2} &= h^2 \frac{b^2 c^2 \sin^2 \alpha}{V^2} + k^2 \frac{a^2 c^2 \sin^2 \beta}{V^2} + l^2 \frac{a^2 b^2 \sin^2 \gamma}{V^2} \\ &+ 2hk \frac{abc^2 (\cos \alpha \cos \beta - \cos \gamma)}{V^2} + 2kl \frac{a^2 bc (\cos \beta \cos \gamma - \cos \alpha)}{V^2} \\ &+ 2lh \frac{ab^2 c (\cos \gamma \cos \alpha - \cos \beta)}{V^2} \end{aligned}$$

In the case of the hexagonal wurtzite cell of ZnO, the relation is simplified as

$$\frac{1}{d_{hkl}^2} = \frac{4}{3} \frac{h^2 + k^2 + hk}{a^2} + \frac{l^2}{c^2}$$

And in the case of the cubic CeO<sub>2</sub> lattice

$$\frac{1}{d_{hkl}^2} = \frac{h^2 + k^2 + l^2}{a^2}$$

In the case of a cubic crystal, the measurement of  $d$  for one single arbitrary direction is sufficient to determine  $a$ . In general, however, more than one measurement is necessary. When possible, it is convenient to measure the  $d$  spacing along directions in which two of the Miller indices are zero.

---

## APPENDIX D – Optical absorption and band structure

Optical measurement constitutes the most-important means of determining the band structures of semiconductors. Photon-induced electronic transitions can occur between different bands or within a single band such as the free-carrier absorption.

Since the absorption cannot be measured directly, the absorption coefficient  $\alpha(E)$  must be calculated from other measurements. For example, a rough calculation of  $\alpha$  from reflectance and transmittance measurements is possible when the material is surrounded by a transparent medium. A second, in certain cases more accurate, method involves the calculation of the extinction coefficient  $k$  from ellipsometric data. For thin films on opaque substrates and relatively flat surfaces, and using an appropriate dispersion formula, this second method proved to give the best results.

Once  $k$  is known, the absorption coefficient at a certain photon wavelength  $\lambda$  can be calculated as  $\alpha(\lambda) = 2\pi k(\lambda)/\lambda$ .

In the case of semiconductors and insulators, the absorption coefficient can be used to determine the optical gap  $E_g^{\text{opt}}$ .

The behavior of the absorption in crystalline solids can be successfully modelled and the interpretation of the optical gap lays on solid grounds.

Covalent crystalline solids will be considered in which the one-electron wavefunctions are delocalized Bloch functions specified by the electron wavevector  $\vec{k}$  and defined such that the normalization or probability integral is unity when taken over the entire crystal. The Bloch functions can be written as:

$$\phi_v(\vec{r}, \vec{k}_v) = \frac{u_{\vec{k}_v}(\vec{r}) \exp(i\vec{k}_v \cdot \vec{r})}{\sqrt{\Omega}}$$

where the index  $v$  distinguishes states in different bands and  $\Omega$  is the volume of the crystal. Here,  $u_{\vec{k}_v}$  is the part of the Bloch functions having the periodicity of the lattice, i.e.,  $u_{\vec{k}_v}(\vec{r}) = u_{\vec{k}_v}(\vec{r} + \vec{R}_l)$ , where  $\vec{R}_l$  is a lattice vector [260].

In this case, one must distinguish between *direct* interband transitions between Bloch wavefunctions in which  $k$  is virtually unchanged in the transitions and *indirect* interband transitions in which  $k$  changes significantly due to an interaction of the electron wave with vibrations of the crystalline lattice.

Ionic crystalline solids exhibit a behavior that could be considered intermediate between the covalent solids with delocalized electronic wavefunctions and weakly interacting atoms with atomic wavefunctions. If the one-electron wavefunctions are localized as in a highly ionic solid, however, the wavefunctions must be considered as a sum of Bloch functions with a wide range of  $k$  values. As a result, the transitions in these materials have been called non-direct, i.e., there is no apparent dependence on  $k$  in the optical absorption process [261]. Similar such non-direct behavior occurs in amorphous semiconductors, in which the lack of atomic periodicity in the network implies that the electron crystal momentum  $\hbar\vec{k}$  is no longer a valid quantum number for describing the one-electron wavefunction. The empirical formula describing amorphous semiconductors will be given later in the text.

If exciton formation (electron-hole interaction) is neglected, the form of the absorption coefficient  $\alpha(E)$  as a function of photon energy  $E$  is related to the dependence on energy of the density of states  $N(E)$  of the bands containing the initial and final states.

There exist two types of band-to-band transitions: allowed and forbidden. Forbidden transitions take into account the small but finite momentum of photons and are much less probable. For direct band gap materials, transitions mostly occur between two bands of the same  $k$  value, as transitions (a) and (b) in

Figure D1. While allowed direct transitions can occur in all  $k$  values, forbidden direct transitions can only occur at  $k \neq 0$ . In the following, forbidden transitions will not be considered.

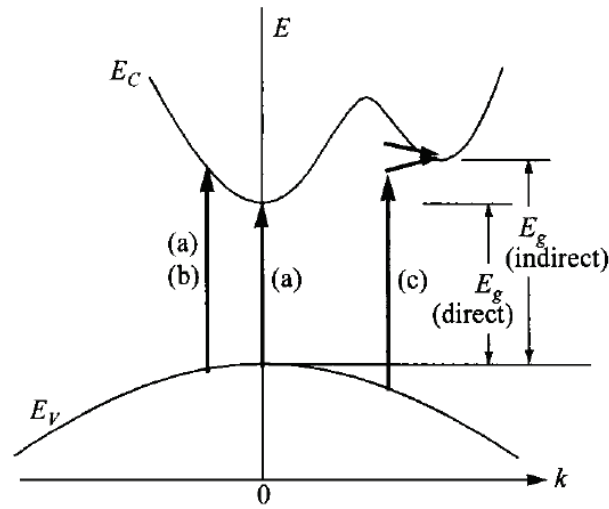


**Figure D1** - Optical transitions: (a) allowed and (b) forbidden direct transitions; (c) indirect transition involving phonon emission (upper arrow) and phonon absorption (lower arrow).

### Direct transitions

In treating crystalline semiconductors, it is assumed that the crystalline solid is optically isotropic and that transitions occur from valence band ( $v$ ) to conduction band ( $c$ ) states each characterized by the same electron wavevector  $k$ . Moreover, transitions are considered as occurring from a set of one-electron Bloch states in completely occupied valence bands ( $v$ ) (Partially filled bands leading to intraband transitions are not considered).

In the case of a semiconductor with both valence and conduction bands that are parabolic and isotropic in  $k$ -space, one has:

$$E_{c-v}(\vec{k}) = E_g + \frac{\hbar^2 k^2}{2\mu_{cv}}$$

$E_{cv}(\vec{k})$  is the energy difference between the pair of conduction and valence band states and  $\mu_{cv}$  is the reduced effective mass

$$\frac{1}{\mu_{cv}} = \frac{1}{m_e} + \frac{1}{m_h}$$

With the additional assumption that the momentum matrix element is nearly constant over the range of  $k$  of interest, and defines a mean-square value of the momentum matrix elements, then [260]:

$$\alpha(E)n(E)E \propto (E - E_g)^{1/2}; \quad E > E_g$$

$$\alpha(E) = 0; \quad E < E_g$$

In most cases, the dependence of the refractive index  $n$  on the energy can be neglected and the equation reads:

$$\alpha(E)E \propto (E - E_g)^{1/2}; \quad E > E_g$$

The band gap value can then be determined by plotting  $(\alpha E)^2$  over the photon energy and extrapolating the intersection of the linear part of the curve with the x-axis. This sort of graph is called Tauc plot, as it has been drawn for the first time by Tauc in the 60's [262, 263].

Although this equation is designed to be used in such applications near the absorption onset for the lowest energy direct transitions in semiconductors, the one-electron model breaks down under these circumstances. In fact, the inclusion of the effects of many-body interactions is required here for a complete understanding of the shape of the experimental absorption spectra. Specifically, a Coulomb interaction binds the excited electron and the hole left behind in the valence band, forming an exciton.

Therefore, using a Tauc plot to determine the band gap of crystalline materials does not yield the value of  $E_g^{\text{opt}}$  defined as the gap between the conduction and valence band, but only a threshold energy at which the absorption starts.

### Indirect transitions

The interaction of a classical electromagnetic wave with an electron in a perfect lattice can only lead to direct transitions in which  $k$  is conserved. If one considers possible interactions of the electron with imperfections of the lattice, then  $k$ -conservation in the electron transitions is relaxed, and this gives rise to indirect transitions. Quantized lattice vibrations, or phonons, constitute an important source of imperfections and are unavoidable even in a perfect crystal.

Because of the second order nature of this process, it is necessary to use second order perturbation theory.

It is sufficient here to consider only (i) transitions from a single valence band maximum at  $k=0$  to a single conduction band minimum away from the Brillouin zone center, and (ii) single phonon absorption or emission. In addition, all other valence and conduction bands are assumed to be distant in energy so that only two intermediate states designated 'a' and 'b' need to be considered as shown in Figure D2.

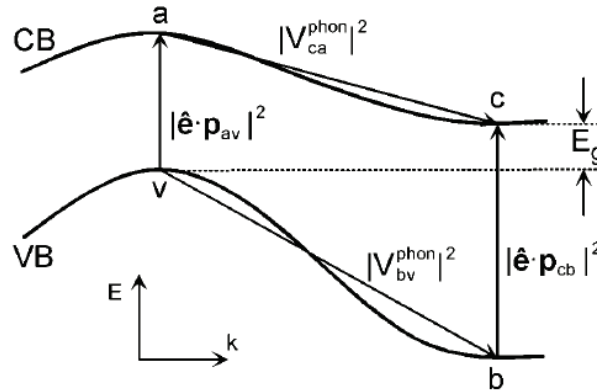


**Figure D2** - Semiconductor band diagram showing two possible pathways for the indirect excitation of an electron from the valence band (VB) maximum  $v$  to the conduction band (CB) minimum  $c$ . In one case, the electron is excited in a virtual direct transition to  $a$  followed by phonon-assisted scattering to  $c$ . In the other case, an electron is excited in a direct transition from  $b$  to  $c$ , and the hole left behind is scattered to  $v$ . The matrix elements describing the electron-photon and electron-phonon coupling for the transitions are included.

The transition rates for the two pathways increase as the square of the lifetimes in the intermediate states. By integrating over all possible transitions one can arrive at the following practical formulas that incorporate the absorption coefficient

$$\alpha(E)n(E)E(E_{a-v} - E)^2 = \frac{C}{\exp(\beta_{\vec{k}}) - 1} (E + \hbar\omega_{p\vec{k}} - E_g)^2; \quad E > E_{c-v} - \hbar\omega_{p\vec{k}}$$

$$\alpha(E)n(E)E(E_{a-v} - E)^2 = \frac{C' \exp(\beta_{\vec{k}})}{\exp(\beta_{\vec{k}}) - 1} (E - \hbar\omega_{p\vec{k}} - E_g)^2; \quad E > E_{c-v} + \hbar\omega_{p\vec{k}}$$

In these expressions,  $E$  is the photon energy,  $C$  and  $C'$  are constants, and  $\beta_{\vec{k}} = \hbar\omega_{p\vec{k}}/k_B T$ , where  $k_B$  is Boltzmann's constant. For photon energies below the specified ranges,  $\alpha(E) = 0$ .

Over a sufficiently narrow range one can neglect all photon-energy dependent terms on the left except for  $\alpha$  in applying these formulas to identify indirect transitions.

In deriving these equations, one assumes that the momentum matrix element connecting the valence and conduction band states near  $k = 0$  is independent of energy. This is invalid when the dominant direct transition here is forbidden. A derivation in this case leads to analogous equations, but with the quadratic dependence replaced by the cubic dependence  $(E - \hbar\omega_{p\vec{k}} - E_g)^3$ .

### **Amorphous semiconductors**

There is no well established theoretical model describing the band structure of amorphous semiconductors, due to the complexity of the behavior of electrons in disordered structures. Tauc and Mott independently derived an empirical equation for the optical band transition of amorphous materials, which has the same form as that for direct allowed transitions in crystalline materials:

$$\alpha = B \frac{(h\nu - E_g)^2}{h\nu}$$

---

---

## References

- [1] IEA World Energy Outlook 2013, Chapter 6 - Renewable Energy Outlook.
- [2] IEA report 2011 - Renewable energies technologies, Solar energy perspectives.
- [3] GTM Research - PV Technology and Cost Outlook 2013-2017.
- [4] Richards, B.S., *Enhancing the Performance of Silicon Solar Cells via the Application of Passive Luminescence Conversion Layers*. Solar Energy Materials and Solar Cells, 90, 15, **2006**. p. 2329-2337.
- [5] Shockley, W. and H.J. Queisser, *Detailed Balance Limit of Efficiency of p-n Junction Solar Cells*. Journal of Applied Physics, 32, 3, **1961**. p. 510-519.
- [6] Landsberg, P.T., *Thermodynamics and Statistical Mechanics*. **1990**, Dover, New York.
- [7] Green, M.A., *Third Generation Photovoltaics*. Springer Series in Photonics. Vol. 12. **2003**. Springer. 162.
- [8] Martí, A. and G.L. Araújo, *Limiting efficiencies for photovoltaic energy conversion in multigap systems*. Solar Energy Materials and Solar Cells, 43, 2, **1996**. p. 203-222.
- [9] Green, M.A., *Third generation photovoltaics: solar cells for 2020 and beyond*. Physica E: Low-dimensional Systems and Nanostructures, 14, 1–2, **2002**. p. 65-70.
- [10] Green, M.A., *Third generation photovoltaics: Ultra-high conversion efficiency at low cost*. Progress in Photovoltaics: Research and Applications, 9, 2, **2001**. p. 123-135.
- [11] Conibeer, G., *Third-generation photovoltaics*. Materials Today, 10, 11, **2007**. p. 42-50.
- [12] Hirst, L.C. and N.J. Ekins-Daukes, *Fundamental losses in solar cells*. Progress in Photovoltaics: Research and Applications, 19, 3, **2011**. p. 286-293.
- [13] McGuire, J.A., J. Joo, J.M. Pietryga, R.D. Schaller, and V.I. Klimov, *New Aspects of Carrier Multiplication in Semiconductor Nanocrystals*. Accounts of Chemical Research, 41, 12, **2008**. p. 1810-1819.
- [14] Takeda, Y. and T. Motohiro, *Requisites to realize high conversion efficiency of solar cells utilizing carrier multiplication*. Solar Energy Materials and Solar Cells, 94, 8, **2010**. p. 1399-1405.
- [15] Würfel, P., *Solar energy conversion with hot electrons from impact ionisation*. Solar Energy Materials and Solar Cells, 46, 1, **1997**. p. 43-52.
- [16] Trupke, T., M.A. Green, and P. Würfel, *Improving solar cell efficiencies by up-conversion of sub-band-gap light*. Journal of Applied Physics, 92, 7, **2002**. p. 4117-4122.
- [17] Trupke, T., M.A. Green, and P. Würfel, *Improving solar cell efficiencies by down-conversion of high-energy photons*. Journal of Applied Physics, 92, 3, **2002**. p. 1668-1674.
- [18] Trupke, T., A. Shalav, B.S. Richards, P. Würfel, and M.A. Green, *Efficiency enhancement of solar cells by luminescent up-conversion of sunlight*. Solar Energy Materials and Solar Cells, 90, 18–19, **2006**. p. 3327-3338.
- [19] Abrams, Z.R., A. Niv, and X. Zhang, *Solar energy enhancement using down-converting particles: A rigorous approach*. Journal of Applied Physics, 109, 11, **2011**. p. 114905 - 114905-9.
- [20] Hovel, H.J., R.T. Hodgson, and J.M. Woodall, *The effect of fluorescent wavelength shifting on solar cell spectral response*. Solar Energy Materials, 2, 1, **1979**. p. 19-29.
- [21] Danos, L., T. Parel, T. Markvart, V. Barrioz, W.S.M. Brooks, and S.J.C. Irvine, *Increased efficiencies on CdTe solar cells via luminescence down-shifting with excitation energy transfer between dyes*. Solar Energy Materials and Solar Cells, 98, **2012**. p. 486-490.
- [22] Kalytchuk, S., *et al.*, *Semiconductor Nanocrystals as Luminescent Down-Shifting Layers To Enhance the Efficiency of Thin-Film CdTe/CdS and Crystalline Si Solar Cells*. The Journal of Physical Chemistry C, 118, 30, **2014**. p. 16393-16400.
- [23] Luque, A. and A. Martí, *Theoretical Limits of Photovoltaic Conversion*, in *Handbook of Photovoltaic Science and Engineering*. **2005**. John Wiley & Sons, Ltd. p. 113-151.

- 
- [24] Goldschmidt, J.C., *Novel Solar Cell Concepts*. PhD Thesis, **2009**, Universität Konstanz / Fraunhofer institute for solar energy systems (ISE)
- [25] Yablonoitch, E., *Thermodynamics of the fluorescent planar concentrator*. Journal of the Optical Society of America, 70, 11, **1980**. p. 1362-1363.
- [26] van Sark, W.G.J.H.M., *Luminescent solar concentrators – A low cost photovoltaics alternative*. Renewable Energy, 49, **2013**. p. 207-210.
- [27] Dexter, D.L., *A Theory of Sensitized Luminescence in Solids*. The Journal of Chemical Physics, 21, 5, **1953**. p. 836-850.
- [28] Dexter, D.L., *Possibility of Luminescent Quantum Yields Greater than Unity*. Physical Review, 108, 3, **1957**. p. 630-633.
- [29] Piper, W.W., J.A. DeLuca, and F.S. Ham, *Cascade fluorescent decay in Pr<sup>3+</sup>-doped fluorides: Achievement of a quantum yield greater than unity for emission of visible light*. Journal of Luminescence, 8, 4, **1974**. p. 344-348.
- [30] Sommerdijk, J.L., A. Bril, and A.W. de Jager, *Two photon luminescence with ultraviolet excitation of trivalent praseodymium*. Journal of Luminescence, 8, 4, **1974**. p. 341-343.
- [31] Bloembergen, N., *Solid State Infrared Quantum Counters*. Physical Review Letters, 2, 3, **1959**. p. 84-85.
- [32] Auzel, F., *Upconversion and Anti-Stokes Processes with f and d Ions in Solids*. Chemical Reviews, 104, 1, **2004**. p. 139-174.
- [33] Auzel, F., *Up-conversions in RE-doped Solids*, in *Spectroscopic Properties of Rare Earths in Optical Materials*, Ch. 5, R. Hull, et al., Editors. **2005**. Springer Berlin Heidelberg. p. 266-319.
- [34] Zhang, Q.Y. and X.Y. Huang, *Recent progress in quantum cutting phosphors*. Progress in Materials Science, 55, 5, **2010**. p. 353-427.
- [35] Förster, T., *Zwischenmolekulare Energiewanderung und Fluoreszenz*. Annalen der Physik, 437, 1-2, **1948**. p. 55-75.
- [36] Desurvier, E.D., *Erbium-doped Fiber Amplifiers: Principles and Applications*. **1994**. Wiley, New York.
- [37] Nalwa H.S., R.L.S., *Handbook of luminescence, display materials and devices*. Vol. 2 - Inorganic Display Materials **2003**. American Scientific Publisher.
- [38] Kenyon, A.J., *Recent developments in rare-earth doped materials for optoelectronics*. Progress in Quantum Electronics, 26, 4–5, **2002**. p. 225-284.
- [39] Miyakawa, T. and D.L. Dexter, *Phonon Sidebands, Multiphonon Relaxation of Excited States, and Phonon-Assisted Energy Transfer between Ions in Solids*. Physical Review B, 1, 7, **1970**. p. 2961-2969.
- [40] Reisfeld, R., *Excited states and energy transfer from donor cations to rare earths in the condensed phase*, in *Rare Earths*, Ch. 2. **1976**. Springer Berlin Heidelberg. p. 65-97.
- [41] van Dijk, J.M.F. and M.F.H. Schuurmans, *On the nonradiative and radiative decay rates and a modified exponential energy gap law for 4f–4f transitions in rare-earth ions*. The Journal of Chemical Physics, 78, 9, **1983**. p. 5317-5323.
- [42] Schuurmans, M.F.H. and J.M.F. van Dijk, *On radiative and non-radiative decay times in the weak coupling limit*. Physica B+C, 123, 2, **1984**. p. 131-155.
- [43] Suyver, J.F., J. Grimm, K.W. Krämer, and H.U. Güdel, *Highly efficient near-infrared to visible up-conversion process in NaYF<sub>4</sub>:Er<sup>3+</sup>, Yb<sup>3+</sup>*. Journal of Luminescence, 114, 1, **2005**. p. 53-59.
- [44] Güdel, H.U. and M. Pollnau, *Near-infrared to visible photon upconversion processes in lanthanide doped chloride, bromide and iodide lattices*. Journal of Alloys and Compounds, Vol. 303–304, **2000**. p. 307-315.
- [45] de Wild, J., A. Meijerink, J.K. Rath, W.G.J.H.M. van Sark, and R.E.I. Schropp, *Upconverter solar cells: materials and applications*. Energy & Environmental Science, 4, 12, **2011**. p. 4835-4848.
- [46] Meijerink, A., R. Wegh, P. Vergeer, and T. Vlugt, *Photon management with lanthanides*. Optical Materials, 28, 6–7, **2006**. p. 575-581.

- 
- [47] Yuan, J.-L., X.-Y. Zeng, J.-T. Zhao, Z.-J. Zhang, H.-H. Chen, and X.-X. Yang, *Energy transfer mechanisms in Tb<sup>3+</sup>, Yb<sup>3+</sup> codoped Y<sub>2</sub>O<sub>3</sub> downconversion phosphor*. Journal of Physics D: Applied Physics, 41, 10, **2008**. p. 105406.
- [48] Wegh, R.T., H. Donker, K.D. Oskam, and A. Meijerink, *Visible quantum cutting in LiGdF<sub>4</sub>:Eu<sup>3+</sup> through downconversion*. Science, 283, 5402, **1999**. p. 663-6.
- [49] Bird, R.E., R.L. Hulstrom, A.W. Kliman, and H.G. Eldering, *Solar spectral measurements in the terrestrial environment*. Applied Optics, 21, 8, **1982**. p. 1430-1436.
- [50] Bird, R.E. and C. Riordan, *Simple Solar Spectral Model for Direct and Diffuse Irradiance on Horizontal and Tilted Planes at the Earth's Surface for Cloudless Atmospheres*. Journal of Climate and Applied Meteorology, 25, 1, **1986**. p. 87-97.
- [51] Goldschmidt, J.C., S. Fischer, P. Löper, K.W. Krämer, D. Biner, M. Hermle, and S.W. Glunz, *Experimental analysis of upconversion with both coherent monochromatic irradiation and broad spectrum illumination*. Solar Energy Materials and Solar Cells, 95, 7, **2011**. p. 1960-1963.
- [52] Smestad, G., H. Ries, R. Winston, and E. Yablonovitch, *The thermodynamic limits of light concentrators*. Solar Energy Materials, 21, 2-3, **1990**. p. 99-111.
- [53] van Sark, W.G.J.H.M., A. Meijerink, and R.E.I. Schropp, *Solar Spectrum Conversion for Photovoltaics Using Nanoparticles in Third Generation Photovoltaics*, 1, V. Fthenakis, Editor. **2011**. InTech, Open Access.
- [54] Gaponenko, S.V., *Optical Properties of Semiconductor Nanocrystals*. Cambridge Studies in Modern Optics. **2005**. Cambridge University Press, Cambridge, UK.
- [55] Binks, D.J., *Multiple exciton generation in nanocrystal quantum dots - controversy, current status and future prospects*. Physical Chemistry Chemical Physics, 13, 28, **2011**. p. 12693-12704.
- [56] Nozik, A.J., *Multiple exciton generation in semiconductor quantum dots*. Chemical Physics Letters, 457, 1-3, **2008**. p. 3-11.
- [57] Bruchez, M., M. Moronne, P. Gin, S. Weiss, and A.P. Alivisatos, *Semiconductor Nanocrystals as Fluorescent Biological Labels*. Science, 281, 5385, **1998**. p. 2013-2016.
- [58] Freeman, A.J. and R.E. Watson, *Theoretical Investigation of Some Magnetic and Spectroscopic Properties of Rare-Earth Ions*. Physical Review, 127, 6, **1962**. p. 2058-2075.
- [59] Minowa, T., *Rare Earth Magnets: Conservation of Energy and the Environment*. Resource Geology, 58, 4, **2008**. p. 414-422.
- [60] Miller, G.J., *Complex rare-earth tetrelides, RE<sub>5</sub>(Si<sub>x</sub>Ge<sub>1-x</sub>)<sub>4</sub>: New materials for magnetic refrigeration and a superb playground for solid state chemistry*. Chemical Society Reviews, 35, 9, **2006**. p. 799-813.
- [61] Gschneidner Jr, K.A., V.K. Pecharsky, and A.O. Tsokol, *Recent developments in magnetocaloric materials*. Reports on Progress in Physics, 68, 6, **2005**. p. 1479.
- [62] Iqbal, M.J. and Z. Ahmad, *Electrical and dielectric properties of lithium manganate nanomaterials doped with rare-earth elements*. Journal of Power Sources, 179, 2, **2008**. p. 763-769.
- [63] Xu, J., Z. Zhang, R. Yan, and Y. Luo, *New research progress in investigation of AB<sub>5</sub> rare earth-based hydrogen storage alloys in Ni-MH battery* Chinese Journal of Power Sources, 10, **2009**. p. 923-926.
- [64] Jüstel, T., H. Nikol, and C. Ronda, *New Developments in the Field of Luminescent Materials for Lighting and Displays*. Angewandte Chemie International Edition, 37, 22, **1998**. p. 3084-3103.
- [65] Dieke, G.H., *Spectra and Energy Levels of Rare Earth Ions in Crystals*. **1968**. Interscience Publishers, New York.
- [66] Levine, A.K. and F.C. Palilla, *A New, Highly Efficient Red-Emitting Cathodoluminescent Phosphor (YVO<sub>4</sub>:Eu) For Color Television*. Applied Physics Letters, 5, 6, **1964**. p. 118-120.
- [67] Duczynski, E.W., G. Huber, and P. Mitzscherlich, *Laser Action of Cr, Nd, Tm, Ho-Doped Garnets, in Tunable Solid-State Lasers II*, A. Budgor, L. Esterowitz, and L. DeShazer, Editors. **1986**. Springer, Berlin and Heidelberg. p. 282-290.
- [68] Huber, G., E.W. Duczynski, and K. Petermann, *Laser pumping of Ho-, Tm-, Er-doped garnet lasers at room temperature*. Quantum Electronics, IEEE Journal of, 24, 6, **1988**. p. 920-923.

- 
- [69] Nakazawa, M., Y. Kimura, and K. Suzuki, *Efficient Er<sup>3+</sup>-doped optical fiber amplifier pumped by a 1.48 μm InGaAsP laser diode*. Applied Physics Letters, 54, 4, **1989**. p. 295-297.
- [70] Maniloff, E.S., A.E. Johnson, and T.W. Mossberg, *Spectral Data Storage Using Rare-Earth-Doped Crystals*. MRS Bulletin, 24, 09, **1999**. p. 46-50.
- [71] Steckl, A.J., J.H. Park, and J.M. Zavada, *Prospects for rare earth doped GaN lasers on Si*. Materials Today, 10, 7–8, **2007**. p. 20-27.
- [72] Steckl, A.J., J.C. Heikenfeld, L. Dong-Seon, M.J. Garter, C.C. Baker, W. Yongqiang, and R. Jones, *Rare-earth-doped GaN: growth, properties, and fabrication of electroluminescent devices*. IEEE Journal of Selected Topics in Quantum Electronics, 8, 4, **2002**. p. 749-766.
- [73] Dexter, D.L., *Two ideas on energy transfer phenomena: Ion-pair effects involving the OH stretching mode, and sensitization of photovoltaic cells*. Journal of Luminescence, 18–19, Part 2, **1979**. p. 779-784.
- [74] Munz, P. and E. Bucher, *The Use of Rare Earths in Photovoltaics*, in *The Rare Earths in Modern Science and Technology*, G. McCarthy, et al., Editors. **1982**. Springer US. p. 547-556.
- [75] Reisfeld, R., *Future technological applications of rare-earth-doped materials*. Journal of the Less Common Metals, 93, 2, **1983**. p. 243-251.
- [76] Reisfeld, R., *Industrial applications of rare earths in fiber optics, luminescent solar concentrators and lasers*. Inorganica Chimica Acta, 140, **1987**. p. 345-350.
- [77] Bransden, B.H. and C.J. Joachain, *Physics of Atoms and Molecules*. 2nd ed. **2003**. Prentice Hall.
- [78] Thiel, C.W., *Energies of rare-earth ion states relative to host bands in optical materials from electron photoemission spectroscopy*. **2004**, Montana State University
- [79] Saxena, K.M.S. and G. Malli, *Accurate Numerical Hartree–Fock Self-Consistent-Field Wave Functions for Rare-Earth Ions having 4f<sup>N</sup>6s Configuration*. Canadian Journal of Physics, 49, 20, **1971**. p. 2619-2620.
- [80] Dorenbos, P., *Anomalous luminescence of Eu<sup>2+</sup> and Yb<sup>2+</sup> in inorganic compounds*. Journal of Physics: Condensed Matter, 15, 17, **2003**. p. 2645.
- [81] Adachi, G.-y. and N. Imanaka, *The Binary Rare Earth Oxides*. Chemical Reviews, 98, 4, **1998**. p. 1479-1514.
- [82] S. Puppalwar, S.D., G. Singh and A. Kumar, *Blue emission in Ce<sup>3+</sup> and Eu<sup>2+</sup> activated Lithium fluoro borate phosphors*. Journal of Modern Physics, Vol. 2, No. 12, **2011**. p. 1560-1566.
- [83] *Phosphors for lamps*, in *Phosphor Handbook*, Ch. 5, S. Shionoya, W.M. Yen, and H. Yamamoto, Editors. **2006**. CRC Press. p. 517.
- [84] Slater, J.C., *The Theory of Complex Spectra*. Physical Review, 34, **1929**. p. 1293-1322.
- [85] Vleck, J.H.V., *The Puzzle of Rare-earth Spectra in Solids*. The Journal of Physical Chemistry, 41, 1, **1937**. p. 67-80.
- [86] Broer, L.J.F., C.J. Gorter, and J. Hoogschagen, *On the intensities and the multipole character in the spectra of the rare earth ions*. Physica, 11, 4, **1945**. p. 231-250.
- [87] Racah, G., *Theory of complex spectra. IV*. Physical Review, 76, **1949**. p. 1352–1365.
- [88] Judd, B.R., *Optical Absorption Intensities of Rare-Earth Ions*. Physical Review, 127, 3, **1962**. p. 750-761.
- [89] Ofelt, G.S., *Intensities of Crystal Spectra of Rare-Earth Ions*. The Journal of Chemical Physics, 37, 3, **1962**. p. 511-520.
- [90] Leavitt, R.P. and C.A. Morrison, *Crystal-field analysis of triply ionized rare earth ions in lanthanum trifluoride. II. Intensity calculations*. The Journal of Chemical Physics, 73, 2, **1980**. p. 749-757.
- [91] Goldner, P. and F. Auzel, *Application of standard and modified Judd-Ofelt theories to a praseodymium-doped fluorozirconate glass*. Journal of Applied Physics, 79, 10, **1996**. p. 7972-7977.
- [92] Peacock, R.D., *The intensities of lanthanide f ↔ f transitions*, in *Rare Earths*, Ch. 3. **1975**. Springer Berlin Heidelberg. p. 83-122.
- [93] Wybourne, B.G., *Structure of f<sup>N</sup> Configurations. I. Calculation of the Energy Levels*. The Journal of Chemical Physics, 36, 9, **1962**. p. 2295-2300.

- [94] Wybourne, B.G., *Structure of  $f^n$  Configurations. II.  $f^5$  and  $f^6$  Configurations*. The Journal of Chemical Physics, 36, 9, **1962**. p. 2301-2311.
- [95] Wybourne, B.G., *Spectroscopic Properties of the Rare Earths*. **1965**. Interscience, New York.
- [96] Bethe, H., *Termaufspaltung in Kristallen*. Annalen der Physik, 395, 2, **1929**. p. 133-208.
- [97] Needels, M., M. Schlüter, and M. Lannoo, *Erbium point defects in silicon*. Physical Review B, 47, 23, **1993**. p. 15533-15536.
- [98] Przybylinska, H., W. Jantsch, Y. Suprun-Belevitch, M. Stepikhova, L. Palmetshofer, G. Hendorfer, A. Kozanecki, R.J. Wilson, and B.J. Sealy, *Optically active erbium centers in silicon*. Physical Review B, 54, 4, **1996**. p. 2532-2547.
- [99] Adler, D.L., D.C. Jacobson, D.J. Eaglesham, M.A. Marcus, J.L. Benton, J.M. Poate, and P.H. Citrin, *Local structure of 1.54- $\mu$ m-luminescence  $Er^{3+}$  implanted in Si*. Applied Physics Letters, 61, 18, **1992**. p. 2181-2183.
- [100] Ishii, M., S. Komuro, T. Morikawa, and Y. Aoyagi, *Local structure analysis of an optically active center in Er-doped ZnO thin film*. Journal of Applied Physics, 89, 7, **2001**. p. 3679-3684.
- [101] Yen, W.M., *General factors governing the efficiency of luminescent devices*. Physics of the Solid State, 47, 8, **2005**. p. 1393-1399.
- [102] Bos, A.J.J., P. Dorenbos, A. Bessière, A. Lecointre, M. Bedu, M. Bettinelli, and F. Piccinelli, *Study of TL glow curves of  $YPO_4$  double doped with lanthanide ions*. Radiation Measurements, 46, 12, **2011**. p. 1410-1416.
- [103] Dorenbos, P., *Valence Stability of Lanthanide Ions in Inorganic Compounds*. Chemistry of Materials, 17, 25, **2005**. p. 6452-6456.
- [104] Dorenbos, P., *Electronic Structure Engineering of Lanthanide Activated Materials*. Journal of Materials Chemistry, 22, 42, **2012**. p. 22344-22349.
- [105] Dorenbos, P. and E. van der Kolk. *Lanthanide impurity level location in GaN, AlN, and ZnO*. in Proc. SPIE. **2007**. San José, California. p. 647313 - 647313-10.
- [106] Deiters, E., F. Gumy, and J.-C.G. Bünzli, *Acridone-Benzimidazole Ring-Fused Ligands: A New Class of Sensitizers of Lanthanide Luminescence via Low-Energy Excitation*. European Journal of Inorganic Chemistry, 2010, 18, **2010**. p. 2723-2734.
- [107] Ohwaki, J. and M. Otsuka,  *$Dy^{3+}$ - and  $Er^{3+}$ -codoped  $YBr_3$  upconversion phosphor for detection of 1.3- $\mu$ m band infrared light*. Electronics and Communications in Japan (Part II: Electronics), 79, 8, **1996**. p. 23-30.
- [108] Ganem, J. and S. Bowman, *Use of thulium-sensitized rare earth-doped low phonon energy crystalline hosts for IR sources*. Nanoscale Research Letters, 8, 1, **2013**. p. 455.
- [109] Hömmerich, U., E.E. Nyein, and S.B. Trivedi, *Crystal growth, upconversion, and infrared emission properties of  $Er^{3+}$ -doped  $KPb_2Br_5$* . Journal of Luminescence, 113, 1-2, **2005**. p. 100-108.
- [110] Klingshirn, C., M. Grundmann, A. Hoffmann, B. Meyer, and A. Waag, *Zinkoxid - ein alter, neuer Halbleiter*. Physik Journal, 5, 1, **2006**. p. 33-38.
- [111] Reynolds, D.C., D.C. Look, B. Jogai, C.W. Litton, G. Cantwell, and W.C. Harsch, *Valence-band ordering in ZnO*. Physical Review B, 60, 4, **1999**. p. 2340-2344.
- [112] Akimov, A.V., S.A. Cavill, A.J. Kent, N.M. Stanton, T. Wang, and S. Sakai, *Phonon emission by photoexcited carriers in InGaN/GaN multiple quantum wells*. Journal of Physics: Condensed Matter, 14, 13, **2002**. p. 3445.
- [113] Link, A., K. Bitzer, W. Limmer, R. Sauer, C. Kirchner, V. Schwegler, M. Kamp, D.G. Ebling, and K.W. Benz, *Temperature dependence of the E2 and A1(LO) phonons in GaN and AlN*. Journal of Applied Physics, 86, 11, **1999**. p. 6256-6260.
- [114] Petalas, J., S. Logothetidis, S. Bouladakis, M. Alouani, and J.M. Wills, *Optical and electronic-structure study of cubic and hexagonal GaN thin films*. Physical Review B, 52, 11, **1995**. p. 8082-8091.
- [115] Johnson, J.C., H.-J. Choi, K.P. Knutsen, R.D. Schaller, P. Yang, and R.J. Saykally, *Single gallium nitride nanowire lasers*. Nat Mater, 1, 2, **2002**. p. 106-110.
- [116] Li, Y., et al., *Realizing a  $SnO_2$ -based ultraviolet light-emitting diode via breaking the dipole-forbidden rule*. NPG Asia Mater, 4, **2012**. p. e30.

- 
- [117] Yu, B., C. Zhu, and F. Gan, *Exciton spectra of SnO<sub>2</sub> nanocrystals with surficial dipole layer*. Optical Materials, 7, 1–2, **1997**. p. 15-20.
- [118] Sikora, R., *Ab initio study of phonons in the rutile structure of TiO<sub>2</sub>*. Journal of Physics and Chemistry of Solids, 66, 6, **2005**. p. 1069-1073.
- [119] Rucker, G., J.A. Schaefer, and W. Göpel, *Localized and delocalized vibrations on TiO<sub>2</sub> (110) studied by high-resolution electron-energy-loss spectroscopy*. Physical Review B, 30, 7, **1984**. p. 3704-3708.
- [120] Chiodo, L., J.M. García-Lastra, A. Iacomino, S. Ossicini, J. Zhao, H. Petek, and A. Rubio, *Self-energy and excitonic effects in the electronic and optical properties of TiO<sub>2</sub> crystalline phases*. Physical Review B, 82, 4, **2010**. p. 045207.
- [121] Yamada, Y. and Y. Kanemitsu, *Band-to-band photoluminescence in SrTiO<sub>3</sub>*. Physical Review B, 82, 12, **2010**. p. 121103.
- [122] Evarestov, R.A., E. Blokhin, D. Gryaznov, E.A. Kotomin, and J. Maier, *Phonon calculations in cubic and tetragonal phases of SrTiO<sub>3</sub>: A comparative LCAO and plane-wave study*. Physical Review B, 83, 13, **2011**. p. 134108.
- [123] Bosacchi, B. and J.E. Robinson, *Urbach's rule in polar semiconductors*. Solid State Communications, 10, 9, **1972**. p. 797-802.
- [124] Cardona, M., *Optical Properties and Band Structure of SrTiO<sub>3</sub> and BaTiO<sub>3</sub>*. Physical Review, 140, 2A, **1965**. p. A651-A655.
- [125] Wang, S., W. Wang, J. Zuo, and Y. Qian, *Study of the Raman spectrum of CeO<sub>2</sub> nanometer thin films*. Materials Chemistry and Physics, 68, 1–3, **2001**. p. 246-248.
- [126] Kosacki, I., T. Suzuki, H.U. Anderson, and P. Colomban, *Raman scattering and lattice defects in nanocrystalline CeO<sub>2</sub> thin films*. Solid State Ionics, 149, 1–2, **2002**. p. 99-105.
- [127] Colis, S., A. Bouaine, G. Schmerber, C. Ulhaq-Bouillet, A. Dinia, S. Choua, and P. Turek, *High-temperature ferromagnetism in Co-doped CeO<sub>2</sub> synthesized by the coprecipitation technique*. Phys Chem Chem Phys, 14, 20, **2012**. p. 7256-63.
- [128] Martinet, C. and R.A.B. Devine, *Analysis of the vibrational mode spectra of amorphous SiO<sub>2</sub> films*. Journal of Applied Physics, 77, 9, **1995**. p. 4343-4348.
- [129] Vella, E., F. Messina, M. Cannas, and R. Boscaino, *Unraveling exciton dynamics in amorphous silicon dioxide: Interpretation of the optical features from 8 to 11 eV*. Physical Review B, 83, 17, **2011**. p. 174201.
- [130] Oliva, A.I., O. Solis-Canto, R. Castro, R., and P. Quintana, *Formation of the band gap energy on CdS thin films growth by two different techniques*. Thin Solid Films, 391, 1, **2001**. p. 28-35.
- [131] Ueda, M., H. Kanzaki, K. Kobayashi, Y. Toyozawa, and E. Hanamura, *Excitonic Processes in Solids*. **1986**. Springer, Berlin.
- [132] Agura, H., A. Suzuki, T. Matsushita, T. Aoki, and M. Okuda, *Low resistivity transparent conducting Al-doped ZnO films prepared by pulsed laser deposition*. Thin Solid Films, 445, 2, **2003**. p. 263-267.
- [133] Wu, H.-W., C.-H. Chu, Y.-F. Chen, Y.-W. Chen, W.-H. Tsai, S.-H. Huang, and G.-S. Chen. *Study of AZO Thin Films Under Different Ar Flow and Sputtering Power by rf Magnetron Sputtering*. in *International MultiConference of Engineers and Computer Scientists (IMECS)*. **2013**. Hong Kong. p.
- [134] Ozgur, U., Y.I. Alivov, C. Liu, A. Teke, M.A. Reshchikov, S. Dogan, V. Avrutin, S.-J. Cho, and H. Morkoc, *A Comprehensive Review of ZnO Materials and Devices*. Journal of Applied Physics, 98, 4, **2005**. p. 041301.
- [135] Lin, B., Z. Fu, and Y. Jia, *Green Luminescent Center in Undoped Zinc Oxide Films Deposited on Silicon Substrates*. Applied Physics Letters, 79, 7, **2001**. p. 943-945.
- [136] Wang, Y.G., S.P. Lau, X.H. Zhang, H.H. Hng, H.W. Lee, S.F. Yu, and B.K. Tay, *Enhancement of near-band-edge photoluminescence from ZnO films by face-to-face annealing*. Journal of Crystal Growth, 259, 4, **2003**. p. 335-342.

- 
- [137] Bouzid, K., A. Djelloul, N. Bouzid, and J. Bougdira, *Electrical Resistivity and Photoluminescence of Zinc Oxide Films Prepared by Ultrasonic Spray Pyrolysis*. *Physica Status Solidi (a)*, 206, 1, **2009**. p. 106-115.
- [138] Djurišić, A.B., Y.H. Leung, K.H. Tam, L. Ding, W.K. Ge, H.Y. Chen, and S. Gwo, *Green, yellow, and orange defect emission from ZnO nanostructures: Influence of excitation wavelength*. *Applied Physics Letters*, 88, 10, **2006**. p. 103107 - 103107-3.
- [139] Studenikin, S.A., M. Cocivera, W. Kellner, and H. Pascher, *Band-Edge Photoluminescence in Polycrystalline ZnO Films at 1.7 K*. *Journal of Luminescence*, 91, 3–4, **2000**. p. 223-232.
- [140] Rakshesh, V., M. Junaid Bushiri, and V.K. Vaidyan, *Visible Luminescence Centers in Zinc Oxide Films Deposited by Spray Pyrolysis*. *Journal of Optoelectronics and Advanced Materials*, 9, 12, **2007**. p. 3740-3742.
- [141] Reynolds, D.C., D.C. Look, and B. Jogai, *Fine Structure on the Green Band in ZnO*. *Journal of Applied Physics*, 89, 11, **2001**. p. 6189-6191.
- [142] Yoon, K.H. and J.Y. Cho, *Photoluminescence characteristics of zinc oxide thin films prepared by spray pyrolysis technique*. *Materials Research Bulletin*, 35, 1, **2000**. p. 39-46.
- [143] Soumahoro, I., *et al.*, *Structural, Optical, and Electrical Properties of Yb-Doped ZnO Thin Films Prepared by Spray Pyrolysis Method*. *Journal of Applied Physics*, 109, 3, **2011**. p. 033708 - 033708-5.
- [144] Petersen, J., *et al.*, *Optical Properties of ZnO Thin Films Prepared by Sol–Gel Process*. *Microelectronics Journal*, 40, 2, **2009**. p. 239-241.
- [145] Behera, D. and B.S. Acharya, *Nano-star formation in Al-doped ZnO thin film deposited by dip-dry method and its characterization using atomic force microscopy, electron probe microscopy, photoluminescence and laser Raman spectroscopy*. *Journal of Luminescence*, 128, 10, **2008**. p. 1577-1586.
- [146] Reynolds, D.C., D.C. Look, B. Jogai, C.W. Litton, T.C. Collins, W. Harsch, and G. Cantwell, *Neutral-donor–bound-exciton complexes in ZnO crystals*. *Physical Review B*, 57, 19, **1998**. p. 12151-12155.
- [147] Thonke, K., T. Gruber, N. Teofilov, R. Schönfelder, A. Waag, and R. Sauer, *Donor–acceptor pair transitions in ZnO substrate material*. *Physica B: Condensed Matter*, 308–310, **2001**. p. 945-948.
- [148] Kong, Y.C., D.P. Yu, B. Zhang, W. Fang, and S.Q. Feng, *Ultraviolet-emitting ZnO nanowires synthesized by a physical vapor deposition approach*. *Applied Physics Letters*, 78, 4, **2001**. p. 407-409.
- [149] Teng, X.M., H.T. Fan, S.S. Pan, C. Ye, and G.H. Li, *Photoluminescence of ZnO thin films on Si substrate with and without ITO buffer layer*. *Journal of Physics D: Applied Physics*, 39, 3, **2006**. p. 471-476.
- [150] Studenikin, S.A., N. Golego, and M. Cocivera, *Fabrication of green and orange photoluminescent, undoped ZnO films using spray pyrolysis*. *Journal of Applied Physics*, 84, 4, **1998**. p. 2287-2294.
- [151] Chen, J., Z. Feng, P. Ying, M. Li, B. Han, and C. Li, *The visible luminescent characteristics of ZnO supported on SiO<sub>2</sub> powder*. *Physical Chemistry Chemical Physics*, 6, 18, **2004**. p. 4473-4479.
- [152] Leiter, F., H. Alves, D. Pfisterer, N.G. Romanov, D.M. Hofmann, and B.K. Meyer, *Oxygen vacancies in ZnO*. *Physica B: Condensed Matter*, 340–342, **2003**. p. 201-204.
- [153] Vanheusden, K., W.L. Warren, C.H. Seager, D.R. Tallant, J.A. Voigt, and B.E. Gnade, *Mechanisms behind green photoluminescence in ZnO phosphor powders*. *Journal of Applied Physics*, 79, 10, **1996**. p. 7983-7990.
- [154] Kang, J.S., H.S. Kang, S.S. Pang, E.S. Shim, and S.Y. Lee, *Investigation on the origin of green luminescence from laser-ablated ZnO thin film*. *Thin Solid Films*, 443, 1–2, **2003**. p. 5-8.
- [155] Liu, M., A.H. Kitai, and P. Mascher, *Point defects and luminescence centres in zinc oxide and zinc oxide doped with manganese*. *Journal of Luminescence*, 54, 1, **1992**. p. 35-42.
- [156] Greene, L.E., M. Law, J. Goldberger, F. Kim, J.C. Johnson, Y. Zhang, R.J. Saykally, and P. Yang, *Low-Temperature Wafer-Scale Production of ZnO Nanowire Arrays*. *Angewandte Chemie International Edition*, 42, 26, **2003**. p. 3031-3034.

- [157] Luo, Q., X. Qiao, X. Fan, and X. Zhang, *Near-infrared emission of Yb<sup>3+</sup> through energy transfer from ZnO to Yb<sup>3+</sup> in glass ceramic containing ZnO nanocrystals*. *Optics Letters*, 36, 15, **2011**. p. 2767-2769.
- [158] Wu, X.L., G.G. Siu, C.L. Fu, and H.C. Ong, *Photoluminescence and cathodoluminescence studies of stoichiometric and oxygen-deficient ZnO films*. *Applied Physics Letters*, 78, 16, **2001**. p. 2285-2287.
- [159] Fujihara, S., Y. Ogawa, and A. Kasai, *Tunable Visible Photoluminescence from ZnO Thin Films through Mg-Doping and Annealing*. *Chemistry of Materials*, 16, 15, **2004**. p. 2965-2968.
- [160] Wu, L., Y. Wu, X. Pan, and F. Kong, *Synthesis of ZnO nanorod and the annealing effect on its photoluminescence property*. *Optical Materials*, 28, 4, **2006**. p. 418-422.
- [161] Leontiev, S.A., S.V. Koshcheev, V.G. Devyatov, A.E. Cherkashin, and é.P. Mikheeva, *Detailed XPS and UPS studies of the band structure of zinc oxide*. *Journal of Structural Chemistry*, 38, 5, **1997**. p. 725-731.
- [162] Zhang, X.D., M.L. Guo, W.X. Li, and C.L. Liu, *First-principles study of electronic and optical properties in wurtzite Zn<sub>1-x</sub>Cd<sub>x</sub>O*. *Journal of Applied Physics*, 103, 6, **2008**. p. 063721.
- [163] Kumar, P., H.K. Malik, A. Ghosh, R. Thangavel, and K. Asokan, *Bandgap tuning in highly c-axis oriented Zn<sub>1-x</sub>Mg<sub>x</sub>O thin films*. *Applied Physics Letters*, 102, 22, **2013**. p. 221903.
- [164] Ji, S., L. Yin, G. Liu, L. Zhang, and C. Ye, *Synthesis of Rare Earth Ions-Doped ZnO Nanostructures with Efficient Host-Guest Energy Transfer*. *The Journal of Physical Chemistry C*, 113, 37, **2009**. p. 16439-16444.
- [165] Li, H., K. Luo, M. Xia, and P.W. Wang, *Synthesis and Optical Properties of Pr<sup>3+</sup>-Doped ZnO Quantum Dots*. *Journal of Non-Crystalline Solids*, 383, **2014**. p. 176-180.
- [166] Liu, Y., W. Luo, R. Li, G. Liu, M.R. Antonio, and X. Chen, *Optical Spectroscopy of Eu<sup>3+</sup> Doped ZnO Nanocrystals*. *The Journal of Physical Chemistry C*, 112, 3, **2008**. p. 686-694.
- [167] Zeng, X., J. Yuan, and L. Zhang, *Synthesis and Photoluminescent Properties of Rare Earth Doped ZnO Hierarchical Microspheres*. *The Journal of Physical Chemistry C*, 112, 10, **2008**. p. 3503-3508.
- [168] Liu, Y., W. Luo, R. Li, H. Zhu, and X. Chen, *Near-infrared luminescence of Na<sup>3+</sup> and Tm<sup>3+</sup> ions doped ZnO nanocrystals*. *Optics Express*, 17, 12, **2009**. p. 9748-9753.
- [169] Sato, Y., J.P. Buban, T. Mizoguchi, N. Shibata, M. Yodogawa, T. Yamamoto, and Y. Ikuhara, *Role of Pr Segregation in Acceptor-State Formation at ZnO Grain Boundaries*. *Physical Review Letters*, 97, 10, **2006**. p. 106802.
- [170] Jiang, N., S. Ye, and J. Qiu, *Electron energy-loss spectroscopy study of Yb doped ZnO*. *Journal of Applied Physics*, 108, 8, **2010**. p. 083535.
- [171] Han, H.L., L.W. Yang, Y.X. Liu, Y.Y. Zhang, and Q.B. Yang, *Up-conversion luminescence switching in Er<sup>3+</sup>-containing ZnO nanoparticles through Li<sup>+</sup> co-doping*. *Optical Materials*, 31, 2, **2008**. p. 338-341.
- [172] Gu, F., S.F. Wang, M.K. Lü, G.J. Zhou, D. Xu, and D.R. Yuan, *Structure Evaluation and Highly Enhanced Luminescence of Dy<sup>3+</sup>-Doped ZnO Nanocrystals by Li<sup>+</sup> Doping via Combustion Method*. *Langmuir*, 20, 9, **2004**. p. 3528-3531.
- [173] Gao, B., Y. Yang, H. Yang, S. Zhang, and X. Liu, *Study of lanthanide doped zinc oxide nanoparticles synthesized via a sonochemical method*. *Science China Physics, Mechanics and Astronomy*, 56, 7, **2013**. p. 1280-1284.
- [174] Du, Y.-P., Y.-W. Zhang, L.-D. Sun, and C.-H. Yan, *Efficient Energy Transfer in Monodisperse Eu-Doped ZnO Nanocrystals Synthesized from Metal Acetylacetonates in High-Boiling Solvents*. *The Journal of Physical Chemistry C*, 112, 32, **2008**. p. 12234-12241.
- [175] Bai, Y., Y. Wang, K. Yang, X. Zhang, Y. Song, and C.H. Wang, *Enhanced upconverted photoluminescence in Er<sup>3+</sup> and Yb<sup>3+</sup> codoped ZnO nanocrystals with and without Li<sup>+</sup> ions*. *Optics Communications*, 281, 21, **2008**. p. 5448-5452.
- [176] Bachir, S., K. Azuma, J. Kossanyi, P. Valat, and J.C. Ronfard-Haret, *Photoluminescence of polycrystalline zinc oxide co-activated with trivalent rare earth ions and lithium. Insertion of rare-earth ions into zinc oxide*. *Journal of Luminescence*, 75, 1, **1997**. p. 35-49.

- 
- [177] Gottardi, G., R. Pandiyan, V. Micheli, G. Pepponi, S. Gennaro, R. Bartali, and N. Laidani, *Effect of Nd<sup>3+</sup> incorporation on the microstructure and chemical structure of RF sputtered ZnO thin films*. Materials Science and Engineering B-Advanced Functional Solid-State Materials, 178, 9, **2013**. p. 609-616.
- [178] Davesne, C., A. Ziani, C. Labbé, P. Marie, C. Frilay, and X. Portier, *Energy Transfer Mechanism Between Terbium and Europium Ions in Zinc Oxide and Zinc Silicates Thin Films*. Thin Solid Films, 553, **2014**. p. 33-37.
- [179] Petersen, J., *et al.*, *Correlation of structural properties with energy transfer of Eu-doped ZnO thin films prepared by sol-gel process and magnetron reactive sputtering*. Journal of Applied Physics, 107, 12, **2010**. p. 123522 - 123522-6.
- [180] Douayar, A., *et al.*, *Investigation of the structural, optical and electrical properties of Nd-doped ZnO thin films deposited by spray pyrolysis*. European Physical Journal-Applied Physics, 61, 1, **2013**. p. 10304.
- [181] Pearton, S.J., D.P. Norton, K. Ip, Y.W. Heo, and T. Steiner, *Recent progress in processing and properties of ZnO*. Progress in Materials Science, 50, 3, **2005**. p. 293-340.
- [182] Wöll, C., *The chemistry and physics of zinc oxide surfaces*. Progress in Surface Science, 82, 2–3, **2007**. p. 55-120.
- [183] Sokol, A.A., S.A. French, S.T. Bromley, C.R.A. Catlow, H.J.J.v. Dam, and P. Sherwood, *Point defects in ZnO*. Faraday Discussions, 134, **2006**. p. 267-282.
- [184] Chen, Q.J., W.J. Zhang, X.Y. Huang, G.P. Dong, M.Y. Peng, and Q.Y. Zhang, *Efficient Down- and Up-Conversion of Pr<sup>3+</sup>-Yb<sup>3+</sup> Co-Doped Transparent Oxyfluoride Glass Ceramics*. Journal of Alloys and Compounds, 513, **2012**. p. 139-144.
- [185] Hu, J., H. Xia, H. Hu, Y. Zhang, H. Jiang, and B. Chen, *Synthesis and Efficient Near-Infrared Quantum Cutting of Pr<sup>3+</sup>/Yb<sup>3+</sup> Co-Doped LiYF<sub>4</sub> Single Crystals*. Journal of Applied Physics, 112, 7, **2012**. p. 073518-5.
- [186] Man, S.Q., H.L. Zhang, Y.L. Liu, J.X. Meng, E.Y.B. Pun, and P.S. Chung, *Energy Transfer in Pr<sup>3+</sup>/Yb<sup>3+</sup> Codoped Tellurite Glasses*. Optical Materials, 30, 2, **2007**. p. 334-337.
- [187] Katayama, Y. and S. Tanabe, *Mechanism of Quantum Cutting in Pr<sup>3+</sup>-Yb<sup>3+</sup> Codoped Oxyfluoride Glass Ceramics*. Journal of Luminescence, 134, **2013**. p. 825-829.
- [188] Lawrence, N.J., *et al.*, *Defect Engineering in Cubic Cerium Oxide Nanostructures for Catalytic Oxidation*. Nano Letters, 11, 7, **2011**. p. 2666-2671.
- [189] Murugan, B. and A.V. Ramaswamy, *Defect-Site Promoted Surface Reorganization in Nanocrystalline Ceria for the Low-Temperature Activation of Ethylbenzene*. Journal of the American Chemical Society, 129, 11, **2007**. p. 3062-3063.
- [190] Mayernick, A.D. and M.J. Janik, *Methane Activation and Oxygen Vacancy Formation over CeO<sub>2</sub> and Zr, Pd Substituted CeO<sub>2</sub> Surfaces*. The Journal of Physical Chemistry C, 112, 38, **2008**. p. 14955-14964.
- [191] Lubna, R.S., A. Bakhtyar, Z. Hao, W.G. Wang, Y.Q. Song, H.W. Zhang, S.I. Shah, and J.Q. Xiao, *Detailed study on the role of oxygen vacancies in structural, magnetic and transport behavior of magnetic insulator: Co-CeO<sub>2</sub>*. Journal of Physics: Condensed Matter, 21, 48, **2009**. p. 486004.
- [192] Chen, S.-Y., *et al.*, *Concentration Dependence of Oxygen Vacancy on the Magnetism of CeO<sub>2</sub> Nanoparticles*. The Journal of Physical Chemistry C, 116, 15, **2012**. p. 8707-8713.
- [193] Kirk, N.B. and J.V. Wood, *Glass polishing*. British Ceramic Trans., 93, 1, **1994**. p. 25–30.
- [194] Powell, B.R., R.L. Bloink, and C.C. Eickel, *Preparation of Cerium Dioxide Powders for Catalyst Supports*. Journal of the American Ceramic Society, 71, 2, **1988**. p. C-104-C-106.
- [195] Van Herle, J., T. Horita, T. Kawada, N. Sakai, H. Yokokawa, and M. Dokiya, *Fabrication and Sintering of Fine Ytria-Doped Ceria Powder*. Journal of the American Ceramic Society, 80, 4, **1997**. p. 933-940.
- [196] Liu, W., B. Li, H. Liu, and W. Pan, *Fabrication of Sm<sup>3+</sup> and Nd<sup>3+</sup> co-doped CeO<sub>2</sub> thin-film electrolytes by radio frequency magnetron sputtering*. Electrochimica Acta, 56, 24, **2011**. p. 8329-8333.

- 
- [197] Trovarelli, A., *Structural properties and non-stoichiometric behavior of CeO<sub>2</sub>*, in *Catalysis by Ceria and Related Materials*. **2002**. p. 15-50.
- [198] Nakamoto, K., *Infrared and Raman Spectra of Inorganic and Coordination Compounds*. 5<sup>th</sup> ed. **1997**. John Wiley & Sons, New York.
- [199] Ryzhkov, M.V., V.A. Gubanov, Y.A. Teterin, and A.S. Baev, *Electronic structure, chemical bonding and X-ray photoelectron spectra of light rare-earth oxides*. *Zeitschrift für Physik B Condensed Matter*, 59, 1, **1985**. p. 1-6.
- [200] Ryzhkov, M.V., V.A. Gubanov, Y.A. Teterin, and A.S. Baev, *Electronic structure, chemical bonding and X-ray photoelectron spectra of heavy rare-earth oxides*. *Zeitschrift für Physik B Condensed Matter*, 59, 1, **1985**. p. 7-14.
- [201] Prokofiev, A.V., A.I. Shelykh, and B.T. Melekh, *Periodicity in the band gap variation of Ln<sub>2</sub>X<sub>3</sub> (X = O, S, Se) in the lanthanide series*. *Journal of Alloys and Compounds*, 242, 1–2, **1996**. p. 41-44.
- [202] Sham, T.K., R.A. Gordon, and S.M. Heald, *Resonant inelastic x-ray scattering at the Ce L3 edge of CePO<sub>4</sub> and CeO<sub>2</sub>: Implications for the valence of CeO<sub>2</sub> and related phenomena*. *Physical Review B*, 72, 3, **2005**. p. 035113.
- [203] Pfau, A. and K.D. Schierbaum, *The electronic structure of stoichiometric and reduced CeO<sub>2</sub> surfaces: an XPS, UPS and HREELS study*. *Surface Science*, 321, 1–2, **1994**. p. 71-80.
- [204] Marabelli, F. and P. Wachter, *Covalent insulator CeO<sub>2</sub>: Optical reflectivity measurements*. *Physical Review B*, 36, 2, **1987**. p. 1238-1243.
- [205] Hay, P.J., R.L. Martin, J. Uddin, and G.E. Scuseria, *Theoretical study of CeO<sub>2</sub> and Ce<sub>2</sub>O<sub>3</sub> using a screened hybrid density functional*. *The Journal of Chemical Physics*, 125, 3, **2006**. p. 034712-1 - 8.
- [206] Guo, S., H. Arwin, S.N. Jacobsen, K. Järrendahl, and U. Helmersson, *A spectroscopic ellipsometry study of cerium dioxide thin films grown on sapphire by rf magnetron sputtering*. *Journal of Applied Physics*, 77, 10, **1995**. p. 5369-5376.
- [207] Krill, G., J.P. Kappler, A. Meyer, L. Abadli, and M.F. Ravet, *Surface and bulk properties of cerium atoms in several cerium intermetallic compounds: XPS and X-ray absorption measurements*. *Journal of Physics F: Metal Physics*, 11, 8, **1981**. p. 1713.
- [208] Bianconi, A., A. Marcelli, H. Dexpert, R. Karnatak, A. Kotani, T. Jo, and J. Petiau, *Specific intermediate-valence state of insulating 4f compounds detected by L3 x-ray absorption*. *Physical Review B*, 35, 2, **1987**. p. 806-812.
- [209] Dexpert, H., R.C. Karnatak, J.M. Esteva, J.P. Connerade, M. Gasgnier, P.E. Caro, and L. Albert, *X-ray absorption studies of CeO<sub>2</sub>, PrO<sub>2</sub>, and TbO<sub>2</sub>. II. Rare-earth valence state by LIII absorption edges*. *Physical Review B*, 36, 3, **1987**. p. 1750-1753.
- [210] Jo, T. and A. Kotani, *Theory of core photoabsorption spectra in CeO<sub>2</sub>*. *Solid State Communications*, 54, 5, **1985**. p. 451-456.
- [211] Kotani, A., T. Jo, and J.C. Parlebas, *Many-body effects in core-level spectroscopy of rare-earth compounds*. *Advances in Physics*, 37, 1, **1988**. p. 37-85.
- [212] Nakazawa, M., S. Tanaka, T. Uozumi, and A. Kotani, *Theory of resonant X-ray emission spectra in Ce compounds*. *Journal of Electron Spectroscopy and Related Phenomena*, 79, **1996**. p. 183-186.
- [213] Nakano, T., A. Kotani, and J. C. Parlebas, *Theory of XPS and BIS Spectra in Ce<sub>2</sub>O<sub>3</sub> and CeO<sub>2</sub>*. *Journal of the Physical Society of Japan*, 56, 6, **1987**. p. 2201-2210.
- [214] Aškračić, S., Z.D. Dohčević-Mitrović, V.D. Araújo, G. Ionita, J. M. M. de Lima, and A. Cantarero, *F-centre luminescence in nanocrystalline CeO<sub>2</sub>*. *Journal of Physics D: Applied Physics*, 46, 49, **2013**. p. 495306.
- [215] Andersson, D.A., S.I. Simak, B. Johansson, I.A. Abrikosov, and N.V. Skorodumova, *Modeling of CeO<sub>2</sub>, Ce<sub>2</sub>O<sub>3</sub>, and CeO<sub>2-x</sub> in the LDA+U formalism*. *Physical Review B*, 75, 3, **2007**. p. 035109.
- [216] Henderson, M.A., C.L. Perkins, M.H. Engelhard, S. Thevuthasan, and C.H.F. Peden, *Redox properties of water on the oxidized and reduced surfaces of CeO<sub>2</sub> (111)*. *Surface Science*, 526, 1–2, **2003**. p. 1-18.
- [217] Shannon, R., *Revised Effective Ionic Radii and Systematic Studies of Interatomic Distances in Halides and Chalcogenides*. *Acta Crystallographica Section A*, 32, 5, **1976**. p. 751-767.

- [218] Tiseanu, C., B. Cojocaru, D. Avram, V.I. Parvulescu, A.V. Vela-Gonzalez, and M. Sanchez-Dominguez, *Isolated centres versus defect associates in Sm<sup>3+</sup>-doped CeO<sub>2</sub>: a spectroscopic investigation*. Journal of Physics D: Applied Physics, 46, 27, **2013**. p. 275302.
- [219] Tiseanu, C., V.I. Parvulescu, M. Boutonnet, B. Cojocaru, P.A. Primus, C.M. Teodorescu, C. Solans, and M.S. Dominguez, *Surface versus volume effects in luminescent ceria nanocrystals synthesized by an oil-in-water microemulsion method*. Physical Chemistry Chemical Physics, 13, 38, **2011**. p. 17135-17145.
- [220] Wu, H., Z. Yang, J. Liao, S. Lai, J. Qiu, Z. Song, Y. Yang, D. Zhou, and Z. Yin, *Upconversion luminescence properties of three-dimensional ordered macroporous CeO<sub>2</sub>: Er<sup>3+</sup>, Yb<sup>3+</sup>*. Journal of Alloys and Compounds, 586, **2014**. p. 485-487.
- [221] Fujihara, S. and M. Oikawa, *Structure and luminescent properties of CeO<sub>2</sub>:RE (RE = Eu<sup>3+</sup> and Sm<sup>3+</sup>) thin films*. Journal of Applied Physics, 95, 12, **2004**. p. 8002-8006.
- [222] Wang, X., D. Zhang, Y. Li, D. Tang, Y. Xiao, Y. Liu, and Q. Huo, *Self-doped Ce<sup>3+</sup> enhanced CeO<sub>2</sub> host matrix for energy transfer from Ce<sup>3+</sup> to Tb<sup>3+</sup>*. RSC Advances, 3, 11, **2013**. p. 3623-3630.
- [223] Hussein, G.A.M. and B.A.A. Balboul, *Ytterbium oxide from different precursors: formation and characterization: Thermoanalytical studies*. Powder Technology, 103, 2, **1999**. p. 156-164.
- [224] Scherrer, P., *Bestimmung der Größe und der inneren Struktur von Kolloidteilchen mittels Röntgenstrahlen*. Nachrichten von der Gesellschaft der Wissenschaften zu Göttingen, Mathematisch-Physikalische Klasse, 1918, **1918**. p. 98-100.
- [225] Cullity, B.D., *Elements Of X-Ray Diffraction*. **1956**. Addison-Wesley Publishing Company, Inc. 531.
- [226] Stöhr, J., *NEXAFS Spectroscopy*. Springer Series in Surface Sciences. Vol. 25. **1992**. Springer-Verlag. 429.
- [227] Kang, M.-I., S.W. Kim, Y.-G. Kim, and J.-W. Ryu, *Dependence of the Optical Anisotropy of ZnO Thin Films on the Structural Properties*. Journal of the Korean Physical Society, 57, 2, **2010**. p. 389- 394.
- [228] Forouhi, A.R. and I. Bloomer, *Optical properties of crystalline semiconductors and dielectrics*. Physical Review B, 38, 3, **1988**. p. 1865-1874.
- [229] Forouhi, A.R. and I.I. Bloomer, *Optical dispersion relations for amorphous semiconductors and amorphous dielectrics*. Phys Rev B Condens Matter, 34, 10, **1986**. p. 7018-7026.
- [230] Yoshikawa, H. and S. Adachi, *Optical Constants of ZnO*. Japanese Journal of Applied Physics, 36, 10R, **1997**. p. 6237-6243.
- [231] Hall, E.H., *On a New Action of the Magnet on Electric Currents*. American Journal of Mathematics, 2, 3, **1879**. p. 287-292.
- [232] Thole, B.T., G. van der Laan, J.C. Fuggle, G.A. Sawatzky, R.C. Karnatak, and J.M. Esteva, *3d x-ray-absorption lines and the 3d<sup>9</sup>4f<sup>n+1</sup> multiplets of the lanthanides*. Physical Review B, 32, 8, **1985**. p. 5107-5118.
- [233] de Groot, F. and A. Kotani, *Core Level Spectroscopy of Solids*. Advances in Condensed Matter Science. **2008**. CRC Press.
- [234] Alim, K.A., V.A. Fonoberov, M. Shamsa, and A.A. Balandin, *Micro-Raman investigation of optical phonons in ZnO nanocrystals*. Journal of Applied Physics, 97, 12, **2005**. p. 124313.
- [235] Balestrieri, M., D. Pysch, J.P. Becker, M. Hermle, W. Warta, and S.W. Glunz, *Characterization and optimization of indium tin oxide films for heterojunction solar cells*. Solar Energy Materials and Solar Cells, 95, 8, **2011**. p. 2390-2399.
- [236] Macleod, H.A., *Thin-Film Optical Filters*. Third Edition ed. **2001**. Institute of Physics Publishing, Bristol and Philadelphia. 641.
- [237] Alaria, J., H. Bieber, S. Colis, G. Schmerber, and A. Dinia, *Absence of ferromagnetism in Al-doped Zn<sub>0.9</sub>Co<sub>0.10</sub>O diluted magnetic semiconductors*. Applied Physics Letters, 88, 11, **2006**. p. 112503.
- [238] Alaria, J., P. Turek, M. Bernard, M. Bouloudenine, A. Berbadj, N. Brihi, G. Schmerber, S. Colis, and A. Dinia, *No ferromagnetism in Mn doped ZnO semiconductors*. Chemical Physics Letters, 415, 4-6, **2005**. p. 337-341.

- 
- [239] Schugar, H.J., E.I. Solomon, W.L. Cleveland, and L. Goodman, *Simultaneous pair electronic transitions in ytterbium oxide*. Journal of the American Chemical Society, 97, 22, **1975**. p. 6442-6450.
- [240] Pandey, S.D., K. Samanta, J. Singh, N.D. Sharma, and A.K. Bandyopadhyay, *Anharmonic behavior and structural phase transition in Yb<sub>2</sub>O<sub>3</sub>*. AIP Advances, 3, 12, **2013**. p. 122123.
- [241] Nie, Z., J. Zhang, X. Zhang, X. Ren, G. Zhang, and X.-j. Wang, *Evidence for Visible Quantum Cutting via Energy Transfer in SrAl<sub>12</sub>O<sub>19</sub>:Pr,Cr*. Optics Letters, 32, 8, **2007**. p. 991-993.
- [242] Srivastava, A.M. and W.W. Beers, *Luminescence of Pr<sup>3+</sup> in SrAl<sub>12</sub>O<sub>19</sub>: Observation of Two Photon Luminescence in Oxide Lattice*. Journal of Luminescence, 71, 4, **1997**. p. 285-290.
- [243] Wegh, R.T., H. Donker, E.V.D. van Loef, K.D. Oskam, and A. Meijerink, *Quantum Cutting Through Downconversion in Rare-Earth Compounds*. Journal of Luminescence, 87-89, **2000**. p. 1017-1019.
- [244] Chanthima, N., K. Boonin, P. Limsuwan, and J. Kaewkhao, *Visible Luminescence of Pr<sup>3+</sup> in Bismuth Borate Glasses*. Advanced Materials Research, 770, **2013**. p. 59-63.
- [245] An, Y., C. Labbé, L. Khomenkova, M. Morales, X. Portier, and F. Gourbilleau, *Microstructure and Optical Properties of Pr<sup>3+</sup>-Doped Hafnium Silicate Films*. Nanoscale Research Letters, 8:43, **2013**.
- [246] Sato, Y., T. Mizoguchi, F. Oba, M. Yodogawa, T. Yamamoto, and Y. Ikuhara, *Identification of Native Defects Around Grain Boundary in Pr-Doped ZnO Bicrystal Using Electron Energy Loss Spectroscopy and First-Principles Calculations*. Applied Physics Letters, 84, 26, **2004**. p. 5311-5313.
- [247] Zhou, X., G. Wang, K. Zhou, and Q. Li, *Near-Infrared Quantum Cutting in Pr<sup>3+</sup>/Yb<sup>3+</sup> Co-Doped Transparent Tellurate Glass via Two Step Energy Transfer*. Optical Materials, 35, 3, **2013**. p. 600-603.
- [248] Wen, H. and P.A. Tanner, *Energy Transfer and Luminescence Studies of Pr<sup>3+</sup>, Yb<sup>3+</sup> Co-Doped Lead Borate Glass*. Optical Materials, 33, 11, **2011**. p. 1602-1606.
- [249] Guille, A., A. Pereira, and B. Moine, *NaLaF<sub>4</sub>:Pr<sup>3+</sup>, Yb<sup>3+</sup>, an efficient blue to near infra-red quantum cutter*. APL Materials, 1, 6, **2013**. p. 062106.
- [250] van der Ende, B.M., L. Aarts, and A. Meijerink, *Near-Infrared Quantum Cutting for Photovoltaics*. Advanced Materials, 21, 30, **2009**. p. 3073-3077.
- [251] Xian, F. and X. Li, *Effect of Nd doping level on optical and structural properties of ZnO:Nd thin films synthesized by the sol-gel route*. Optics & Laser Technology, 45, **2013**. p. 508-512.
- [252] Douayar, A., M. Abd-Lefdil, K. Nouneh, P. Prieto, R. Diaz, A.O. Fedorchuk, and I.V. Kityk, *Photoinduced Pockels effect in the Nd-doped ZnO oriented nanofilms*. Applied Physics B, 110, 3, **2013**. p. 419-423.
- [253] Rinnert, H., P. Miska, M. Vergnat, G. Schmerber, S. Colis, A. Dinia, D. Muller, G. Ferblantier, and A. Slaoui, *Photoluminescence of Nd-doped SnO<sub>2</sub> thin films*. Applied Physics Letters, 100, 10, **2012**. p. 101908 - 101908-3.
- [254] Liu, Y., W. Luo, R. Li, and X. Chen, *Optical Properties of Nd<sup>3+</sup> Ion-Doped ZnO Nanocrystals*. Journal of Nanoscience and Nanotechnology, 10, 3, **2010**. p. 1871-1876.
- [255] Fix, T., H. Rinnert, M.G. Blamire, A. Slaoui, and J.L. MacManus-Driscoll, *Nd:SrTiO<sub>3</sub> thin films as photon downshifting layers for photovoltaics*. Solar Energy Materials and Solar Cells, 102, **2012**. p. 71-74.
- [256] Petit, L., A. Svane, Z. Szotek, and W. Temmerman, *Electronic Structure of Rare Earth Oxides, in Rare Earth Oxide Thin Films*, Ch. 19, M. Fanciulli and G. Scarel, Editors. **2007**. Springer Berlin Heidelberg. p. 331-343.
- [257] Petit, L., A. Svane, Z. Szotek, and W.M. Temmerman, *First-principles study of rare-earth oxides*. Physical Review B, 72, 20, **2005**. p. 205118.
- [258] Meftah, A., J.-F. Wyart, J. Sinzelle, W.-Ü.L. Tchang-Brillet, N. Champion, N. Spector, and J. Sugar, *Spectrum and energy levels of the Nd<sup>4+</sup> free ion (Nd V)*. Physica Scripta, 77, 5, **2008**. p. 055302.
- [259] Li, L., S.W. Wang, G.Y. Mu, X. Yin, Y. Tang, W.B. Duan, and L.X. Yi, *Investigation on photoluminescence properties of CeO<sub>2</sub>/Sm<sub>2</sub>O<sub>3</sub> multilayer films based on Si substrates*. Physica Status Solidi (b), 251, 4, **2013**. p. 737-740.

- 
- [260] Collins, R.W. and A.S. Ferlauto, 2 - *Optical Physics of Materials*, in *Handbook of Ellipsometry*, H.G. Tompkins and E.A. Irene, Editors. **2005**. William Andrew Publishing, Norwich, NY. p. 93-235.
- [261] Wooten, F., *Optical Properties of Solids*. **1972**. Academic Press, New York.
- [262] Tauc, J., *Optical properties and electronic structure of amorphous Ge and Si*. *Materials Research Bulletin*, 3, 1, **1968**. p. 37-46.
- [263] Tauc, J., R. Grigorovici, and A. VanCu, *Optical Properties and Electronic Structure of Amorphous Germanium*. *Physica Status Solidi (b)*, 15, 2, **1966**. p. 627-637.

---

---

## Remerciements

Une thèse est un projet complexe qui se déroule sur trois ans au sein d'une ou plusieurs équipes de recherche. Le travail collaboratif et l'apport de chacun est essentiel pour une bonne réussite du projet.

Je voudrais donc ici remercier les personnes qui m'ont aidé dans cette tâche, en commençant par ceux qui m'ont directement encadré : Silviu Colis, Aziz Dinia, Abdelilah Slaoui et Gérard Ferblantier. Je remercie aussi les techniciens qui m'ont aidé dans certaines des mesures plus complexes. En particulier, je remercie Guy Schmerber pour (entre autre) son apport dans les mesures des rayons X et Raman ; Corinne Ulhaq-Bouillet pour les mesures TEM ; Cedric Leuvrey pour les mesures SEM ; Paul Bazylewski, Brett Leedahl et le Prof. Gap Soo Chang (University of Saskatchewan, Canada) pour les mesures NEXAFS ; Mathieu Gallart et Jérémy Bartringer pour leur aide dans les mesures de photoluminescence ; le Prof. Rodrigue Lardé de l'Université de Rouen pour les mesures de sonde atomique tomographique ; Dominique Muller pour les mesures RBS ; Gilles Versini et Sophie Barre pour les dépôts de PLD, Stéphane Roques et Claude Heitz pour la préparation des cellules solaires.

Je remercie aussi les personnes qui ont contribué à mon travail, mais dont l'apport n'a pas pu être mis en lumière dans cette thèse : Ernst Kurmaev (Institute of Metal Physics, Yekaterinburg, Russia), Maxime Bernard (Université de Strasbourg), Gaël Reecht et Guillaume Schull.

Je souhaite aussi remercier tous les doctorants et stagiaires qui ont contribué à mon travail et à tous ceux qui ont rendu agréable mon séjour au sein de l'IPCMS.

---

## Résumé en français

Suite à la demande croissante d'énergie dans un cadre où les ressources fossiles sont limitées et le nucléaire suscite de plus en plus de questions, un effort de recherche fondamentale important doit être produit pour tirer profit des énergies renouvelables. Ce projet s'inscrit dans le développement de la filière solaire photovoltaïque (PV).

A l'heure actuelle, le marché du photovoltaïque est toujours dominé par les cellules à base de silicium cristallin (90%). Le restant 10% du marché est exploité par les cellules à base de couches minces. Les autres technologies (organique, tandem, ...) n'occupent pour le moment qu'une part insignifiante de la production.

Cette situation est due aux nombreux avantages que l'utilisation du silicium réserve : bon rendement (14-20 %) et durabilité excellente des modules (> 20 ans), abondance et non-toxicité du matériau de base, facilité de production à grande échelle, grand nombre de fabricants grâce au marché de la microélectronique.

Le prix élevé de production du silicium cristallin, qui avait poussé initialement le développement d'autres technologies, n'est désormais plus d'actualité. Le coût de production des modules est descendu en dessous de 0.5 \$/W<sub>p</sub> en 2012 et devrait atteindre les 0.36 \$/W<sub>p</sub> en 2017 <sup>26</sup>. Une réduction ultérieure du prix de fabrication est une des promesses du nouveau procédé de fabrication de cristaux « mono-like » à partir de germes de silicium monocristallin.

Si d'autres technologies ont des coûts de production encore plus faibles (par exemple le PV organique), leur rendement et/ou durabilité n'ont pas encore atteint ceux des modules au silicium.

Depuis 2013, une nouvelle technologie semble avoir des chances d'occuper une part du marché. Il s'agit des cellules à base de perovskites, qui promettent des rendements comparables à ceux du silicium pour un coût très faible.

---

<sup>26</sup> Source: PV Technology and Cost Outlook, 2013-2017, GTM Research

Ce travail est focalisé sur les cellules à base de silicium, mais potentiellement utile pour toute cellule basé sur une simple jonction. Un des problèmes principaux des cellules à simple jonction est que la fraction spectrale effectivement utilisée par une cellule standard et convertie en photocourant est relativement faible par rapport au rayonnement solaire reçu. Ceci est dû à la fois à l'énergie perdue en relaxation thermique par les photons de haute énergie (30%) et à celle perdue par les photons de basse énergie non absorbés par le semi-conducteur (~20%), mais aussi aux pertes électriques intrinsèques (~20%). Le rendement de conversion maximal obtenu actuellement est de 25 % sur cellules basées sur un monocristal de silicium <sup>27</sup>, ce qui est près du rendement théorique de 30% prévu par Shockley et Queisser (Shockley et al. 1961). Pour cette raison, on observe actuellement un effort de R&D très important au niveau mondial visant à augmenter le rendement pour les cellules de nouvelle génération. Ne pouvant pas agir sur les pertes électriques intrinsèques, il ne reste qu'à essayer de rendre la cellule plus compatible avec le spectre solaire ou vice-versa. La première approche est celle des cellules tandem et demande une coûteuse <sup>28</sup> modification de la structure de la cellule. La deuxième, caractérisée par des coûts beaucoup moins importants, est celle de la division spectrale (qui utilise filtres et miroirs sélectifs (Zhao et al. 2012)) et de la conversion photonique (à travers les couches minces ou les concentrateurs fluorescents (Richards 2006, van Sark 2013)).

En particulier, l'utilisation des couches minces promet d'augmenter le rendement théorique d'à peu près 10 points (Richards 2006, Bünzli et al. 2010), sans modifier la structure de la cellule. Pour y parvenir, l'utilisation de matériaux capables d'effectuer une modification spectrale est nécessaire. Des trois processus principaux capables de convertir les photons, c'est-à-dire le down shifting (DS), la down conversion (DC) et la up conversion (UC), seulement les deux premiers seront pris en compte par la suite. L'objectif est de convertir les photons de grande énergie en photons dont l'énergie se situe dans le maximum d'efficacité des cellules. Cette modification spectrale sera mise en œuvre par des couches minces déposées en face avant des cellules et la conversion spectrale sera basée sur les remarquables

---

<sup>27</sup> Source: Record cell efficiency chart 2014, NREL

<sup>28</sup> > 40000 \$/m<sup>2</sup> pour la cellule tandem (III-V) qui détient le record actuel de rendement (43.5%).

propriétés de luminescence des ions de terre rare. Malgré leur prix élevé, la faible quantité utilisée fait que le cout lié à leur utilisation ne dépasse pas 1 centime de dollar par m<sup>2</sup> <sup>29</sup>.

Parmi les systèmes les plus prometteurs se situent les couches minces de ZnO et CeO<sub>2</sub> utilisées dans ce travail. Ces matrices hôtes seront dopées par différentes terres rares (Yb, Nd, Pr) afin d'obtenir les propriétés de conversion recherchées.

La raison pour laquelle nous avons choisi de travailler avec l'oxyde de zinc (ZnO) est que ce matériau est l'un des plus prometteurs pour substituer l'ITO (oxyde d'indium-étain) en tant que couche antireflet et électrode transparente. L'oxyde de cérium, qui n'est pas utilisé dans le PV mais qui est compatible avec des cellules à base de silicium, a été choisi en raison de la grande section efficace d'absorption dans l'ultraviolet (> 3.6 eV) et du rayon ionique (du Ce<sup>4+</sup>) proche de celui des dopants, ce qui devrait faciliter l'insertion.

Les techniques de dépôt utilisées sont la pulvérisation cathodique, qui est compatibles avec les procédés de fabrication actuels des cellules standards, et la déposition par ablation laser pulsé, qui permet un contrôle plus fin de la stœchiométrie grâce à l'incorporation du dopant dans les cibles qui peuvent être préparées au sein du laboratoire.

Les couches d'oxyde de zinc ont été déposées par pulvérisation cathodique magnétron à partir d'une cible de Zn pur sur des substrats de silicium cristallin et de verre. Grâce à la configuration « substrat-en-haut », le dépôt des couches dopées a été particulièrement simple. Un simple disque de terre rare métallique a été posé au-dessus d'une cible de Zn. Les études compositionnelles par spectroscopie à rétrodiffusion de Rutherford (RBS) et par sonde atomique tomographique ont montré que le dopage est uniforme. Les analyses structurales telles que la diffraction de rayons X (XRD) et la microscopie électronique en transmission (TEM et HR-TEM) indiquent que toutes les couches de ZnO présentent la structure attendue de type wurtzite avec une direction préférentielle [002] perpendiculaire à la surface du substrat. Aucune autre phase n'est visible dans la limite de la détection expérimentale (voir fig. 1).

---

<sup>29</sup> Un cout d'environ 1 millième de dollar par m<sup>2</sup> a été calculé à partir du prix moyen de 100 \$/Kg (Frontier Rare Earths, 2014) d'un oxyde de terre rare pur à 99%. Les pertes éventuelles liées à la technique de dépôt sont ignorées.

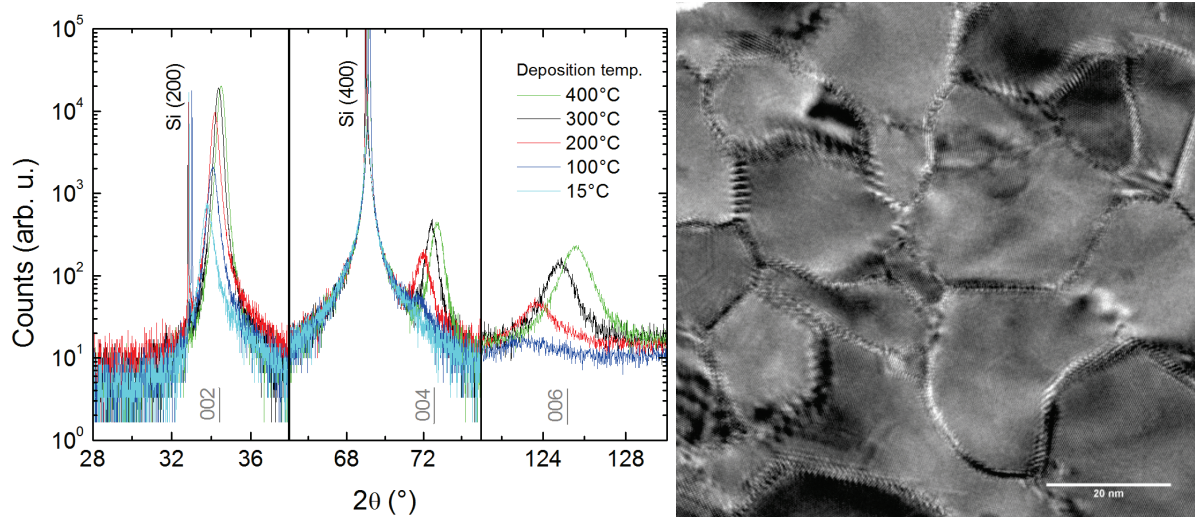


Fig. 1 – Exemples d’analyses structurales effectuées sur les couches de ZnO : a) diffraction de rayons X et b) vue plane obtenue par TEM d’une couche de ZnO de 100 nm déposée à 400°C.

L’étude très vaste effectuée sur les couches de ZnO déposées par pulvérisation cathodique a montré que toutes les terres rares utilisées (Yb, Pr, Nd) peuvent être bien insérées dans le ZnO en utilisant cette technique sans altérer sensiblement la structure de la couche et qu’elles peuvent être activées optiquement, à condition de choisir les bons paramètres d’élaboration et de recuit ex-situ.

Les études de photoluminescence ont montré que le transfert d’énergie entre le ZnO et la terre rare est toujours possible, mais avec une efficacité qui dépend de la terre rare (en fonction de la résonance entre niveaux et donc des mécanismes de transfert) et des autres chemins de recombinaison, fortement liés aux défauts présents dans le matériau. La figure 2 donne un exemple des spectres d’émission des couches de ZnO et de ZnO dopé au Nd et à l’Yb, si la couche est excitée avec de la lumière UV.

La première terre rare qui a été essayée est l’ytterbium. La raison derrière ce choix est que son état ionisé  $\text{Yb}^{3+}$  a un seul état excité  $^2\text{F}_{5/2}$  à environ 1.18 eV de l’état fondamentale  $^2\text{F}_{7/2}$  (Dieke 1968). Cela signifie que l’énergie des photons émis est juste au-dessus du gap du silicium (1.12 eV). Pour cette raison, la plupart de matériaux étudiés dans la littérature et visant la down-conversion sont basés sur des couples  $\text{Ln}^{3+}\text{-Yb}^{3+}$  (Chen et al. 2012). A cause de l’écart énergétique entre le gap du ZnO et l’unique transition de l’Yb, on ne peut pas s’attendre à une down conversion en utilisant ce système, mais seulement à du down-shifting. L’optimisation des paramètres menant au plus haut transfert

énergétique et donc aux down-shifting plus efficace s'est traduite dans une première publication (Balestrieri et al. 2013).

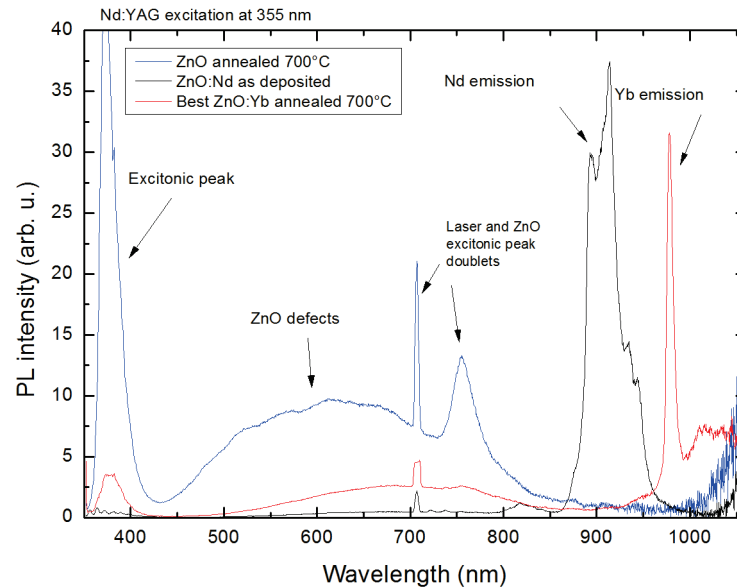


Fig. 2 – Spectres de photoluminescence des couches de ZnO, ZnO:Yb et ZnO:Nd suite à l'excitation du ZnO à 355nm.

Ensuite, le dopage et le codopage avec d'autres terres rares comme le praséodyme (Pr) et le néodyme (Nd) a été effectué. L'émission du Pr s'est avérée plus faible de celle de l'Yb, ce qui indique que le transfert à partir du ZnO est moins efficace. Les mesures de fluorescence près du front d'absorption de rayons X (NEXAFS) ont montré la présence de l'état d'oxydation 4+, qui n'est pas luminescent.

Les analyses de photoluminescence en fonction de l'excitation (PLE) à température ambiante et à basse température ont permis de localiser les niveaux d'absorption et d'émission et obtenir ainsi un diagramme presque complet des états excités du  $\text{Pr}^{3+}$  dans le ZnO. Pour ce qui concerne le codopage avec praséodyme et ytterbium, il en résulte que les transitions  $^3\text{P}_0 \rightarrow ^1\text{G}_4$  et  $^1\text{G}_4 \rightarrow ^3\text{H}_4$  ne sont pas en bonne résonance avec la transition de l'Yb, ce qui pourrait expliquer pourquoi aucun transfert n'a été observé dans les couches codopées. Les informations obtenues et en particulier le diagramme d'énergie

des niveaux du  $\text{Pr}^{3+}$  et de  $\text{Yb}^{3+}$  dans le ZnO ont valu une deuxième publication (Balestrieri, Gallart, et al. 2014).

Le néodyme a donné des résultats très prometteurs avec une luminescence beaucoup plus intense que celle de  $\text{Yb}^{3+}$ . En particulier, la température de 400 °C s'est avérée critique pour l'apparition de nouvelles raies d'émission, vraisemblablement liées à la présence de d'un nouveau site actif pour la terre rare. Les résultats se trouvent résumés dans une troisième publication (Balestrieri, Colis, et al. 2014).

La figure 3 résume les transitions principales et les niveaux d'énergie des trois terres rares dans le ZnO, obtenus à partir des mesures de PL et PLE.

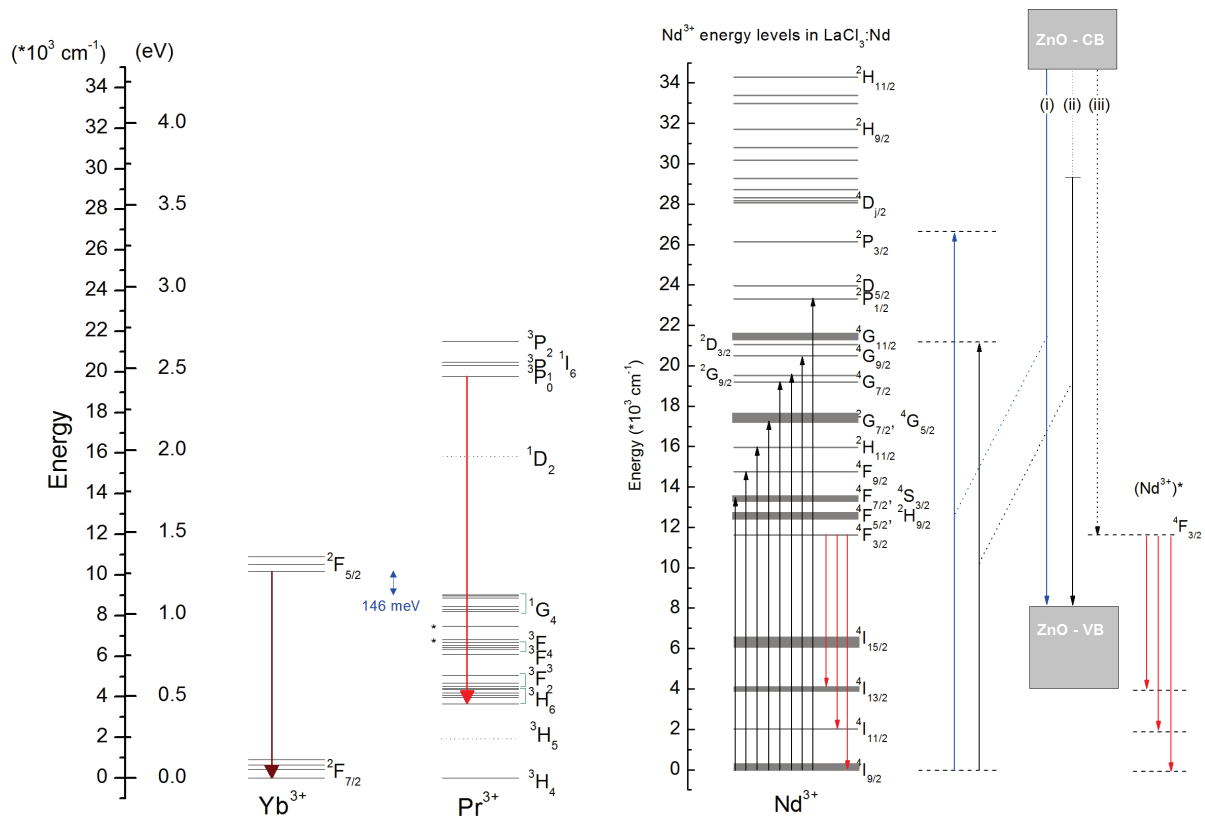


Fig. 3 – Transitions principales et niveaux d'énergie des ions  $\text{Yb}^{3+}$ ,  $\text{Pr}^{3+}$  et  $\text{Nd}^{3+}$  dans le ZnO. Les mécanismes de transfert possibles sont schématisés pour le  $\text{Nd}^{3+}$ .

Si les terres rares sont optiquement actives et démontrent que ces matériaux peuvent être utilisés pour la conversion photonique, il y a d'autres paramètres à considérer pour des applications photovoltaïques. Des mesures de spectrophotométrie et d'ellipsométrie ont permis de vérifier que la compatibilité optique avec des cellules au silicium est préservée suite au dopage. Par contre, toutes les

couches de ZnO déposées dans des conditions favorables à la conversion photonique présentent une faible conductivité. Ce fait a été expliqué par une quantité trop importante d'oxygène dans le ZnO, un matériau dont la conductivité est basée sur les lacunes d'oxygène. L'insertion d'un deuxième dopant comme l'Al pourrait résoudre le problème, mais l'effet d'une telle insertion n'a pas été testé dans ce travail. Le fait que l'insertion et l'activation des terres rares demandent un apport en oxygène conséquent pendant la croissance nous montre combien les terres rares soient sensibles à cet élément et explique pourquoi nous avons souvent attribué les grandes différences en PL observées à des différents types de défauts liés à l'oxygène et non pas aux propriétés structurelles des couches, qui ne présentent pas des variations très prononcées.

Il est difficile d'estimer correctement la stœchiométrie de l'oxygène dans les couches et encore plus de détecter tous les différents types de défauts. Même en utilisant une technique très sophistiquées comme la NEXAFS, nous n'avons pas pu établir un lien certain entre la luminescence un type de défaut. Il faut dire que même une très petite population de défauts qui serait difficile à détecter peut avoir un effet important sur l'activité optique de ces matériaux.

La présence de plusieurs types de défauts nous a conduits à proposer des mécanismes de transfert d'énergie différent pour les différentes terres rares. Cela peut sembler arbitraire, mais nous avons montré que chaque terre rare se comporte différemment si l'on change la température de dépôt, celle de recuit ou la quantité d'oxygène dans le deux processus. Comme ces paramètres ont une influence sur la population de défauts, nous pouvons imaginer que les différents comportements soient dus à des mécanismes différents.

Des trois terres rares testés dans le ZnO, le Nd est la seule qui offre un rendement optique de down-shifting acceptable à une température relativement basse d'élaboration (400 °C) compatible avec la technologie typique des cellules solaires au silicium. C'est donc une couche de ZnO:Nd qui a été sélectionné pour un test sur cellule.

Pour résumer, l'oxyde de zinc s'est révélé une excellente matrice capable d'accueillir des impuretés de grande taille comme les ions de terre rares sans que la structure cristalline en soit sensiblement

dégradée. Bien que ces ions ne soient pas actifs électriquement (toutes les couches sont très résistives), l'objectif principal qui était l'étude des propriétés de conversion photonique a été atteint. En particulier, le transfert d'énergie entre le ZnO et les terres rares a pu être démontré.

Dans un deuxième temps, les propriétés de conversion photonique de l'oxyde de cérium dopé aux terres rares ont été étudiées. En raison du grand rayon ionique du cérium, l'insertion du dopant se fait plus facilement dans cette matrice. En conséquence, les propriétés de luminescence sont très différentes par rapport au ZnO. L'analyse de l'absorption optique des cibles préparées par frittage et de leur activité optique nous a montré que l'émission est particulièrement efficace pour des faibles concentrations et que le  $\text{CeO}_2$  est un matériau plus compliqué de ce qu'on pourrait imaginer à cause de sa non-stœchiométrie naturelle.

Les couches minces ont été déposées par ablation laser sur du silicium cristallin et montrent que les meilleurs résultats s'obtiennent avec de hautes températures. Cependant, des résultats acceptables sont atteints déjà dans des conditions compatibles avec des cellules solaires ( $T = 400\text{ °C}$ ).

Tous les films de  $\text{CeO}_2$  sont polycristallins et les cristallites montrent une orientation partielle (voir fig. 4). L'insertion jusqu'à 10 % de terre rare ne modifie pas la structure des couches et permet de garder des propriétés optiques compatibles avec les cellules solaires.

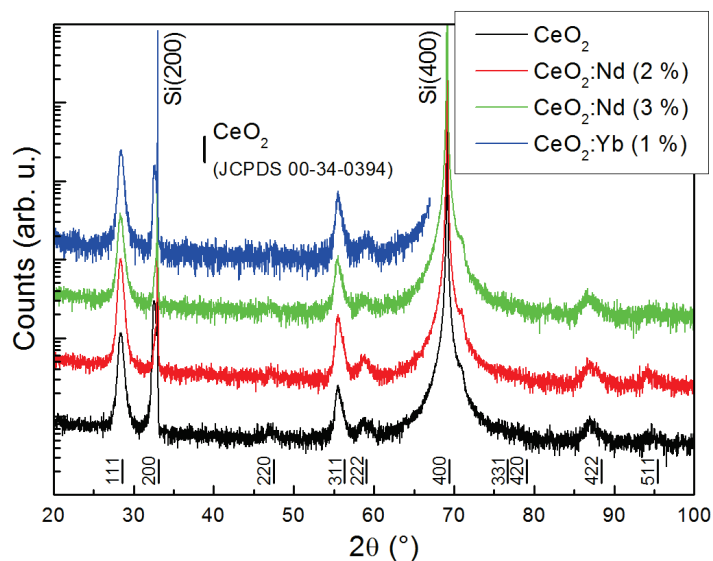


Fig. 4 – Diffractogrammes des rayons X de couches de  $\text{CeO}_2$  dopées aux terres rares.

L'expérience acquise avec le ZnO nous a permis d'aller rapidement vers de paramètres de dépôt qui donnent lieu à une émission efficace. Les analyses de PL et PLE ont montré qu'un transfert d'énergie à lieu entre la matrice et le dopant (voir fig. 5) et qu'il est probablement lié à la présence de ions  $Ce^{3+}$ . Des trois terres rares testées (Nd, Yb, Pr), seul le Pr ne montre pas d'activité optique. Une oxydation de cet élément en  $Pr^{4+}$  à cause de la présence de  $Ce^{4+}$  est probable. Cette étude a montré que le Nd et le Sm (présent comme impureté dans la poudre de départ) sont très prometteur pour la conversion photonique. Les résultats pour ce type de matrice font l'objet de deux publications en cours de rédaction.

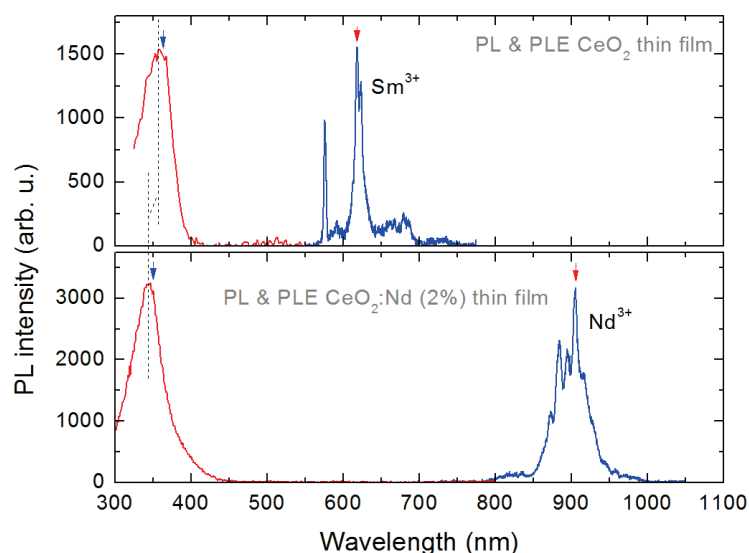


Fig. 5 – Spectres de PL (en bleu) et de PL en fonction de l'excitation (en rouge) du Nd<sup>3+</sup> et du Sm<sup>3+</sup> dans des couches minces de CeO<sub>2</sub>.

L'influence de ces couches sur le rendement des cellules a été mesurée afin de valider expérimentalement ces nouveaux systèmes en vue d'une utilisation industrielle. Les résultats de réponse spectrale montrent que même les couches les plus prometteuses (dans les deux cas des couches dopées au Nd) n'ont pas d'effet positif sur le rendement de la cellule, ce qui indique que le transfert entre la matrice et le dopant n'est pas assez efficace. Les raisons peuvent être multiples et la difficulté d'obtenir des matériaux efficaces dans la conversion de photons ont été discuté dans la partie

introduitive de ce travail. En effet, le matériau idéal pour la conversion photonique doit avoir beaucoup de qualités et ce n'est pas évident de trouver de matériaux réels avec ces caractéristiques.

Par exemple, même dans le cas le plus simple, le processus de conversion photonique est un processus à plusieurs étapes qui implique des résonances entre transitions électroniques, des transitions interdites au premier ordre et souvent l'interaction avec des phonons. De plus, le site d'absorption et les différents ions de terre rare sur lesquels a lieu l'émission sont souvent séparés dans l'espace. L'efficacité de ces processus dans les matériaux réels est loin d'être idéale et peut réduire l'efficacité de plusieurs ordres de grandeur.

Malgré ces résultats, l'étude de ces systèmes est fondamentale et permet de comprendre comment concevoir un matériau plus performant. Ce travail nous a permis d'obtenir des informations importantes sur le ZnO et le CeO<sub>2</sub> dopés avec différentes terres rares et montre que les oxydes dopés aux terres rares sont prometteurs pour le photovoltaïque, mais aussi que la route est encore longue avant une application industrielle.

## Références

Balestrieri, M., S. Colis, M. Gallart, G. Ferblantier, D. Muller, P. Gilliot, P. Bazylewski, G. S. Chang, A. Slaoui and A. Dinia (2014). "Efficient energy transfer from ZnO to Nd<sup>3+</sup> ions in Nd-doped ZnO films deposited by magnetron reactive sputtering." Journal of Materials Chemistry C **2**(43): 9182-9188.

Balestrieri, M., G. Ferblantier, S. Colis, G. Schmerber, C. Ulhaq-Bouillet, D. Muller, A. Slaoui and A. Dinia (2013). "Structural and Optical Properties of Yb-Doped ZnO Films Deposited by Magnetron Reactive Sputtering for Photon Conversion." Solar Energy Materials and Solar Cells **117**(0): 363-371.

Balestrieri, M., M. Gallart, M. Ziegler, P. Bazylewski, G. Ferblantier, G. Schmerber, G. S. Chang, P. Gilliot, D. Muller, A. Slaoui, S. Colis and A. Dinia (2014). "Luminescent Properties and Energy Transfer in Pr<sup>3+</sup> Doped and Pr<sup>3+</sup>-Yb<sup>3+</sup> Co-doped ZnO Thin Films." The Journal of Physical Chemistry C **118**(25): 13775-13780.

Bünzli, J.-C. G. and S. V. Eliseeva (2010). "Lanthanide NIR luminescence for telecommunications, bioanalyses and solar energy conversion." Journal of Rare Earths **28**(6): 824-842.

Chen, D., Y. Wang and M. Hong (2012). "Lanthanide nanomaterials with photon management characteristics for photovoltaic application." Nano Energy **1**(1): 73-90.

Dieke, G. H. (1968). Spectra and Energy Levels of Rare Earth Ions in Crystals. New York, Interscience Publishers.

Richards, B. S. (2006). "Enhancing the Performance of Silicon Solar Cells via the Application of Passive Luminescence Conversion Layers." Solar Energy Materials and Solar Cells **90**(15): 2329-2337.

Richards, B. S. (2006). "Luminescent Layers for Enhanced Silicon Solar Cell Performance: Down-Conversion." Solar Energy Materials and Solar Cells **90**(9): 1189-1207.

Shockley, W. and H. J. Queisser (1961). "Detailed Balance Limit of Efficiency of p-n Junction Solar Cells." Journal of Applied Physics **32**(3): 510-519.

van Sark, W. G. J. H. M. (2013). "Luminescent solar concentrators – A low cost photovoltaics alternative." Renewable Energy **49**: 207-210.

Zhao, Y., M.-Y. Sheng, W.-X. Zhou, Y. Shen, E.-T. Hu, J.-B. Chen, M. Xu, Y.-X. Zheng, Y.-P. Lee, D. W. Lynch and L.-Y. Chen (2012). "A solar photovoltaic system with ideal efficiency close to the theoretical limit." Optics Express **20**(S1): A28-A38.

# Oxydes transparents conducteurs et convertisseurs de photons pour des applications photovoltaïques

## Résumé

L'objectif de cette thèse était d'étudier les propriétés de conversion de photons des ions terres rares insérées dans des matrices d'oxydes transparents en vue d'application photovoltaïques. En particulier, le but était de fonctionnaliser des couches minces déjà utilisées dans les cellules solaires comme couches antireflet ou oxydes transparents conducteurs.

Nous avons donc sélectionné deux matériaux ( $\text{ZnO}$  et  $\text{CeO}_2$ ) compatibles avec les cellules solaires au silicium.

Ce travail a montré que les couches minces dopées aux terres rares peuvent être utilisées pour convertir les photons dans des applications photovoltaïques, mais qu'il n'est pas facile d'obtenir des rendements élevés.

Cependant, nous avons obtenu des informations très importantes sur l'influence de la matrice sur les propriétés de conversion des terres rares et sur les mécanismes de transfert d'énergie entre la matrice et la terre rare.

**Mots-clés** : conversion photonique, terres rares, photovoltaïque,  $\text{ZnO}$ ,  $\text{CeO}_2$

## Résumé en anglais

The objective of this thesis was to investigate the photon converting properties of rare earths (RE) ions embedded in transparent oxide hosts in view of potential application on silicon solar cells. In particular, the goal was to functionalize thin films that are already used in solar cells such as anti-reflection coatings or transparent conductive oxides.

Two host materials ( $\text{ZnO}$  and  $\text{CeO}_2$ ) have been selected, which are compatible with silicon solar cells.

This work shows that RE-doped transparent oxide films are a viable low-cost solution for obtaining photon-converting layers that can be applied on solar cells, but that achieving high efficiencies is much more difficult than it might appear in theory.

Nevertheless, very valuable information has been obtained on the effect of the host material on the photon management properties and on the energy transfer mechanisms in these systems. In particular, the energy level diagram of some of the rare earth ions in the specific matrices has been reconstructed.

**Mots-clés** : photon conversion, rare earths, photovoltaics,  $\text{ZnO}$ ,  $\text{CeO}_2$